ISSN en trámite

Geofísica Internacional

Revista Trimestral Publicada por el Instituto de Geofísica de la Universidad Nacional Autónoma de México

México
Volume 53 Number 3
July - September
2014

— Geofísica Internacional —

GEOFÍSICA INTERNACIONAL, Año 53, Vol. 53, Núm. 3, julio - septiembre de 2014 es una publicación trimestral, editada por la Universidad Nacional Autónoma de México, Ciudad Universitaria, Alcaldía Coyoacán, C.P. 04150, Ciudad de México, a través del Instituto de Geofísica, Circuito de la Investigación Científica s/n, Ciudad Universitaria, Alcaldía Coyoacán, C.P. 04150, Ciudad de México, Tel. (55)56 22 41 15. URL: http://revistagi.geofisica.unam.mx, correo electrónico: revistagi@igeofisica.unam.mx. Editora responsable: Andrea Rostan Robledo. Certificado de Reserva de Derechos al uso Exclusivo del Título: 04-2022-081610251200-102, ISSN: en trámite, otorgados por el Instituto Nacional del Derecho de Autor (INDAUTOR). Responsable de la última actualización Saúl Armendáriz Sánchez, Editor Técnico. Fecha de la última modificación: 30 de junio 2014, Circuito de la Investigación Científica s/n, Ciudad Universitaria, Alcaldía Coyoacán, C.P. 04150, Ciudad de México.

Geofísica Internacional

Vol. 53, Núm. 3, julio-septiembre de 2014

Contents

Geofísica
Internacional

Geofísica Internacional (2014) 53-3: 221-239

Original paper

Neural estimation of strong ground motion duration

Leonardo Alcántara Nolasco*, Silvia García, Efraín Ovando-Shelley and Marco Antonio Macías Castillo

Received: November 09, 2012; accepted: November 19, 2013; published on line: July 01, 2014

Resumen

Este artículo presenta y discute el uso de las redes neuronales para determinar la duración de los movimientos fuertes del terreno. Para tal efecto se desarrolló un modelo neuronal, utilizando datos acelerométricos registrados en las ciudades mexicanas de Puebla y Oaxaca, que predice dicha duración en términos de la magnitud, distancia epicentral, profundidad focal, caracterización del suelo y el azimut. Por lo que, el modelo considera los efectos tanto de la zona sismogénica como del tipo de suelo en la duración del movimiento. El esquema final permite una estimación directa de la duración a partir de variables de fácil obtención y no se basa en hipótesis restrictivas. Los resultados presentados en este artículo indican que la alternativa del cómputo aproximado, particularmente las redes neuronales, es una poderosa aproximación que se basa en los registros sísmicos para explorar y cuantificar los efectos de las condiciones sísmicas y de sitio en la duración del movimiento. Un aspecto esencial y significante de este nuevo modelo es que a pesar de ser extremadamente simple ofrece estimaciones de duración con notable eficiencia. Adicional e importante son los beneficios que arroja esta simplicidad sobre la separación natural de los efectos de la fuente, patrón o directividad y de sitio además de la eficiencia computacional.

Palabras clave: duración del movimiento de terreno, parámetros de movimientos de terreno, duración significativa, intensidad de Árias, redes neuronales, cómputo aproximado.

Abstract

This paper presents and discusses the use of neural networks to determine strong ground motion duration. Accelerometric data recorded in the Mexican cities of Puebla and Oaxaca are used to develop a neural model that predicts this duration in terms of the magnitude, epicenter distance, focal depth, soil characterization and azimuth. According to the above the neural model considers the effect of the seismogenic zone and the contribution of soil type to the duration of strong ground motion. The final scheme permits a direct estimation of the duration since it requires easy-to-obtain variables and does not have restrictive hypothesis. The results presented in this paper indicate that the soft computing alternative, via the neural model, is a reliable recording-based approach to explore and to quantify the effect of seismic and site conditions on duration estimation. An essential and significant aspect of this new model is that, while being extremely simple, it also provides estimates of strong ground motions duration with remarkable accuracy. Additional but important side benefits arising from the model's simplicity are the natural separation of source, path, and site effects and the accompanying computational efficiency.

Key words: strong ground motion duration, ground motion parameters, significant duration, Árias Intensity, neural networks, soft computing.

L. Alcántara Nolasco
S. García
E. Ovando-Shelley
M. Antonio Macías Castillo
Instituto de Ingeniería
Universidad Nacional Autónoma de México
Delegación Coyoacán, 04510
México D.F., México
Corresponding author: leonardo@pumas.ii.unam.mx

Introduction

The principal objective of engineering seismology is to supply quantitative estimations of expected ground-motions for earthquake-resistant design, evaluation of seismic hazards, and seismic risk assessment through the proper characterization of complex time series (accelerograms). Since the first strong-motion accelerograms were recorded a large number of parameters have been defined to characterize movements. The usefulness of strong-motion parameters is dependent primarily upon their intended use. The parameters that can be employed in earthquake-resistant design are few and are directly related to the methods of structural analysis used in current practice. Once a parameter has been selected to characterize the ground motion, it is necessary to develop relationships between this parameter and important seismic features as earthquake source, travel path, and site conditions.

The essence of such predictive relationships for the duration of strong motions depends very heavily on the way duration is defined. In fact many strong-motion duration definitions have been presented; however, all of them attempt to isolate a certain portion of the time series where strongest motion occurs. In general terms, it has been accepted that all of these definitions can be grouped into one of four generic categories (Bommer and Martínez-Pereira, 1996): i) the bracketed duration, the interval between the first and last excursion of particular threshold amplitude, ii) the uniform duration, the sum of all of the time intervals during which the amplitude of the record is above the threshold, iii) the significant duration, which is determined from the Husid plot (Husid, 1969) based on the interval during which a certain portion of the total Árias intensity is accumulated and iv) the structural response duration, determined by applying one of the above three categories to the response of a specific single-degree-of-freedom oscillator.

In this investigation, and considering the definition of significant duration, the connection between data and knowledge is found using a soft computing SC tool: the neural networks NNs. This alternative improves the theory and understanding of the driven parameters (of all kinds including indeterminate ones, possibly expressed in words) of ground-motion duration behavior. SC, NNs particularly, utilize a discovery approach to examine the multidimensional data relationships simultaneously and to identify those that are unique or frequently represented, permitting the acquisition of structured knowledge.

A neuronal empirical model for strong motion duration is proposed here, derived from seismic information registered in Puebla and Oaxaca, México. This model predicts the strong ground motion duration as a function of earthquake magnitude, epicentral distance, focal depth, azimuth (established from epicenters to stations) and soil characterization. The final scheme permits a direct estimation of the duration since it requires easy-to-obtain variables and does not have restrictive hypothesis

Soft Computing

The term Soft Computing SC represents the combination of emerging problem-solving technologies such as Fuzzy Logic FL, Probabilistic Reasoning PR, Neural Networks NN, and Genetic Algorithms GAs. Each of these provides complementary reasoning and searching methods to solve complex, real-world problems. In ideal problem formulations, the systems to be modeled or controlled are described by complete and precise information. In these cases, formal reasoning systems, such as theorem proofs, can be used to attach binary true or false values to statements describing the state or behavior of the physical system.

Soft Computing technologies are flexible computing tools to perform these approximate reasoning and search tasks handling imperfect information. According to Zadeh (Fuzzy Logic pioner): ''…in contrast to traditional, hard computing, soft computing is tolerant of imprecision, uncertainty, and partial truth.'' The only obvious common point between SC tools (Fuzzy Logic FL, Neural Networks NNs and Genetic Algorithms GAs) is that they have been inspired by the living: the imprecision of human language and its efficiency in conveying and transmitting information for FL, the architecture of the brain for NNs, and the reproduction of living beings for GAs.

Neural Networks

This section will briefly explain the theory of neural networks NN. For a more in depth explanation of these concepts consult Hassoun, (1995); Hertz *et al*., (1991) and Tettamanzi and Tomassini, (2001).

In the brain, a NN is a network consisting of connected neurons. The nucleus is the center of the neuron and it is connected to other nuclei through the dendrites and the axon. This connection is called a synaptic connection. The neuron can fire electric pulses through its synaptic connections, which are received

by the dendrites of other neurons. Figure 1 shows how a simplified neuron looks like. When a neuron receives enough electric pulses through its dendrites, it activates and fires a pulse through its axon, which is then received by other neurons. In this way information can propagate through the NN. The synaptic connections change throughout the lifetime of a neuron and the amount of incoming pulses needed to activate a neuron (the threshold) also change. This process allows the NN to learn (Tettamanzi and Tomassini, 2001).

Mimicking the biological process the artificial NN are not "intelligent" but they are capable for recognizing patterns and finding the rules behind complex data-problems. A single artificial neuron can be implemented in many different ways. The general mathematic definition is given by equation 1.

$$y(x) = g\left(\sum_{i=0}^{n} w_i x\right) \tag{1}$$

where x is a neuron with n input dendrites $(x_0, \ldots, x_n)$ and one output axon $y(x)$ and $(w_0, \ldots, w_n)$ are weights determining how much the inputs should be weighted; g is an activation function that weights how powerful the output (if any) should be from the neuron, based on the sum of the input. If the artificial neuron mimics a real neuron, the activation function g should be a simple threshold function returning 0 or 1. This is not the way artificial neurons are usually implemented; it is better to have a smooth (preferably differentiable) activation function (Bishop, 1996). The output from the activation function varies between 0 and 1, or between -1 and 1, depending on which activation function is used. The inputs and the weights are not restricted in the same way and can in principle be between -∞ and +∞, but they are very often small values centered on zero (Broomhead and Lowe, 1988). Figure 2 provides a schematic view of an artificial neuron.

As mentioned earlier there are many different activation functions, some of the most commonly used are threshold (Eq. 2), sigmoid (Eq.3) and hyperbolic tangent (Eq.4).

$$g(x) = \begin{cases} 1 \; if \; x + t > 0 \\ 0 \; if \; x + t \leq 0 \end{cases} \tag{2}$$

$$g(x) = \frac{1}{1 + e^{-2s(x-t)}} \tag{3}$$

$$g(x) = \tanh(s(x+t)) = \frac{\sinh(s(x+t))}{\cosh(s(x+t))} = \frac{e^{s(x+t)} - e^{-s(x+t)}}{e^{s(x+t)} + e^{-s(x+t)}} = \frac{e^{2(s(x+t))} - 1}{e^{2(s(x+t))} + 1} \tag{4}$$

where t is the value that pushes the center of the activation function away from zero and s is a steepness parameter. Sigmoid and hyperbolic tangent are both smooth differentiable functions, with very similar graphs. Note that the output range of the hyperbolic tangent goes from -1 to 1 and sigmoid has outputs that range from 0 to 1. A graph of a sigmoid function is given in Figure 3 to illustrate how the activation function looks like. The t parameter in an artificial neuron can be seen as the amount of incoming pulses needed to activate a real neuron. A NN learns because this parameter and the weights are adjusted.

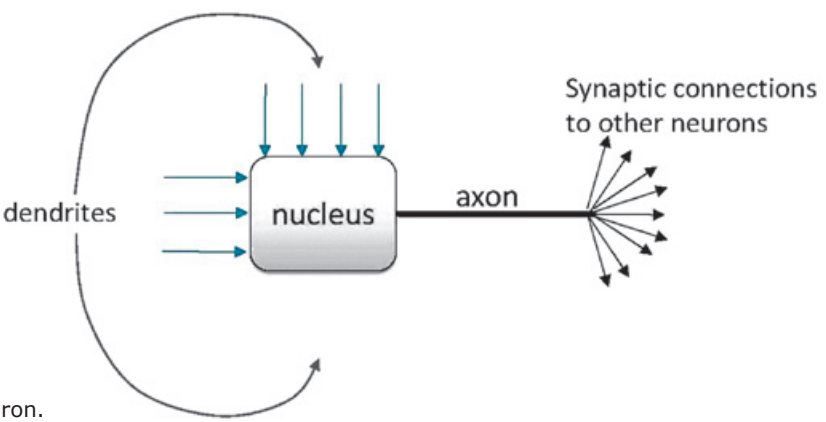

Figure 1. Simplified biological neuron.

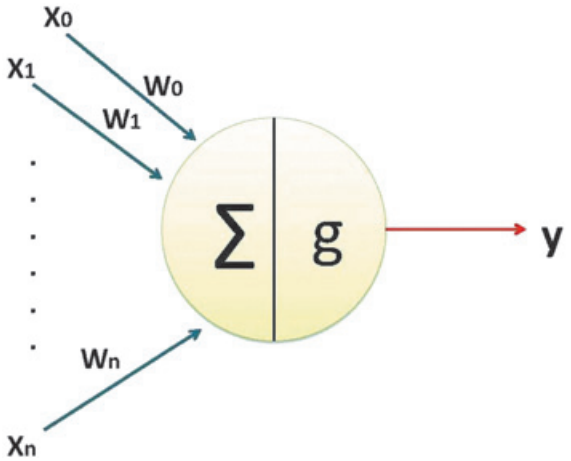

Figure 2. An artificial neuron.

NN architecture

The NN used in this investigation is a multilayer feedforward neural network MFNN, which is the most common NN. In a MFNN, the neurons are ordered in layers, starting with an input layer and ending with an output layer. There are a number of hidden layers between these two layers. Connections in these networks only go forward from one layer to the next (Hassoun, 1995). They have two different phases: a training phase (sometimes also referred to as the learning phase) and an execution phase. In the training phase the NN is trained to return a specific output given particular inputs, this is done by continuous training on a set of data or examples. In the execution phase the NN returns outputs on the basis of inputs. In the NN execution an input is presented to the input layer, the input is propagated through all the layers (using equation 1) until it reaches the output layer, where the output is returned. Figure 4 shows a MFNN where all the neurons in each layer are connected to all the neurons in the next layer, what is called a fully connected network.

Two different kinds of parameters can be adjusted during the training, the weights and the t value in the activation functions. This is impractical and it would be easier if only one of the parameters were to be adjusted. To cope with this problem a bias neuron is introduced. The bias neuron lies in one layer, connected to all the neurons in the next layer, but none in the previous layer and it always emits 1. A modified equation for the neuron, where the weight for the bias neuron is represented as w_n+1, is shown in equation 5.

$$y(x) = g\left(w_{n+1}\sum_{i=0}^{n} w_i x_i\right) \tag{5}$$

Adding the bias neuron allows the removal of the t value from the activation function, leaving the weights to be adjusted, when the NN is being trained. A modified version of the sigmoid function is shown in equation 6.

$$g(x) = \frac{1}{1+e^{-2sx}} \tag{6}$$

The t value cannot be removed without adding a bias neuron, since this would result in a zero output from the sum function if all inputs where zero, regardless of the values of the weights

Training a NN

When training a NN with a set of input and output data, we wish to adjust the weights in the NN to make the NN gives outputs very close to those presented in the training data. The training process can be seen as an optimization problem, where the mean square error between neural and desired outputs must be minimized. This problem can be solved in many different ways, ranging from standard optimization heuristics, like simulated annealing, to more special optimization techniques like genetic algorithms or specialized gradient descent algorithms like backpropagation BP.

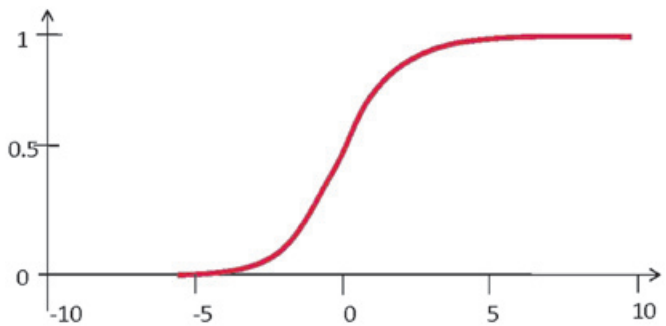

Figure 3. A graph of a sigmoid function with s= 0.5 and t= 0

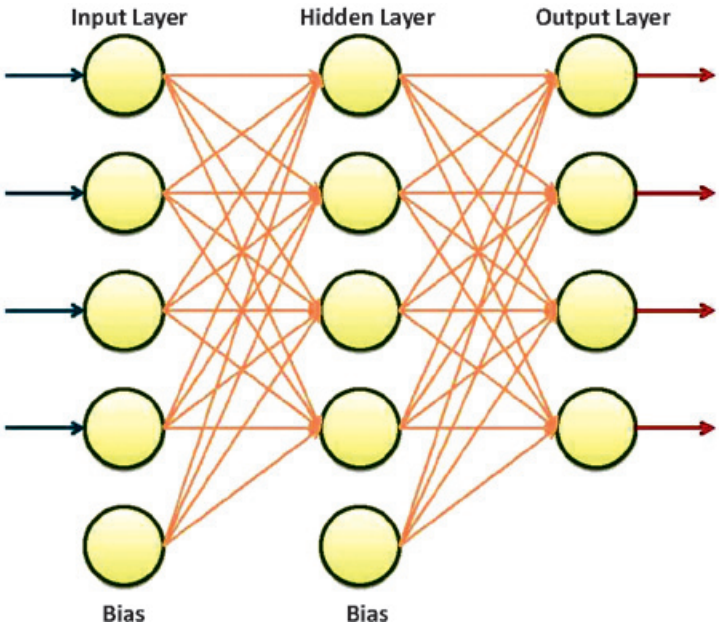

Figure 4. A fully connected multilayer feedforward network with one hidden layer and bias neurons

The backpropagation algorithm

The BP algorithm works in much the same way as the name suggests: after propagating an input through the network, the error is calculated and the error is propagated back through the network while the weights are adjusted in order to make the error smaller. Although we want to minimize the mean square error for all the training data, the most efficient way of doing this with the BP algorithm, is to train on data sequentially one input at a time, instead of training the combined data.

BP application steps. First the input is propagated through the NN to the output. Then the error e_k on a single output neuron k can be calculated as:

$$e_k = d_k - y_k \tag{7}$$

where y_k is the calculated output and d_k is the desired output of neuron k. This error value is used to calculate a δ_k value, which is again used for adjusting the weights. The δ_k value is calculated by:

$$\delta_k = e_k g'(y_k) \tag{8}$$

where g' is the derived activation function. When the δ_k value is calculated, the δ_j values can be calculated for preceding layers. The δ_j values of the previous layer are calculated from the δ_k values of this layer by the following equation:

$$\delta_j = \eta g'(y_j) \sum_{k=0}^{K} \delta_k w_{jk} \tag{9}$$

where K is the number of neurons in this layer and η is the learning rate parameter, which determines how much the weight should be adjusted. The more advanced gradient descent algorithms does not use a learning rate, but a set of more advanced parameters that makes a more qualified guess to how much the weight should be adjusted. Using these δ values, the Δw values that the weights should be adjusted by, can be calculated:

$$\Delta w_{jk} = \delta_j y_k \tag{10}$$

The Δw_{jk} value is used to adjust the weight w_{jk} by $w_{jk} = w_{jk} + \Delta w_{jk}$ and the BP algorithm moves on to the next input and adjusts the weights according to the output. This process goes on until a certain stop criteria is reached. The stop criterion is typically determined by measuring the mean square error of the training data while training with the data, when this mean square error reaches a certain limit, the training is stopped.

In this section the mathematics of the BP algorithm have been briefly discussed, but since this report is mainly concerned with the implementation of NN, the details necessary for implementing the algorithm has been left out (for details see Hassoun, 1995 and Hertz *et al*., 1991).

Duration: predictive relationships

Predictive relationships usually express ground motion parameters as functions of earthquake magnitude, distance, source characteristics, site characteristics, etc. A typical predictive relationship may have the form:

$$InY = C_1 + C_2 M + C_3 M^{C4} + C_5 In[R + C_6 \exp(C_7 M)] + C_8 R + f(source) + f(site)$$

$$\sigma_{lnY} = C_9 \quad (12)$$

where Y is the ground motion parameter of interest, M the magnitude of the earthquake, R a measure of the distance from the source to the site being considered. C_1-C_9 are constants to be determined. The σ_{lnY} term describes the uncertainty in the value of the ground motion parameter given by the predicative relationship.

Regarding duration parameters many types of predictive relationships have been proposed (Bommer and Martinez-Pereira, 1999), but bracketed duration and significant duration relationships are the most commonly used. The former is defined as the time elapsed between the first and last excursions beyond a specified threshold acceleration. That definition has shown to be sensitive to the threshold acceleration considered and to small events that occur at the final part of a recording. Significant duration is based on the dissipation of energy, within a time interval, and this energy is represented by the integral of the square of the ground motions. In the case of acceleration is related to the Árias intensity IA (Árias, 1970):

$$I_A = \frac{\pi}{2g}\int_0^T a^2(t)\,dt \quad (13)$$

here $a\,(t)$ is the acceleration time history, g is the acceleration of gravity, and T represents the complete duration of recording $a\,(t)$. Figure 5 present the procedure followed to determine the significant parameters (Husid, 1969). The most common measure of significant duration is a time interval between 5-95% of IA and is denoted by $D_{a5\text{-}95}$.

Predictive relationships have also been developed for frequency-dependent duration parameters evaluated from bandpassed accelerograms (e.g., Bolt, 1973, Trifunac and Westermo, 1982; Mohraz and Peng, 1989; and Novikova and Trifunac, 1994). These relationships have several limitations that are basically associated with a deficient representation of magnitude or site effects. Additionally, none of these have been derived from the energy integral. Some other restrictions are related to measured distance (normally the epicentral distance, not the closest site-source distance) and finally there are still others having to do with the regression method used to derive the relationships (Kempton and Stewart, 2006).

In what follows we develop a predictive neuronal model for significant duration that:

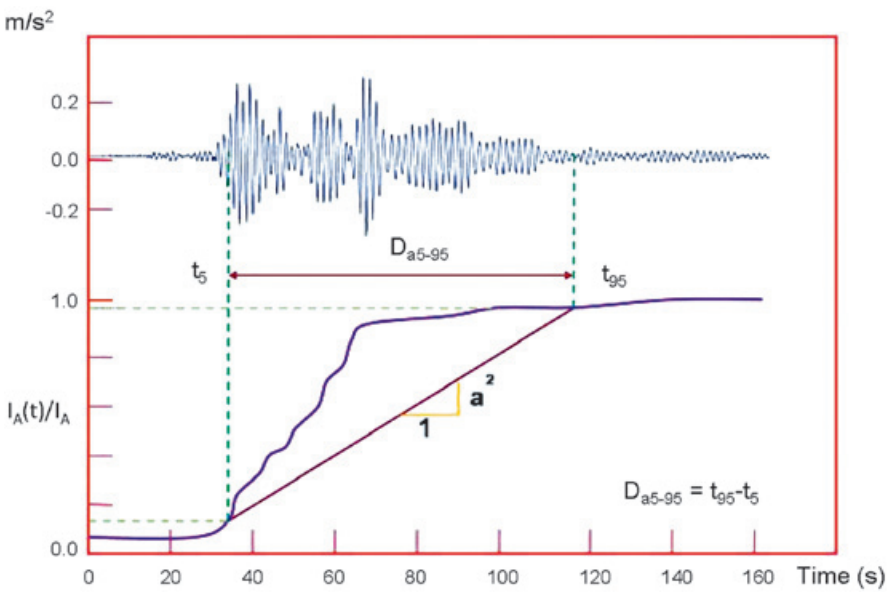

Figure 5. Significant duration parameters (acceleration 5-95%).

1) considers the seismic effects associated to magnitude, focal distance, near-fault rupture directivity and soil conditions and 2) is based on a soft computing procedure that accounts for inter- and intra-event ground-motion variability. Significant duration, from the Árias integral, was selected because of the stability of the method with respect to the definitions of initial and final threshold (Bommer and Martinez-Pereira 1999).

Neural estimation of duration

The ground motion duration model developed here captures the effects of the amount of energy radiated at the source using a neural representation of phenomena implicit in the data, the attenuation of seismic waves along the path due to geometric spreading and energy absorption; it also considers a local modification of the seismic waves as they traverse near-surface materials. The strong-motion duration D is the dependent variable of the NN formulation. The primary predictor variables (independent variables in a typical regression analysis) are M moment magnitude; R epicentral distance; focal depth FD, soil characterization expressed by Ts natural period; and Az azimuth.

NN based on information compiled from Puebla

Database

The city of Puebla has currently an accelerograph network composed of 11 seismic stations, three of which are located on rock, seven on compressible soil, and one in the basement of a structure. The general characteristics are provided in Table 1 and their locations indicated in Figure 6. Although, the first station (SXPU) was installed in 1972, the number of accelerogram records is relatively low mainly due to the low rate of seismicity in the region and the long process taken to install seismic stations.

In the first stage for the integration of our database, records with low signal-to-noise ratios were not taken into account. Hence, only 42 three-component accelerograms associated to three seismic stations (PBPP, SXPU and SRPU) are included in the database. These records were obtained from records of both subduction and normal-faulting earthquakes, originated, respectively, at the contact of the North America and Cocos plates, and by the fracture of the subducted Cocos plate.

Table 1. Puebla City Accelerograph network (Alcántara, 1999)

Station Code	Station name	Soil	Geo-Coordinates	
			Lat N	Long W
BHPP	Barranca Honda	Basaltic rock	19.109	-98.227
CAPP	Central de Abasto	Compressible	19.089	-98.188
LMPP	Lomas del Mármol	Marble stone	19.001	-98.182
PBPP	Paseo Nicolás Bravo	Travertine deposit	19.046	-98.208
PHPU	Parque Habana	Compressible	19.040	-98.167
PZPU	La Paz, Puebla	Volcanic cone	19.055	-98.227
RFPP	Río San Francisco	Structure basement	19.050	-98.190
SAPP	San Alejandro	Lacustrine deposit	19.060	-98.210
SRPU	San Ramón Castillotla	Compressible	18.965	-98.260
SXPU	Sismex Puebla	Compressible	19.040	-98.215
UAPP	Facultad de Ingeniería Civil	Compressible	19.002	-98.202

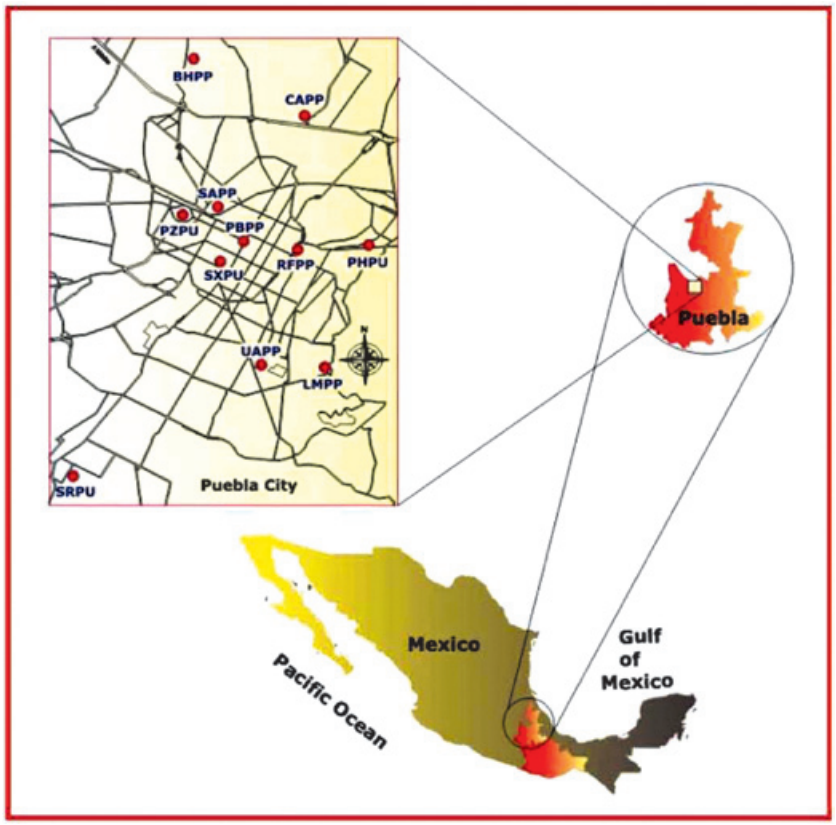

Figure 6. Strong motion network in Puebla (RACP).

The earthquakes in the database have magnitudes ranging from 4.1 to 8.1. Most of the events originated along coast of the Pacific Ocean in the states of Michoacan, Guerrero and Oaxaca. The epicenters of the remaining three events, those of October 24, 1980, April 3, 1997 and June15, 1999 were located in the Puebla-Oaxaca border. Epicentral distances to stations in the city of Puebla range from 300 to 500 km and in only one case it reached 800 km. That is why accelerations produced by the earthquakes considered in this research did not exceed 10 gal in Puebla.

In a second stage the database was expanded with accelerograms from the Instituto de Ingeniería UNAM Accelerographic Network (Alcántara *et al*., 2000). The added acceleration histories were recorded in stations on rock located the coastal region of the states of Michoacan, Guerrero and Oaxaca, and forcefully had to be generated by one of the earthquakes we had already catalogued in Table 1. The seismic stations we considered are shown in Figure 7 (filled squares), as well as the locations of the epicenters (inverted triangles). They were 88 three-component accelerograms in the final database.

A set of 26 events was used (Table 2) to design the topology of the NNs. These events were selected on the basis of the quality and resolution of the records. Accelerograms with low signal to noise ratios were deleted from the database. Both horizontal components and vertical direction of each seismic event were considered.

It is clear that the inputs and output spaces are not completely defined; the phenomena knowledge and monitoring process contain fuzzy stages and noisy sources. Many authors have highlighted the danger of inferring a process law using a model constructed from noisy data (Jones *et al*., 2007). It is imperative we draw a distinction between the subject of this investigation and that of discovering a process from records. The main characteristic of NN model is unrevealed functional forms. The NN data-driven system is a black-box representation that has been found exceedingly useful in seismic issues but the natural principle that explains the underlying processes remains cryptic. Many efforts have been developed to examine the input/output relationships in a numerical data-set in order to improve the NN modeling capabilities, for example Gamma test (Kemp *et al*., 2005; Jones *et al*., 2007; Evans

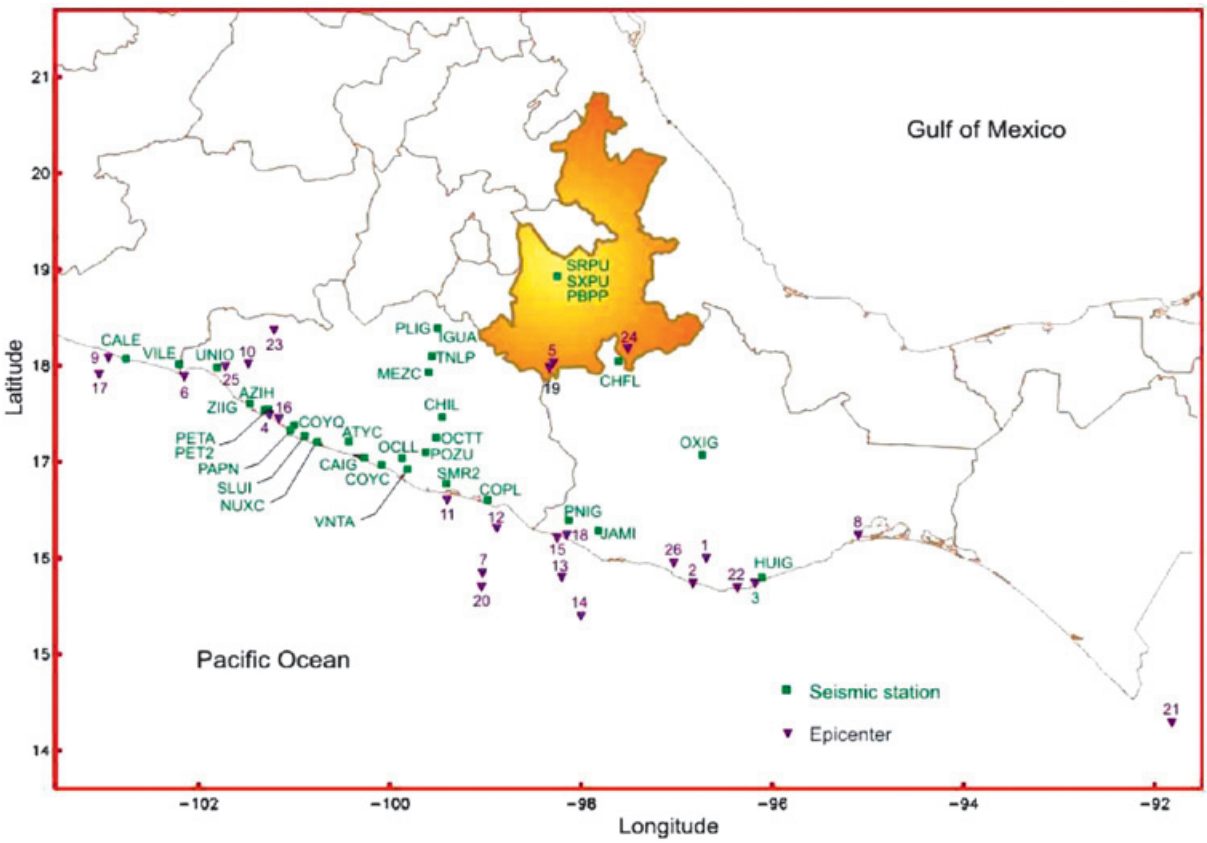

Figure 7. Location of epicenters and seismic stations

Table 2. RACP Selected records

#	Event date	M	Recording station
1	7811291	7.8	SXPU
2	7811292	5.3	SXPU
3	7811293	4.5	SXPU
4	7903141	7	SXPU
5	8010241	7	SXPU
6	8110251	7.3	SXPU
7	8407021	6	SXPU
8	8502111	5.2	SXPU
9	8509191	8.1	SXPU
10	8509211	7.5	SXPU
11	8904251	6.9	PBPP
12	9509141	7.2	PBPP, SRPU, SXPU
13	9602251	6.7	PBPP, SXPU
14	9602255	5	PBPP
15	9603271	5	SRPU
16	9607151	6.5	PBPP, SRPU, SXPU
17	9701111	6.9	PBPP, SRPU, SXPU
18	9701211	5	PBPP, SRPU, SXPU
19	9704031	4.8	PBPP
20	9712161	5.9	PBPP
21	9801101	6.3	PBPP
22	9802031	6.2	PBPP, SRPU, SXPU
23	9804201	5.5	PBPP, SRPU, SXPU
24	9906151	6.5	PBPP, SRPU
25	9906211	5.8	PBPP, RPU
26	9909301	7.5	PBPP, SXPU

and Jones, 2002), but as far as the authors' experience, none of these attempts are applicable to the high dimension of the seismic phenomena or the extremely complex neural models for predicting seismic attributes.

Neural approximation

The first step in developing a NN is the representation of the set of input and output cells. There are no clear-cut procedures to define this construction step. While the optimum architecture --hidden nodes and associated weights-- is obtained when the error function is minimized (i.e., the sum of the patterns of the squared differences between the actual and desired outputs is minimum) the numerical or categorical representation of inputs and outputs also depends on the modeler's experience and knowledge and a trial-and-error procedure must be followed in order to achieve a suitable design.

The RACP database has been modeled using the BP learning algorithm and Feed Forward Multilayer architecture. Time duration in horizontal (mutually orthogonal D_{H1}, N-S, and D_{H2}, E-W) and vertical components (D_V) are included as outputs for neural mapping and this attempt was conducted using five inputs (M, R, F_D, T_s and A_Z). After trying many topologies, we found out that the best model during the training and testing stages has two hidden layers with 200 nodes each. As seen in Figure 8a, the training correlation for D_{H1}, D_{H2} and D_V was quite good, but when the same model is tested (unseen cases are presented to predict the output) considerable differences between measured and estimated duration times are found (Figure 8b). It is important to point out that the results shown in that figure are the best we were able to obtain after trying 25 different topologies. Thus, this can be considered as the model having the best generalization capabilities using the selected learning algorithm, architecture, and nodal hidden structure. In Figure 9 the estimated values obtained for a second set of unseen patterns (validation set) are compared with the numerical predictions obtained using the relationship proposed by Reinoso and Ordaz (2001). The neuronal relationship follows more narrowly the overall trend but fails in some cases, (coefficients of correlation around R^2=0.75). It should be stressed that the NN has better interpolation and extrapolation capabilities than the traditional functional approaches. Furthermore, the influence of directivity and fault mechanism on duration can be identified with the NN, based on a multidimensional environment (Figure 10)

NN based on information compiled from Oaxaca

Database

The information used in the study is taken from the Oaxaca accelerographic array (RACO, Red Acelerográfica de la Ciudad de Oaxaca, in Spanish). The first recording station was installed in 1970 and nowadays the network comprises seven stations deployed around the urban area.

The instruments in these stations are located on ground surface. Each station has a digital strong-motion seismograph (i.e., accelerograph) with a wide frequency-band and wide dynamic range. Soil conditions at the stations vary from soft compressible clays to very stiff deposits (see Table 3). Locations of these observation sites are shown in Figure 11. From 1973 to 2004, the network recorded

Table 3. Oaxaca City Accelerograph network (Alcántara et al., 2000)

Station Code	Station name	Soil	Geo-Coordinates	
			Lat N	Log W
OXFM	Facultad de Medicina	Alluvium	17.084	-96.716
OXLC	Las Canteras	Rock	17.065	-96.703
OXPM	Primaria Múgica	Clay	17.061	-96.717
OXBJ	Primaria Benito Juárez	Clay	17.067	-96.744
OXAL	Alameda de León	Clay	17.061	-96.725
OXCU	Ciudad Universitaria	Clay	17.049	-96.713
OXTO	Instituto Tecnológico	Alluvium	17.078	-96.744

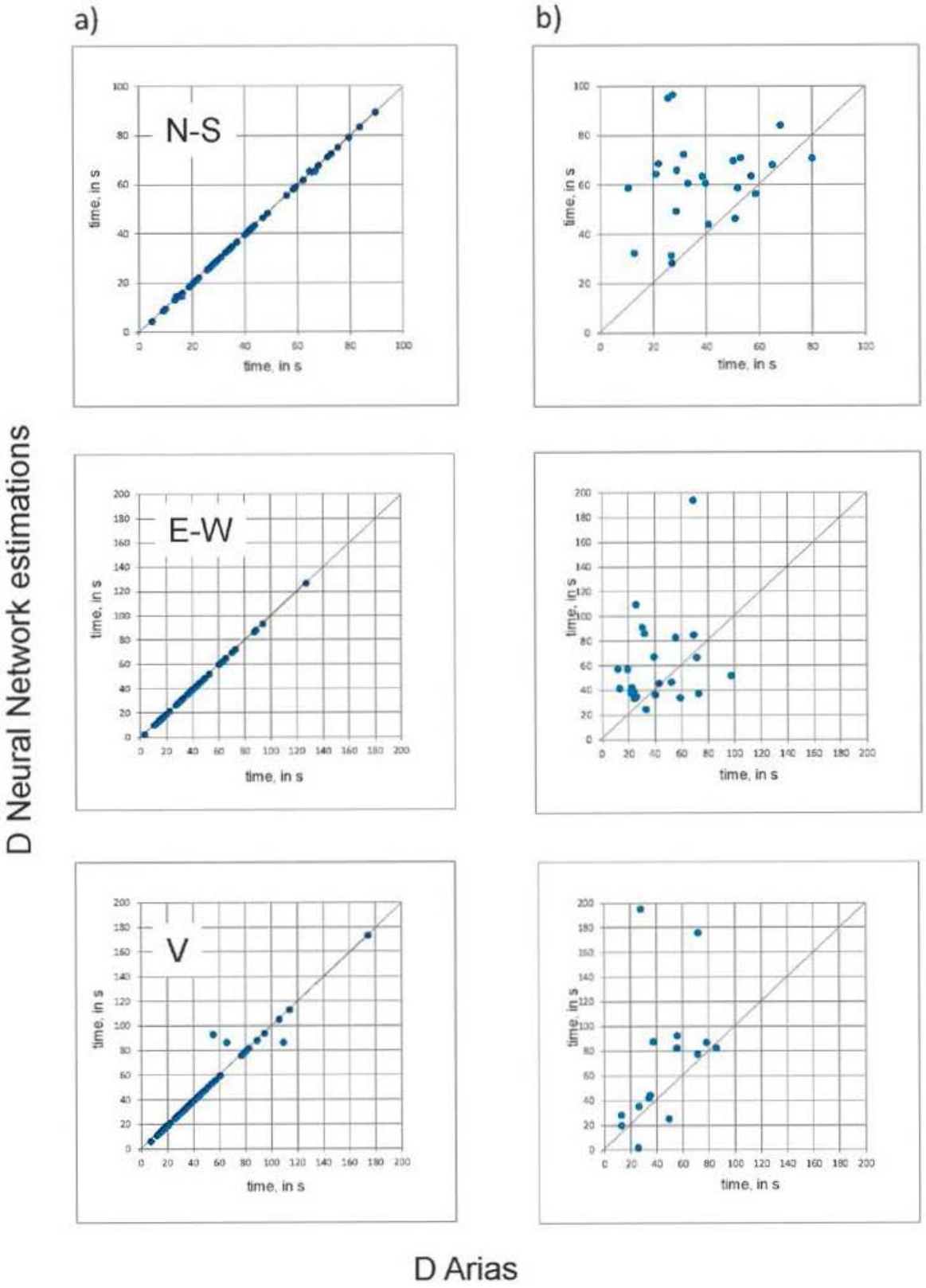

Figure 8. NN results for RACP, training and testing stages

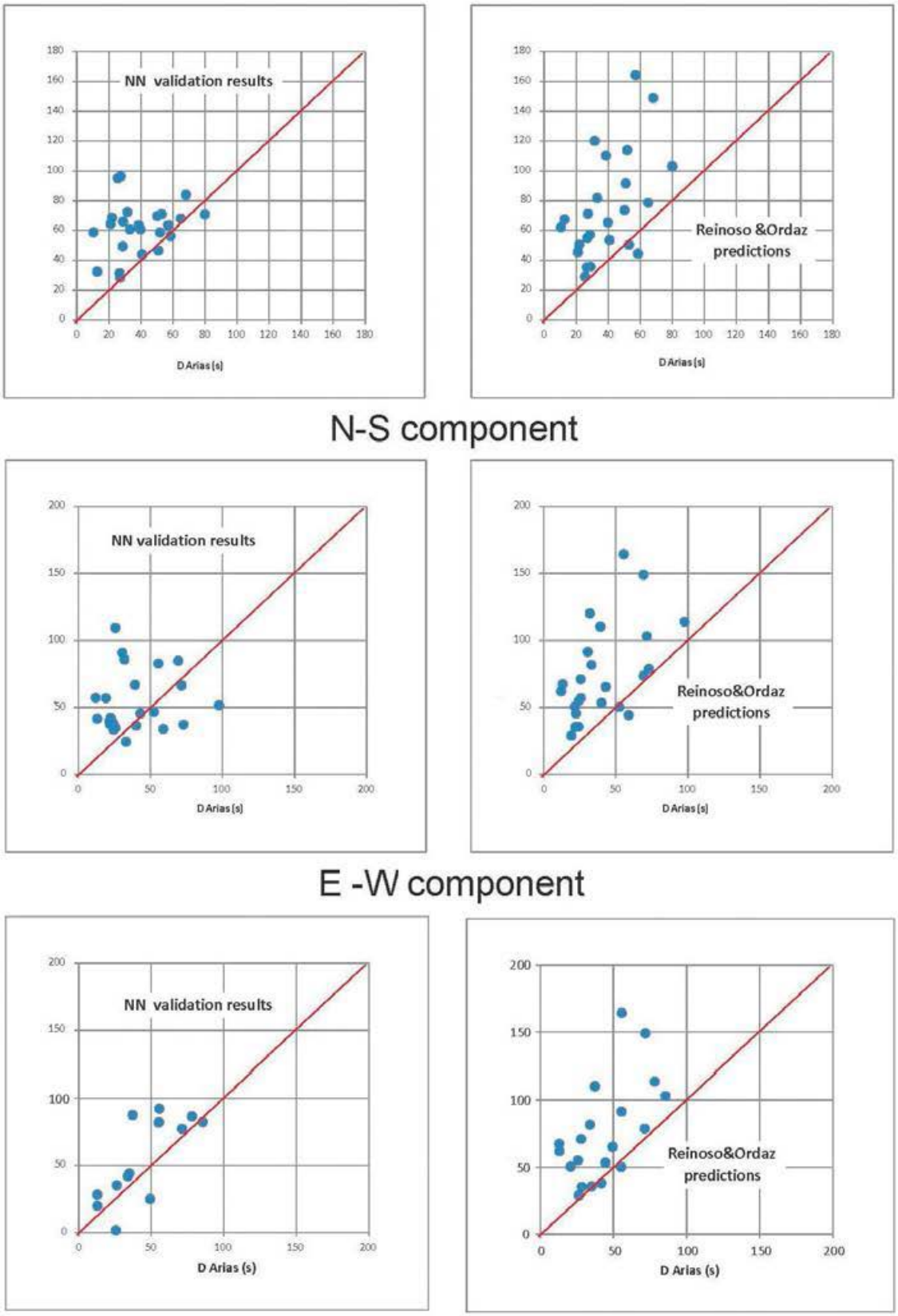

Figure 9. NN results for RACP, validation stage

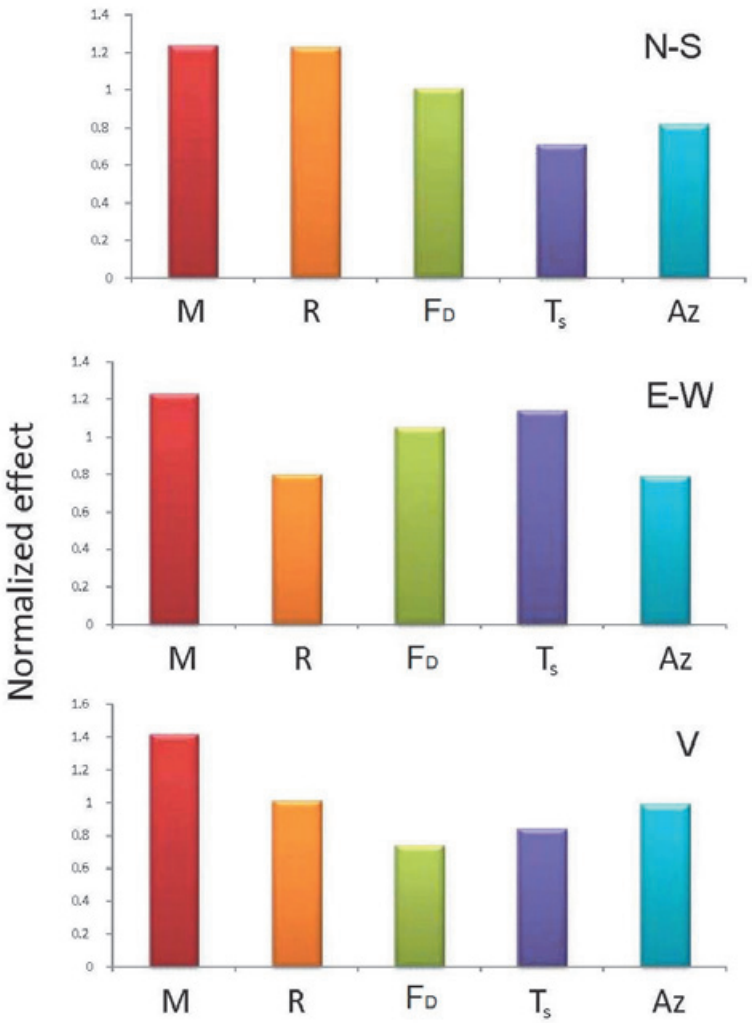

Figure 10. Input sensitivity analysis for RACP NN

171 time series from 67 earthquakes with magnitudes varying from 4.1 to 7.8 (Table 4). Events with poorly defined magnitude or focal mechanism, as well as records for which site-source distances are inadequately constrained, or records for which problems were detected with one or more components were removed from the data sets. The final training/testing set contains 147 three-component accelerograms that were recorded in five accelerograph stations OXLC, OXFM, OXAL, OXPM and OXTO. This catalogue represents wide-ranging values of directivity, epicentral distances and soil-type conditions (see Figure 12).

Neural modeling

The NN for Oaxaca City was developed using a similar set of independent parameters as those used for Puebla exercise. As the input/output behavior of the previous system is physical meaning the same five descriptors are included as inputs. This action permits to explore both systems' behaviors and to get wide-ranging conclusions about these variables.

Epicentral distance R was selected as a measure of distance because simple source-site relationships can be derived with it. Focal depth FD, was introduced for identifying data from interface events (FD < 50 km) and intraslab events (FD > 50 km). Together with the Azimuth Az, it associates the epicenter with a particular seismogenic zone and directivity pattern (fault mechanism).

To start the neuro training process using the Oaxaca database Ts is disabled and a new soil classification is introduced. Three soil classes were selected: rock, alluvium and clay. The final topology for RACO data contains BP as the learning algorithm and Feed Forward Multilayer

Table 4. RACO selected records

#	Event date	M	Recording station
1	197308281	6.8	OXFM
2	197811291	7.8	OXFM
3	198010241	7	OXFM
4	198206072	7	OXFM
5	198301241	5.3	OXFM
6	199407041	5.9	OXFM
7	199408271	5	OXFM
8	199408281	5.2	OXFM
9	199509141	7.2	OXFM
10	199604011	5	OXFM
11	199802031	6.2	OXFM
12	199805021	4.4	OXFM
13	199906151	6.5	OXFM, OXLC
14	199906152	4.5	OXFM, OXLC
15	199909301	7.5	OXFM, OXLC
16	199910071	4.4	OXAL, OXTO
17	199910251	4.6	OXTO
18	199911061	4.5	OXFM, OXAL, OXLC, OXPM, OXTO
19	199911101	4.3	OXAL, OXPM, OXTO
20	199911291	4.4	OXTO
21	199912171	4.4	OXPM, OXTO
22	200001191	4.5	OXLC, OXPM, OXTO
23	200003011	4.7	OXFM, OXLC, OXPM, OXTO
24	200003121	6.4	OXLC, OXTO
25	200005101	4.7	OXFM, OXPM, OXTO
26	200007211	5.9	OXTO
27	200008171	4.4	OXTO
28	200009291	4.7	OXLC, OXPM, OXTO
29	200010171	5.4	OXTO
30	200101261	5	OXTO
31	200102191	4.8	OXTO
32	200102201	4.7	OXTO
33	200109081	4.8	OXAL, OXLC, OXPM, OXTO
34	200110031	4.4	N/A
35	200111101	6	OXPM, OXTO
36	200111281	6	OXTO
37	200201161	6.3	OXLC, OXPM, OXTO
38	200201301	5.1	OXFM, OXLC, OXPM, OXTO
39	200202261	5	OXTO
40	200205111	4.5	OXPM, OXTO
41	200206071	4.7	OXFM, OXTO
42	200206072	5.6	OXFM, OXAL, OXLC, OXPM, OXTO
43	200206111	4.9	OXTO
44	200206181	4.5	OXFM
45	200208051	5.3	OXFM, OXLC, OXPM, OXTO
46	200208271	4.9	OXFM, OXAL, OXLC, OXPM, OXTO
47	200211081	5.2	OXTO
48	200212021	4.7	OXTO
49	200212291	4.6	OXFM, OXPM, OXTO
50	200301221	7.6	OXLC
51	200302011	5.3	OXTO
52	200306131	4.1	OXTO
53	200307081	4.6	OXTO
54	200309251	4.6	OXTO
55	200312011	4.3	OXAL, OXPM, OXTO
56	200401131	5.1	OXFM, OXAL, OXLC, OXPM, OXTO
57	200401132	5.5	OXFM, OXAL, OXLC, OXPM, OXTO
58	200401141	4.6	OXTO
59	200401171	4.7	OXFM, OXAL, OXLC, OXPM, OXTO
60	200402101	4.4	OXFM, OXAL, OXTO
61	200402181	4.3	OXFM, OXAL, OXLC, OXPM, OXTO

Table 4. Continue.

#	Event date	M	Recording station
62	200404201	5.4	OXFM, OXAL, OXPM, OXTO
63	200405061	4.3	OXTO
64	200406141	5.8	OXFM, OXAL, OXPM, OXTO
65	200408011	4.6	OXFM, OXAL, OXTO
66	200408071	5.3	OXFM, OXAL, OXLC, OXPM, OXTO
67	200408181	5.7	OXFM, OXAL, OXLC, OXPM, OXTO

as the architecture. Again D_{H1}, D_{H2}, and D_V are included as outputs for neural mapping and between the five inputs, four are numerical (M, R, F_D, and A_Z) and one is a class node (soil type S_T). The best model during the training and testing stages has two hidden layers of 150 nodes each and was found through an exhaustive trial and error process.

The results of the RACO NN are summarized in Figure 13. These graphs show the predicting capabilities of the neural system comparing the task-D values with those obtained during the NN training phase. It can be observed that the durations estimated with the NN match quite well calculated values throughout the full distance and magnitude ranges for the seismogenic zones considered in this study. Duration times from events separated to be used as testing patterns are presented and compared with the neuronal blind evaluations in Figure 14. The results are very consistent and remarkably better than those obtained when analyzing RACP database. The linguistic expression of soil type is obviously a superior representation of the soil effect on D prediction.

A sensitivity study for the input variables was conducted for the three neuronal modules. The results are given in Figure 15 and are valid only for the data base utilized. Nevertheless, after conducting several sensitivity analyses changing the database composition, it was found that the RACO trend prevails: S_T (soil type) is the most relevant parameter (has the larger relevance), followed by azimuth Az, whereas M, F_D and R turned out to be less influential. NNs for the horizontal and vertical components are complex topologies that assign nearly the same weights to the three input variables that describe the event, but an important conclusion is that the material type in the deposit and the seismogenic zone are very relevant to define D. This finding can be explained if we conceptualize the soil deposit as a system with particular stiffness and damping characteristics that determine how will the soil column vibrate and for how long, as seismic waves traverse it and after their passage through the deposit.

Through the $\{M, R, F_D, A_Z, S_T\} \rightarrow \{D_{H1}, D_{H2}, D_V\}$ mapping, the neuronal approach we presented offers the flexibility to fit arbitrarily complex trends in magnitude and distance dependence and to recognize and select among the tradeoffs that are present in fitting the observed parameters within the range of variables present in data.

Conclusions

Artificial neural networks were used to estimate strong ground motion duration. These networks were developed using a back propagation algorithm and multi-layer feed-forward architecture in the training stage. In developing the networks it was assumed that the parameters that have the greatest influence on strong motion duration are magnitude, epicentral distance, focal depth, soil characterization and azimuth. These parameters include the effects of seismic source, distance, materials and directivity. The many topologies tested and the input sensitivity developed drive to the conclusion that a broad soil-type classification (in these investigation three soil types) provides a better correlation with seismic phenomena than the more commonly used natural period T_s.

Overall, the results presented here show that artificial neural networks provide good and reasonable estimates of strong ground motion duration in each one of the three orthogonal components of the accelerograms recorded in the cities of Puebla and Oaxaca using easy-to-obtain input parameters: S M, R, F_D and A_z.

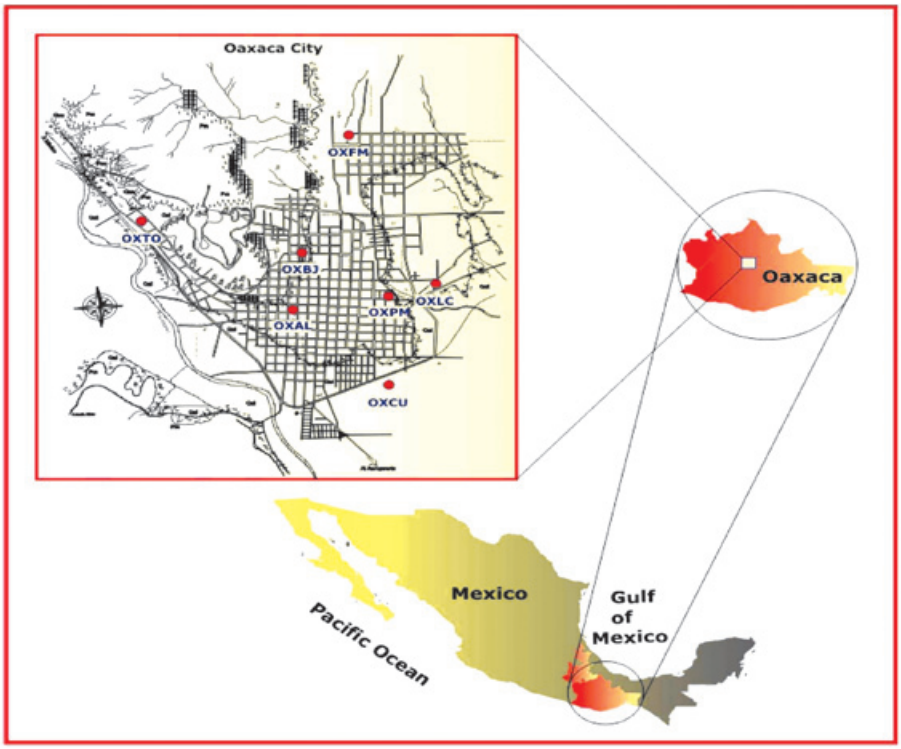

Figure 11. Strong motion network in Oaxaca City (RACO).

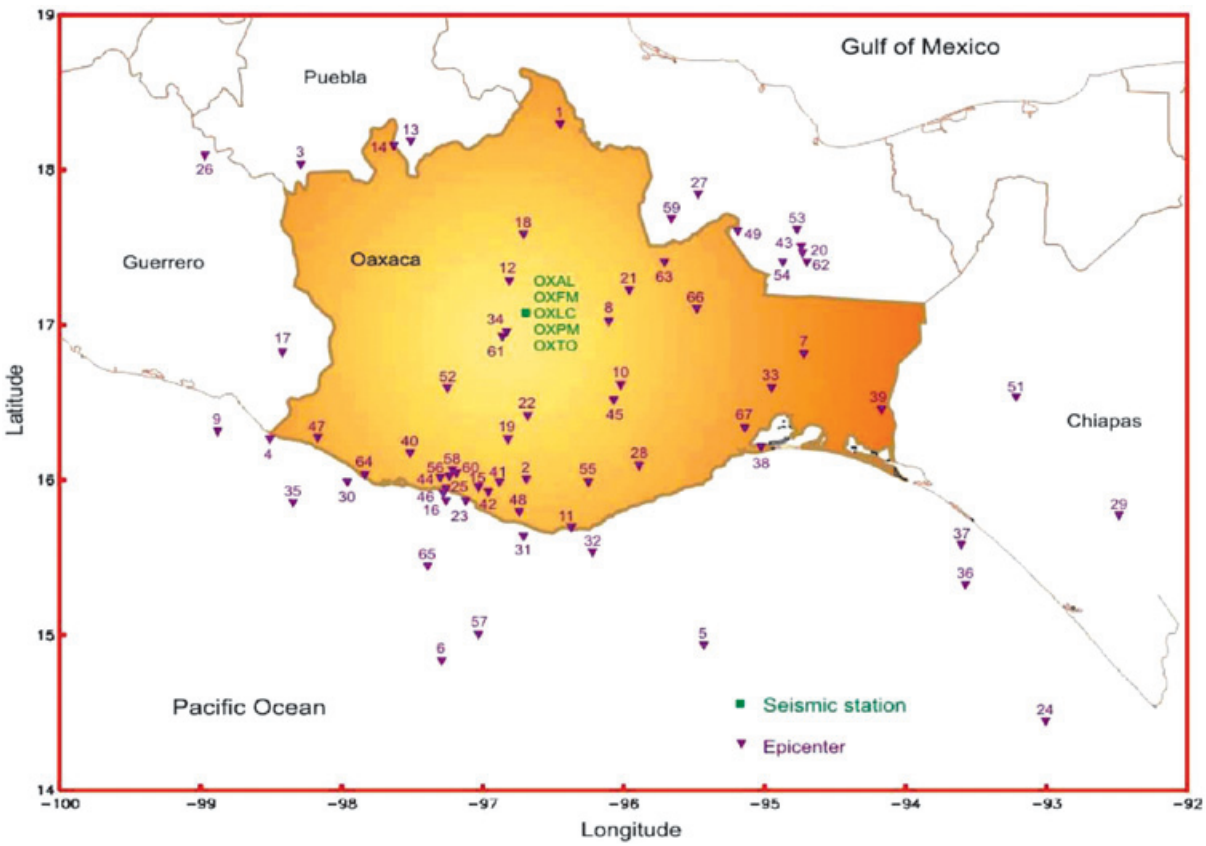

Figure 12. Epicenters and Seismic stations.

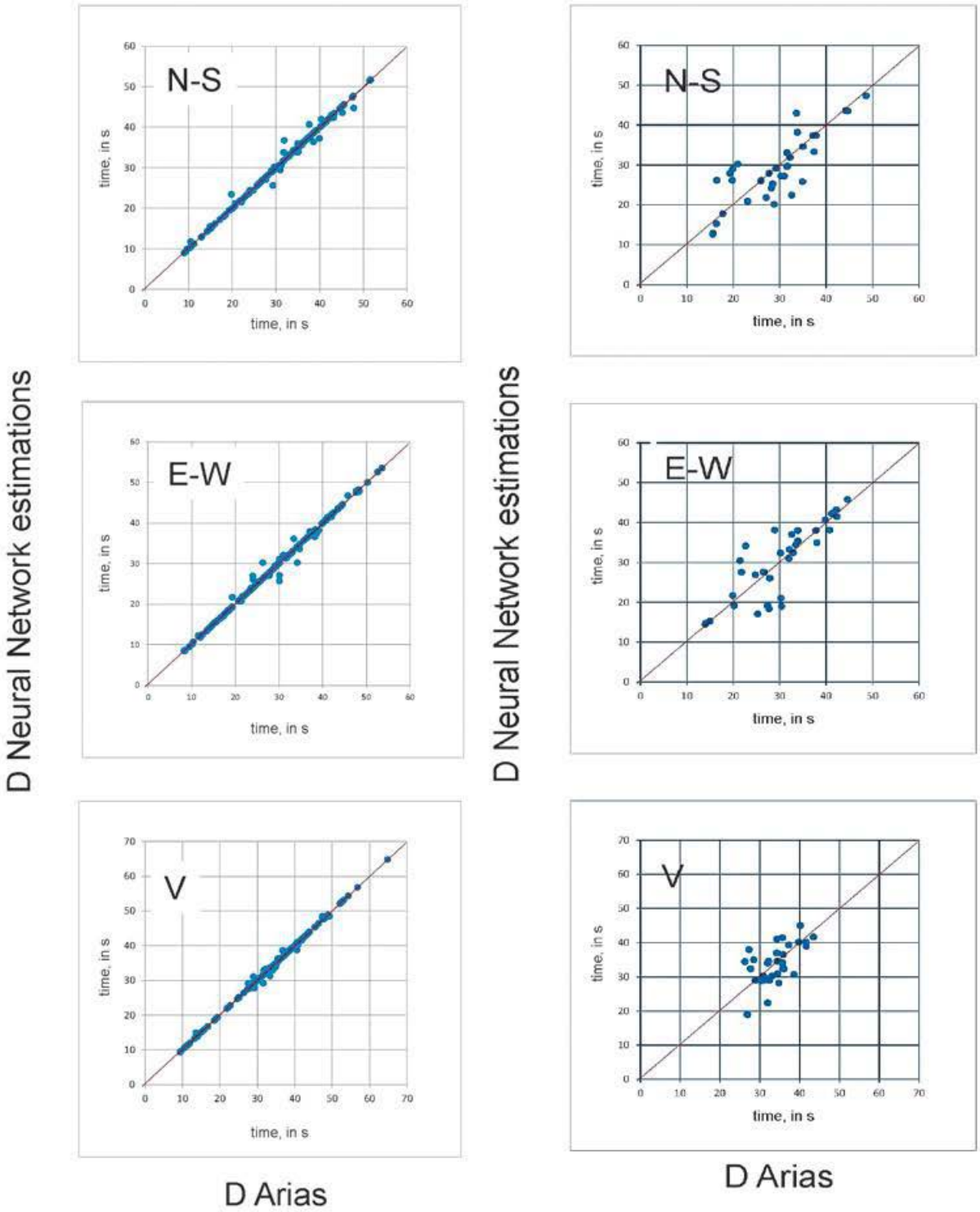

Figure 13. NN results for RACO, training stage.

Figure 14. NN results for RACO, testing stage.

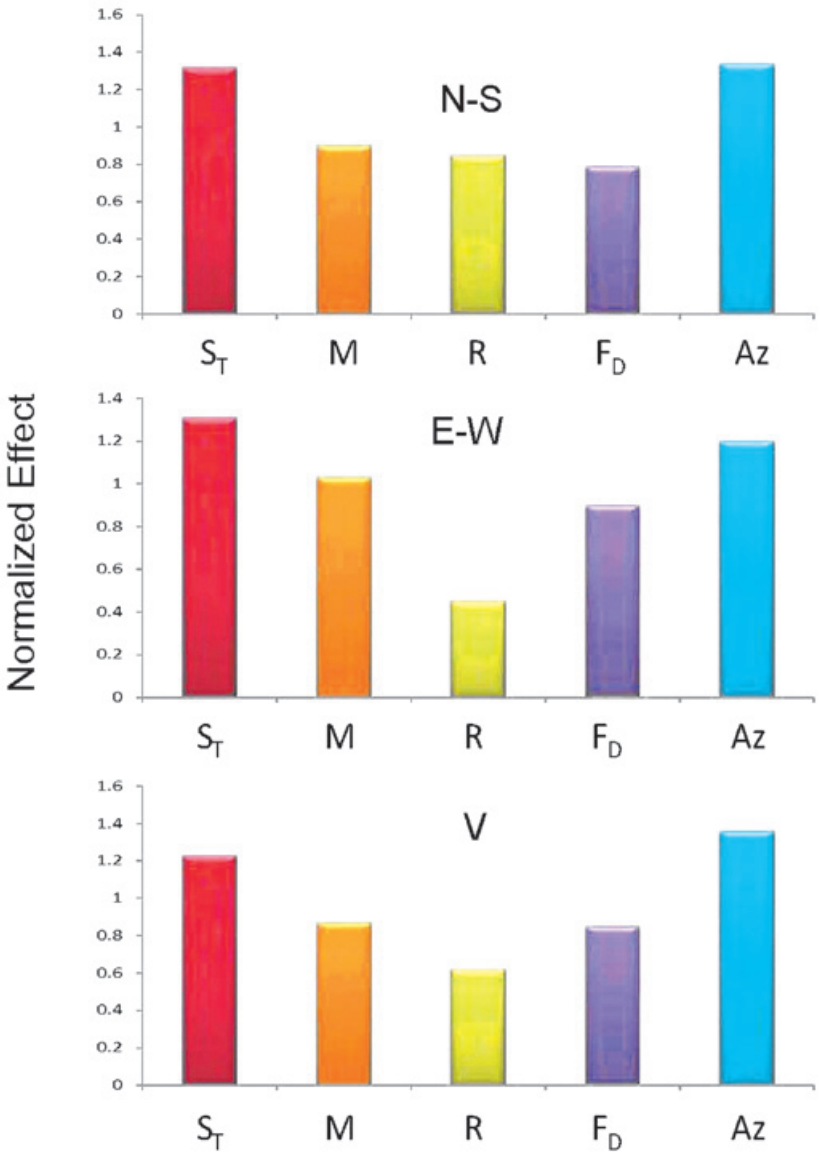

Figure 15. Input sensitivity analysis for RACO NN.

Finally, it is important to highlight that the capabilities of a NN ultimately depend on various factors that require the knowledge of the user about the problem under consideration. This knowledge is essential for establishing the pattern parameters that best represent it. Experience to set and to select the network architecture (including learning rules, transfer functions and hidden nodal structure) and the proper integration of training, test and validation data sets are also very important.

Acknowledgments

The recordings used in this paper were obtained thanks to Instituto de Ingeniería, UNAM and the Benemérita Universidad Autónoma of Puebla (BUAP). We are also grateful to Professor Miguel P Romo for his useful comments.

References

Adalbjörn S., Končar N., Jones A.J., 1997, A note on the Gamma test. *Neural Computing and Applications*, 5, 3, 131-133.

Alcántara L., González G., Almora D., Posada-Sánchez A.E., Torres M., 1999, Puebla City Accelerograph Network, activities in 1996, RACP-II/BUAP-01. Internal Report Institute of Engineering, UNAM and Autonomous University of Puebla, México, April (in Spanish).

Alcántara L., Quaas R., Pérez C., Ayala M., Macías M.A., Sandoval H., (II-UNAM), Javier C., Mena E., Andrade E., González F., Rodríguez E., (CFE), Vidal A., Munguía L.,

Luna M.,(CICESE), Espinosa J.M., Cuellar A., Camarillo L., Ramos S., Sánchez M., (CIRES), Quaas R., Guevara E., Flores J.A., López B., Ruiz R., (CENAPRED), Guevara E., Pacheco J., (IG-UNAM), Ramírez M., Aguilar J., Juárez J., Vera R., Gama A., Cruz R., Hurtado F., M. del Campo R., Vera F., (RIIS), Alcántara L. (SMIS), 2000, Mexican Strong Motion Data Base, CD Rom Vol 2. Mexican Society for Earthquake Engineering.

Anderson J.G., 2004, Quantitative measure of goodness-of-fit of synthetic seismograms, in 13th World Conference on Earthquake Engineering, 243, Vancouver, Canada, 1-6 August.

Árias A., 1970, A measure of earthquake intensity, Seismic Design of Nuclear Power Plants. R. Hansen, Editor, MIT Press, Cambridge, Mass., 438-483.

Bishop C.M., 1996, Neural networks for pattern recognition. Oxford University Press, New York, 482 pp.

Bolt B.A., 1973, Duration of strong ground motion, in 5th World Conference on Earthquake Engineering, 292, Rome, Italy, 25-29 June.

Bommer J.J., Martinez-Pereira A., 1996, The prediction of strong-motion duration for engineering design, in 11th World Conference on Earthquake Engineering, 84, Acapulco, Mexico, 23-28 June.

Bommer J.J., Martinez-Pereira A., 1999, The effective duration of earthquake strong motion. *Journal of Earthquake Engineering*, 3:2, 127–172.

Broomhead D.S., Lowe D., 1988, Multivariable functional interpolation and adaptive networks, *Complex Systems*, 2, 321-355.

Evans D., Jones A.J., 2002, A proof of the Gamma test. Proc. R. Soc. Lond., 458, 2759-2799.

Hassoun M.H., 1995, Fundamentals of Artificial Neural Networks. MIT Press, Massachusetts, 511 pp.

Hertz J., Krogh A., Palmer R.G., 1991, Introduction to the Theory of Neural Computing. Addison-Wesley, California, 327 pp.

Jones A.J., Evans D., Kemp S.E., 2007, A note on the Gamma test analysis of noisy input/output data and noisy time series. *Physica D*, 229:1, 1-8.

Tettamanzi A., Tomassini M., 2001, Soft Computing: integrating evolutionary, neural, and fuzzy systems. Springer-Verlag, Berlin, 328 pp.

Husid L.R., 1969, Características de terremotos - análisis general. Revista del IDIEM, 8, 21–42.

Kemp S.E., Wilson I.D., Ware J.A., 2005, A tutorial on the Gamma test. *International Journal of Simulation: Systems, Science and Technology*, 6:1-2, 67-75.

Kempton J., Stewart J., 2006, Prediction equations for significant duration of earthquake ground motions considering site and near-source effects. *Earthquake Spectra*, 22:4, 985–1013.

Mohraz B., Peng M.H., 1989, The use of low-pass filtering in determining the duration of strong ground motion. Publication PVP-182, Pressure Vessels and Piping Division, ASME, 197–200.

Novikova E.I., Trifunac, M.D., 1994, Duration of strong ground motion in terms of earthquake magnitude, epicentral distance, site conditions and site geometry. Earthquake Eng. Struct. Dyn., 23, 1023–1043.

Reinoso E., Ordaz M., 2001, Duration of strong ground motion during Mexican earthquakes in terms of magnitude, distance to the rupture area and dominant site period. *Earthquake Eng. Struct. Dyn*, 30, 653-673.

Sarma S.K., 1970, Energy flux of strong earthquakes. *Tectonophysics*, 11, 159–173.

Trifunac M.D., Westermo B.D., 1982, Duration of strong earthquake shaking. *Soil Dynamics and Earthquake Engineering*, 1:3, 117-121.

Geofísica Internacional (2014) 53-3: 241-257

Original paper

Inference of fault and fracture systems beneath the Matatlan waste dump basement, a VLF study

Miguel Ángel Alatorre-Zamora*, José Oscar Campos-Enríquez, Salvador Isidro Belmonte-Jiménez and Jaime Ibarra-Nuño

Received: December 13, 2012; accepted: November 20, 2013; published on line: July 01, 2014

Resumen

Se utilizó la técnica VLF para inferir zonas de fallas o de grandes fracturas que pudiesen servir como conductos para fluidos de desechos contaminantes en el vertedero de Matatlán, en Guadalajara, al oeste de México. Para interpretar los datos se usaron los filtros de Fraser y de Karous-Hjelt.

Se interpretaron perfiles de forma directa empleando el filtro modificado de Karous-Hjelt. Se aplicaron los filtros de Fraser y de Karous-Hjelt conjugados a todos los datos. Los resultados de ambas técnicas muestran similitud en las posiciones y orientaciones de rasgos anómalos que se asocian a zonas de fracturas o de fallas. Se observa una zona de falla en el centro del sitio, que tiene un rumbo NEE-SWW. Otros rasgos importantes inferidos tienen direcciones NW-SE y se observan en la parte occidental del área.

El uso conjunto de las técnicas basadas en los filtros de K-H y de Fraser dan resultados como una estructura N-S inferida en el límite occidental del vertedero, así como rasgos anómalos de dirección NW-SE, principalmente en la mitad occidental del sitio. La estructura N-S tiene la misma dirección que el Cañón del Río Grande de Santiago, mientras que los rasgos NW-SE coinciden con las direcciones del rift Tepic-Zacoalco. Hacia el centro del área aparecen otros rasgos con direcciones NE-SW. Todos estos rasgos y sus direcciones coinciden de manera fuerte con la predominancia de grupos de fracturas mostrados en el análisis estadístico de fracturas, y podrían servir como conductos para la migración de lixiviados hacia el Cañón Coyula, al sur, y hacia el Cañón del Río Grande de Santiago, al este del sitio.

Un análisis estadístico de direcciones de fracturas mostró 4 direcciones principales N-S (A), N75-80E (B), N60-65W (C) y N25-30W (D), y dos direcciones secundarias que son N45-55E (E) y 90E (F). El patrón primario A coincide con la dirección del Cañón del Río Grande de Santiago, mientras que el patrón secundario F tiene una dirección paralela a la del Cañón Coyula.

Palabras clave: very Low Frequency, vertedero de Matatlán, zonas de fracturas, distribución de corriente, filtros Fraser y Karous-Hjelt.

M.A. Alatorre-Zamora*
Departamento de Ingeniería Civil y Topografía
Centro Universitario de Ciencias Exactas e Ingeniería
Universidad de Guadalajara
*Corresponding author: alatorre2004@hotmail.com

J.O. Campos-Enríquez
Instituto de Geofísica
Universidad Nacional Autónoma de México
Delegación Coyoacán, 04510
México D.F., México

S. Belmonte-Jiménez
Centro Interdisciplinario de Investigación
para el Desarrollo Integral Regional
Instituto Politécnico Nacional
Unidad Oaxaca

J. Ibarra-Nuño
Departamento de Física
Universidad de Guadalajara

Abstract

We used the VLF technique to infer fault or major fracture zones that might serve as path for contaminant waste fluids in the Matatlan dumpsite, in Guadalajara, western Mexico. To interpret the data we used the Fraser, and Karous-Hjelt filters.
Profiles were interpreted with 2D direct modeling based on Karous-Hjelt modified filter (K-H). The Fraser and Karous-Hjelt conjugated filter were applied to the entire data. The results of both techniques show similarities in the directions and positions of anomalous features, which are assumed fault or fracture zones. We observed one fault zone at the centre of the site, with a NEE-SWW strike. Other important inferred structures have NW-SE directions at the western part of the site.
The cooperative use of both techniques, based on K-H filter and the Fraser filter give results as an N-S inferred structure in the westernmost part of the zone, as well as NW-SE linear anomalies, mainly in the western half of the site. The N-S structure has the same direction as that of Rio Grande de Santiago Canyon. The NW-SE features coincide with the directions of the Tepic-Zacoalco rift. Others NE-SW lineaments are located towards the centre of the area. These facts coincide strongly with the predominance of fracture groups show in the fracture analysis. The inferred structures could serve as conduits for the leachates to migrate towards the Coyula canyon as well as towards the Rio Grande de Santiago Canyon.
Statistic analysis of fracture orientations showed N-S (A), N75-80E (B), N60-65W (C), and N25-30W (D) main directions, and N45-55E (E), and 90E (F) secondary directions. Group A coincides with the direction of the Rio Grande de Santiago Canyon, whereas pattern F have the same direction as Coyula Canyon.

Key words: Very low frequency, Matatlan dumpsite, fracture zones, current distribution, Fraser and Karous-Hjelt filters.

Introduction

Very Low Frequency technique (VLF) is based on measurements of parameters of the polarization ellipse arising from the vector sum of magnetic components of primary and secondary electromagnetic fields. Primary VLF field sources are generated by powerful transmitting antennas specially designed for transoceanic communication; these antennas are disseminated in the north hemisphere. Several antennas do not transmit actually, representing a disadvantage for the method. The frequency of some transmitters have changed over time; for example, Cutler, Maine (NAA), transmitting with 17.8 kHz in 1970 (after Paterson and Ronka, 1970), transmitted in 1996 with 24.8 kHz, and Jim Creek, Washington (NLK/NPG) transmitting with 18.6 kHz, now transmits with 24.0 kHz. The VLF band itself has been modified: 15-25 kHz (Kaikkonen, 1979), 10-30 kHz (Olsson, 1980), and 15-30 kHz (Beamish, 1994).

The emitted primary field travels along the entire world, and at distances of more than 100 km, its magnetic component is almost horizontal and perpendicular to the source azimuth (Bozzo *et al*., 1994). In presence of a conductor, the primary EM field penetrates into the ground and generates a secondary field that interacts with the primary field. The resultant field is controlled by the electric structure of ground. This field is elliptically polarized and characteristics of magnetic secondary field can be represented by polarization ellipse parameters. In particular, two parameters of this ellipse are usually used to analyze the secondary field: the tilt angle α (inclination of major axis) and the eccentricity or ellipticity $e=H_2/H_1$ (the rate between minor and major axis). Moreover, since secondary field intensity is always smaller than primary field intensity, they can be written as

$$\alpha = Re/Hp \qquad e = Im/Hp$$

(see for example, Saydam, 1981; Sinha, 1990a) and therefore it is possible to evaluate both in-phase, *Re,* and out-phase or quadrature, *Im,* components, both normalized with respect to the *Hp* main field.

Considering main components of the polarization ellipse, tilt angle and ellipticity would be:

$$\tan 2\alpha = \frac{2(H_z / H_x)\cos\Delta\phi}{1-(H_z / H_x)^2}$$

and

$$e = \frac{H_z H_x \sin\Delta\phi}{H_1^2}$$

Where ϕ is a tilted angle (it is a wavetilt parameter).

Tilt angle tangent and ellipticity are good approximations to in-phase and quadrature components of vertical secondary field, respectively; both components can be employed to represent those components in acceptable limits, and to conduit an interpretation of results.

Applications

VLF method is widely used in detection and delineation of shallow conductors as well as in groundwater exploration and in engineering studies. The method has been combined with seismic and magnetic methods to locate and to investigate fractures and cavities in carstic environments, which constitutes an engineering and hydrogeology problem (Armadillo *et al*., 1998); also has been used in mineral location (Bayrak, 2002), in Earth surface structure studies (Alexandros *et al*., 1999), in filtration studies of oil derived products at groundwater (Benson, *et al*,1997), in archaeological zones, or in monitoring and assessing impact from volcanic areas, in geological mapping, and particularly to locate narrow fault zones (Phillips and Richards, 1975). In particular, VLF has been employed with success in sites with pollution problems (Greenhouse and Harris, 1983), and in studies from mineralized areas (Paál, 1968; Paterson and Ronka, 1971).

One of the main impacts produced by dumpsites is ground and surface water contamination, caused by leachates. The contamination may lasts over 20 or 30 years after closure of the dumpsite (Kjeldsen *et al*., 2002; Jones and Dixon, 2005; Christensen *et al*., 2000; Bekaert *et al*., 2002). A leachate is the liquid that seeps to lower levels of ground and extracts, dissolves or suspends materials. The VLF method is very sensitive to water quality, as well as to the presence of hydrocarbons. Pollution is often favored by the presence of large fractures and faults that acts as conduits for the migration of contaminating fluids. The VLF method is also sensitive to the presence of wet faults and fractures.

In this work is described a study in which the VLF method was applied with success to infer fractures. The case comprises an urban waste dumpsite, located at western Mexico. VLF data in this area are analyzed with Fraser (1969) and Karous-Hjelt (1983) techniques. At the dumpsite, it is expected to recognize ground areas contaminated with leachates. Fracture measurements support the presence of the path-sources inferred by mean of VLF anomalies.

Study area description

The area corresponds to the urban waste Matatlan dumpsite of Guadalajara, Jalisco, at western Mexico (Figure 1a). This dumpsite is named Matatlan that has been developed on top of a small plateau at the edge of the Rio Grande de Santiago Canyon; this Canyon limits to the north and east, the Guadalajara urban area (Figure 1b). It comprises andesitic flows intercalated with rhyolithic emissions from Cerro de la Reyna (Figure 1b). This dumpsite started to work in 1989, receiving about 800 tons per day, and closed in 2004 with a daily uptake of 1,500 tons.

A private company controlled the dumpsite several years, interspersed the waste with soil and coarse grain geologic material, constituted mainly by andesitic and tobaceous fragments; in this way, organic matter degradates and non-contaminant organic gases are expulsed to the atmosphere.

During summer there exists a large quantity of leachates, when rainy season occurs. Although there are catchment pits for the leachates in the edges of the site, high grade fracturing at the andesitic basement could permit without-control migration of leachates outside the dumpsite; this could impact in a severe way the Canyon environment, considered as a natural area that should be environmentally protected.

Adjacent local geology

The dumping site is located in an island-plateau, surrounded by three canyons. Coyula Canyon surrounds the site at its southwestern limits, along the southern, and almost all its western portion to turn then into an E-W direction to join the N-S to NW-SE Rio Grande de Santiago Canyon. In the north, the study area is limited by a small canyon that also intersects the Rio Grande de Santiago Canyon with an E-W to NE-SW direction (Figure 1b).

Dumpsite geologic features correspond to a boundary environment between two major geologic provinces: the Sierra Madre Occidental (SMOc) and the Trans-Mexican Volcanic Belt (TMVB) (Figure 1a). Both provinces impose their structural signature at the dumpsite. The dumpsite basement is formed by basaltic andesites and acid tuffs, according to petrographic analysis (Alatorre-Zamora, 2003). These volcanic products seem to proceed from

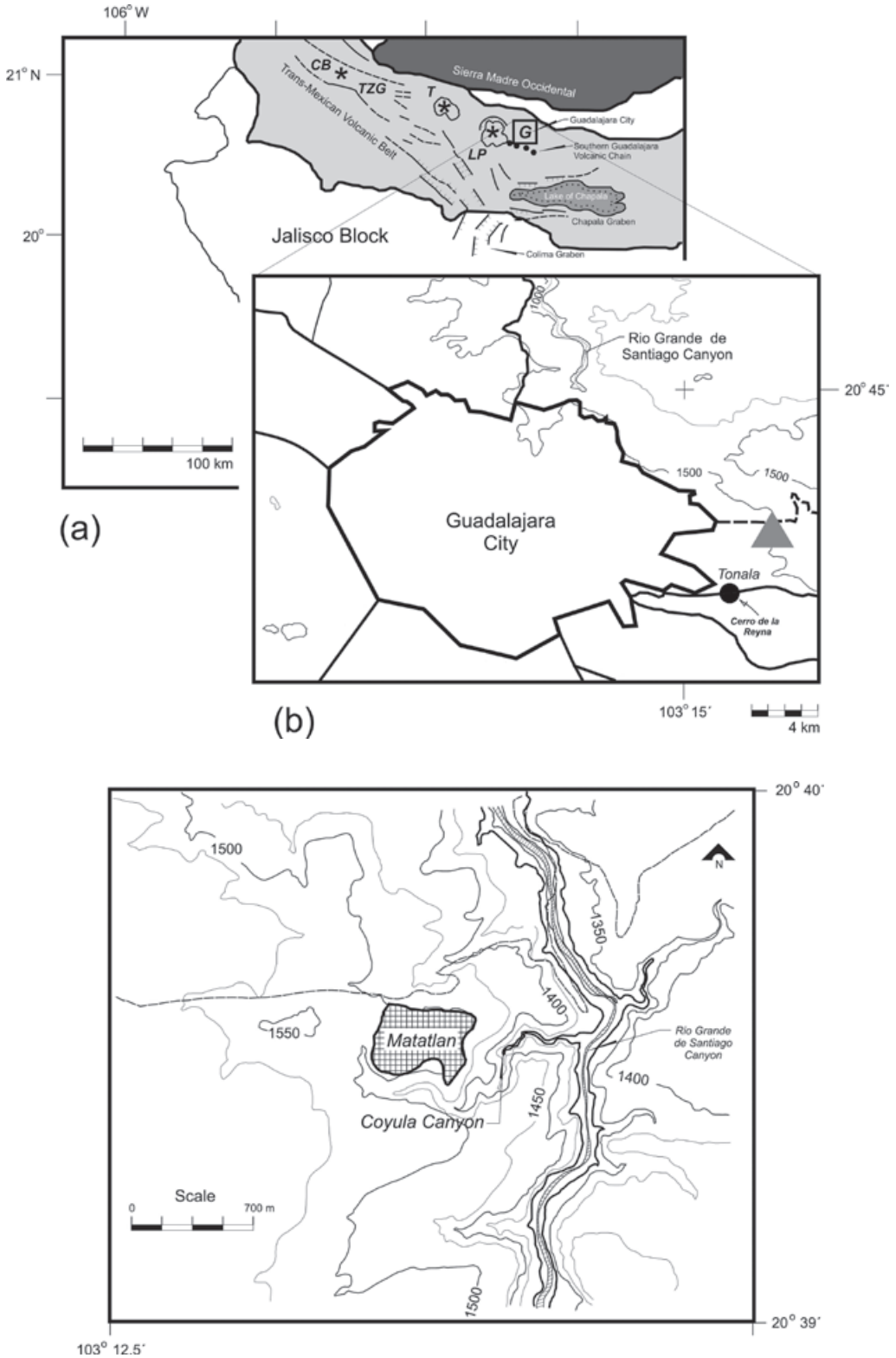

Figure 1. (a) Western Mexico showing main geologic features. CB-Ceboruco volcano; TZG- Tepic-Zacoalco Graben; T-Tequila volcano; LP-La Primavera Caldera; G-Guadalajara urban area. (b) Detail of Guadalajara City and Matatlan dumpsite location, marked with a gray triangle at the east of Guadalajara. A black circle south of the grey triangle indicates the position of the andesitic volcano Cerro de la Reyna. The topographic curves are in meters above sea level. (c) Detailed topography at Matatlan dumping site; the Rio Grande de Santiago Canyon is clearly observed.

Cerro de la Reyna volcano. The outcroppings exhibit a high fracture degree (Figure 2) due to a combination of tectonism (characterizing a secondary porosity) with fractures originated at cooling lava moment (characterizing a primary porosity). Tectonic origin is proposed by observation of fault striae in the outcrops, although fractures due to listric movements are also possible.

First geological works in neighboring areas were done by Watkins *et al*. (1971), Mahood (1980), Gilbert *et al*. (1985) and Luhr and Lazaar (1985). The surrounding area is characterized by volcanic rocks successions, mainly pumitic deposits with ignimbrites, rhyolites, andesites and basaltic andesites intercalations. Into this general volcanic sequence the San Gaspar and Guadalajara ignimbrites are distinguished as good stratigraphic indicators (Gilbert *et al*., 1985); standing out also are the so-called Guadalajara and San Cristobal groups, both from the Río Grande de Santiago Canyon and the Los Altos plateau, respectively.

The zone is surrounded by major faults. Neotectonic control from Quaternary volcanic activity reveals NW-SE alignments one of which is approximately tangent to Guadalajara urban area (Luhr and Lazaar, 1985; Alatorre-Zamora and Campos-Enríquez, 1991; Rosas-Elguera and Urrutia-Fucugauchi, 1998). Extensions occurring from Late Miocene at the Guadalajara area have been postulated in response to an initial opening of the S of California Gulf (Ferrari, 1995).

Methodology

Equipment

Equipment used in this case-study is an OMNI MAG Scintrex VLF equipment with three channels (Wright, 1988), to have access to three transmitting stations. For its management one must know both the locations and frequency of power stations and parameters as provided by the instrument itself.

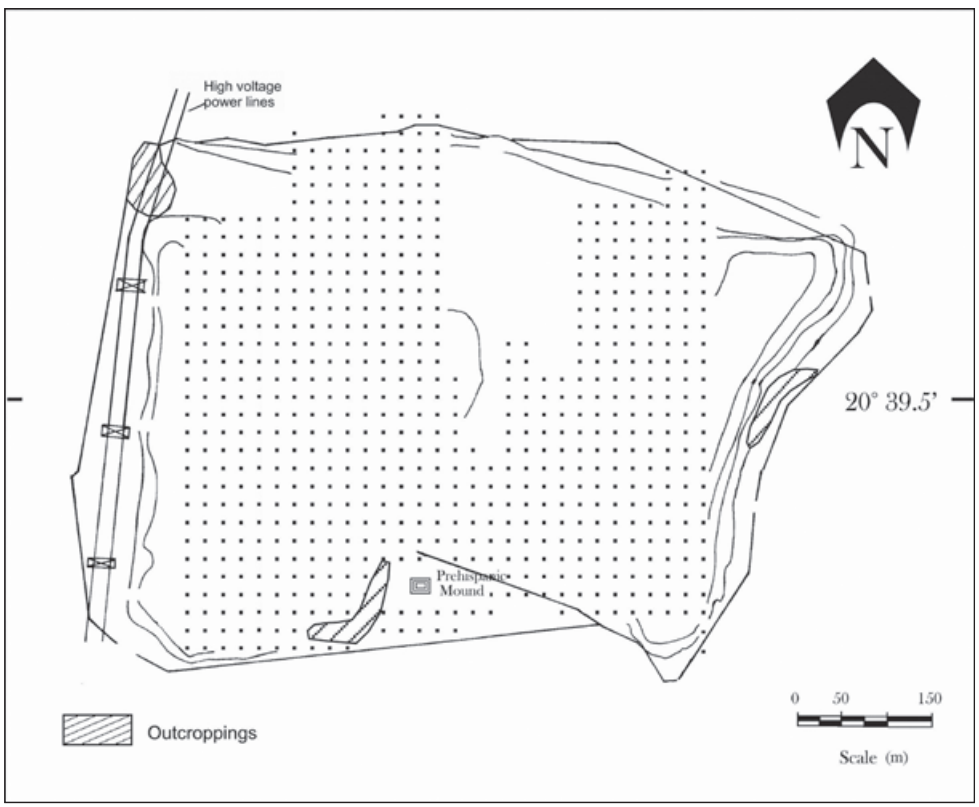

Figure 2. Detailed diagram of the Matatlan dumpsite. Points are measuring stations, with 20 m of separation. The box in the south is a pre-Columbian mound, whereas the boxes with two lines in diagonal, along the west side, correspond to towers of high-voltage wire lines. Andesitic outcrops, showed as shaded areas, are indicated. The continuous lines that surround the site are indicators of the limits and topography.

The OMNI MAG measures in-phase (Hx) and quadrature (imaginary, Hy) components normalized with the main field, along with complementary information as primary field intensity and tilt angle. In VLF methods both electric and magnetic components can be used. However, currently only the magnetic field *H* is used, because it is easier to calculate. In fact, the vertical component H_z is analyzed, as it is generated only by induction phenomena. The main field H_p lies almost in the horizontal plane.

VLF data

In Matatlan dumpsite, measurements were realized in 1997 along N-S profiles. NAA (located in Cuttler, Maine), NLK/NPG (located in Jim Creek, Washington State) and NPM (located in Lualualei, Hawaii) stations were used, with respective frequencies of 24.8, 24.0 and 23.4 kHz (see Table 1). At the time of these measurements NAA station showed a weak signal-to-noise ratio, so we decided to work with NLK/NPG station signal, assuming the presence of perpendicular structures to line of sight of this station. These measurements were taken each 2Om, forming the data grid shown in Figure 2. In some areas it was not possible to conduct measurements because of dumping works were been conducted at that time. High-voltage N-S transmission lines are located at the western side of the dumpsite (Figure 2). A lineal distance near to 80 meters separates the measurement area from high-voltage lines.

VLF anomalies processing

Traditionally, the interpretation of VLF tilt angle data was conducted qualitatively. VLF quantitative interpretation owes its beginnings to Fraser (1969) and Karous and Hjelt (1983) filtering techniques. However, as with other geophysical methods, VLF first interpretation techniques are based on the use of simple geometric bodies (Paterson and Ronka, 1978). Baker and Myers (1979) from laboratory modeling obtain VLF responses similar to that obtained by Paterson and Ronka (1978), who employ analytic methods.

A realistic VLF modeling of the subsurface must take into account media with different conductivities, irregular geometry and anisotropy to model VLF anomalies (Kaikkonen, 1979). So far, these factors are difficult to incorporate in numerical models to account for real geologic situations. Models from Vozoff (1971), Ward *et al*. (1974) and Kaikkonen (1979) are applicable to very simple structural situations and do not include the effect from conductive shields (covers). The high electric conductivity of these shields avoid the EM wave transmit to depth; this behavior reduces the searched thickness and produces a marginal penetration beneath the surface. Thickness and electric conductivity of the upper layer (or uppermost cover) control the VLF response (Olsson, 1980).

In a direct interpretative process Kaikkonen (1979) employs a finite element formulation starting from Maxwell equations in the frequency domain, to model ellipticity, tilt angle and amplitude ratio; he uses isotropic and anisotropic models of an inclined dike encased in a resistive media. With the ellipticity and the tilt angle it is possible to discriminate between good and poor conductors. Both parameters have same polarity for a poor conductor, but ellipticity changes polarity and shape for a good conductor (Kaikkonen, 1979).

One of the first VLF inversion methods was developed by Olsson (1980), that approaches an integral equation as a system of equations which is solved by iterative numerical techniques (Olsson, 1980). In this way, response curves for different models with a conductive cover are obtained. Since

Table 1. VLF stations used in Matatlan dumpsite.

Station	Operative Frequency for 1997	Operative Frequency for 2007	Location
NAA	24.8 KHz	17.8 KHz	Cuttler, maine (40° NE of Matatlan)
NLK/NPG	24.0 KHz	18.6 KHz	Jim Creek, Washington (20° NW of Matatlan)
NPM	23.4 KHz	23.4 KHz	Lualualei, Hawai (90° W of Matatlán)

then, several inversion methods have been developed, including 1-D inversion (Hjelt *et al*., 1985), regularized bidimensional inversion (Beamish, 1994), 3-D inversion (Beamish, 1998), and VLF and VLF-R data joint inversion using simulated annealing (Kaikkonen and Sharma, 1998). In one case Hjelt *et al*. (1985) work with VLF-resistive data, which is an extension from conventional VLF-Z (Beamish, 1994) or VLF-EM techniques (Reynolds, 1998). In VLF-R information from just one frequency is obtained, measuring perpendicular components of electric and magnetic horizontal fields, giving in this manner impedance values. Beamish (1994) and Kaikkonen and Sharma (1998) also work with VLF-R data. Beamish (1994) makes an extension from a non-lineal inversion techniques for MT data to VLF-R measurements, employing a 2-D Occam procedure.

In this study we applied the filtering techniques of Fraser and Karous-Hjelt, as primary approximations to an interpretation of VLF data.

Fraser filter

Fraser filtering comprises a process applied to data profiles whose results can be contoured. This method (Fraser, 1969) is designed for those parameters that exhibit a response with zero crossings, as in the in-phase vertical component (H_x) or the tilt angle of the polarization ellipse (α). In this method horizontal gradients are calculated and parts of the data are smoothed, so as to place the maximum value over a conductive surface. This is obtained with the following relation (Bayrak, 2002),

$$F_{2,3} = (M_3 + M_4) - (M_1 + M_2) \qquad (1.1)$$

where F are the stations, the subscript are the station numbers, whereas M_1 to M_4 are consecutive tilt angle stations (Bayrak, 2002). This anomaly is antisymetric over conductors, and is often indicated as gradient. The anomaly is convolved along several profiles, with the filter adjusting its length to the anomaly shape.

The interpretation of the results is qualitative. Very sharp responses indicate shallow sources, whereas wide anomalies progressively indicate deeper sources.

Karous-Hjelt filter

A very interesting technique for interpreting VLF data is based on the filter designed by Karous and Hjelt (1983), that although is a direct modeling technique, provides good locations of bodies and underground features giving rise to VLF anomalies. Karous and Hjelt (1983) based its algorithm on Biot-Savart law to describe the surface magnetic field of a 2-D distribution. They assume a small horizontal layer, with several current densities located at a depth equal to the distance between stations. When this method is used for data correction, results can be contoured as a proxy of conductivity as a depth function.

The idea of modeling VLF-EM data by mean of Karous-Hjelt filtering technique consists basically in considering subsurface electric heterogeneities as giving rise to current lines that distort primary EM fields. The developed lineal filter is applied in conjunction with a lowpass filter. As result this method provides a vertical distribution of apparent current densities (López-Sánchez, 1998). These current densities are associated with conductive zones below the surface (Marroquin, 2000).

Formulation of Karous-Hjelt filter for calculating current density, *I(0,)* is

$$l(0) = k\,(-0.102H_{-3}+0.059H_{-2}-0.561H_{-1}+0.059H_{2} +0.102H_{3}) \qquad (1.1)$$

where k depends from station interval and H_n is the $n\text{-}th$ stations behind (-) or forward (+) of filtered station (0).

We have employed academic computer programs developed by Edsen and Nissen (1997) and Pirttijärvi (2004); the first one forms the direct models with cells with constant resistivities and variable dimensions and depths. The second one applies both the Fraser, and Karous-Hjelt filters. The interpretation of the profiles obtained in this study was done in two steps.

Results and discussions

Fracture measurements

A Brunton compass was used to measure orientation of a wide group of fractures along the three existing outcroppings located inside and around the dumpsite limits (Figure 2).

The southern and northern outcrops consist of densely fractured basaltic andesites, whereas that to east comprises andesites plus altered tuffs (Figure 2).

The orientation of the fractures were plotted in a polar histogram with divisions each five degrees (Figure 3). The statistic analysis shows

the presence of primary and secondary fracture groups. Among the primary groups the most conspicuous has a North-South direction; the second one has N75-80E orientation; the third one has a mean azimuth of N60-65W direction, and the last one has a N25-30W direction. There are two secondary alignment groups that may be related to the primary directions. The most clear of them presents a N45-55E orientation, whereas the last one is outlined with a 90E direction. These fracture groups are referred to as A to F, respectively (Figure 3). Pattern A coincides with the direction of the Rio Grande de Santiago Canyon, whereas pattern F has the same direction as Coyula Canyon in its main part.

VLF parameters

Although the kind of information provided by the VLF method must be filtered to be represented in contour maps (what emphasizes positive features), it was decided to first present in raw form the in-phase, the out-of-phase, and tilt angle. Using triangular interpolation, we contoured the respective maps of the VLF parameters showed at Figures 4a, 4b, and 5a. These results will now be qualitatively interpreted.

Frequently occurring fluctuations in VLF measurements are not caused by temporal or spatial variations of the signal. These variations are attributed to anthropogenic noise and often have a typical morphology. Along the western boundary runs a high voltage line but its noisy effect (high amplitude and strong separation between components after Bozzo *et al*., 1994) is not as obvious as the effect induced by the metallic fence that surrounds a pre-Columbian mound, at the south center of the area (Figures 4a, 4b and 5a). The effect of the high voltage lines can be observed only in the first 40 m approximately, whereas the wire fence surrounding the pre-Columbian mound produces an effect due to its high conductivity. Its influence is still observed at approximately 70 meters away from the mound (see Figures 4a, 4b and 5a).

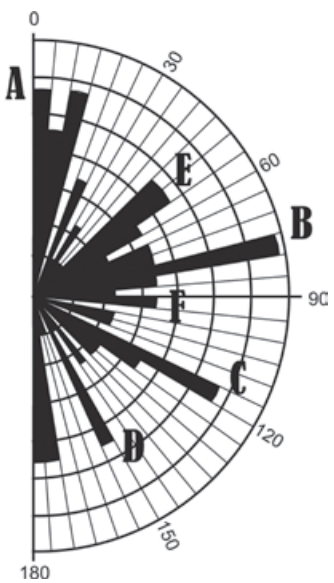

Figure 3. Polar histogram from fracture pattern measurements in andesitic outcrops showed in the Figure 2. The divisions are given each 5°. The letters indicate main directions of groups of fractures.

Conspicuous anomalies in the in-phase and the out-of-phase components, (Figures 4a and 4b) occur at points where leachate ponding is very extensive (A in Figures 4a to 5b). An interesting observation that arises from the comparison of the two maps is the north-south elongated feature of the central part, which is positive in both components (B in Figures 4a and 4b) but is accompanied by a negative in the in-phase component (referred to C in Figures 4a and 5a). In addition, areas of deposition and new mixed garbage at the date of the VLF survey are clearly visible as closed anomalies (D in Figures 4a to 5b). This behavior prevails in the northeastern part of the landfill, which is seen as a major negative pattern in the in-phase component (Figure 4a).

Many times the VLF response simply can not be interpreted. This is due to overlapping effects of other anomalies, and attenuation and phase change induced by conductive cover.

Certainly, the bulk of the interpretation in the VLF method remains up today qualitative in nature. In fact, until 1980 the interpretation was mainly based on qualitative arguments, neglecting the influence of rock covers and guest conductors (e.g., Olsson, 1980). A more complete interpretation should include the recognition of type anomaly selecting a general model type, and some rudimentary analysis to locate depths to the source. In addition, some general idea would be obtained about, for example, the conductivity of the target.

The differences between tilt angle (Figure 5a) and its respective 3D Fraser-filtered map (Figure 5b) are more or less significatives. One of these differences is that the elongated N-S minimum located at centre of the dump in the tilt angle map (C in Figure 5a) has

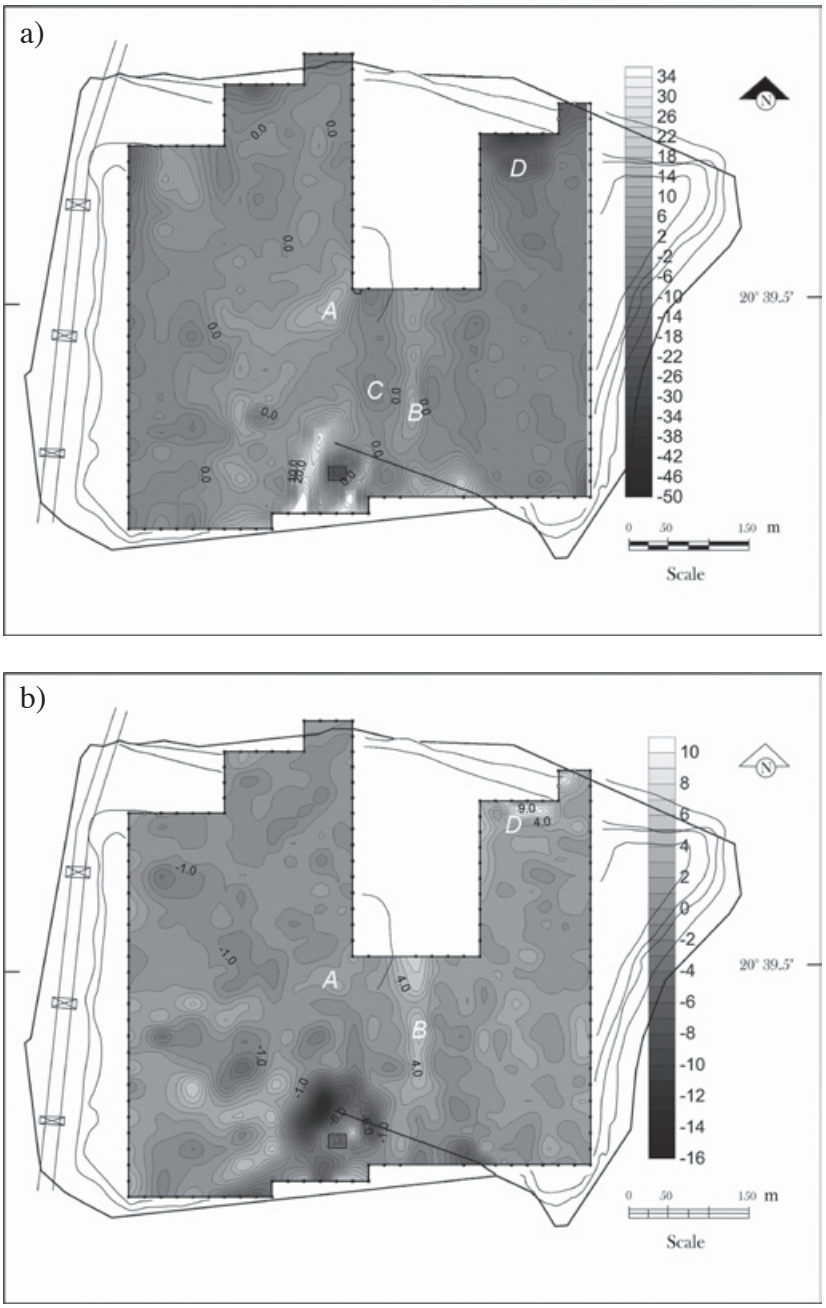

Figure 4. (a) VLF field in-phase component contoured each 2.0 %. Values in the scale at the left side are in %. The letters indicate most conspicuous anomalous features. (b) VLF out-of-phase component contoured each 1%. Values in the scale at the left side are in %. The letters indicate most conspicuous anomalous features.

been smoothed and eastward displaced in the filtered map (Figure 5b). Main positive features in the filtered map could be interpreted in two ways: 1) the elongated positive feature on the west side (E in Figure 5b) may be due to a structure roughly oriented NW-SE that acts as conduit for leachate, and 2) the positive feature referred to as A in Figure 5b, might be due to an accumulation of lixiviates. Altogether, three main groups of elongated anomalies can be noted. In the western half and in the centre occurs the major quantity of elongated positive anomalies, with NW-SE, N-S, and NE-SW orientations (A, E, F, H, and I in Figure 5b), whereas in the eastern portion, it seems to be present some NW-SE and N-S anomalies (B, D, G, and N in Figure 5b). Their orientations are highlighted with continuous lines in Figure 5b. Their elongated nature could indicate a major fracture system or groups of fractures. The southeastern portion is featured by very small and isolated anomalies.

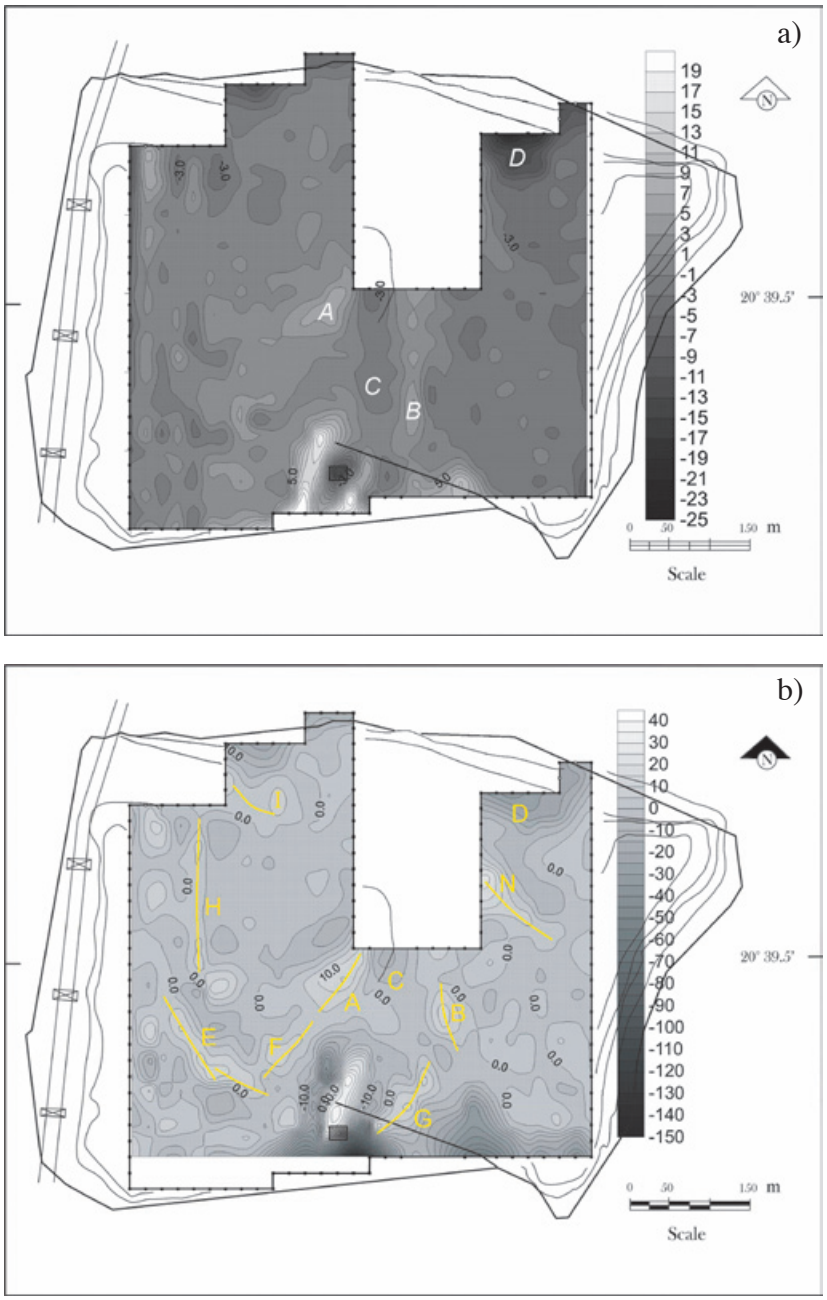

Figure 5. (a) Tilt angle contoured each 2%. Values in the scale at the left side are in %. The letters indicate most conspicuous anomalous features. (b) Fraser filtering applied to tilt angle. Contours are given each 5%. Values in the scale at the left side are in %. The letters indicate most conspicuous anomalous features. Yellow continuous lines are structure alignments inferred.

Quantitative Interpretation

In a first quantitative step we applied the Fraser and Karous-Hjelt's technique modified to model VLF data by means of cell-shaped sources with constant resistivities (Edsen and Nissen, 1997). Several N-S and E-W profiles, corresponding to 24 KHz, were selected (Figure 6) for this purpose (Alatorre-Zamora, 2003) considering the behavior of real and imaginary components, and taking into account noise areas covered within the survey, and results obtained by other geophysical methods (Alatorre-Zamora *et al*., submitted); just three of the most representative modeled profiles are presented.

The modeling was based on the VLFMOD program from Edsen and Nissen (1997), which models VLF-EM or VLF-R data and generates a simple model considering the source frequency and just one resistivity for the host media. This simple model can then be modified or other bodies can be added. In this case the respective model was formed based upon information given by resistive tomography (Alatorre-Zamora, 2003) and potential field models (Alatorre-Zamora *et al*., submitted).

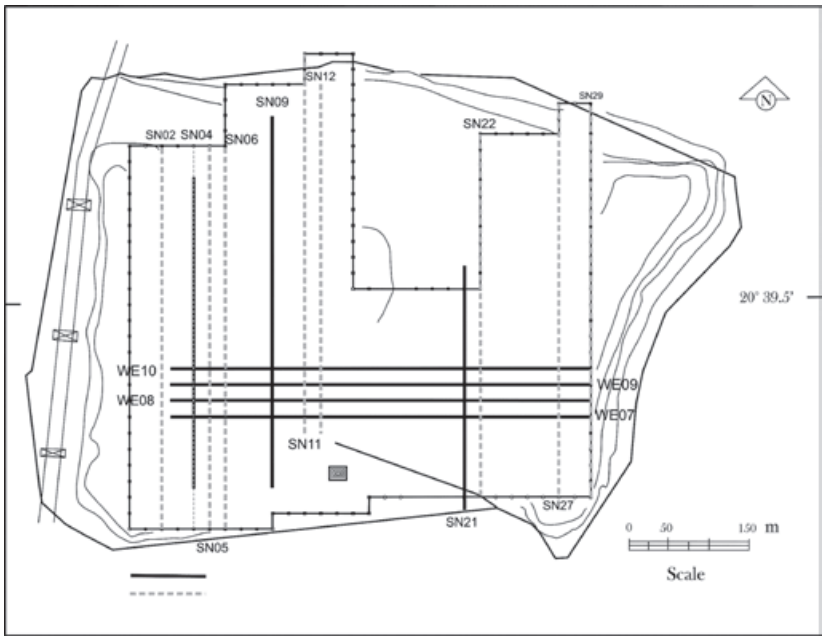

Figure 6. Location of interpreted profiles at Matatlan dumpsite. Solid black lines are profiles interpreted with VLFMOD program, whereas gray dashed lines are profiles interpreted with KHFFILT program. Symbols like WE10 or SN11 are the names of the consecutive profiles.

In this first stage our models comprise cells simulating fault or fracture zones, approach part of the landfill, and the top of the andesitic basement. In all cases, we assume a variable resistivity for the host layer along the dump-site due to the presence of soil plus urban waste composition for the overall site, and andesitic blocks mainly at the SW sector. Indeed, andesitic blocks could occur beneath the entire study area, but they are covered by terrigenous material and the proper waste disposal, and this fact is considered in the modeling. The resistivity for the host layer varies from 170 to 440 Ω-m. To the andesitic basement were assigned resistivities from 92 to 268 Ω-m along the profiles, whereas fault and fracture zones were assigned lower resistivities. Interpreted profiles are showed in Figures 7a to 7c.

Although adjustment errors between computed and observed component anomalies are large, the outlined behavior of the computed anomalies is fairly similar to observed ones. These misfits show the difficulty to model VLF data, specially the imaginary (or out-of-phase) component.

EW-8, EW-9 and EW-10 profiles show continuity both in anomaly behavior and in location and resistivities of modeled bodies (Figures 7a to 7c). An example is represented by the fault zone inferred at about 300 m, with a proposed resistivity from 70 to 36 W-m (black filled boxes in profiles EW-08 to EW-10; in general, small boxes in these three profiles). This fault zone seems to have reached a depth between 10 to 20 m, and in general show a southern dip. The same structure is observable in the Fraser filtered map (A and F elongated features in Figure 5b).

Another important feature of the models constitutes the use of a resistivity value for the host material of the sources, consistent with the andesitic basement of the landfill. This establishes that the lowest body cells seem to show the topography of the andesitic basement, i.e., this basement has depths from 5 to 7.5 m.

The low resistivity values assigned to the structures inferred as faults let to assume that these structures allow the migration of leachate to lower levels in the basement, although the fault zones inferred are deeper than the top of the andesitic basement (i.e., they cut it). The resistivities decrease with leachate, and this seems to cause these anomalies.

Fault zones actually agree with those inferred by mean of resistive tomography and magnetics and gravity interpretation (Alatorre-Zamora, 2003; Alatorre-Zamora *et al*., submitted).

In a second step we conduit a profile interpretation using the Pirttijärvi's (2004) KHFFILT non-commercial program. This applies the Karous-Hjelt filtering technique and provides the vertical distribution of apparent current densities (López-Sánchez,

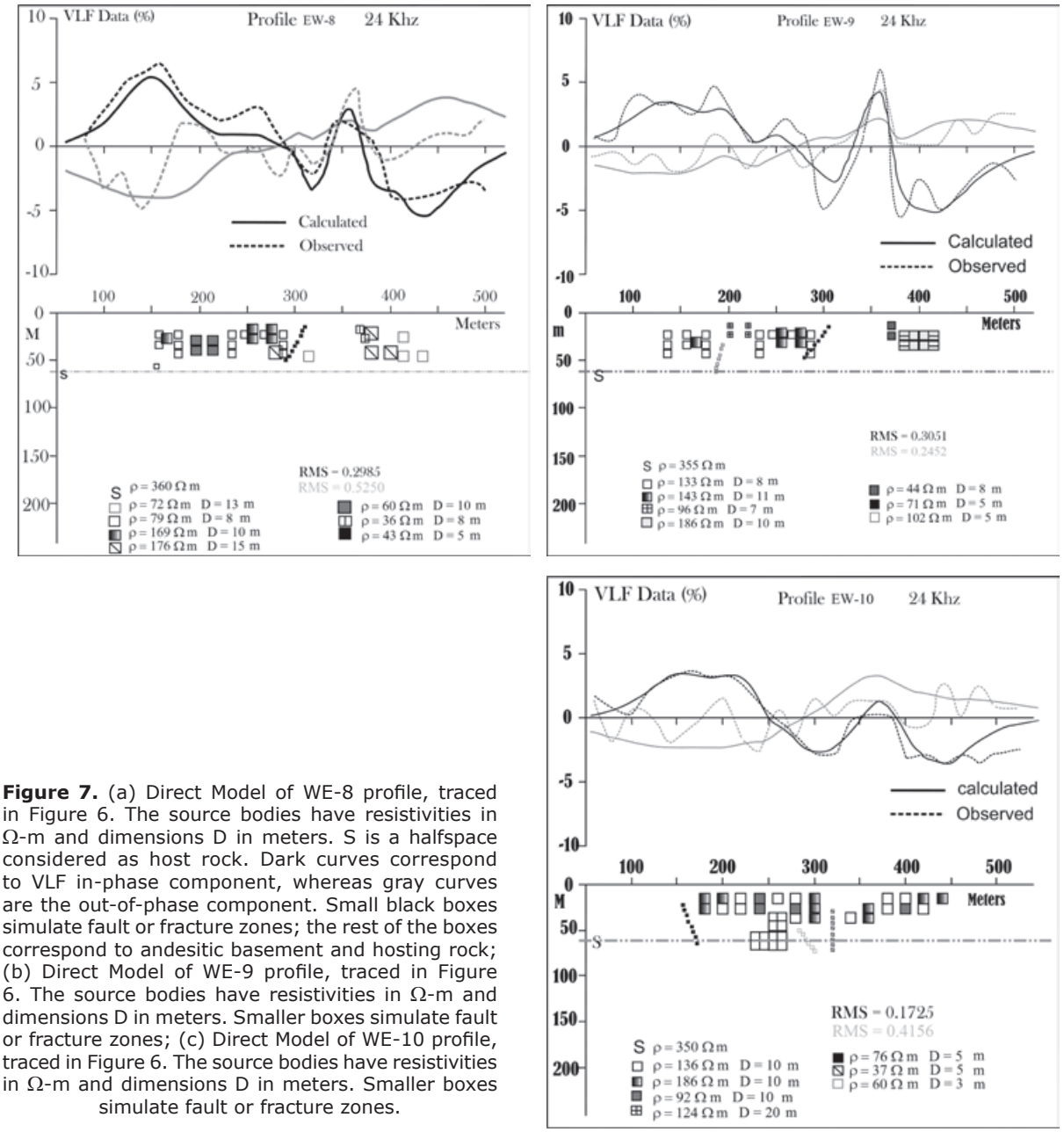

Figure 7. (a) Direct Model of WE-8 profile, traced in Figure 6. The source bodies have resistivities in Ω-m and dimensions D in meters. S is a halfspace considered as host rock. Dark curves correspond to VLF in-phase component, whereas gray curves are the out-of-phase component. Small black boxes simulate fault or fracture zones; the rest of the boxes correspond to andesitic basement and hosting rock; (b) Direct Model of WE-9 profile, traced in Figure 6. The source bodies have resistivities in Ω-m and dimensions D in meters. Smaller boxes simulate fault or fracture zones; (c) Direct Model of WE-10 profile, traced in Figure 6. The source bodies have resistivities in Ω-m and dimensions D in meters. Smaller boxes simulate fault or fracture zones.

1998), which can be interpreted as to represent conductive zones below the surface (Benson *et al*., 1997; Marroquin, 2000). In addition, the software provides a Fraser filtered profile, which correlates with the Karous-Hjelt filtered profile.

For each profile three plots are shown (see Figure 8a). The upper panel presents the raw data. The middle one presents the Fraser filtered profile. Finally, the lower panel corresponds to Karous–Hjelt (K-H) filtered profile, where we can note that low current density values correlates with high resistivity values (Karous and Hjelt, 1977). Besides, peaks in the Fraser filter profile locate conductive structures.

Good correlation between the peaks of Fraser filter and conductive zones (survey as inferred by high current density values) of Karous-Hjelt filter is observed for profile NS-04 (Figure 8b). The profile NS-02 does not show conductive surfaces below the peaks of Fraser filtering (Figure 8a). This could be significative, because this last profile corresponds almost entirely to the western sector of the dumpsite (Figure 6),

whereas many conductive sources, as most recent deposition of waste and terrigenous material at the time, as well as the presence of heavy machinery, occurred at the NE part of the site.

Correlation of parallel Karous-Hjelt filtering profiles makes it possible to observe the continuity of features attributable to planar sources as fault and major fracture zones. In this manner we can appreciate the presence of 2D structures that are orthogonal to the VLF station used, it is to say, they are normal to NAA station, which has an NE-SW orientation with respect to Matatlan dumpsite. This indicates that we must infer mainly structures with NW-SE directions. According to the statistical analysis of fractures, we expect to locate fractures similar to groups C and D (see Figure 6).

To enable a better visualization of positive KH features, image maps with the resulting current densities from the modeled profiles were elaborated. These maps are showed in Figures 9a and 9b, and represent pseudodistributions of current density at depths of 20 and 40 m.

In these results it is possible to consider that there is not effect from conductive cover. Three main high current density features which have continuity in depth are: 1) an almost NE-SW elongated feature at the centre of the area (A in Figures 9a and 9b); 2) two elongated lineaments located in the western half of the site, that are parallel, with a N-S direction to the north, and become NW-SE to the south (E and H in Figures 9a and 9b). These last features reach depths of 40 m (Figure 9b), where they are clear; 3) a minor feature at the NW sector, whose direction is NW-SE (I in Figures 9a and 9b).

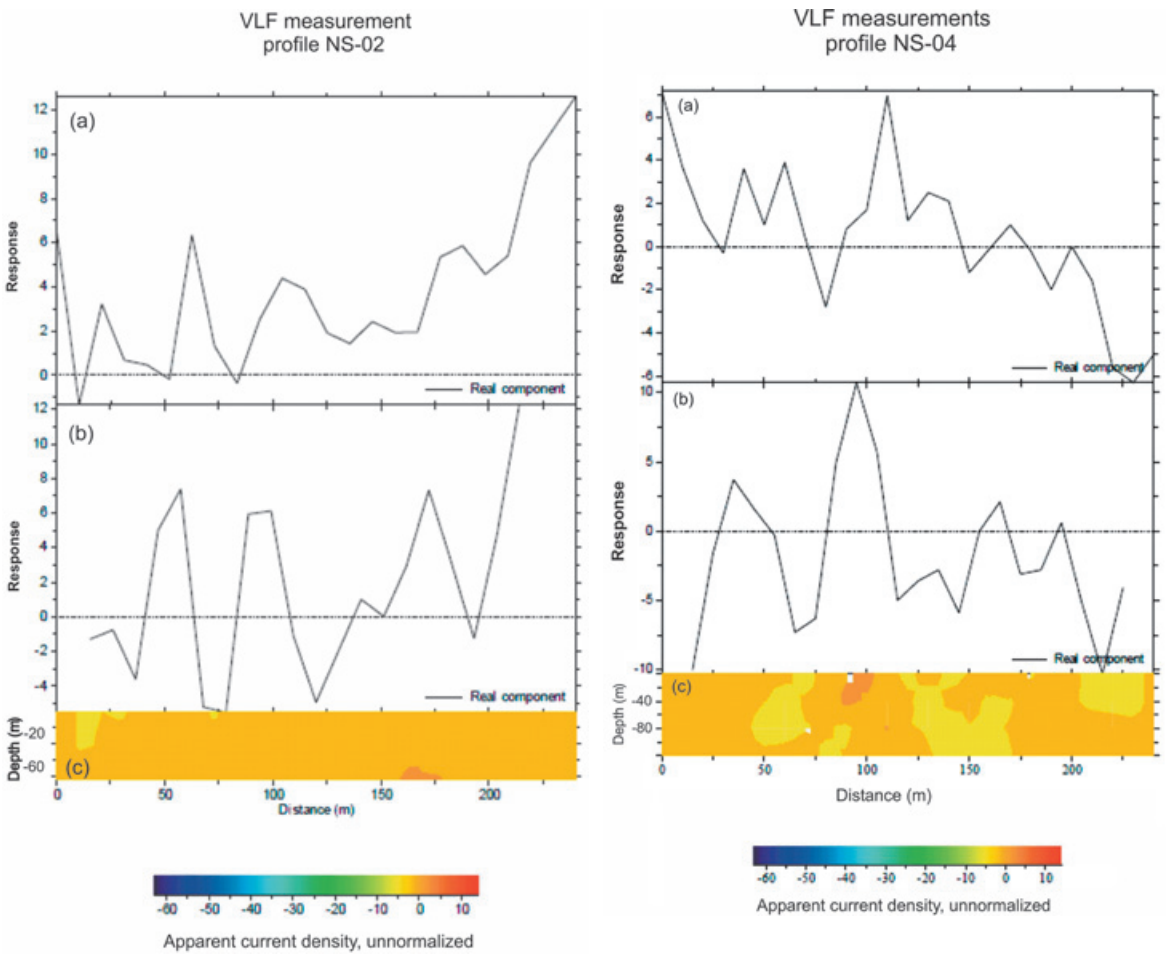

Figure 8. Fraser and Karous-Hjelt filtering results for the NS-02 (left plot) and NS-04 (right plot) profiles at Matatlan dumpsite. (a) raw data, given in %; (b) Fraser filter result, and (c) pseudosection of current density resulting to apply Karous-Hjelt filter.

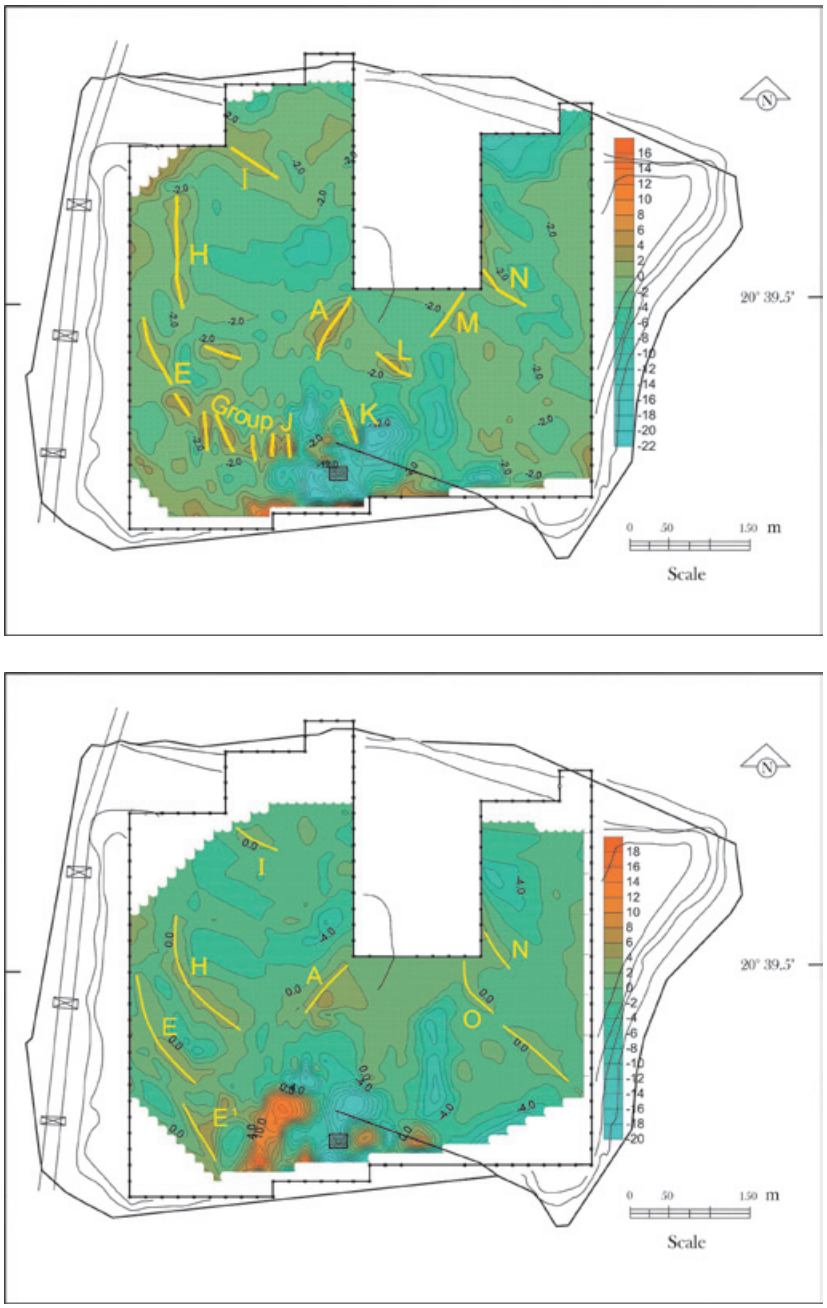

Figure 9. (a) Current density pseudodistributions located at 20 m in depth obtained with Karous-Hjelt filter; (b) Current density pseudodistributions located at 40 m in depth obtained with Karous-Hjelt filter.

These elongated high current density features could be owed to a major fracture system. A higher current density elongated feature that is not referred to in Figure 9b is observed also at 40 m in depth, in the SW edge of the site. It could be caused by the metallic fence that surrounds the pre-Columbian mound, but it does not appears at 20 m. Its almost N-S direction and its position (location) coincides with the outcropping there located.

Comparing maps from Figures 9a and 9b, a major high current density between 0 and 20 m is observed (Figure 9a); at this depth range, the higher value is located conspicuously, near the pre-Columbian mound, at the south side of the site.

Whereas some anomalies could be produced by leachate filtration or leachate presence into the dumpsite layer, the southern one near to the mound would be due to a wide fault zone.

Comparison between VLFMOD and KHFFILT results is possible, although in the first case we have a direct modeling, whereas the second one provides vertical current density pseudodistributions. KHFFILT seems to give better approximations when their results are combined together with Fraser results. Nevertheless, the modeled cells in the direct approach have parameters as resistivity and location that show fair correlation with Karous-Hjelt filtering results, showing that there is a good agreement (correlation) between the results of both methods used.

Comparison between 3D Fraser filtered results and KHFFILT results (Figures 5b, with Figures 9a and 9b) indicates very interesting correlations. Both techniques highlight same features that could be the signature of faults or major fracture systems. The major similarity occurs between results from Figure 5b and Figure 9b, showing a strong continuity for the VLF anomalies with depth.

We finally observe two generalized features: (1) several positive features with orientations mainly NW-SE that appears along the dumpsite, would show a possible influence of Tepic-Zacoalco rift. (2) The long N-S positive feature given by the two techniques and the 3D Fraser filtered tilt angle, at the westernmost sector of the dumpsite, could be result of the tectonic that controls the Rio Grande de Santiago Canyon. This last could be of listric nature.

Conclusions

Very low frequency geophysical method has been proved to be an excellent media to infer 2D structures as faults and fractures through which water or contaminants flow might take place. Thereby providing a means to recognize and delineate the presence of 2D structures as faults and fractures that could function as migration paths for the leachates in urban waste dumpsites. Here we can conclude about the use of three techniques to interpret VLF data, that is, the Fraser filter applied to tilt VLF parameter, Karous-Hjelt filter applied to in-phase and out-of-phase VLF components, and a modified K-H filtering technique applied to the same components as a direct modeling, in the scope of the task described previously.

The statistic analysis of fracture direction measurements showed the presence of primary and secondary fracture groups. The primary groups have N-S, NE-SW, and NW-SE directions, in order of predominance.

Conspicuous anomalies in both, the in-phase component and the out-of-phase component occur with N-S orientation at the central and westernmost parts of the dumpsite. Areas of deposition and new mixed garbage at the date of the VLF survey are clearly visible as closed negative anomalies in the in-phase component. Tilt angle parameter showed the same behavior as the in-phase component.

The Fraser filtered results presents nine features of interest to the scope of the study. Four of them are NW-SE oriented, whereas three have NE-SW directions. The most conspicuous anomalous feature, however, has a long N-S direction, and is located at the westernmost part of the site.

With respect to the K-H filtering results, three main high current density features are inferred which have continuity with depth: 1) an almost NE-SW elongated feature at the centre of the area, 2) two elongated N-S parallel lineaments located in the western half of the site, that become NW-SE to the south. These last features continue in depth, being most clear at 40 m depth, 3) a minor feature at the NW sector, whose direction is NW-SE. These elongated high current density features could be owed to fracture systems. A higher current density elongated feature is observed also at a depth of 40 m, in the SW edge of the site. It could be caused by the metallic fence that surrounds the pre-Columbian mound, but it does not appears at 20 m. Its almost N-S direction and its location coincide with the andesitic outcrop there located.

The comparison between Fraser and Karous-Hjelt filters and two different techniques that provides model sources and current distribution respectively, showed good-to-fair results in the location of some fracture or fault zones.

Finally, it is interesting to note the correlation between the lineaments inferred by means of the cooperative use of both techniques, based on K-H and the Fraser filter and the major tectonic features. Accordingly, a N-S structure in the westernmost part of the zone, that have same direction as Rio Grande de Santiago Canyon, as well as NW-SE features, mainly in the western half of the site. These NW-SE features coincide with the directions of the Tepic-Zacoalco rift. Others NE-SW features appear towards the centre of the area. These facts correlate with the predominance of fracture groups showed in the fracture analysis.

Finally, the structures inferred and their directions could act to migrate lixiviates outside the dump, mainly towards the Coyula Canyon, located along the south border of the site, as well as in a minor effect towards the Rio Grande de Santiago Canyon.

Acknowledgements

The first author was supported with a grant from SUPERA-PROMEP and is indebted to CAABSA-EAGLE for allowing the study. The text improved thanks to criticism of Dr. Shevnin and an anonymous reviewer.

References

Alatorre-Zamora M.A., Campos-Enríquez J.O., 1991, La Primavera Caldera (Mexico): structure inferred from gravity and hydrogeological considerations. *Geophysics,* 56, 992-1,002.

Alatorre-Zamora M.A., 2003, Estudio Geofísico Integrado Realizado en el Vertedero de Desechos Urbanos de la Ciudad de Guadalajara. Ph D Thesis. Instituto de Geofísica, UNAM. 132–154 pp.

Alatorre-Zamora M.A., Campos-Enríquez J.O., Chávez-Segura R., Belmonte-Jiménez S.I., in press. Mapping major fractures affecting the basement of an urban waste dump (Matatlan, western Mexico). Assessment of use of Euler deconvolution, analytical signal, and the micromagnetic method. Submitted to *Near Surface Geophysics*.

Alexandros S. Savvaidis, Tsokas G.N., Vargemezis G., Dimopoulos G., 1999, Geophysical prospecting in the Akropotamos dam (N. Greece) by GPR and VLF methods. *Journal of the Balkan Geophysical Society*, 2, 120-127.

Armadillo E., Massa F., Caneva G., Gambetta M., Bozzo E., 1998, Modelling of Karst structures by geophysical methods. An example: the doline of S. Pietro dei Monti (Western Liguria). Annli di Geofisica, 41, 3 páginas.

Baker H.A., Myers J.O., 1979, VLF-EM model studies and some simple quantitative applications to field results. *Geoexploration,* 17, 55-63.

Bayrak M., 2002, Exploration of chrome ore in Southwestern Turkey by VLF-EM. *Journal of the Balkan Geophysical Society*, 5, 35-46.

Beamish D., 1994, Two-dimensional, regularised inversion of VLF data. *Journal of Applied Geophysics*, 32, 357-374.

Beamish D., 1998, Three-dimensional modeling of VLF data. *Journal of Applied Geophysics*., 39, 63-76.

Bekaert C., Budka A., Lambolez-Michel L., Matichard Y., Martin I., 2002, Los vertederos y el desarrollo sostenible. *Revista Residuos*, 64 páginas.

Benson A.K., Payne K.L., Stubben M.A., 1997, Mapping groundwater contamination using dc resistivity and VLF geophysical methods—A case study. *Geophysics*, 62, 80–60.

Bozzo E., Lombardo S., Merlanti F., 1994, VLF prospecting: observations about field experiments. Annali di Geofisica, 37, 5 páginas.

Campos-Enríquez J.O., Alatorre-Zamora M.A., 1998, Shallow crustal structure of the junction of the grabens of Chapala, Tepic-Zacoalco and Colima, Mexico. *Geofísica Internacional,* 37, 263-282.

Christensen T.H., Cossu R., Diaz L., Lechner P., Stegmann R., Lagerkvist A., 2000, Alternative approach to the elimination of greenhouse gases from old landfill. Curso superior sobre gestión y diseño de vertederos. CER (Club Español de los Residuos).

Edsen N.A., Nissen J., 1997, VLFMOD, a free forward VLF modeling software package. ftp: http://home1.swipnet.se/~w-11019/ABEM-ftp/

Ferrari L., 1995, Miocene shearing along the northern boundary of the Jalisco block and the opening of the southern Gulf of California. *Geology*, 23, 751-754.

Fraser D.C., 1969, Contouring of VLF-EM data. *Geophysics*, 34, 958-967.

Gilbert C.M., Mahood G.A., Carmichael I.S.E., 1985, Volcanic stratigraphy of the Guadalajara area, Mexico. *Geofísica Internacional*, 24, 169-191.

Greenhouse J.P., Harris R.D., 1983, Migration of contaminants in groundwater at a landfill: a case study, 7. DC, VLF, and inductive resistivity surveys. In: J.A. CHERRY (Guest Editor), Migration of contaminants in

groundwater at a landfill: A Case Study. *Journal of Hydrology*, 63, 177-197.

Hjelt S.E., Kaikkonen P., Pietila R., 1984/85, On the Interpretation of VLF Resistivity Measurements, *Geoexploration*, 23, 171-181.

Jones D.R.V., Dixon N., 2005, Landfill lining stability and integrity: the role of waste settlement. *Geotextiles and Geomembranes*, 23, 27-53.

Kaikkonen P., 1979, Numerical VLF modeling, 1979, *Geophysical Prospecting*, 17, 815-834.

Kaikkonen P., Sharma S.P., 1998, 2-D nonlinear joint inversion of VLF and VLF-R data using simulated annealing, *Journal of Applied Geophysics*, 39, 155-176.

Karous M., Hjelt S.E., 1983, Linear filtering of VLF dip-angle measurements, *Geoph. Prospecting*, 31, 782-794.

Kjeldsen P., Barlaz M.A., Rooker A.P., Baun A., Ledin A., Christensen T.H., 2002, Present and long-term composition of MSW landfill leachate. A review. Critical Reviews In *Environmental Science and Technology*, 32, 297-336.

Lopez-Sanchez M., 1998, *www.geophysicsgpr.com/aben/wadi_vlf.htm.*

Luhr J., Lazaar P., 1985, The southern Guadalajara volcanic chain, Jalisco, Mexico. *Geofísica Internacional*, 24, 691-700.

Mahood G.A., 1980b, Geological evolution of a Pleistocene rhyolitic center – Sierra La Primavera, Jalisco, Mexico. *Journal of Volcanologic and Geothermal Research,* 8, 199-230.

Marroquin I.D., 2000, Proyecto de Maestría. *www.wlba.net/ivan/vprm.es.html*.

Milsom J., 2003, Field Geophysics, 3° edition; John Wiley & Sons, 244 Pp.

Olsson O., 1980, VLF Anomalies from a perfectly conducting half plane below an overburden. *Geophysical prospecting*, 18, 415–434.

Paál G., 1968, Very low frequency measurements in northern Sweden. *Geoexploration*, 6, 141-149.

Paterson N.R., Ronka V., 1971, Five years of surveying with the Very Low Frecuency Electromagnetics Method. *Geoexploration*, 9, 7–26.

Phillips W.J., Richards W.E., 1975, A study of the effectiveness of the VLF method for the location of narrow-mineralized fault zones. *Geoexploration*, 13, 215-226.

Pirttijärvi M., 2004, Karous-Hjelt and Fraser filtering of VLF measurements, version 1.1a, http://www.cc.oulu.fi/~mpi/Softat/Khffilt.html

Reynolds J.M., 1998, An Introduction to Applied and Environmental Geophysics, John Wiley & Sons, eds., 796 pp.

Rosas-Elguera J., Urrutia-Fucugauchi J., 1998, Tectonic control of the volcanosedimentary sequence of the Chapala graben, western Mexico. *Intern. Geol. Rev.*, 40, 350-362.

Saydam A.S., 1981, Very low frequency electromagnetic interpretation using tilt angle and ellipticity measurements. *Geophysics*, 46, 1594-1605.

Sinha A.K., 1990a, Interpretation of ground VLF EM data in terms of inclined sheet like conductor models. PAGEOPH, 132, 213-231.

Vozoff K., 1971, The effects of overburden on vertical component anomalies in AFMAG and VLF exploration: a computer model study. *Geophysics*, 36, 53-57.

Ward S.H., Ryu J., Glenn W.E., Homann G.W., Dey A., Smith B.D., 1974, Electromagnetic methods in conducive terrains. *Geoexploration*, 12, 121-183.

Watkins N.D., Gunn B.M., Baksi A.K., Ade-Hall J., 1971, Paleomagnetism, geochemistry, and potassium-argon ages of the Río Grande de Santiago volcanics, central Mexico. *Geological Society of America Bulletin*, 82, 1,955-1,968.

Wright J.L., 1988, VLF interpretation manual: EDA Instruments (now Scintrex), Toronto.

Geofísica Internacional (2014) 53-3: 259-275

Original paper

Crustal structure of eastern Cuba, derived by constrained 3D gravity inversion

Eduardo Diego Arango-Arias*, Marco Antonio Pérez-Flores and José Alberto Batista-Rodríguez

Received: February 21, 2013; accepted: October 08, 2013; published on line: July 01, 2014

Resumen

Se obtuvo un modelo tridimensional de la corteza mediante un proceso de inversión de datos gravimétricos para la región oriental de Cuba. Los datos y el modelo cubren un área rectangular de 64 600 km^2. El modelo inicial fue constreñido con la geología de superficie, la información sísmica y de perforación. Se aplicó un algoritmo de inversión que utiliza los datos de gravedad para estimar las topografías 3D a partir de las unidades geológicas principales. El modelo nos proporciona información cuantitativa sobre las profundidades y espesores de las formaciones geológicas más importantes. En el mismo se observan las secuencias alóctonas de diferente composición y origen sobre el basamento carbonatado de la Plataforma de Bahamas. La mayoría de los máximos en la anomalía de la gravedad se deben a la presencia de mantos más densos de ofiolitas poco profundas. Se destaca al suroeste el máximo gravimétrico provocado por la presencia de la corteza oceánica más densa generada en el Centro de Dispersión de Caimán.

Palabras clave: corteza, inversión, gravedad, ofiolitas, acreción.

Abstract

A three-dimensional crustal model for Eastern Cuba, obtained through a process of gravity data inversion is presented. The study area cover a rectangular area of 64 600 km^2. The initial model for the inversion was constrained by surface geology, seismic and drilling data. The inversion algorithm uses gravity data to estimate 3-D topographies from the main geological units. The model provides quantitative information on the depths and thicknesses of the geological formations. The resulting model provides new information about the regional composition of the crust. Alien sequences are observed with different compositions and origin over the basement of Bahamas carbonate platform. Most of the maximum gravity anomalies are associated with presence of dense shallow ophiolite sheets. The most remarkable detail is the gravity "southwest" maximum, related to the presence of denser oceanic crust generated in the Cayman spreading center.

Key words: Eastern Cuba, crustal structure, constrained inversion, gravity, ophiolites, accretion.

E. D. Arango-Arias*
Centro Nacional de Investigaciones Sismológicas
Calle 17 No. 61, Rpto. Vista Alegre
Santiago de Cuba, Cuba

Centro de Investigación Científica
y de Educación Superior de Ensenada
Applied Geophysics Department
Carr. Ensenada-Tijuana, 3918
Zona Playitas, Ensenada
Baja California, México
*Corresponding author: elgato601115@gmail.com

M. A. Pérez-Flores
Centro de Investigación Científica
y de Educación Superior de Ensenada
Applied Geophysics Department
Carr. Ensenada-Tijuana, 3918
Zona Playitas, Ensenada
Baja California, México

J. A. Batista-Rodríguez
Universidad Autónoma de Coahuila
Escuela Superior de Ingeniería.
Blvd. Adolfo López Mateos
26800 Nueva Rosita
Coahuila, México

Introduction

Models of genesis and evolution for the Caribbean-Cuba region show little agreement; in-situ (Giunta *et al*., 1997,James, K.H; 2003) and allochthonous (Pindell *et al*., 1990, 2009; Iturrade-Vinent, 1998, 2002; Cobiella, 2005; García-Casco *et al*., 2008 and Sommer *et al*., 2011). Allochthonous models indicate the area is formed by fragments of the ancient Caribbean plate that overrode the continental Bahamas margin. Over this margin are the Paleocene Volcanic Arc (PVA) and Neogene-Quaternary sediments forming basins. Other studies took into consideration seismic refraction, gravity, deep drilling boreholes and satellite images. Studies from 30 years ago showed that the island is on transitional crust, with 17 to 30 km thick and characterized by three layers: an upper volcanic-sedimentary layer with P velocity of 4.0-4.8 km/s, a lower layer with P of 5.8-6.4 km/s and the deepest layer with P of 6.3-6.7 km/s (Bovenko *et al*., 1982; Otero *et al*., 1998; Bush and Shcherbakova, 1986). Alternatively, Eastern Cuba is constituted to the south by an oceanic crust and to the north by continental crust (Tenreyro *et al*., 1994). Otero *et al*. (1998) based on re-interpreted seismic and gravity data proposed that the crust southward of Cauto-Nipe (Figure 1) is oceanic, ~20 km thickness, and below the basin there is a fine-transitional crust with 20 to 30 km thick and northward continental crust. Through teleseismic data, Palau *et al*. (2006) determined the presence of a 1 km thick shallow layer with P velocity of 3.6 km/s, underneath a 6 km thick layer with P of 5.8 km/s and a deeper 13 km thick layer with 6.9 km/s for P. Recently, Gonzalez *et al*. (2011) defined a 16 to 30 km earth crust thickness for eastern Cuba, through joint inversion of Rayleigh waves dispersion and receptor functions. All these models are assumed one-dimensional or horizontal stratified.

Such varied results and explanations indicate that a further research is required. The main purpose of our research is to obtain the structure of the earth crust for Eastern Cuba using a dense gravity data. We extended a method that was previously used in a reduced area of Eastern Cuba with mining purposes and using only magnetic data (Batista *et al*., 2007). We used the Gallardo *et al*. (2003) algorithm, which minimizes the quadratic norm of differences between gravity data and the model response, constraining the solution or model with the surface geology, boreholes (~3.5 km as maximum) and seismic reflection profiles. Every unit is simulated with a regular mesh of 10 km x 10 km prisms. Along the iterative inverse process, the depths to every prism is moved automatically in order to fit the gravity data and restricted to obey the constraints imposed.

The study area is a rectangle of 190 km by 360 km that covers the southeast of Cuba. A large land area and two pieces of oceanic crust are involved; the Atlantic Ocean and the Caribbean Sea where the Oriente Fault Zone (OFZ) is located (Figure 1). The area limits in "Southern Cuba coordinates system" are (100,000; 290,000) m North and (420,000; 760,000) m East. The rectangular region was divided into a grid of prisms with 10 km x 10 km on surface as shown in Figure 1.

Geologic context

Iturralde (1998) recognizes two levels of the geological structure of Cuba: the substrate folding and the neo-autochthonous. Each consisting of different geological units.

The existing folded substrate is formed by pieces from the North-American and the ancient Caribbean and Pacific plates. Neo-autochthonous units are sediments from the Neogene-Quaternary.

In our study area (Figure 2), the folded substrate is composed by: ophiolites, Cretaceous and Paleogene Volcanic Arcs. Ophiolites (West-East strips) located at the north, are over the Bahamas platform and under the Cretaceous Volcanic Arc (CVA). Sometimes, ophiolites and CVA are mixed forming an ophiolitic mélange. It is assumed that this ophilites were emplaced when the collision between the extinct CVA and the Bahamas Platform occurred.

Ophiolites eastward the area (Figure 2) are located in the Mayarí-Sagua-Baracoa massif. These ophiolites sheets are over olistostromes and over the CVA.

The Albian-Campanian volcanic arc is Cretaceous in age. It lies in tectonic contact with the northern ophiolites. Near the contact, the arc rocks are even more deformed, with fissured and foliated areas, and with chaotic masses that contain a mixture of ophiolites blocks, vulcanite and plutons.

For simplification, we refer to this volcanic arc as CVA. This is constituted by volcanogenic-sedimentary complexes (calc-alkaline and alkaline composition), plutons and the metamorphic complex.

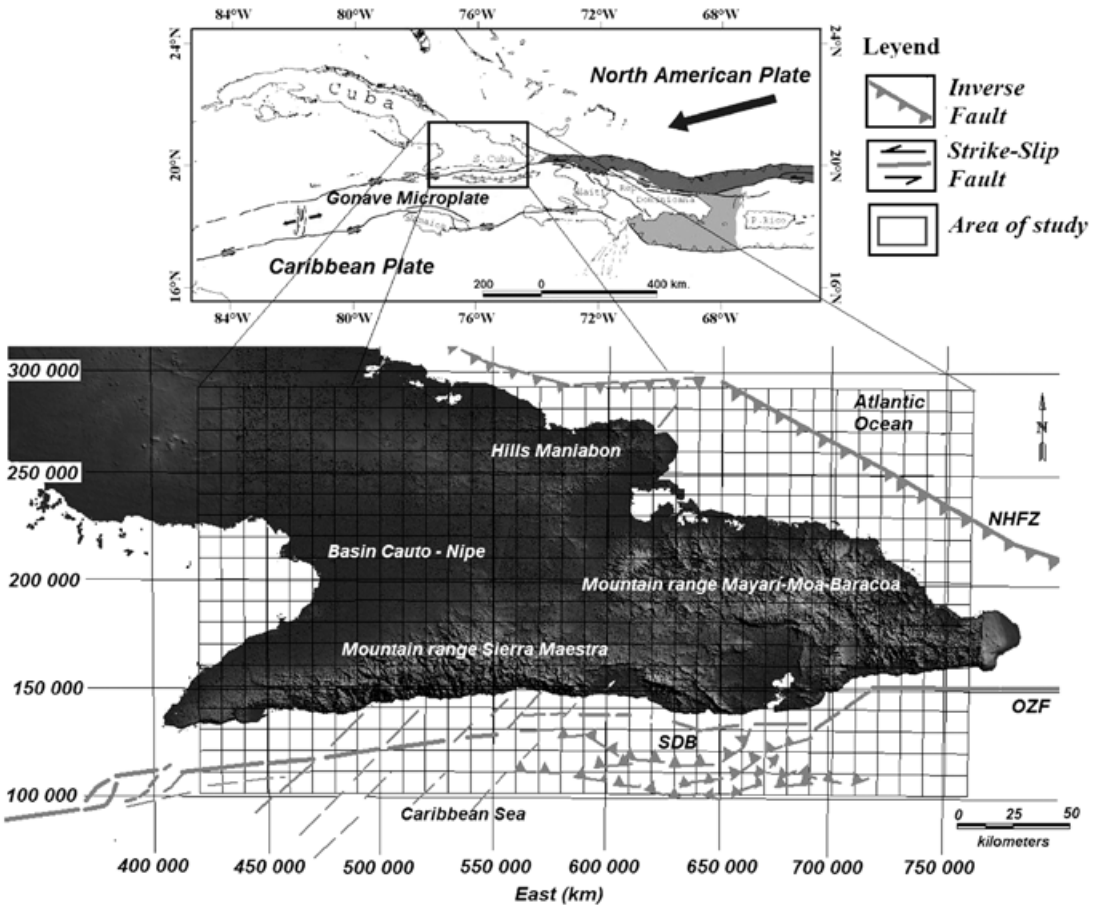

Figure 1. The study area is located at southeastern Cuba Island. The area was divided in a regular grid of 646 prisms of 10 km x 10 km at surface. One grid represents one geological unit. Nine grids are located stratifie. Density contrast is kept constant for every unit. OFZ: Oriente Fault Zone. NHFZ: North Hispaniola Fault Zone.

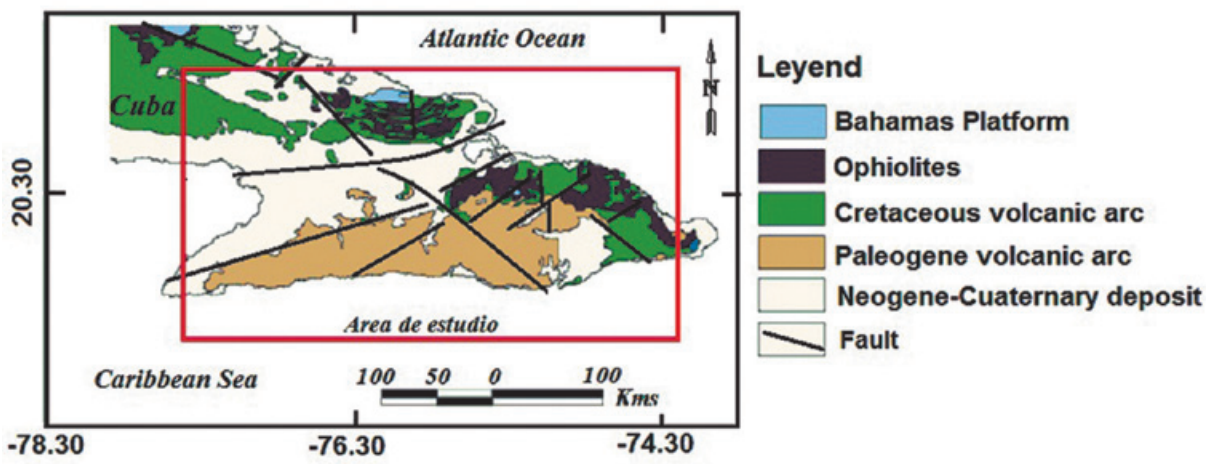

Figure 2. Outline of the different geologic units and faults presented in the study area (Iturralde-Vinent., 1998).

The Paleocene volcanic arc (VPA) is a characteristic of the oriental south portion of the island (our area). Its age goes from the upper Daniense to the lower Eocene in the western part of Cuba, Jamaica, Hispaniola, Puerto Rico and Virgin Islands. The Paleocene arc was formed over the deformed remains of the CVA-Ophiolites units. VPA is constituted by volcano-sedimentary and plutonic rocks with different composition.

Neo-autochthonous units are represented by sedimentary rocks originated from the upper Eocene to recent. Three sedimentary cycles can be recognized; first, a stadium of the upper Eocene to the Oligocene, second, the lower to upper Miocene, and the Pliocene to the recent.

Method

Gravity data consist of a rectangular mesh of 340 km East direction and 190 km North direction, with interpolated data every 3 km. This design is optimal because we are looking for low spatial frequency structures. This produces at least nine observations over every 10 km x 10 km prism. Data was collected and processed by Instituto de Geología y Paleontología de Cuba (IGP) and represents the complete Bouguer anomaly (Blakely, 1996), using 2.3 gr/cm^3 for the earth crust density (Figure 3).

To derive the 3D density model from the complete Bouguer gravity anomaly the software by Gallardo *et al*. [2005] was used. The top and bottom depths for multiple rectangular prisms were determined using inequality or equality constraints for those depths. We assume that the ground consists of geological units with irregular bottom and top topography in contact with other units. We simulate every unit with a conglomerate of rectangular prisms as shown in Figures 1 and 4. The whole 3D model is constituted of separate geological units or set of prisms with different density contrasts. In Figure 4 we show an example of a 3D model with four geological units and their respective set of prisms. A constant horizontal cross-section area for all the prisms is assumed.

The inversion process moves the top and bottom depth for every single prism at every geological unit. Restrictions are imposed to not allow overlap or spaces between prisms. The quadratic norm of the differences is minimized between data (g_o) and model response (g_r) plus a smoothing term (equation 1).

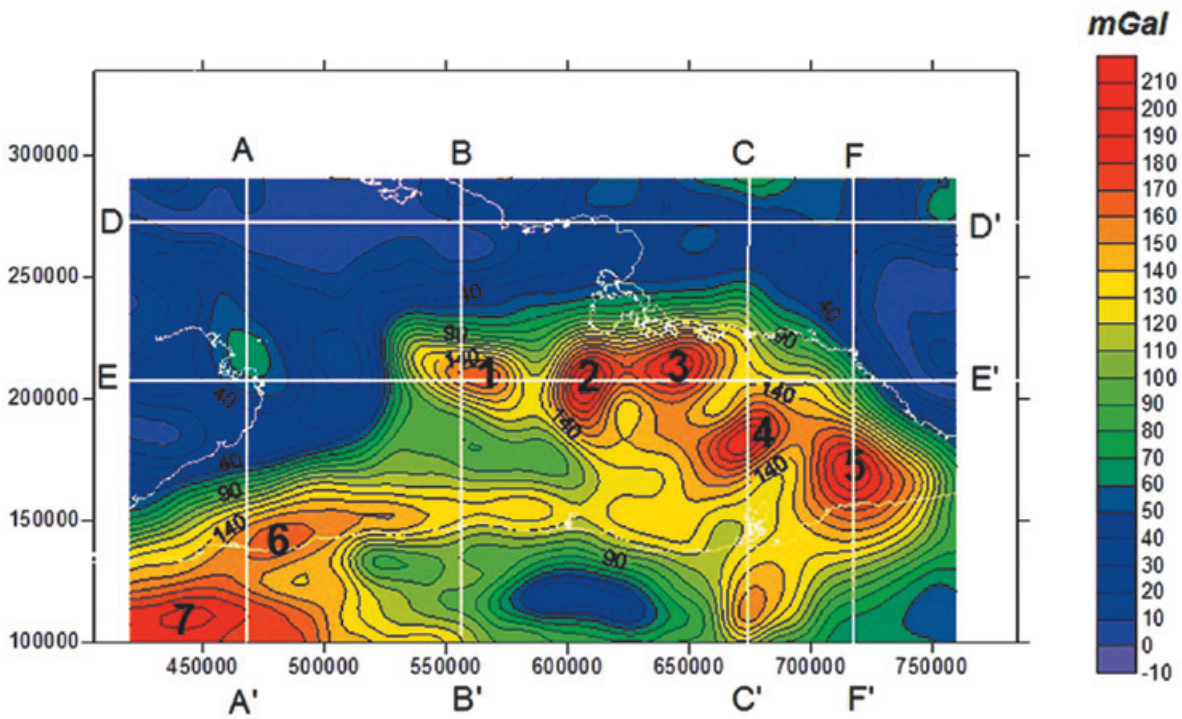

Figure 3. Complete Bouguer anomaly map for Southeastern Cuba island. Gravity anomaly highs are named; 1 Levingstone, 2 La Guira, 3 Piloto, 4 El Salvador, 5 La Perrera, 6 Eje Magmático Sur, 7 New oceanic crust coming from the Cayman dispersion center. Capital letters and lines indicate the six 2D cross-sections made to the 3D density model.

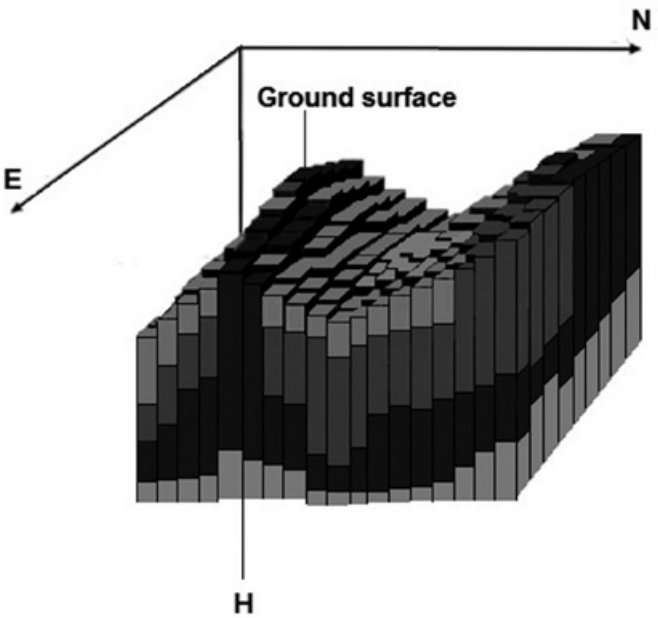

Figure 4. Example of a 3D model with only four geological units. Grids are stratified at the beginning but through the iterations the prisms depths vary. Some prisms' thickness collapses to zero allowing the outcropping of the lower geological units. Numerically, those zero thickness prisms exist but geologically, they do not exist.

$$F(m) = \left\| g_o - g_r \right\|^2 + \beta \left\| Dm \right\|^2 \quad (1)$$

subject to

$$m_{low} \leq m \leq m_{upper}$$

Where m is the unknown vector containing the depths from every prism. Matrix D is the horizontal (x, y) first derivatives of the depths. This term minimizes the top depths differences between adjacent prisms. Term β magnifies or dismisses this term. When it is zero the model shows very rough top topography for every unit; when large, every topographic unit looks very smooth, except where the data (first term in equation 1) requires larger jumps. This can happen where geological faults are located.

Depth determination is quoted by means of quadratic programming (Gill *et al*., 1986), using inequalities or equalities. This allows introduction of surface geology, wells and seismic data as constraints.

Surface geology is introduced as a priori information. Figure 4 shows that unit-1 prisms are displaced to allow units-2 and 3 prisms outcropping. This is performed in the algorithm by collapsing the prisms' thickness to zero.

For the modeling, the horizontal prism area was fixed in 10 km x 10 km as shown in Figure 1, giving a set of 646 prisms for every geological unit.

In order to reduce the non-uniqueness, density contrasts are considered as known. Densities were obtained by direct sampling on the surface. Those densities have a variance range due to heterogeneities inside the geological unit. In the inversion process we adjusted the density contrasts along those ranges. The inversion is not completely automatic because we had to try different density contrasts as fine adjustments.

Geologic models allowed us to establish seven geological units (Iturralde-Vinent 1998, 2002; Cobiella, 2005; Sommer *et al*., 2011). We expanded from the simplest model (Occam's razor) with only seven units to nine units (Table 1) for the inversion process. We considered only those units that exhibit a density change, plus the gravity response of the sea, and the mantle response which was subtracted when corrected by theoretical ellipsoid (Blakely, 1996). Twenty iterations were performed to arrive at the final model.

Results and discussions

The most recent hypothesis about the Southeastern Cuba states the crustal structure consists of folded basement overriding Bahamas platform. The folded basement is constituted of ophiolites thin sheets intercalated over and under the Cretaceous Volcanic Arc (CVA). At the Southeast of our study area, the Paleogene Volcanic Arc (PVA) rocks are predominant and lay over the ophiolites flakes and CVA package (Iturralde-Vinent 1998; Iturralde-Vinent *et al*. 2002; Cobiella *et al*. 2011). These geological

Table 1. Listed are the nine geological units used to obtain the 3D density model. We worked with the shown density contrasts in gr/cm^3.

	Units	Density (g/cm^3)	Density Contrast
1	Sea	1.03	-1.27
2	Neogene-Cuaternary deposits	2.25	-0.05
3	Paleogene Volcanic Arc	2.29	-0.01
4	Ophiolite 1 (Maffic Mayarí -Sagua - Baracoa)	3.05	0.75
5	Cretaceous Volcanic Arc (Tunas - Holguín y Sagua- Baracoa)	2.95	0.65
6	Ophiolite 2 (North Holguín)	3.1	0.7
7	Bahamas Platform	2.2	-0.1
8	Oceanic crust	3.15	0.85
9	Mantle	3.3	0

models were constructed from petrological data taken from surface rocks. The geological unit at depth is inferred with a large probability error that increases with depth. In contrast, our 3D model obtained from gravity data has a quantitative character. We can estimate depths, thickness and dip angles with some probability error that also increases with depth, but these errors are smaller than the geological ones. Thus the algorithm takes the surface geology and boreholes information as geologists would and then guides the 3D structures at depth obeying the physics behind the gravity data. Our procedure reduces the uncertainly at depth considerably.

Before presenting the 3D model obtained, it is important to show the model response (Figure 5B) and the differences between data and response (Figure 5C). Model response has a 6% data misfit. We reproduced the gravity highs (from 140 to 214 mGal), and also the Cauto-Nipe basin gravity low at the NW with values from 0 to 10 mGal. The differences map has a minimum and maximum of -4 to 4 mGal and shows almost a random behavior. The main differences concentrate at the south border of the island because the 10 km x10 km prisms do not fit exactly the steep coastline (Fig 1). There is a surface excess or deficiency of mass producing a misfit. Excluding that border misfit, general misfit must be lower than 6%.

In Figure 6 is shown the 3D density model obtained. We show the bottom topography for every geological unit. Figure 6A shows the surface topography and bathymetry. This surface is known and therefore constrained. Sea effect was taken in consideration. According with the units shown in Table 1, sea bottom topography corresponds with sediments top topography, sediments bottom corresponds with PVA top and so on. Top mantle topography is not shown because it corresponds with the bottom oceanic crust depth. In the bottom depth maps, positive value means above and negative value below sea level are shown. For example: PVA outcrops at Sierra Maestra, therefore showing positive elevation levels at sediments bottom topography (Figure 6A). While these contour plots are not visually informative, they can be digitized and used for future research.

For Central and Eastern Cuba (see oval in Figure 7), Otero *et al*. (1998) argued that there is an oceanic crust transitioning to continental northward. In order to test that hypothesis, we obliged the 3D model to put oceanic crust at the very bottom of the crust (denser than continental). The gravity response was so high that the algorithm never got a good convergence as we can see in Figure 7B. If we put a continental crust instead (Bahamas platform), the fitness is optimal as we can see in Figure 7A. We therefore postulate that Bahamas platform must be there because it is less dense than oceanic crust.

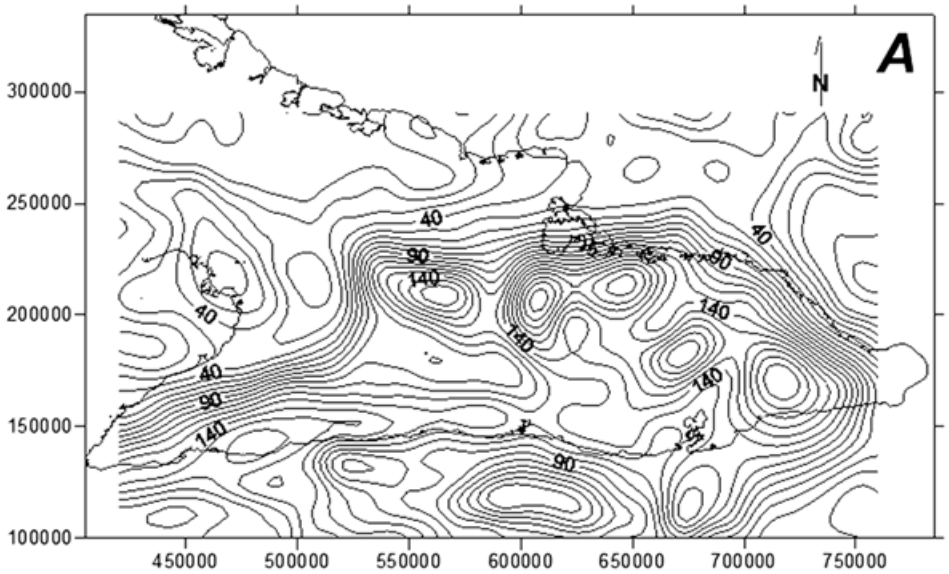

Figure 5. (A) Complete Bouguer anomaly.

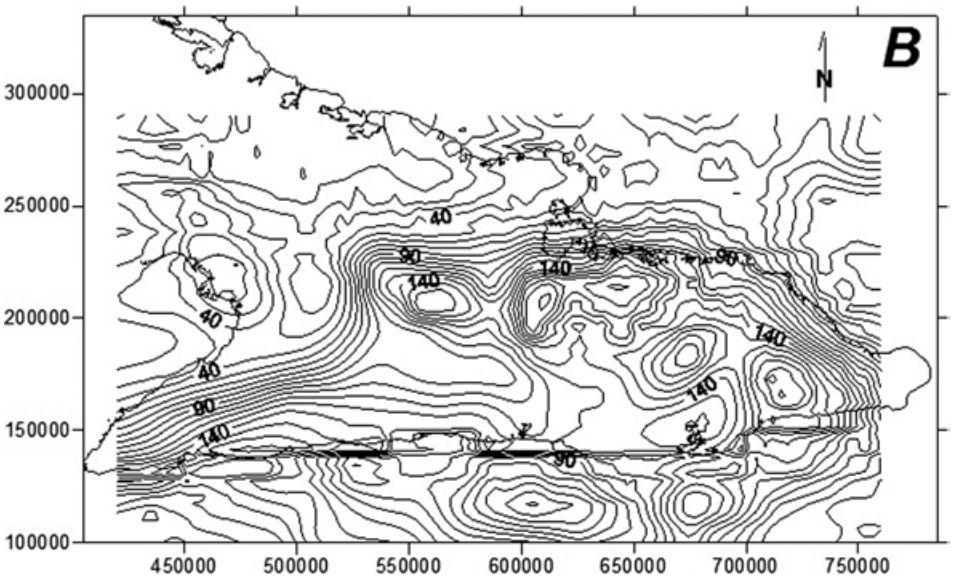

Figure 5. (B) 3D density model response,

Figure 8A shows the surface geology declared at every surface prism. It also shows the location of four cross-section of the 3D model. Figure 8B show those cross-sections. At cross-section AA' and BB', we can see that the Bahamas platform dips inside the mantle with a slope close to 45_o. However at the East (cross-section CC'), the same platform arises forming the Mayarí-Moa-Baracoa massif. Cuevas (1998) believes that this massif was raised by isostatic compensation movements. Chang (2003) argues that the Mohorovicic boundary is moving upward. Based on our model, the latter hypothesis is more probable, because we do not see isostatic roots in cross-section DD'.

The Bahamas platform belongs to the North-America continental plate (Figure 1). Cross-section AA' (Figure 8) shows clearly how this platform penetrates the mantle in a kind of slab with an approximate thickness of 10 to 12 km, dipping southward. It begins with a low angle at North, where it almost outcrops, increasing the angle southward to 45_o below the Cauto-Nipe basin. Cross-section

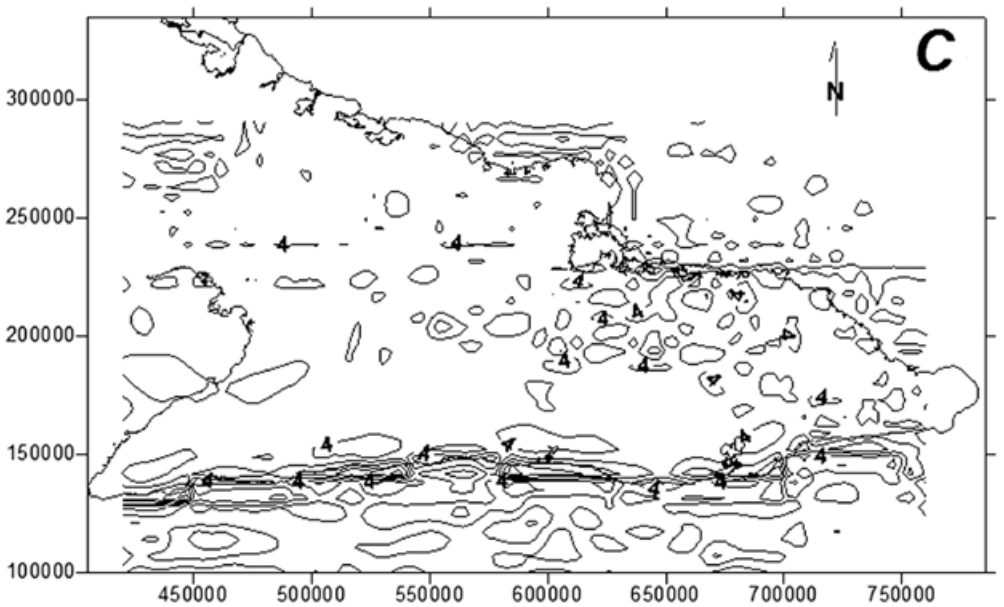

Figure 5. (C) Differences between data and response in mGal. RMS misfit is 6%. Average misfit ranges (-4, +4) mGal. Southern border island exhibits larger differences.

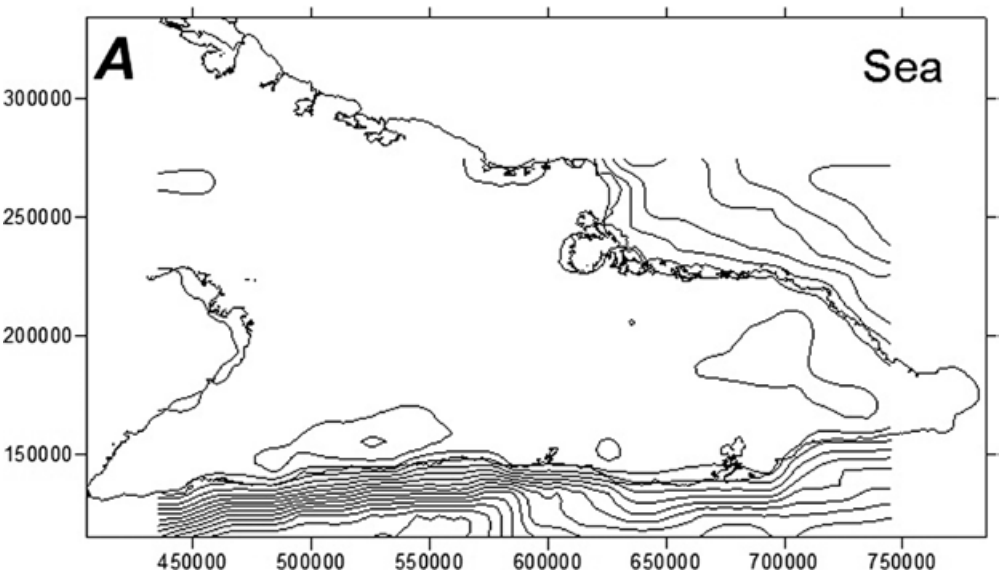

Figure 6. 3D density model obtained. Maps represent the bottom topography for every grid or geological unit with respect to the sea level. **Figure 6. (A)** Terrain topography (positive levels) and bathymetry (negative levels).

BB' is similar but the PVA is less overlapped. Cross-section CC' shows a rebound or vertical uplift of the Bahamas platform. It seems that the PVA is distributed more at the West of this part of the island. Iturralde-Vinent (1998), Cobiella (2005), García-Casco *et al*. (2008) and Sommer *et al*. (2011) have suggested this slab before, but this is the first geophysical evidence. The Bahamas platform density is very close to 2.3 g/cm^3, meaning that density contrast is almost zero. The shallow presence of Bahamas platform at NW (~2 km) justifies the low gravity values.

At cross-section AA', the Cauto-Nipe fault is signed as a high depth gradient. This fault cuts the northern side of the Sierra Maestra massif, dipping northward.

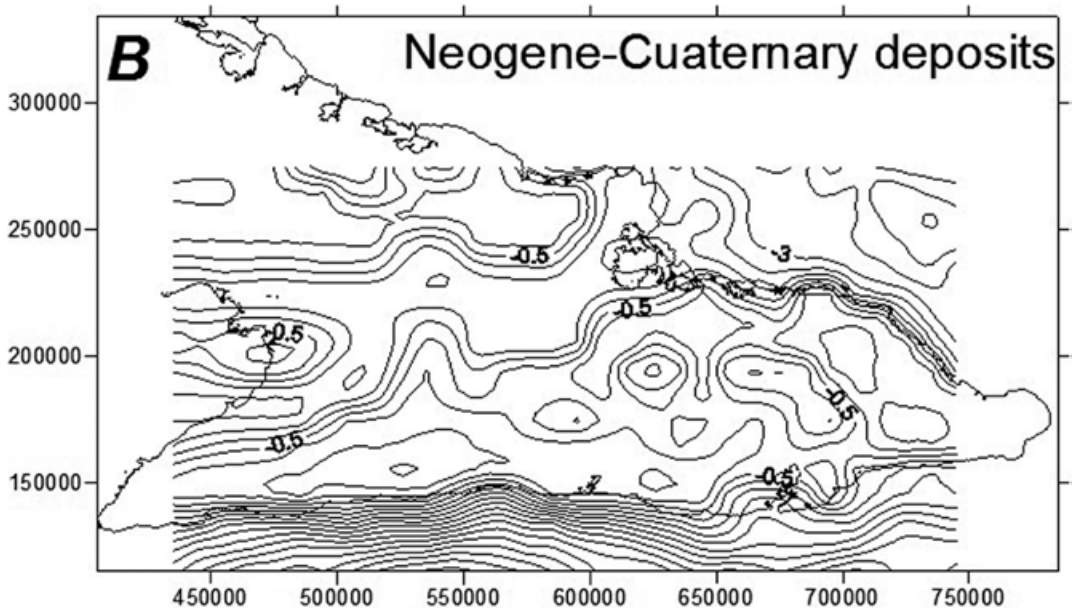

Figure 6. (B) Sediments

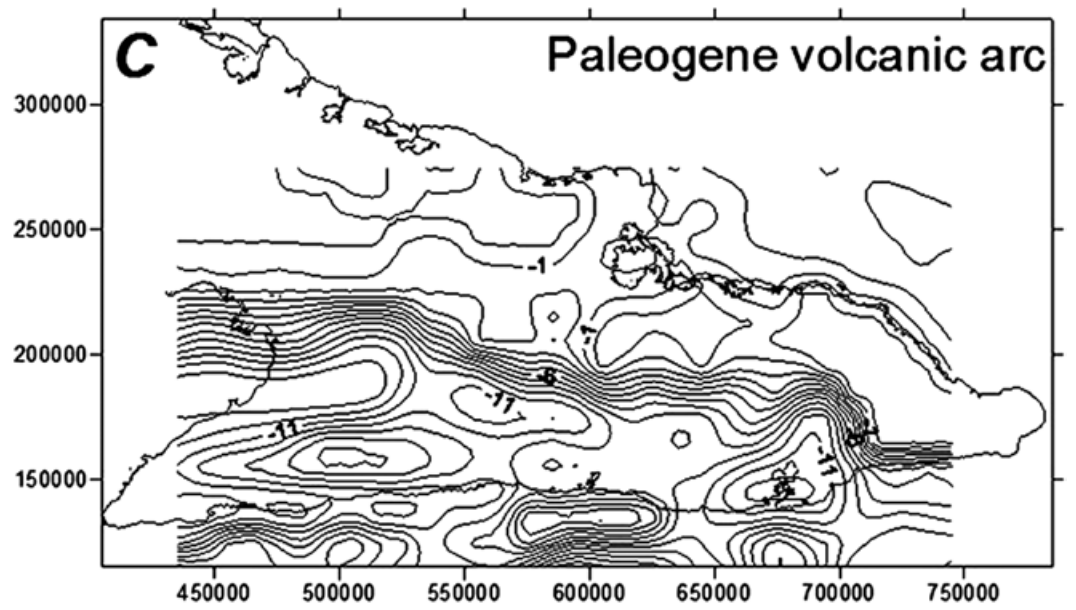

Figure 6. (C) Paleogene Volcanic Arc (PVA).

At the SW corner of the study area, the model needed a high density body (cross-section AA'; Figure 8 B) in order to fit the gravity high (number 6 at Figure 3). Chang (2003) has suggested a pluton below the CVA rocks.

Southward in the Cuba island, the Oriente fault is present (Figure 1). The fault signals the change from continental to oceanic crust. Even southward of cross-section AA' (Figure 8B), the 3D model cuts this fault. The high gravity anomaly requires a denser body which could correspond to oceanic crust. This new oceanic crust has been shifted from West to East by the Caiman trench. The gravity anomaly decreases southward in cross-sections BB' and CC' (Figure 8B). The 3D model justifies this with the less dense Gonave continental micro plate (Calais *et al*. 2002, 2006).

Cross-section BB', at the center cuts an ophiolite body of 4 km thick. This high density body causes the Levingstone high gravity anomaly (number 1 at Figure 3). Levingstone had been interpreted as caused by an ultrabasic mantle intrusion (Otero *et*

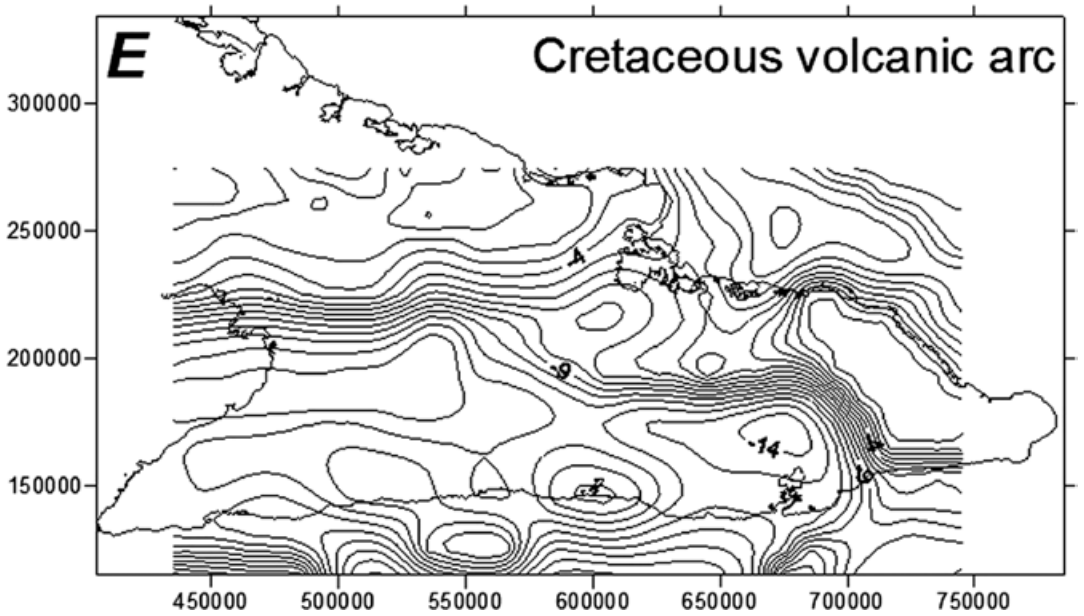

Figure 6. (E) Cretaceous Volcanic Arc (CVA).

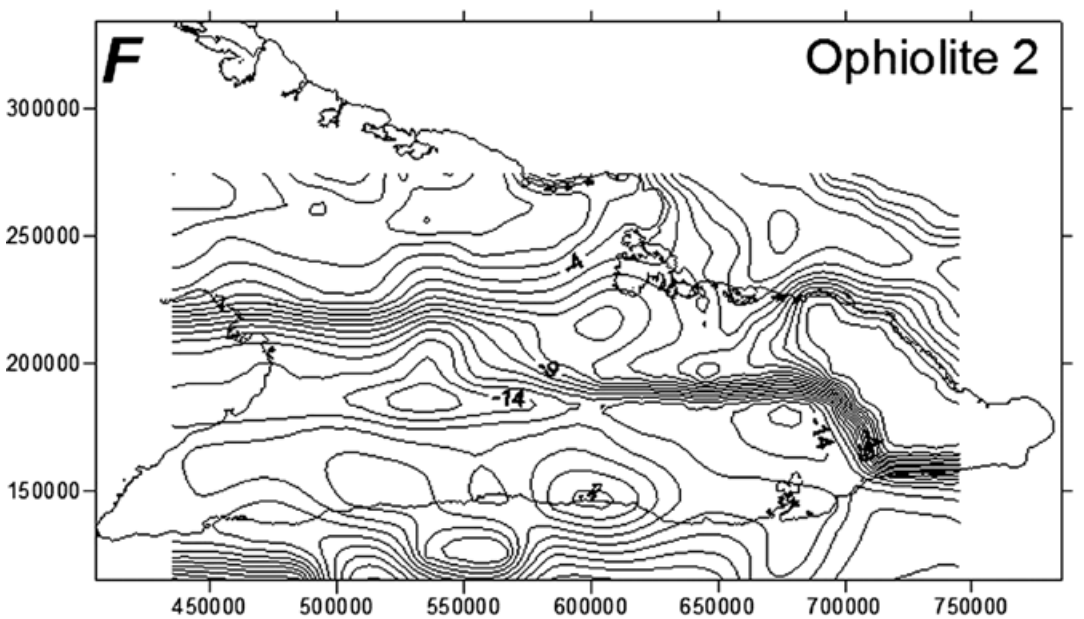

Figure 6. (F) Ophiolites bellow CVA.

al. 1998). We sought to understand the origin of such gravity anomaly highs (Figure 3). We made two additional cross-sections over the 3D density model. Cross-section EE' (Figure 8B) crossed Levingstone, La Guira and Piloto gravity highs (number 1, 2 and 3 at Figure 3). Figure 8A shows a great correspondence between the ophiolites bodies and the gravity anomaly highs. This is explained because the density contrast is +0.75 gr/cm^3 (Table 1) and also because those bodies are shallower producing three high-frequency features over the gravity anomaly. Cross-section CC' passes over the El Salvador gravity high (number 4 at Figure 3). Despite the smoothing (Figure 8), it is clear that ophiolites at km 80 are producing the gravity highs.

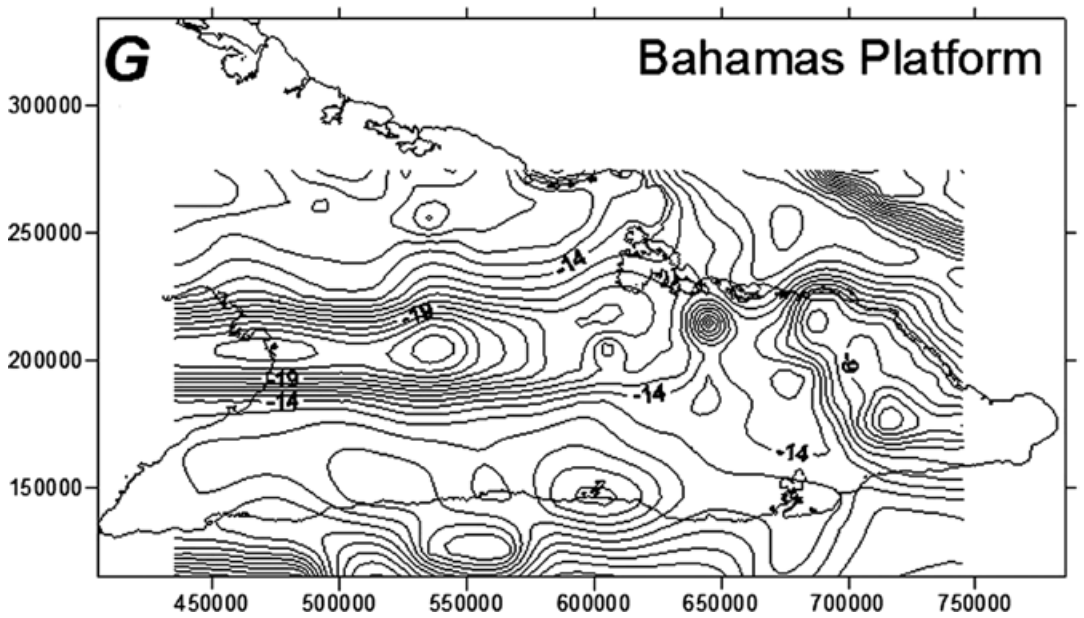

Figure 6. (G) Bahamas Platform.

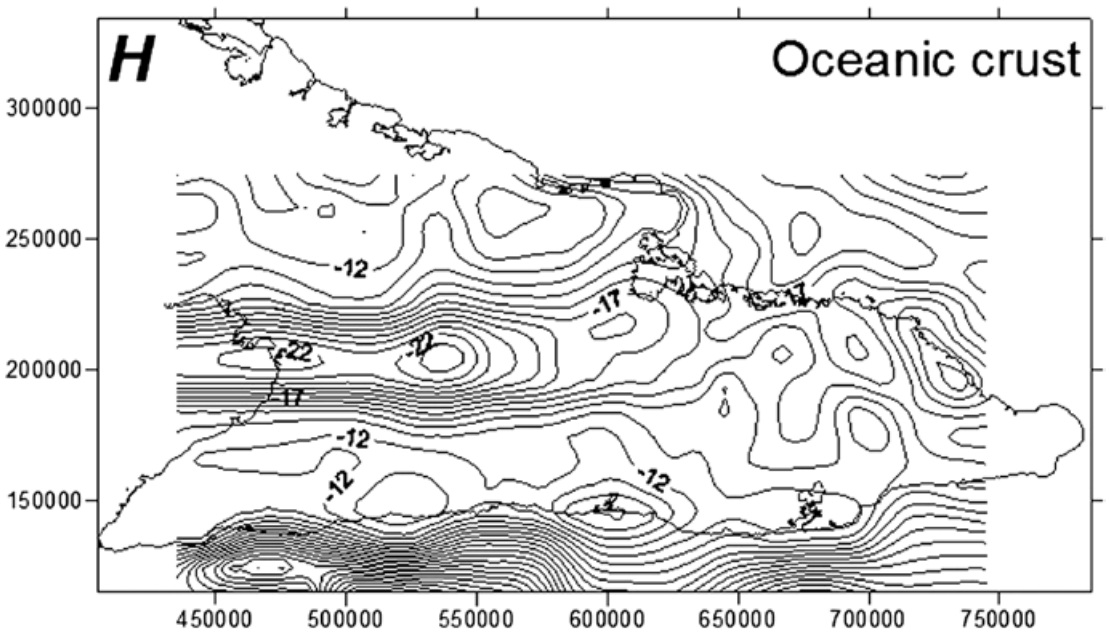

Figure 6. (H) Oceanic Crust. Contour lines every 1 km, except A and B (every 0.5 km).

Cross-section FF' (Figure 9) passes over La Perrera gravity high (number 5 at Figure 3). Figure 9B shows that in this case the ancient ocean crust keeps strong correlation with this anomaly.

The Eastern Island has a more complex geology, including the Mayarí-Moa-Baracoa ophiolitic massif. Iturralde-Vinent (1998), Cobiella (2005) and Sommer *et al*. (2011) suggest that the evolution of this area is different. Cross-section CC' (Figure 8B) shows that the Bahamas carbonate basement raised up, forming a horst bellow the Mayarí-Moa-Baracoa massif. Here, crustal thickness is 15 km.

The southern corner of cross-section CC' (Figure 8B) reached the deformed Santiago de Cuba belt, formed by the rising of the ancient ocean crust. Tectonically this was due to a transpressive process produced by the oblique contact between the Caribbean plate and Gonave microplate. It is important to emphasize that here the Gonave microplate is constituted by the CVA and ophiolites over the ancient oceanic crust that have been migrating from the Yucatan basin and is displaced by the Oriente fault to the present position. Similar crust composition is observed at La Española Island (Case *et al*. 1990) where ophiolites and CVA outcrop.

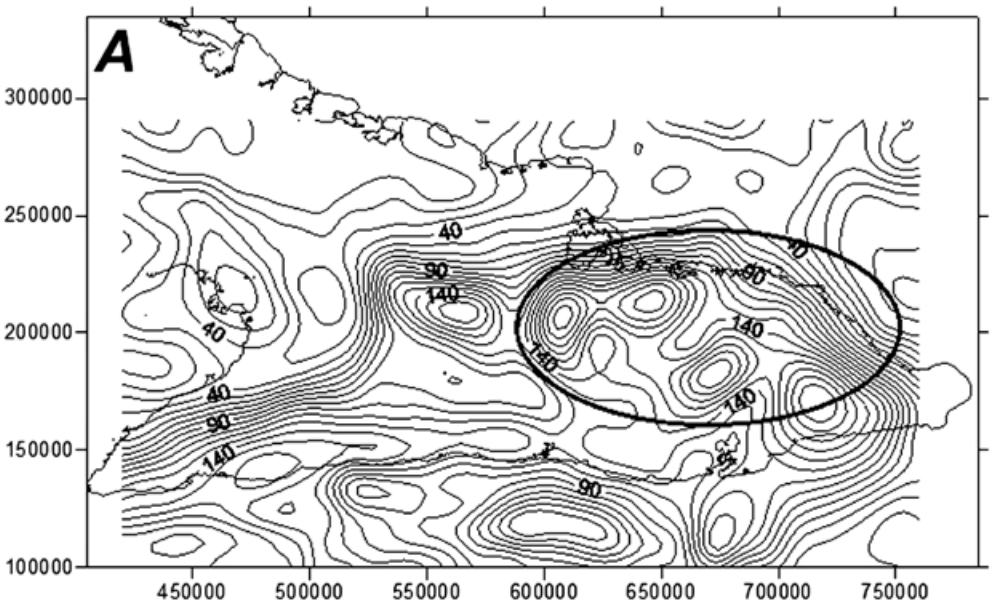

Figure 7. Hypothesis testing. The question is which geological unit is at the central area? (A) Assuming that Bahamas platform comes from North toward the central part.

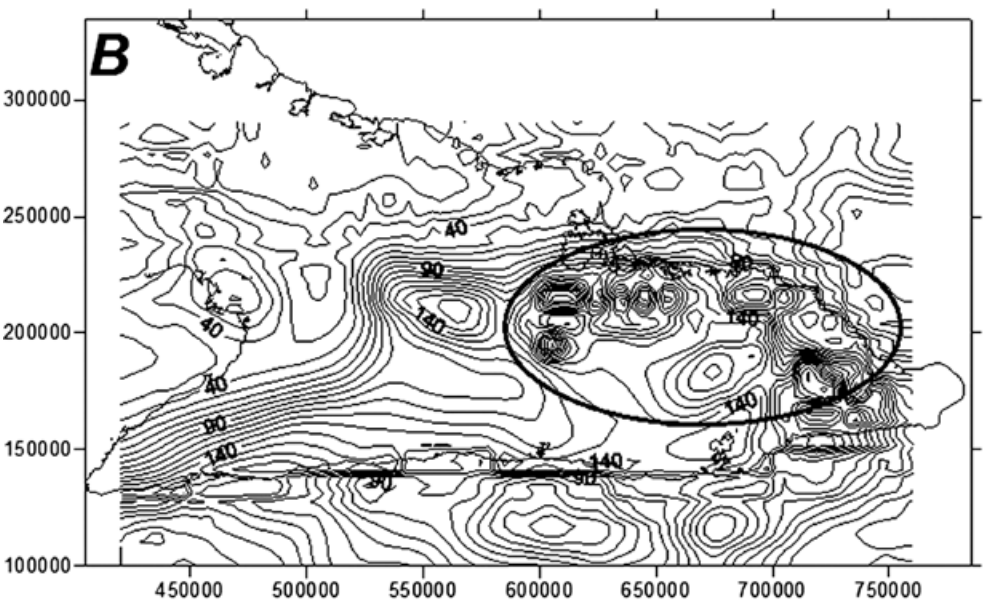

Figure 7. (B) Assuming an oceanic crust coming from south toward the central part.

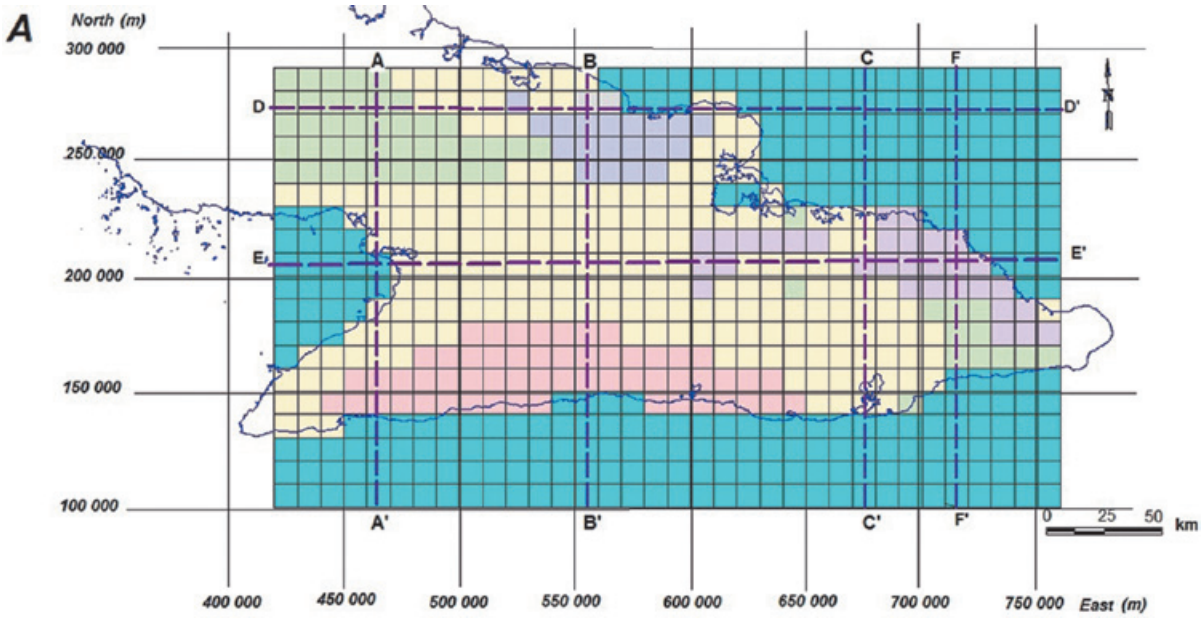

Figure 8. (A) Surface geology as introduced in the 3D model as constraints. Dotted lines indicate the 2D cross-sections over the 3D model.

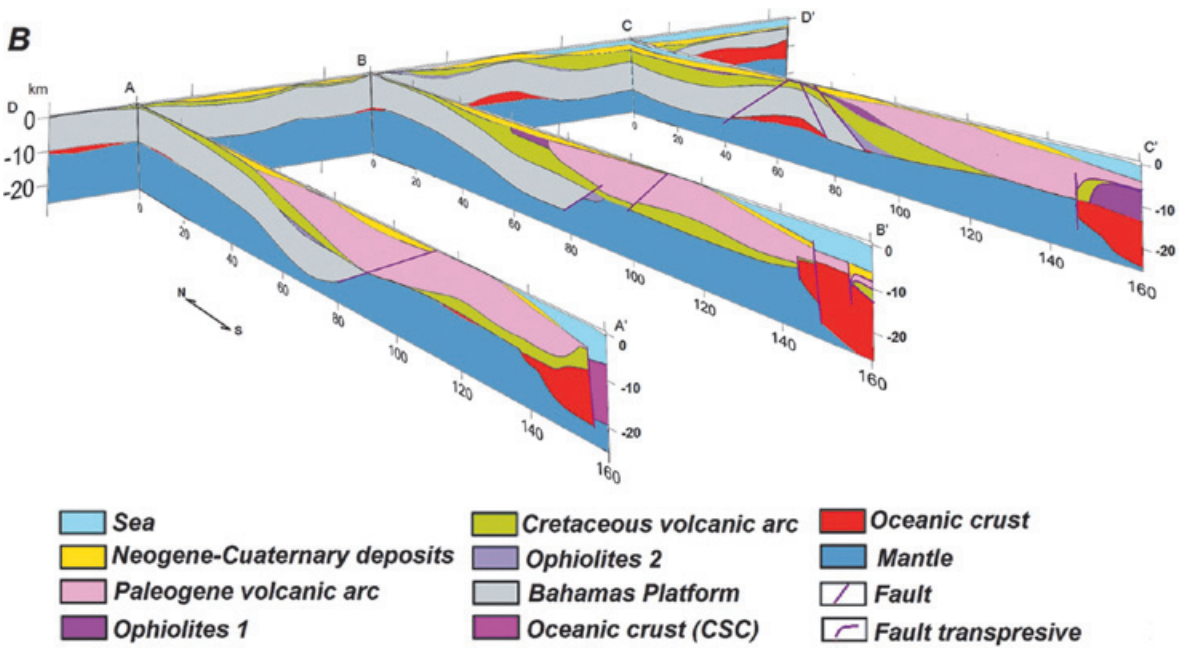

Figure 8. (B) Four two-dimensional cross-sections of the 3D density model only are shown.

Current discussion seeks to explain whether the Bahamas platform and Caribbean plate collisioned or subducted each other. Iturrade-Vinent (1998), Cobiella (2005) and Sommer *et al*. (2011) argue that the Bahamas platform subducted under the Caribbean plate (see cross-section AA' at Figure 8B). García-Casco *et al*. (2008) argues for a collision. From our results, we propose a tectonic emplacement. At Manaibon elevation, the ophiolites can be seen over the Bahamas platform. At Manaibon and Cupey Sierra, olistolites appear inside the ophiolites, indicating that the ophiolites formation dragged over the top of the Bahamas

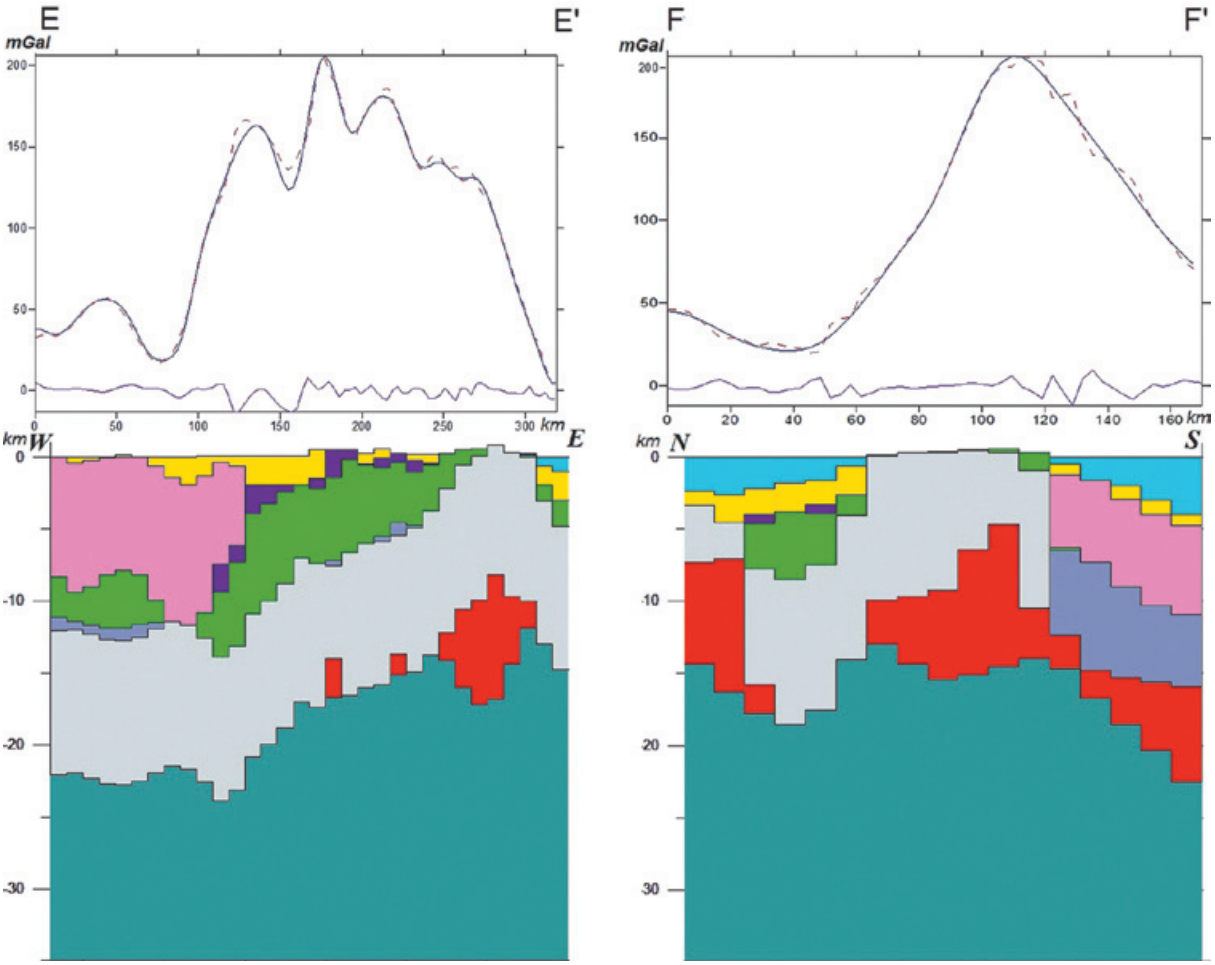

Figure 9. EE' and FF' cross-sections are shown with their respective gravity anomaly and response in mGal. Ophiolites bodies are mainly responsible for the gravity anomaly highs, except La Perrera.

platform when the overriding process occurred. Thus a low density Bahamas platform was overridden by a denser Caribbean plate. Since normal subduction phenomena occurs when a denser layer is overridden by a less dense layer, in this case, collision occurred rather than subduction.

When we conceived the conceptual model, we assumed that might be in the bottom, remains of an ancient crust and an oceanic crust younger (CSC) from the area of generation (Cayman Trench). Both were modeled as a single unit because they have approximately the same density, but in the same cross-section AA' (figure 8) they are shown as two types oceanic crusts.

A limitation of this research is that we used 10 km x 10 km prisms area, therefore, we cannot resolve high spatial frequencies. Nevertheless, the gravity anomaly is very smooth (Figure 3). There is no high frequency information in such a gravity anomaly. Another limitation is that we could not differentiate the Cuban metamorphic complex from the Cretaceous volcanic arc because densities are similar, and also between sedimentary volcanogenic sequences (Paleogene age).

Conclusions

Three-dimensional gravity inversion can be done using the same size grid of prisms and assuming densities as unknowns implying a lineal process with a single iteration solution, but the non-uniqueness is quite high by the huge number of prisms. In this research, our inversion procedure considers depths as unknown and densities as known, bringing a non-lineal problem that must be linearized by an iterative process. In this inversion,

the non-uniqueness diminishes considerably because the number of prisms is much smaller. However, we also applied geological and geophysical constraints to diminish such non-uniqueness even further. We used the Occam's razor criteria that warrants a most probable 3D model.

The uncertainty inside the model is not constant. It increases with depth but also at the 3D model edges because of the lack of data. High frequency details may also have high uncertainty because the gravity anomaly is very smooth. Consequently, we looked for the simplest but the most probable 3D model. For scale purposes, 10 km x 10 km area prisms were optimal.

The smoothing parameter or roughness penalization avoids large depth steps between contiguous prisms. However, if the resolution of gravity data is optimal, the fitness term becomes more important than the smoothing term. In our 3D density model, large depth steps appear when data require them, because we are using an intermediate value for the smoothing parameter.

Parallel 3D topographies mean linear correlations between the unknowns. Problem increases when increasing the prism number and also with deeper formations. However, our model does not exhibit high linear correlation at the deepest part, because we did not use a large number of prisms.

The gravity response from the 3D density model obtained reproduces very well the general shape of the data, particularly the gravity lows at Cauto basin (NW of the map), with values between 0 and 10 mGal. It also fits the named gravity maximums. We determined that those maximums are caused by the presence of shallow ophiolite sheets mainly.

Crustal thickness obtained from the 3D model is 10 to 15 km southward and thicker northward. This result is agree with previous qualitative geological models.

The density model further shows the complex 3D topographies of the Bahamas platform, the Cretaceous volcanic arc, the Paleogene volcanic arc, and the ophiolites sheets, and how they intrude each other.

The 3D density model shows the new oceanic crust from the Gonave microplate (SE of the area) caused by the pull of the Cayman spreading center.

The response of the ophiolites sheets and Cretaceous volcanic arc overriding the Bahamas platform provides evidence for collision rather than subduction between the ancient Caribbean plate and the Bahamas platform (present North-American plate).

Acknowledgements

We thank the Institute of Geology and Paleontology of Cuba and especially Eric Escobar and Fernando Mondelo for giving us the data of the gravity anomaly used in this study.

References

Arango E.D., 1996. Geodynamics in the region of Santiago de Cuba, on the plate boundary between the North America and the Caribbean), MSc thesis, National Polytechnic Institute of Mexico, Internal Report of the National Center for Seismological Research, Santiago de Cuba, 110pp.

Arnaiz-Rodríguez M., Garzon Y., 2012. Nuevos mapas de anomalías gravimétricas del Caribe. *Rev. Interciencia*, 37, 3.

Batista J., Pérez M., Quiroga G., Gallardo l., 2007, Case History. Geometry of ophiolites in eastern Cuba from 3D inversion of aeromagnetic data, constrained by surface geology. *Geophysics*, 72, 3, B81–B91.

Blakely R.J., 1996, Potential Theory in Gravity and Magnetic Applications: Cambridge, UK, Cambridge University, Press.

Bovenko V.G., Shcherbakova B.E., Hernández H., 1982, Novyye geofizicheskiye dannyye o glubinnour stroyenii vostochnoy kuby Sovetskaya Geologiya, 9, 101–109. Translation in *International Geology Review*, 24, 1155–1162.

Bush V.A., Shcherbakova I.N.,1986. New data on the deep tectonics of Cuba, *Geotectonics*, 20, 192–203.

Calais E., Perrot J., Mercier de Lepinay B., 1998, Strike-slip tectonics and seismicity along the northern Caribbean plate boundary from Cuba to Hispaniola. In Active Strike-Slip and Collisional Tectonics of the Northern Caribbean Plate Boundary Zone. *Geol. Soc. Am.*, Special Paper 326.

Calais E., Han J.Y., Demets C., Nocquet J.M., 2006, Deformation of the North American plate interior from a decade of continuous

GPS measurements. *Journal of Geophysical Research*, 111, B06402.

Calais E., Mazabraud Y., Lépinay B.M., Mann P., Mattioli G., Jansma P., 2002, Strain partitioning and fault slip rates in the northeastern Caribbean from GPS measurements. *Geophysical Research Letters*, 29, 18, 1856.

Case J.E., Macdonald W., Fox P, 1990, Caribbean crustal provincies; Seismic and gravity evidence, in The Caribbean region. The Geology of North America, Edited by Dengo, G and Case, J, E. Geol. H, 328, pp. 15-36, The Geological Society of America.

Chang M., 2003, Respuestas de los campos físicos en el territorio de Oriente. Compilación monográfica. Instituto de Geología y Paleontología. La Habana. Cuba. Unpublished.

.

Cobiella-Reguera J.L., 2005, Emplacement of Cuban Ophiolites. *Geologica Acta*, 3, 247–268.

Cuevas J.L.,1998, Estudios sobre Isostasia en Cuba: Una Caracterización y Delimitación de Zonas Potencialmente Sísmicas. Rev. Boletín Geológico y Minero, Inst. Tecnológico GeoMinero de España, 109, 3, 265-278.

Cuevas J.L, Diaz L.A., Polo B., 2001, Regionalización gravimétrica en el Caribe Centro Occidental (I): Nuevos mapas de anomalías de Bouguer total y aire libre de Cuba a escala 1: 500 000 (Gravimetric regionalization in West-central Caribbean (I): New maps of total Bouguer anomalies and free-air of Cuba at 1: 500 000), Mem. GEOMIN, 93–104.

Enman S.V., Belousov T.P., Marquez M.E., Rueda J.S., Jorge G.D., 1997, Recent crustal movements and morpho-structural pattern of Southeastern Cuba: Santiago de Cuba Geodynamic Research Site. *Izv. Phys. Solid Earth*, 1, 55–69.

Gallardo L.A., Pérez-Flores M.A., Gómez-Treviño E., 2003, A versatile algorithm for joint 3D inversion of gravity and magnetic data. *Geophysics*, 68, 949–959.

Gallardo L.A., Pérez-Flores M.A., Gómez-Treviño E., 2005, Refinement of three-dimensional multilayer models of basins and crustal environments by inversion of gravity and magnetic data. *Tectonophysics*, 397, 37–54.

García-Casco A., Iturralde-Vinent M., Pindell M., 2008, Latest Cretaceous Collision/Accretion between the Caribbean Plate and Caribeana: Origin of Metamorphic Terranes in the Greater Antilles, *International Geology Review*, 50, 9, 781-809.

Gill P.E., Hammarling S.J., Murray W., Saunders M.A., Wright M.H., 1986, User's guide for lssol (version 1.0): A Fortran package for constrained linear least squares and convex quadratic programming: Department of Operations Research, Stanford University technical report SOL 86-1.

Gonzalez O., Álvarez L., Guidarelli M., Panza G.F., 2007. Crust and upper mantle structure in the Caribbean region by group velocity tomography and regionalization, *Pure appl. Geophys*., 164, 1985–2007.

González O., Álvarez L., Moreno B., Panza G.F., 2011, S-Wave Velocities of the lithosphere–asthenosphere system in the Caribbean region. *Pure and applied Geophysic*, 169, 1-2, 101-122.

Giunta G., Beccaluva L., Coltorti M., Siena F., 1997, Ophiolitic units of the southern margin of Caribbean plate in Venezuela: a reappraisal of their petrogénesis and original tectonic setting. Memorias del VIII Congreso Geológico Venezolano, tomo 1, 331-337.

Iturralde-Vinent M.A., 1996, Geología de las ofiolitas de Cuba, in Ofiolitas y Arcos Volcánicos de Cuba IGCP Project 364, Special Contribution 1, 83–120.

Iturralde-Vinent M.A., 1998, Sinopsis de la Constitución Geológica de Cuba. Acta Geológica Hispánica, 33, 9–56.

Iturralde-Vinent M., Gahagan, L., 2002, Late Eocene to Middle Miocene Tectonic Evolution of the Caribbean: Some principles and their Implications for Plate Tectonic Modeling. In T. A. Jackson, ed., Caribbean Geology Into the Third Millennium. Transactions of the Fifteenth Caribbean Geological Conference. 47-62. Ed. Pear Tree Press Ltd.

James K.H., 2003, Caribbean Plate Origin: Discussion of Arguments Claiming to Support a Pacific Origin; Arguments for an In-Situ Origin. American Association Petroleum Geologist, International. Conference, 8-9.

Mondelo F., Sánchez R., Pérez P., Pardo M., 2011, Catálogo de mapas gravimétricos

de la República de Cuba. Fourth Cuban convention in Earth Sciences. Congress abstracts in digital version., ISBN 978-959-7117-30-B. 1-34.

Moreno B., Grandison M., Atakan K., 2002, Crustal velocity model along the southern Cuba margin. Implications for the tectonic regime at an active plate boundary. *Geophys. J. Int.*, 151, 632–645.

Otero R., Prol J.L., Tenreyro R., Arriaza G.L., 1998, Características de la corteza terrestre de Cuba y su plataforma marina. *Rev. Min. Geol*., 15, 31–35.

Palau R., Moreno B., Blanco M., 2006, Modelo de velocidades de Cuba Oriental. *Revista Geológica de América Central*, 34-35, 109-119.

Pérez M., Suárez F., Gallardo L., González A., Rogelio F., 2004, Structural pattern of the Todos Santos, Coastal Plain, based on geophysical data. *Ciencias Marinas*, 30, 2. 349–364.

Pindell J.L., Barrett S.F., 1990, Geologic evolution of the Caribbean region: A plate tectonic perspective. In Dengo, G. and Case, J.E. (eds.): The Caribbean Region, The Geology of North America, 405–432, Vol. H, 40:435

Pindell J., Kennan L., 2009, Tectonic evolution of the Gulf of Mexico, Caribbean and northern South America in the mantle reference frame: an update, in The Origin and Evolution of the Caribbean Plate. *Geol. Soc. Lond. Spec. Publ*. 328, 1–55.

Rojas-Agramonte Y., Neubauer F., Garcia-Delgado D.E., Handler R., Friedl G., Delgado-Damas R., 2008, Tectonic evolution of the Sierra Maestra mountains, SE Cuba, during tertiary times: from arc-continent collision to transform motion. *J. South Am. Earth Sci*., 26, 125–151.

Shcherbakova B.E., Bovenko V.G., Hernández H., 1978, Stroyeniye zemnoy kory Zapadnoy Kuby (Crustal structure in West Cuba), Sovetskaya Geologya, 8, 138–143. Translation in *International Geology Review*, 20, 1125–1130.

Sommer M., Hüneke H., Meschede M., Cobiella-Reguera J., 2011, Geodynamic model of the northwestern Caribbean: scaled reconstruction of Late Cretaceous to Late Eocene plate boundary relocation in Cuba. Neues Jahrbuch für Geologie und Paläontologie – Abhandlunge (Band 259, Heft 2), 259(3), 299-312.

Tenreyro R., López J.G., Echevarría G., Álvarez J., Sánchez J.R., 1994, Geologic evolution and structural geology of Cuba, AAPG Annual Convention.

Geofísica Internacional (2014) 53-3: 277-288

Original paper

Stratigraphic Columns Modeling and Cyclicity Analysis of the Misoa Formation, Maracaibo Lake, Venezuela, using Markov Chains

María Beatriz Soto, Evert Leonardo Durán and Milagrosa Aldana*

Received: March 19, 2013; accepted: October 15, 2013; published on line: July 01, 2014

Resumen

Se realiza en este trabajo la caracterización estocástica de un yacimiento constituido por una secuencia de areniscas intercaladas con limolitas y lutitas. La unidad estratigráfica estudiada corresponde a la arena C4 de la formación Misoa, Campo Lama, Lago de Maracaibo (Venezuela). Se desarrolló un algoritmo de Cadenas de Markov, basado en la definición de relaciones genéticas entre litofacies en una columna estratigráfica. La aplicación del método de Monte Carlo utilizando este algoritmo en 11 pozos en el área, permitió obtener pseudo-secuencias en 20 nuevas localizaciones. El algoritmo fue capaz de modelar, apropiadamente, pseudos-secuencias estratigráficas y cuantificar la proporción relativa de facies, mostrando un 82% de certidumbre en términos del contenido relativo de sedimentos en un pozo de prueba. El mapa de arena neta generado integrando las columnas estratigráficas obtenidas de la información de pozos y las pseudo-columnas Markovianas, sugiere la presencia de cuerpos de arena con orientaciones noreste-suroeste, coincidentes con estudios geológicos previos en el área. Este mapa puede ayudar a definir zonas prospectivas en el campo. La aplicación del algoritmo indicó la existencia de memoria estratigráfica a lo largo de las columnas analizadas. El método de Columnas de Markov embebidas usado en el análisis de ciclicidad de toda el área indica que se presentan transiciones cíclicas sólo de areniscas a limolitas y de lutitas a limolitas. Por tanto, para el área de estudio, en promedio, pueden identificarse con el análisis Markoviano procesos de afinamiento hacia arriba y engrosamiento hacia arriba, como era de esperarse para el sistema deltaico dominado por mareas asociado al reservorio analizado.

Palabras clave: cadenas de Markov, ciclicidad, Formación Misoa.

Abstract

A stochastic characterization of a hydrocarbon reservoir, constituted by a sedimentary sequence of sandstones interbbeded with siltstones and shales, has been performed. The stratigraphic unit studied here mainly comprises the C4 sands of the Misoa Formation, located in the Lama Field, Maracaibo Lake (Venezuela). A Markov Chain algorithm, based on the definition of genetic lithofacies relationships along stratigraphic columns, was developed. The application of the Monte Carlo stochastic method using this algorithm, to log data from 11 wells, allowed the generation of pseudo sequences at 20 new locations. This algorithm was able to properly model pseudo stratigraphic sequences and to quantify the relative facies percentage, showing a 82% confidence level related to the proportional content of sediments at a test well. The net sand map obtained integrating the stratigraphic columns, derived from the well information, and the Markov pseudo-columns, suggests the presence of sand bodies with a northeast-southwest orientation that agree with previous geological studies in the area. This map could help in the definition of prospective zones in the field. The existence of stratigraphic memory along the evaluated columns was recognized after applying the algorithm. The embedded Markov method used in the cyclicity analysis of the whole area indicates cyclic transitions just from sandstones to siltstones and from shales to siltstones. Hence for the study area, on average, fining upward and coarsening upward processes can be identified with the Markovian approach, as was expected for the tide-dominated deltaic system associated to the analyzed reservoir.

Key words: Markov chains, cyclicity, Misoa Formation.

M. Beatriz Soto
Coordinación de Ingeniería Geofísica
Universidad Simón Bolívar
Edif. FE II, Piso 3, Valle de Sartenejas
Baruta, Estado Miranda, Venezuela
Present affiliation: Baker Hughes Incorporated
Gaffney-Cline & Associates
Singapore.

E. Leonardo Durán
Departamento de Ciencias de la Tierra
Universidad Simón Bolívar
Edif. FE II, Piso 3, Valle de Sartenejas
Baruta, Estado Miranda, Venezuela
e-mail: evertduran@usb.ve

M. Aldana*
Departamento de Ciencias de la Tierra
Universidad Simón Bolívar, Edif. FE II
Piso 3, Valle de Sartenejas
Baruta, Estado Miranda, Venezuela
*Corresponding author: maldana@usb.ve

Introduction

The knowledge or understanding of the facies architecture of the subsurface is a key aspect in many geological and geophysical problems as, for example, hydrocarbon reservoir characterization. In a reservoir, an alternation of diverse lithological intervals (e.g. sandstones, shales, coals, and/or siltstones) can be observed as a result of the different sedimentation processes involved (Eidsvik *et al*., 2002; Sinvhal & Sinvhal, 1992). This information is usually obtained from the different well logs and core information of the study area. To completely characterize the reservoir, this information, available just at the well locations, should be extended to the whole area or volume of interest. Different geostatistical techniques have been used to mathematically model and characterize reservoir heterogeneities, in order to obtain representative facies alternation that are geologically possible (Elfeki and Dekking, 2001). Some of these techniques use variogram, autocorrelation or autocovariance functions. In these cases, to model the spatial variability from the fitting of the variograms, intensive data sets are needed (Carle and Fogg, 1996).

Markov Chains represent an alternative way to model the spatial structure of a reservoir and have been applied in geology to model lithologies or facies that constitutes discrete variables or categorical data (Elfeki and Dekking, 2001). The Markovian analysis is a statistical technique that enables the definition and description of the facies associations along a stratigraphic sequence. Hence, Markov chains allow modeling stratigraphic sequences through a probabilistic analysis (Miall, 1973; Eidsvik *et al*. 2002; Eidsvik *et al*., 2004a). Within a Markov chain, the transition probability from a discrete state to the next depends on the previous state (Till, 1974). Therefore the occurrence of a particular facies depends, in a certain way, on the previous facies. This dependence suggests that the sedimentary processes that could control at a specific time the facies distribution, have memory (Leeder, 1982). This memory is useful as it might support the environmental interpretation that could be demonstrated analyzing adjacent sections (Suarez, 1997). As gradual changes along a well can be recognized in terms of the different lithologies observed, Markov Chains may be used as a tool for the indirect determination of facies type, thickness and alternation along it (Doveton, 1994; Sinvhal & Sinvhal,1992; Eidsvik *et al*., 2002; Eidsvik *et al*., 2004a).

This stochastic technique can also be used to model complex geologic processes that are related to agents not precisely identified (e.g. sedimentary cycles) (Kulatilake, 1987). In fact, the Markovian analysis allows evaluating the state of change in terms of its relative probability of occurrence. The lithologies are not only repeated vertically, but partially depend from one another. Hence, a sedimentary sequence cycle can be described as a series of rocks or beds which overlay or underlay one another with a predictable probability pattern (Schwarzacher, 1975; Sinvhal and Sinvhal, 1992). Different studies have used this approach for cyclicity analysis of stratigraphic sequences (e.g. Miall, 1973; Kulatilake, 1987). Suarez (1997) used a Markovian analysis to define the lithofacies genetic relationships along the sedimentary column of the Rio Negro Formation, Venezuela. Just one section was included in that study due to the absence of any detailed bibliography about the Uribante Through. Suárez (1997) was able to quantitatively represent a stratigraphic sequence useful for the interpretation of the sedimentary environments of the study area. His results demonstrated the presence of stratigraphic memory within the tested column, even though just one column was analyzed. The inclusion of one column could be a limitation regarding the definition of the stratigraphic memory. Nevertheless, this kind of studies is considered useful in the definition of the genetic relationships among the lithofacies (Miall, 1973) and in the paleo-environmental interpretation (Suárez, 1997).

The main purpose of the present study is to develop and to apply a Markov Chain algorithm in order to model the geological setting and to stochastically characterize a reservoir, located at the Lama Field, Maracaibo Lake, Venezuela, considering the possible cyclicity of the strata of interest. Mathematical simulation and pattern recognition techniques were applied, trying to understand and predict the vertical and horizontal lithological variations at the study area in order to diminish the uncertainty in the stochastic characterization of a hydrocarbon reservoir. The studied reservoir belongs to the C4 sands of the Misoa Formation, which comprises thick layers of sandstones interbedded with thin layers of siltstones and shales. The algorithm will be used to model pseudo stratigraphic sequences and to quantify the relative facies proportion along the reservoir. The Markovian property, and hence the stratigraphic memory of the section analyzed, will be evaluated, as well as the confidence of the algorithm in terms of the relative facies proportion obtained at test wells. The nature of the cyclic sedimentation processes in the area will be analyzed by means of the Markov approach, using more than only one sedimentary sequence, as the information

derived from all the wells available for this study will be integrated.

Geographical and Geological setting

The study area is located in the central part of the Maracaibo Basin, specifically at the Lama Field, southeast of Block IX, Venezuela (see Figure 1).

The west part of the Lama Field is one of the largest hydrocarbon accumulations within the central part of the Maracaibo Lake Basin. This area is in contact with the west boundary of the Lama-Icotea Fault, and it is limited by an inverse northwest-southeast fault system. A series of antithetic normal faults toward the Icotea fault are present along the study area (Arminio *et al*., 1994; Delgado, 1993). In the central and south parts of the field, a different structural tendency can be observed, characterized by the presence of inverted faults to the west southwest – east northeast direction (Delgado, 1993). The major geological feature in the area is a north-northeast-trending anticlinal dome (Ambrose and Ferrer, 1997). Several structural compartments were created between intersecting faults of diverse age, due to the complex tectonic development of the Maracaibo Lake (Ambrose and Ferrer, 1997). Structurally, the main traps are located along the Icotea high, with Cretaceous and Eocene reservoirs (Yoris and Ostos, 1997).

The reservoir of interest in this study corresponds to the C4 sands of the Lower Misoa Formation (Eocene). According to Talukdar and Marcano (1994) and Delgado (1993), the Lower Misoa strata were deposited in a tide-dominated delta setting with the sediment source located to the west or southwest. Ambrose and Ferrer (1997) describe the Lower Misoa Formation as structurally complex, heterogeneous, with estuarine-delta and tide dominated shelf reservoirs. The C4 sands of the Misoa Formation compresses thick layers of sandstones interbedded with thin shale and siltstone layers (Yoris and Ostos, 1997) (Figure 2).

Methodology

In order to define and characterize the litostratigraphic units used as input in the probabilistic and statistic algorithms, a stratigraphic correlation was carried out. This phase makes it possible to define the thickness in depth of the unit of interest. This unit was named as Unit 1 and compresses, mainly, the C4 sands of the Misoa Formation. These sandstones consist of deltaic interbedded sandstones, shales and siltstones, accumulated during the Eocene (Yoris and Ostos, 1997).

Three transects, that include the 11 wells available in the area, were used for the stratigraphic correlation. Figure 3 shows the wells, located to the southwest of the Lama Field, and the selected transects for the stratigraphic correlation sections. The first section has a southwest-northeast direction and includes wells 15, 2, 16, 1 and 12. Along this section, the unit thickness varies between 61 ft (≈19 m) and 168 ft (≈50 m). The major thicknesses are observed in well 12, and could be related to sand bars. The second correlation section has a northwest-southeast direction, including wells 11, 1, 7 and 14. In this case, the

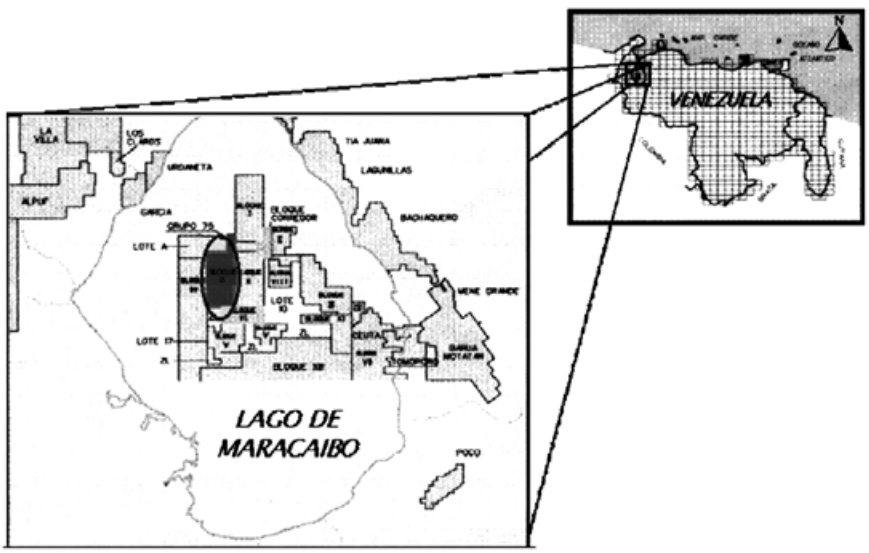

Figure 1. Geographic location of the Lama Field (After Cedillo *et al*., 2004)

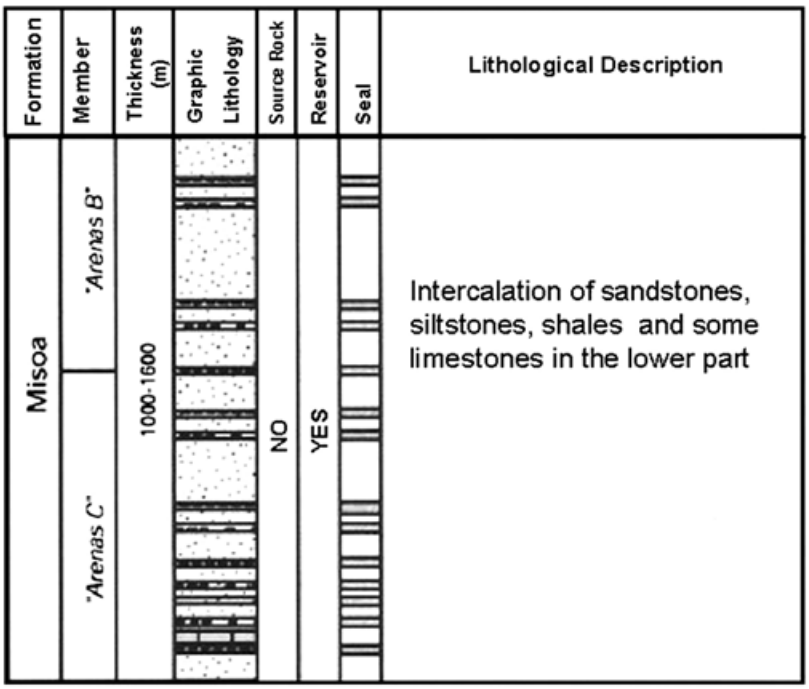

Figure 2. Lithological description of the Misoa Formation. (Modified from Yoris and Ostos, 1997)

strata thicknesses vary gradually between 67 ft (≈20 m) and 91 ft (≈28 m). The last correlation is a north-south stratigraphic section, passing through wells 9, 14, 7, 6, 12 and 17 (Figure 4). In wells 12 and 17, the thickness increases to 106 ft. (≈32 m) and decreases to 52 ft. (≈16 m), respectively.

In this study, the Markovian analysis was used to estimate and quantify vertical and horizontal lithofacies variations. The algorithm developed here is based on previous studies by Sinvhal and Khattri (1983), Sinvhal and Sinvhal (1992), Doveton (1994), Suarez (1997) and Eidsvik *et al*. (2004a). The algorithm, implemented in MatLab, includes four main

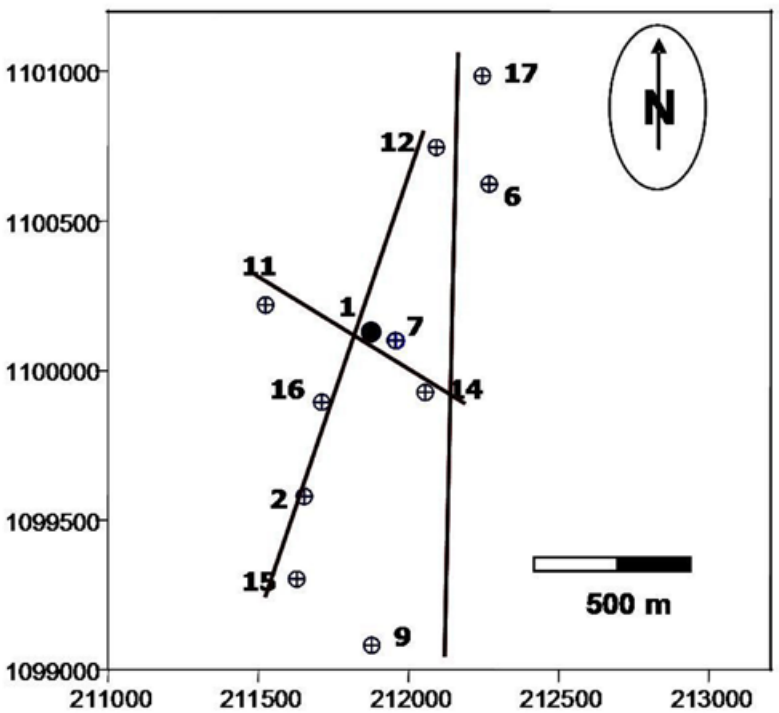

Figure 3. Location of the wells at the study area. The lines represent the stratigraphic correlation sections.

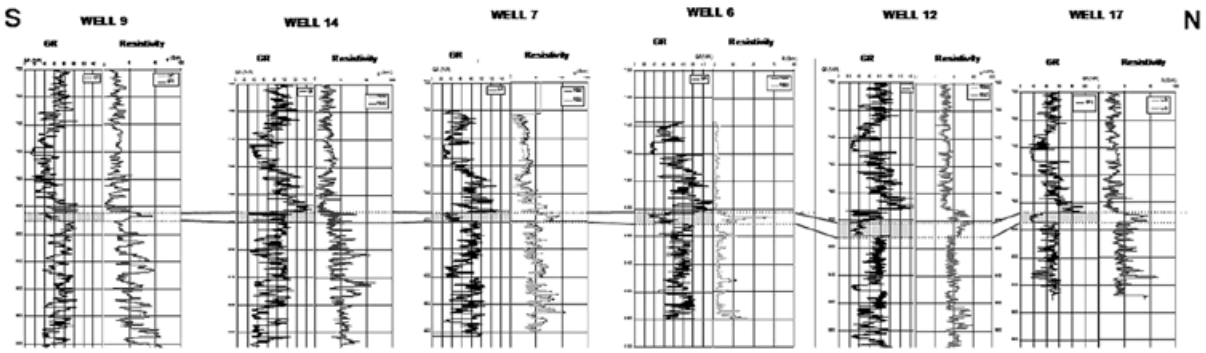

Figure 4. Stratigraphic correlation section (Nort-South direction) that comprises wells 9, 14, 7, 6, 12 and 17.

steps: (a) load and analysis of well logs, (b) counter matrix calculation, (c) probability matrix calculation and (d) pseudo-well estimation and generation.

Gamma ray, Resistivity and/or Spontaneous Potential well logs were used to recognize the main facies and to perform the alternation probability analysis (i.e. the transition probability of overlying and underlying lithologies). To discriminate and select the facies along the wells, response intervals for the input logs were defined and assigned to the interpreted facies (i.e. sandstone, siltstone and shale) in order to automatically discriminate and select them in depth. The response of the different logs depends on the lithology. The gamma-ray log is used to identify different grain sizes. Two cutoff lines are chosen. Gamma-ray values below the lowest cutoff line correspond to bigger grain sizes, i.e., sandstones; between the cutoff lines, middle grain sizes are expected (silts); values above the highest cutoff line represent finer grain sizes, i.e. clays. In the case of the SP logs, clays (that are impermeable) will generate a voltage value and permeable sands in contact with them will generate an opposite one. On the other hand, in resistivity logs high values are observed usually at permeable intervals containing hydrocarbons. The three lithologies were discriminated combining all these responses (Bassiouni, 1994). For each rank, a numeric response was generated to distinguish one facies from another: (1) sandstone, (2) siltstone and (3) shale. Figure 5 shows a lithologic column where every sequence corresponds to a number (1, 2 or 3), i.e. the algorithm generates an alphanumeric response in depth which represents a lithofacies column from a geologic point of view.

The relationship between adjacent geological events can be summarized with a transition counter matrix (T). In this matrix, every cell sums the number of times that a lithotype, identified by the matrix rows, is overlaid by another, identified by the matrix columns (see Figure 5). In this study, the matrix T was obtained for each well according to the lithology identified using the well logs available in the area (mainly Gamma Ray and Resistivity logs). Hence, the counter matrix T has the form:

$$T = \begin{array}{c} \\ 1 \\ 2 \\ 3 \end{array} \begin{array}{c} \begin{array}{ccc} 1 & 2 & 3 \end{array} \\ \begin{pmatrix} a_{11} & a_{12} & a_{13} \\ a_{21} & a_{22} & a_{23} \\ a_{31} & a_{32} & a_{33} \end{pmatrix} \end{array}$$

where aij represents the number of times that the facies j overlies the facies i, i.e. the number of upward transitions from facies i to facies j (see Figure 5).

The transition probability matrix (P) is obtained from the T matrix according to:

$$Pij = aij / sumi$$

In the relation above, sumi corresponds to the sum of the elements of the i row, i.e. the row of the element aij in the T matrix. The P matrix shows the probability that a facies overlays a given one, i.e. the probability of alternation of a given facies.

P and T matrices were calculated for each well. The cumulative probability matrix, Pcum, is obtained from the P matrix as the accumulated sum along each row. The last element of Pcum at a given row should be 1. The Pcum matrix is the starting point for the pseudo columns simulation.

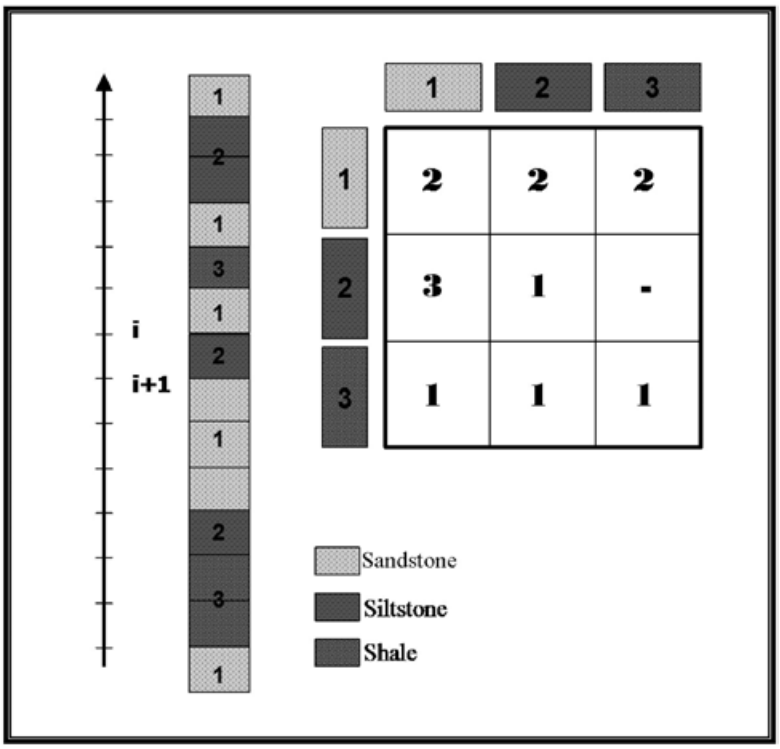

Figure 5. Ideal example of a succession of sandstone (1), siltstone (2) and shale (3), in depth and/or time, and the counter matrix associated to this column. (Modified from Doveton, 1994).

Pseudo-stratigraphic Markov columns were generated at 20 new locations. The grid shown in Figure 6 was used to optimize the spatial sampling of the study area. The pseudo-wells were located equidistant to each pair of original wells. Therefore, only the contribution of the two closest colinear wells was taken into account. No weight dependency on the distance to the estimation point was used. Hence a simple average, that represents the same weight for each pair of wells in the segments, was applied. At each new location, <P> and <Pcum> matrices were generated using the counter transition information of the two equidistant wells. For each new location, 10 Markov realizations were performed with these matrices and a mean pseudo column was finally obtained. Although lithological lateral variability can exist between sequences (Eidsvik *et al*., 2004a; Eidsvik *et al*., 2004b), the analyzed lithological sequences correspond to the same stratigraphic parasequence (i.e the same time interval in a sedimentary setting) and hence, the simple average is enough to take this variation into account. The initial state was selected randomly in each realization, i.e. a random seed from a uniform distribution is generated to obtained the initial state; the next facies was obtained by sampling <Pcum>. In this fashion, to select the next facies along a sequence, the i column of the <Pcum> matrix (i is the number of the present state, i.e. 1, 2 or 3), was sampled to infer the immediate posterior state. A random number (Rn) between 0 and 1 was generated and compared with the ranges of values of the i row of the <Pcum> matrix. If $0<Rn< a_{i1}$, the next facies should be 1. If $a_{i1}<Rn< a_{i2}$, the next facies will be 2; if $a_{i2}<Rn$, the overlaying facies is 3 (Sinvhal and Sinvhal, 1992). This process was iterated until the whole column was completed. The generation of each pseudo-column starts from base and goes to top, trying to simulate the sedimentation process. Pseudo-sequences were estimated at some selected well positions in order to test the reliability of the stochastic Markov Chain simulation and to estimate the prediction error.

At each well and pseudo-well location, the percentage of each lithofacies was calculated and maps of facies distribution were obtained integrating the information given by the facies columns, obtained from the well logs, and the Markovian pseudo-columns.

For the cyclicity analysis, a total <T> and an average occurrence probability matrix <P> were obtained for the study area using all the available wells. Hence, in this study we used more than one vertical sequence to define the genetic relations between lithofacies; in fact, 11 vertical sequences were used to determine a mean facies behavior in the study area. The nature of the cyclic processes observed was

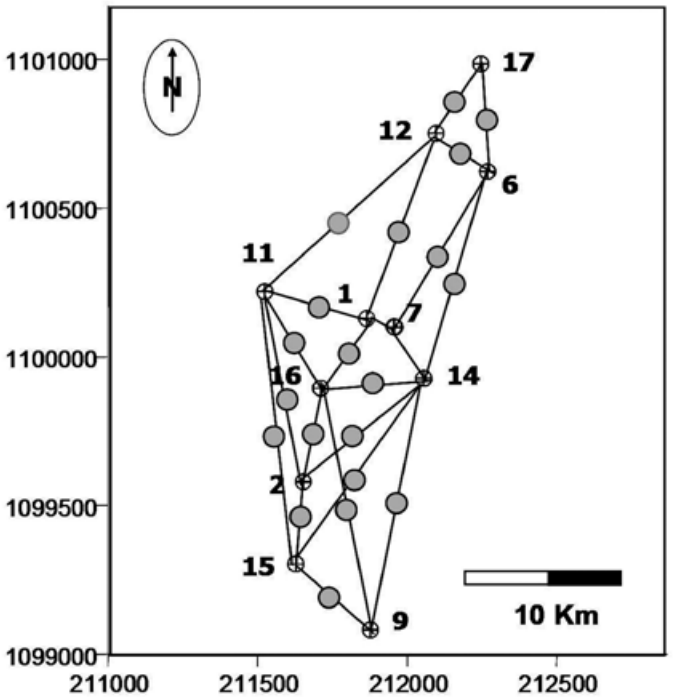

Figure 6. Locations of the pseudo-columns (grey dots). These new locations were placed equidistant to the 11 wells (black dots) available at the study area.

studied using the embedded Markov Chain method (Harbaugh and Bonham-Carter, 1970). To do so, transitions between the same facies are not allowed and, hence, the diagonal of the <T> and <P> matrices should be set to zero. This gives rise to two new matrices, <To> and <Po>. As stated by Miall (1973), this method highlights the actual change, focusing on the evolution of the depositional processes. A matrix that shows the probability that a given transition occurs randomly (an independent trials probability matrix, I) was obtained in the embedded Markov chain case according to (Miall, 1973):

$$Iij = sumj \,/\, (\, \textbf{\textit{total}} - sumi)$$

were ***total*** is the total number of transitions in the matrix <To>, and sumj and sumi are the sum of the elements in column j and in row i of this matrix, respectively. The difference matrix <D> between <Po> and I was also calculated to analyze the cyclicity of the transitions. Positive entries in the <D> matrix indicate which transition occurred with probability greater than a random frequency and, hence, underlies the Markov property (Miall, 1973). The highest values of <Po> and the positive entries of <D> were analyzed to determine the cyclic processes at the studied Block of the Lama Field.

The Markov property of the <Po> matrix was tested using a chi-square (χ^2) test according to (Harbaugh and Bonham-Carter, 1970):

$$-2\ln\lambda = 2\sum_{i,j}^{m} a_{ij} \ln \frac{Po_{ij}}{Po_j}$$

where

Po_{ij}= the element in cell i,j of the mean <Po> transition probability matrix

Po_j=marginal probabilities for the jth column, i.e.

$$= \sum_{i}^{m} aij \Big/ \sum_{ij}^{m} a_{ij}$$

a_{ij}= transition frequency in cell i,j of the <To> matrix

m= number of states

In the expression above, $-2\ln\lambda$ behaves asymptotically as χ^2 with $(m-1)^2$-m degrees of freedom for the embedded Markov case (Harbaugh and Bonham-Carter, 1970).

Results

To evaluate the change of state in terms of its relative occurrence probability, the lithology content at each well location, estimated from the well logs, was considered. Particularly, the sandstone content was analyzed in detail as it represents the reservoir rock in the study area. Table 1 shows the sandstone (P1), siltstone (P2) and shale (P3) content for each of the studied wells in the field. As can be observed, sandstone content predominates, varying from 90.9% to the north of the study area to 19.3% in the central part of it (see well location in figure 4). In spite of the P1 values variation, its mean (68%) indicates high sandstone content in most of the area. These values were calculated for the Markovian pseudo sequences obtained at test well locations. Particularly, for well 2 the pseudo sequence was obtained using the information of the two equidistant wells 15 and 16 (see figure 6); this pseudo well is designated as W15-16. Figure 7 shows the first three runs of the Markovian algorithm for this location. The final column is the mean after ten runs.

The mean P1, P2 and P3 values obtained are 78.7%, 13.6% and 7.7%, respectively. Although the vertical distribution of the shale and siltstone beds differs for the estimated pseudo well, there is a good agreement between the average content of each lithofacies obtained from the pseudo sequences and those calculated from the well logs (see Table 1).

Table 1. Sandstone (P1), siltstone (P2) and shale (P3) content at each well of the study area.

Well	P1(%)	P2(%)	P3(%)
1	80.3	19.7	0.0
2	80.7	10.3	8.9
6	54.5	41.9	3.6
7	81.8	9.5	8.8
9	70.7	29.3	0.0
11	49.3	41.8	8.9
12	90.9	9.1	0.0
14	19.3	34.8	45.9
15	77.1	18.3	4.6
16	81.9	13.6	4.52
17	68.6	1.9	29.5

Proportional (EPROP) and distributive (EDIST) errors were also estimated. The EPROP was estimated from the differences between the normalized lithology proportion (sandstone, siltstone and shale) along well 2 and along the pseudo well W15-16. The EDIST error measures the difference between the lithofacies distribution at both columns. The values obtained indicate that the Markovian technique, applied to this well, has a confidence of 82% regarding the lithology content and 67% related to the lithology distribution.

A net sand content map, combining the information of the original sequences at the well locations and the Markovian pseudo sequences at the 20 new locations, was generated in order to observe the variation of this parameter at Unit 1. The map of figure 8 shows, towards the mid-west part of the study area, a high sand content, that varies between 60% and 80%. This content diminishes gradually to the southeast, where well 14 achieves the lowest sand value (19.3%). This map also shows a SW-NE sedimentary direction, in agreement with previous geological analyses in the area (Arminio *et al*., 1994; Cedillo *et al*., 2004); according to these studies, the thick Eocene fluvial-deltaic sediments prograded eastward and northeastward on the platform (Ambrose and Ferrer, 1997).

The total <T> and the <P> matrices for the study area are:

$$<T> = \begin{array}{c} \\ 1 \\ 2 \\ 3 \end{array} \begin{array}{c} \begin{array}{ccc} 1 & 2 & 3 \end{array} \\ \begin{pmatrix} 1500 & 34 & 0 \\ 35 & 340 & 17 \\ 0 & 16 & 122 \end{pmatrix} \end{array} \qquad <P> = \begin{array}{c} \\ 1 \\ 2 \\ 3 \end{array} \begin{array}{c} \begin{array}{ccc} 1 & 2 & 3 \end{array} \\ \begin{pmatrix} 0.9778 & 0.0222 & 0 \\ 0.0893 & 0.8673 & 0.0434 \\ 0 & 0.1159 & 0.8841 \end{pmatrix} \end{array}$$

According to the <P> matrix, the major number of transitions occurs from sandstone to sandstone. This correlates well with the results of the net sand distribution in the study area. Transitions between shale to shale and from siltstone to siltstone have the next probability to occur. According to this matrix, transitions from sandstone to shale and viceversa are not expected to occur in the study area.

The <To>, <Po>, I and <D> matrices obtained for the cyclicity analysis are:

$$<To> = \begin{array}{c} \\ 1 \\ 2 \\ 3 \end{array} \begin{array}{c} \begin{array}{ccc} 1 & 2 & 3 \end{array} \\ \begin{pmatrix} 0 & 34 & 0 \\ 35 & 0 & 17 \\ 0 & 16 & 0 \end{pmatrix} \end{array} \qquad <Po> = \begin{array}{c} \\ 1 \\ 2 \\ 3 \end{array} \begin{array}{c} \begin{array}{ccc} 1 & 2 & 3 \end{array} \\ \begin{pmatrix} 0 & 1.0000 & 0 \\ 0.6731 & 0 & 0.3269 \\ 0 & 1.0000 & 0 \end{pmatrix} \end{array}$$

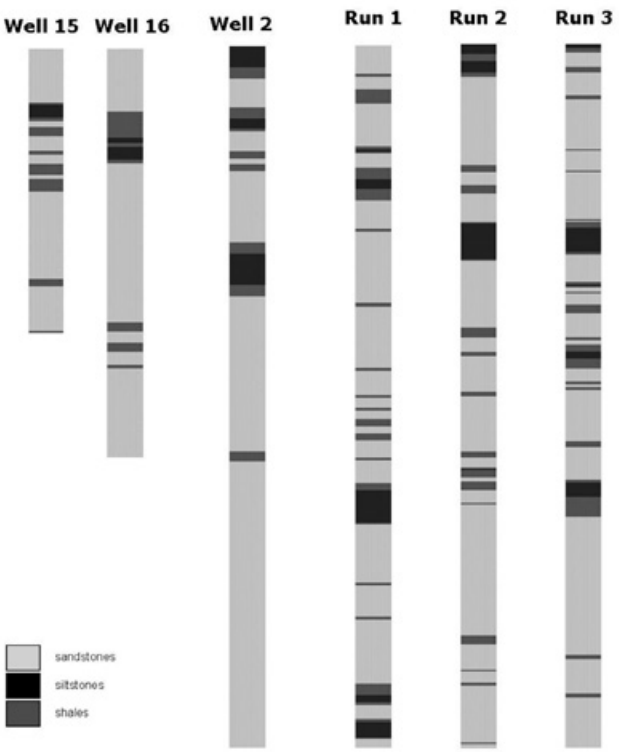

Figure 7. Pseudo-stratigraphic columns generated at the location of well 2, using the information of the equidistant wells 15 and 16. The first three runs are shown. The final column at this location is the mean after ten runs.

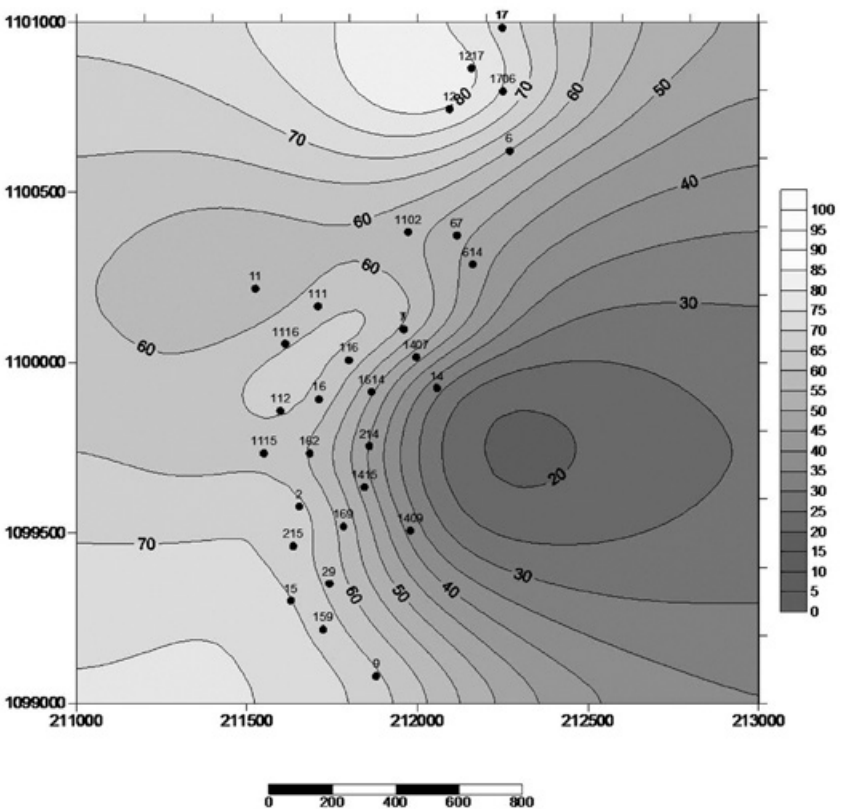

Figure 8. Map of sand percentage obtained after integrating the well and the Markov pseudo-columns

$$I = \begin{array}{c|ccc} & 1 & 2 & 3 \\ 1 & 0 & 0.7353 & 0.25 \\ 2 & 0.70 & 0 & 0.34 \\ 3 & 0.4070 & 0.5814 & 0 \end{array} \qquad \langle D \rangle = \begin{array}{c|ccc} & 1 & 2 & 3 \\ 1 & 0 & 0.2647 & -0.2500 \\ 2 & -0.0269 & 0 & -0.0131 \\ 3 & -0.4070 & 0.4186 & 0 \end{array}$$

A chi-square value of 138.32 was obtained for the <Po> matrix. For a total number of states m=3, as in the case of this study, and hence one degree of freedom for the embedded Markov method, the 95% confidence level has a limit chi-square value of 7.81473. Therefore, the Markovian property is present in the studied sequence and the transitions are not independent (Harbaugh and Bonham-Carter, 1970).

The difference <D> matrix indicates cyclic transitions just from sandstone to siltstone and from shale to siltstone (see figure 9). The transitions not present in the diagram could be considered as random changes of the sedimentation processes or non cyclic transitions (Miall, 1973).

The results obtained suggest that coarsening upward and fining upward processes dominate the study sequence. In a nearby block (Block V) Arzuman (2002) observed that the sandy layers of the C-4 interval show coarsening upward, blocky, and fining upward log patterns on the Gamma Ray trace of the studied well (VLE 196). Previous studies in the Lama Field indicate that the Lower Misoa formation was deposited in a tide-dominated delta setting (Talukdar and Marcano, 1994; Ambrose and Ferrer, 1997). The morphology of these tide-dominated deltaic systems could be the result of the tide action over the fluvial sedimentation. According to Galloway and Hobday (1996) these kinds of systems show few to many estuarine distributary channels, characterized by broad, funnel-shaped mouths, and narrow, sinuous upper reaches. The general upward-coarsening character of the distributary mouth bars tends to produce sandstone bodies that are usually upward-fining (Scheihing and Atkinson, 1992; Arzuman, 2002). It is important to point out that these channel deposits and distributary mouth bars usually involve the best reservoir quality bodies within a delta system (Arzuman, 2002).

Figure 9. Cyclic processes for the study sequence (Unit 1). The probability of occurrence is also indicated

Hence, the combination of the processes indicated above, i.e. the interaction/competition between the tides and the fluvial transport, could explain the Markovian transitions observed in the study area. Ideally, a matrix with sand to silt, silt to sand, silt to clay and clay to silt transitions could be expected for coarsening upward and fining upward processes in a deltaic environment. Nevertheless, it is important to point out that mean matrices for the whole area were used for this cyclicity analysis. Therefore, the <Po> matrix obtained here shows the mean or more significant transitions. In fact, according to Ambrose and Ferrer (1997), the Lower Eocene sandstone depositional axes in the Lama Field are narrow, linear, and commonly projected between the existing control wells at 80-acre spacing as a result of the depositional architecture. According to the lithological percentage observed at the studied well (see Table 1), most of these wells drilled the thick sandstones of the Eocene fluvial-deltaic sediments. If more wells outside the narrow channels are used, it should be possible to observe the siltstone to sandstone and siltstone to shale transitions probably hidden due to the mean analysis performed here.

Conclusions

The Markov analysis of the C4 sands of the Misoa Formation, at the Lama Field, allowed to properly model the vertical and horizontal heterogeneities of the reservoir, as was indicated by the map of sandstone content obtained integrating the columns derived directly from the well logs and the Markovian pseudo-columns. This map clearly depicts a NE-SW axis coincident with the sedimentation direction of the thick Eocene fluvial-deltaic sediments observed in the area. The Markovian embedded analysis of the mean transition probability of the study area indicates cyclic transitions from sandstone to siltstone and shale to siltstone, representative of fining-upward and coarsening-upward processes, expected for delta environments as the tide-dominated one studied here. These transitions were observed with the Markovian approach even though some bias is given by the well distribution, as these wells mainly drilled the thick sandstones of the area. These results emphasize the additional advantages of this kind of stochastic characterization compared with other statistical methods as crossplots or semivariograms analyses.

References

Ambrose W.A., Ferrer E.R., Dutton S.E, Wang F.E, Padron A., Carrasquel W., Yeh J.S., Tyler N., 1995, Production optimization of tide-dominated deltaic reservoirs of the lower Misoa Formation (Lower Eocene), LL-652 Area, Lagunillas Field, Lake Maracaibo, Venezuela: The University of Texas at Austin, Bureau of Economic Geology Report of Investigations No. 226.

Ambrose W.A., Ferrer E.R., 1997, Seismic Stratigraphy and Oil Recovery Potential of Tide-dominated Depositional Sequences in the Lower Misoa Formation (Lower Eocene). LL-652 Area, Lagunillas Field, Lake Maracaibo, Venezuela, *Geophysics*, 62, 5, 1483-1495.

Arminio J.F., Zubizarreta J., González G., 1994, Evolución tectónica y habitat de hidrocarburos del área Lama Sur, Lago de Maracaibo, VII Congreso Venezolano de Gefisica, Caracas, SOVG, pp. 384-392.

Arzuman Sadun, 2002, 3-D structural and seismic stratigraphic interpretation of the Guasare-Misoa Interval, VLE 196 Area, Block V, Lamar Field, Lake Maracaibo, Venezuela. Master's thesis, Texas A&M University. Texas A&M University. Available electronically from http://hdl.handle.net/1969.1/557.

Bassiouni Z., 1994, Theory, Measurement, and Interpretation of Well Logs, SPE Textbook Series Vol. 4, Society of Petroleum Engineers, Richardson, Texas.

Carle S.F., Fogg G.E., 1996, Transition Probability-Based Indicator Geostatistics, *Mathematical Geology*, 28, 4, 453-476.

Cedillo I., Aldana M., Angulo R., 2004, Estudio de transformadas multiatributo para predecir propiedades de registros. Memorias XII Congreso Venezolano de Geofísica. Caracas, Venezuela, pp 1-8.

Delgado I., 1993, Lama Field - Venezuela, Maracaibo Basin, Zulia State, 1993 *in* N. H. Foster and E. Q. Beaumont, eds., Structural Traps VIII, Treatise of Petroleum Geology, Atlas of Oil and Gas Fields: AAPG Special Publications, v.A022 ,271-294.

Doveton J.H., 1994, Theory and application of vertical variability measures from Markov chain analysis, in: *Computer applications in geology, N° 3* (Eds J.M. Yarus J.M. and A.L. Chamberlain) *Am. Assoc. Petrol. Geol*., 55-64.

Eidsvik J., Mukerji T., Switzer P., 2002, Modeling lithofacies alternations from well logs using Hierarchical Markov Chains, SEG Technical Program Expanded Abstracts 2002: 2463-2466.

Eidsvik J., Mukerji T., Switzer P., 2004a, Estimation of geological attributes from well logs: an application of hidden Markov chains. Mathematical *Geology*, 36, 3, 379-398.

Eidsvik J., Avseth P., Omre H., Mukerji T., Mavko G., 2004b, Stochastic reservoir characterization using prestack seismic data, *Geophysics*, 69, 4, 978–993.

Elfeki A., Dekking M. 2001, A Markov Chain Model for Subsurface Characterization: Theory and Applications, *Mathematical Geology*, 33, 5, 569-589.

Galloway W.E., Hobday D.K. , 1996, Terrigenous clastic depositional systems, applications to fossil fuel and ground water resources: Berlin, Germany, Springer-Verlag, 115-120.

Harbaugh J.W., Bonham-Carter G., 1970, Computer Simulation in Geology, Wiley-Interscience, New York, p. 575.

Krumbein W.C., Dacey M.F., 1969, Markov chains and embedded Markov chains in geology. *Journal of Mathematical Geology,* 1, 1, 79-96.

Kulatilake P.H.S.W., 1987, Modelling of cyclical stratigraphy using Markov chains**.** *International Journal of Mining and Geological Engineering*, 5, 2, 121-130.

Leeder M., 1982, Sedimentology: process and product, Allen & Unwin, London, p. 344.

Miall A.D., 1973, Markov chain analysis applied to an ancient alluvial plain succession *Sedimentology* 20, 3, 347-364.

Scheihing M.H., Atkinson C.D., 1992, Lithofacies and environmental analysis of clastic depositional systems, *in* D. Morton-Thompson and A. M. Woods, eds., Development geology reference manual: AAPG Special Publications, Methods in Exploration 10, p.293-265.

Schwarzacher W., 1975, Sedimentation Models and Quantitative Stratigraphy. Elsevier Scientific Publi. Co., Amsterdam, p- 382.

Sinvhal A., Sinvhal H., 1992, Seismic Modelling and Pattern Recognitionin Oil Exploration, Kluwer Academic Publishers, The Nederlands, 178 p.

Sinvhal A., Khattri K., 1983, Application of seismic reflection data to discriminate surface lithostratigraphy, *Geophysics,* 48, 11, 1498-1513.

Suarez C., 1997, Análisis de Markov de la Secuencia Estratigráfica de la Formación Río Negro en la Sección La Vueltosa. Estado Mérida y Barinas. Memorias del Primer Congreso Latinoamericano de Sedimentología, Sociedad Venezolana de Geólogos. Tomo 1. p. 227 – 283, Caracas, Venezuela.

Talukdar S.C., Marcano F., 1994, Petroleum systems of the Maracaibo Basin, Venezuela, *in* L.B. Magoon and W.G. Dow, eds., The petroleum system – from source to trap: AAPG Memoir 60, p.463-481.

Till R., 1974, Statistical methods for the earth scientist-an introduction. The Macmillan Press Ltd., London, pp. 154.

Yoris F**.,** Ostos M., 1997, Geology of Venezuela : General Geology and Oil Basins, in: Singer, J. (Edr.) WEC 1997 Well Evaluation Conference. Schlumberger - Surenco, C.A.; 1ra. Ed. English: Jolley Printing (Texas); Chapt. 1, 1 - 17; 24 -44.

Geofísica Internacional (2014) 53-3: 289-308

Original paper

Edge enhancement in multispectral satellite images by means of vector operators

Jorge Lira* and Alejandro Rodríguez

Received: May 14, 2013; accepted: December 02, 2013; published on line: July 01, 2014

Resumen

El realce de bordes es un elemento de análisis para entender la estructura espacial de imágenes de satélite. Se presentan dos métodos para extraer los bordes de imágenes multiespectrales de satélite. Una imagen multiespectral se modela como un campo vectorial de un número de dimensiones igual al número de bandas en la imagen. En este modelo, un pixel se define como un vector formado por un número d elementos igual al número de bandas. Se aplican dos operadores vectoriales a tal campo vectorial. En nuestro primer método, extendemos la definición de gradiente. En esta extensión, se obtiene el vector diferencia del pixel central de una ventana con los pixels vecinos. Se genera entonces una imagen multiespectral donde cada pixel representa el máximo cambio en la respuesta espectral en la imagen en cualquier dirección. A esta imagen se le denomina el gradiente multiespectral. El otro método considera la generalización del Laplaciano por medio de la transformada de Fourier h-dimensional. A esta imagen se le denomina el Laplaciano multiespectral. Los operadores vectoriales realizan una extracción simultánea del contenido de bordes en las bandas espectrales de la imagen multiespectral. Nuestros métodos son libres de parámetros. Nuestros métodos trabajan para una imagen multiespectral de cualquier número de bandas. Se discuten dos ejemplos que involucran imágenes multiespectrales de satélite a dos escalas. Comparamos nuestros resultados con procedimientos de realces de bordes ampliamente empleados. La evaluación de los resultados muestra un mejor comportamiento de los métodos propuestos comparados con los operadores de bordes ampliamente usados..

Palabras clave: detección de bordes, imagen multiespectral, realce de borde, operador vectorial.

Abstract

Edge enhancement is an element of analysis to derive the spatial structure of satellite images. Two methods to extract edges from multispectral satellite images are presented. A multispectral image is modeled as a vector field with a number of dimensions equal to the number of bands in the image. In this model, a pixel is defined as a vector formed by a number of elements equal to the number of bands. Two vector operators are applied to such vector field. In our first method, we extend the definition of the gradient. In this extension, the vector difference of the window central pixel with neighboring pixels is obtained. A multispectral image is then generated where each pixel represents the maximum change in spectral response in the image in any direction. This image is named a multispectral gradient. The other method, considers the generalization of the Laplacian by means of an η-dimensional Fourier transform. This image is named a multispectral Laplacian. The vector operators perform a simultaneous extraction of edge-content in the spectral bands of a multispectral image. Our methods are parameter-free. Our methods work for a multispectral image of any number of bands. Two examples are discussed that involve multispectral satellite images at two scales. We compare our results with widely used edge enhancement procedures. The evaluation of results shows better performance of proposed methods when compared to widely used edge operators.

Key words: edge detection, multispectral image, edge enhancement, vector operator.

J. Lira*
A. Rodríguez
Instituto de Geofísica
Universidad Nacional Autónoma de México
Delegación Coyoacán, 04510
México D.F., México
*Corresponding author: jlira@geociencias.unam.mx

Introduction

Edge detection has been undertaken for gray-level and color images using a number of methods and procedures. Most of the techniques published in the scientific literature in the last years deal with color images.

Well-established methods such as Kirsch, Sobel, Gradient and Laplacian operators have been widely used to extract edges in gray-level images (Pratt, 2001). Bowyer and co-workers (2001) provided a detailed account of a number of edge operators in gray images. The reviewed operators carry a set of parameters that needs to be defined in terms of heuristic criteria. Ground-truth images were used to derive a classification of edge operator performance (Bowyer *et al*., 2001). A deformable contour, defined by a wavelet snake, is designed to identify the boundary of pulmonary nodules in digital chest radiographs (Yoshida, 2003). In this work (Yoshida 2003), a multi-scale edge representation is obtained by means of the wavelet transform; this produces, however, fragmented edge segments. Therefore, a wavelet snake was used to produce a smooth and closed contour of a pulmonary nodule.

Other methods to detect edges in gray-level images use fuzzy logic. Segmentation of a fuzzy image into regions of similar image properties was achieved by means of a fuzzy procedure (Bigand *et al*., 2001). This method works with fuzzy-like and noisy images. Zero crossings that correspond to gradient maxima were obtained by means of the cosine transform in noisy images (Sundaram, 2003). This scheme favors the detection of weak edges in background noise and suppresses false edges.

The modeling of natural RGB images as vector fields has been exploited to detect edges in color images (Koschan and Abidi, 2005; Evans and Liu, 2006). In their studies, the authors (Koschan and Abidi, 2005) provide an overview of color edge detection techniques, and, in particular, generalizations of Canny and Cumani operators to color spaces were discussed with examples. Evans and Liu (2006) provide a review of color edge detectors.

A parameter-free approach could be obtained when an automatic determination threshold was calculated using a model-based design (Fan *et al*., 2001). With this approach, a color-image edge operator is derived. Cellular neural networks applied to color images resulted in a model to detect edges (Li *et al*., 2008). This model was successfully applied to RGB images with color test patterns. In addition to these results, the authors provided a detailed revision of color edge detection techniques.

Recent advances in edge enhancement for color images show clear advantages over methods for mono-spectral images (Xu *et al*., 2010; Chen and Chen, 2010; Nezhadarya and Kreidieh, 2011; Gao *et al*., 2011; Chu *et al*., 2013). Color images are increasingly used in many applications such as surveillance, computer vision and robotics. Multispectral satellite images are available at several scales. For these two groups of images, edge enhancement is an element of structural analysis.

A general method is needed that works for any number of bands, with no parameters and a reasonable computing time. To fulfill such goal, we model a multispectral satellite image by means of a vector field. The dimension of this field equals the number of bands of the image. Upon this field, we may apply vector operators. We compare our results with those obtained from conventional edge operators (Pratt, 2001; Bowyer *et al*., 2001). We carry out a detailed evaluation of our results. Such evaluation includes qualitative and quantitative analysis. Our evaluation shows a clear improvement with respect to conventional edge operators.

Study area and data

Two multispectral satellite images were used to test the goodness of our method at different scales. Both images cover a portion of Mexico City where the runaways of an airport are clearly visible. One of the images is formed by the visible and near infrared (VNIR) bands of the Advanced Spaceborne Thermal Emission and Reflection Radiometer sensor (ASTER) on board Terra satellite (Figure 1). The four bands of the IKONOS sensor (Figure 2) form the other image. Table 1 provides basic parameters of these images.

Table 1. Basic parameters of multispectral images.

	ASTER	IKONOS
Acquisition date	July 7, 2003	June 14, 2006
Pixel size (m^2)	15 · 15	4 · 4
Dimension (pixels)	500 x 500	1200 x 1200
Bands (μm)	1) 0.52-0.60 2) 0.63-0.69 3N) 0.76-0.86 3B) 0.76-0.86	1) 0.45-0.52 2) 0.52-0.60 3) 0.63-0.69 4) 0.76-0.90

The high density of streets, avenues and buildings of the city results in a large number of edges per unit area. Such edges are of varying shape and size. Therefore, the multiple edges formed by streets, avenues, causeways and building blocks are a good test for our method.

These images are not precisely ortho-rectified since no implications on our method arise. However, rectification with first-order polynomial equation was applied in order to relate pixel coordinates with geographic coordinates.

Methods

In a multispectral image, the information-content of edges varies through the bands. In order to extract the information of edges from the multispectral image, we require a transformation applicable to the image as a whole.

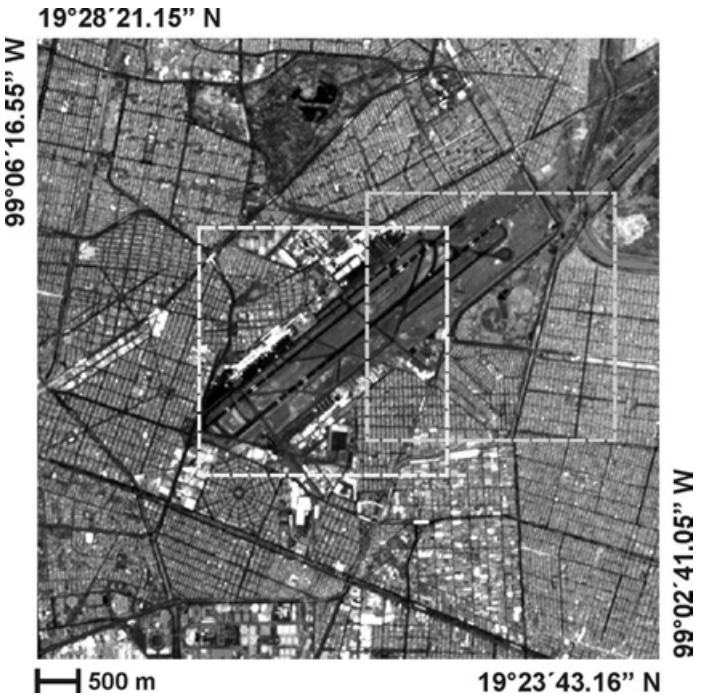

Figure 1. First principal component of ASTER image.

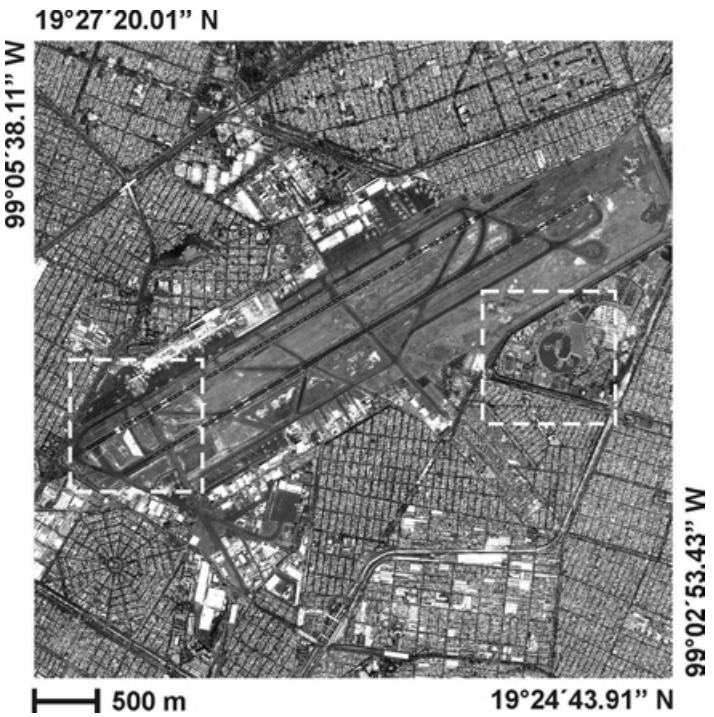

Figure 2. First principal component of IKONOS image.

In addition to the original bands, principal components analysis was performed on the two images. The first principal component of both images is used to apply widely used edge operators (Pratt, 2001; Bowyer *et al*., 2001). These operators are used for the sake of comparison with the methods developed in our work. The first principal component accumulates most of the variance of the images: 78.50% for the ASTER image, and 83.09% for the IKONOS image. Therefore, we applied widely used edge operators to the first principal component.

Vector field of a multispectral image

The modeling of an η-dimensional multispectral image as a vector field will be addressed in section 3.1 (Lira and Rodríguez, 2006). This field holds the same dimension as the original multispectral image. The field is composed by the set of pixels considered as η-dimensional vectors.

In Section 3.2, we determined maximum difference vectors in a moving window that systematically scan the entire image. This maximum difference produces an η-dimensional image where edges are enhanced.

In Section 3.3, we derived an η-dimensional Laplacian using Fourier transform. To do so, we first consider the Fourier transform of second partial derivates of an image (Bracewell, 2003). With this result, we produced the Laplacian of an image. Finally, we generalized the Laplacian for multispectral images composed of η-bands. A flow chart resumes our methods, from the modeling of a multispectral image as a vector field, to the enhancement of edges through the bands of the image (Figure 3)

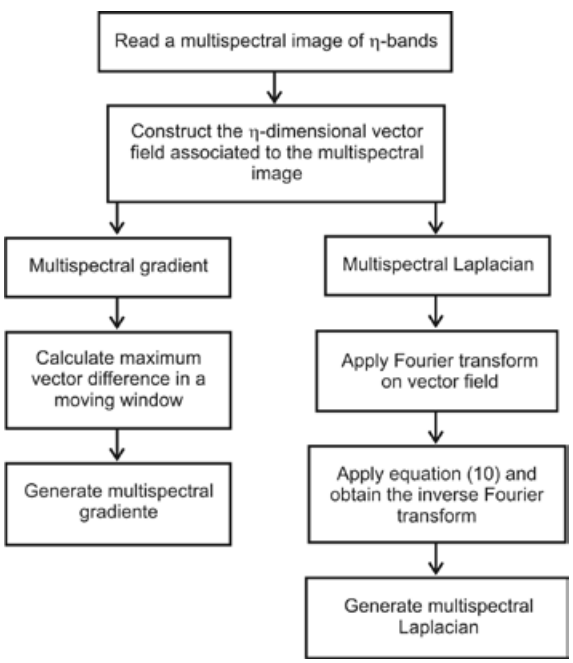

Let $L \equiv \{1, \ldots M\} \cdot \{1, \ldots N\}$ be a rectangular discrete lattice. This lattice is virtually overlaid on the scene. On each node of L, a resolution cell named the instantaneous field of view (IFOV) is located. For each IFOV, an η-dimensional vector $\{b_1,b_2, \ldots b_\eta\}$ is derived by means of a multispectral sensor set. The vector $\{b_1,b_2, \ldots b_\eta\}$ represents the average spectral properties of an IFOV of the scene. This vector is named a picture element (pixel) of a multi-spectral image. In other words, the IFOV is a physical area in the scene, while the pixel is the digital number (DN) in the image. Let the multi-spectral image $\mathbf{g} = \{g_i\}$ be formed by the group of pixels according to the following set $g_i = \{b_j(k,l)\}_i$, $\forall$ i. Where i $\in \mathbb{N}$ is the set $\{1,2, \ldots \eta\}$ representing the collection of bands of the multispectral image.

On the other hand, let X_i be the set

$$X_i \equiv \{X^i \,|\, X^i \in \mathbb{N},\ 0 \le x_i \le 2^m - 1\},\ \forall\ i \quad (1)$$

Where m =8 in most cases. The cartesian product $X^\eta = X_1 \times X_2 \times \ldots X\eta$ defines the set of the ordered η-tuple $(x_1,x_2, \ldots x_\eta)$. We equate $x_i = b_i$, therefore $(b_1,b_2, \ldots b_\eta)$ is an η-tuple in this cartesian coordinate system. To every η-tuple $(b_1,b_2, \ldots b_\eta)$, a vector **u** is associated: $\mathbf{u}(x_1,x_2, \ldots x_\eta) \Leftarrow (b_1,b_2, \ldots b_\eta)$.

The set of vectors $\{\mathbf{u}(x_1,x_2, \ldots x_\eta)\}$ is the result of the mapping of the multispectral image onto a vector field. We note that not every η-tuple $(x_1,x_2, \ldots x_\eta)$, has a vector associated to the vector field, and an *n*-tuple $(x_1,x_2, \ldots x_\eta)$ may have more than one vector associated to the vector field. Hence, the vector field associated with the multispectral image is the set of vectors $\mathbf{U} = \{\mathbf{u}(x_1,x_2, \ldots x_\eta)\}$.

Multispectral gradient

Once the multispectral image is modeled as a vector field, we may proceed to define a multispectral edge. Let v_c be a moving window that systematically scans, pixel by pixel, the whole image. The window v_c is of size 3×3 pixels. Let $D(\mathbf{g})$ be the domain of the image,

Figure 3. Schematic diagram for calculation of multispectral gradient and multispectral Laplacian.

thus the condition that $v_c \subset D(\mathbf{g})$ determines that the border pixels of the image cannot be processed.

Let the vector $\boldsymbol{p}_c$ be the central pixel of such window and let $\boldsymbol{p}_1, \boldsymbol{p}_2, \ldots \boldsymbol{p}_8$ be the neighboring pixels of $\boldsymbol{p}_c$. The set of pixels $\{\boldsymbol{p}_i\}$, i = 1, 2, . . . 8 is the 8-connected neighbor set of $\boldsymbol{p}_c$. We obtain the vector difference of the central pixel with all neighboring pixels of the window

$$\Delta \boldsymbol{p}_i = \boldsymbol{p}_c - \boldsymbol{p}_i, \ \forall \ i \in v_c \tag{2}$$

The vector of the window that makes the largest difference is written in an output multispectral image named **f**

$$\boldsymbol{p}_i \in \mathbf{f} : \underbrace{\max}_{i \in v_c} \left| \boldsymbol{p}_c - \boldsymbol{p}_i \right| \tag{3}$$

Equation (3) means that central pixel $\boldsymbol{p}_c$, in moving window, is replaced by neighboring pixel $\boldsymbol{p}_i$ with the largest Euclidean distance to the central pixel.

The vector difference is calculated employing the Euclidian distance

$$\left| \boldsymbol{p}_c - \boldsymbol{p}_i \right| = \sum_{j=1}^{\eta} (b_j^c - b_j^i)^2 \Bigg)^{1/2} \tag{4}$$

The image **f** contains the edge information across the bands of the original image **g**. Image **f** is dubbed the multispectral gradient (Figure 3).

Average of bands of output edge image **f** is calculated in order to concentrate the information on a single image. Principal components analysis may be applied as well to output image **f** to concentrate in the first component the edge content of the multispectral-edge image. We use the average of the output image bands.

Derivation of η-dimensional Laplacian

A Laplacian is widely used as an edge operator (Pratt, 2001). Nevertheless, actual Laplacian is applied to each separate band of a multispectral image. A multispectral Laplacian is needed to extract edge content from the ensemble of the bands as a whole.

We begin with the consideration of the Laplacian in continuous space, and then we write the result in discrete space. Let $g(x,y) \in \mathbb{R}^2$ be a function that describes a single band image where (x,y) are the coordinates of a pixel in this image. We initiate this step with the use of the equations

$$\mathcal{F}\left[\frac{\partial g^2(x,y)}{\partial x^2}\right] = -(2\pi)^2 \omega_x^2 G(\omega_x, \omega_y) \tag{5}$$

$$\mathcal{F}\left[\frac{\partial g^2(x,y)}{\partial y^2}\right] = -(2\pi)^2 \omega_y^2 G(\omega_x, \omega_y) \tag{6}$$

A detailed explanation on the derivation of equations (5) and (6) is provided in Lira (2010). In equations (5) and (6), $\mathcal{F}$ stands for Fourier transform, $G(\omega_x,\omega_y)$ is the Fourier transform of the image $g(x,y)$ and j is the complex number $\sqrt{-1}$. In equations (5) and (6), (x,y) are spatial coordinates in image domain, whereas (w_x, w_y) are spatial frequencies in Fourier domain.

From equations (5) and (6) we have the Fourier transform of the Laplacian

$$\mathcal{F}[\nabla^2 g(x,y)] = -(2\pi)^2 (\omega_x^2 + \omega_y^2) G(\omega_x, \omega_y) \tag{7}$$

Equation (7) is dubbed the scalar Laplacian.

On the grounds of results given by equation (7), we may generalize the Fourier transform of the Laplacian to *n*-dimensions. Let $\mathbf{f}(\mathbf{r}) \in \mathbb{R}^\eta$, be a vector valued function that describes a multispectral image formed by *n*-bands. The vector $\mathbf{f}(\mathbf{r}) = \{f_1(x,y), f_2(x,y), \ldots f_\eta(x,y)\}$ represents the values of a pixel through the bands, i.e., the image value at a pixel location $\mathbf{r} = (x,y) \in \mathbb{R}^\eta$. The function $\mathbf{f}(\mathbf{r})$ is a vector field that describes the multispectral image according to lineaments described in section 3.1 (Lira and Rodriguez, 2006). The Fourier transform of $\mathbf{f}(\mathbf{r})$ is then (Bracewell, 2003; Ebling and Scheuermann, 2005)

$$\mathbf{F}(\boldsymbol{\omega}) = \mathcal{F}[\mathbf{f}(\mathbf{r})] = \int_{-\infty}^{+\infty} \ldots \int_{-\infty}^{+\infty} \mathbf{f}(\mathbf{r}) \exp\{-2\pi j \mathbf{r} \cdot \boldsymbol{\omega}\} \, d\mathbf{r} \tag{8}$$

The Fourier transform of the vector field $\mathbf{f}(\mathbf{r})$ produces a vector valued function in Fourier space, namely, $\mathbf{F}(\omega) = \mathcal{F}[\mathbf{f}(\mathbf{r})]$. The vector $\mathbf{F}(\omega) = \{F_1(\omega_1, \omega_2), F_2(\omega_1, \omega_2), \ldots F_\eta(\omega_1, \omega_2)\}$, represents the spatial frequency content of the image at the location $\omega = (\omega_1,\omega_2)$. In $\mathbb{R}^\eta$, the coordinates in Fourier domain (ω_1, ω_2), and spatial domain (x, y), cover the same range,

$1 \le (x, w_1) \le M$ and $1 \le (y, \omega_2) \le N$, but their meaning is different: (x, y) represents spatial coordinates, while (ω_1, ω_2) represents spatial frequencies.

In discrete space $\mathbb{Z}^\eta$, the coordinates in Fourier domain $\boldsymbol{k} = (k_1, k_2)$, and spatial domain $\boldsymbol{q} = (m, n)$, cover the same range, $1 \le (m, k_1) \le M$ and $1 \le (n, k_2) \le N$. If $\mathbf{f}(\boldsymbol{q}) \in \mathbb{Z}^\eta$, where $(m, n; k_1, k_2) \in \mathbb{Z}$, then the discrete version of equation (8) is

$$\mathbf{F}(\boldsymbol{k}) = \mathcal{F}[\mathbf{f}(\boldsymbol{q})] = \sum_{i}^{\eta} \ldots \sum_{m}^{N} \mathbf{f}(\boldsymbol{q}) \exp\{-2\pi j \boldsymbol{q} \cdot \boldsymbol{k}\} \quad (9)$$

Where $\mathbf{f}(\boldsymbol{q}) = \{f_1(m, n), f_2(m, n), \ldots f_\eta(m, n)\}$ and $\mathbf{F}(\boldsymbol{k}) = \{F_1(k_1, k_2), F_2(k_1, k_2), \ldots F_\eta(k_1, k_2)\}$. The Laplacian in $\mathbb{Z}^\eta$ of the vector field $\mathbf{f}(\mathbf{q})$ is therefore

$$\mathcal{F}[\nabla^2 \mathbf{f}(\boldsymbol{q})] = -(2\pi)^2 |\boldsymbol{k}|^2 \mathbf{F}(\boldsymbol{k}) \quad (10)$$

Where $\mathbf{F}(\boldsymbol{k}) = \mathcal{F}[\mathbf{f}(\mathbf{q})]$. This equation can be applied to a multispectral image to derive edge content through the bands. Note that equation (7) is a particular case of equation (10). Equation (10) is dubbed the multispectral Laplacian.

To calculate this multispectral Laplacian, we first obtain the Fourier transform of the vector field associated to the image to produce $\mathbf{F}(\boldsymbol{k})$. In Fourier space, we multiply the result by $-(2\pi)^2 |\boldsymbol{k}|^2$ and apply the inverse Fourier transform to obtain the multispectral Laplacian (Figure 3).

Evaluation of edges

The criteria to evaluate the edge enhancement resulting from our methods and from widely known edge operators are divided in qualitative and quantitative. The edges produced by the urban network of streets, avenues, buildings, idle lots and parks occur at random directions in the images. Due to this randomness, a profile of pixel values along any direction is representative of the edge content of the images. We considered pixel values profiles along several directions. We analyzed such profiles for widely known edge operators and for outputs of our methods. We present the plots of two profiles for each sensor, and we include two graphs that condense the behavior of ten profiles for each sensor: ASTER and IKONOS. In total, we analyzed twenty profiles. From these plots, we derive a qualitative and quantitative evaluation as described below. Black dots in figures 5, 6, 7, and 8 indicate the lines where the plots were extracted. Figures 11, 12, 13, and 14 indicate the line, column and angle of the location of profiles.

Qualitative evaluation

We display in a high-resolution monitor the edge enhanced images. We display as well the first principal component of both images. A detailed visual inspection is carried out. On the grounds of previously published work on qualitative image evaluation (Escalante-Ramirez and Lira, 1996), each edge-enhanced image was rated according to the following qualitative criteria: general quality, sharpness, contrast, and noisiness. In addition, we evaluated the number of gray levels and definition of edges. Since the first principal component of the images accumulates most of the variance, we compare the edge enhancement with this component. The aim of this comparison is to evaluate, according to the above criteria, the degree of edge enhancement with respect to the original edge information content of the images.

Quantitative evaluation

We use several indicators to perform a quantitative evaluation (Figure 4): Slope – the more steepness the better the definition of the slope of an edge. Widening – a width as close as possible to the original edge the better. Spatial location – the closest of the enhanced edge to the original location the better. Contrast – the highest the contrast the better.

A computer code was developed for quantitative evaluation. An image is displayed in a high resolution monitor. With the help of a cursor, a line of the image is selected. The profile of pixel values is shown in a plot. A profile is selected that contains one of the edge models given in figure 4. A spline is obtained for the selected edge-model. From such spline, the parameters indicated in the models of figure 4 are calculated. There are many types of edges in the images. To obtain a coherent quantitative evaluation of edges, we considered three types that occur frequently in the images. Figure 4 shows a schematic diagram of such types where the above indicators are depicted. We performed such measurement for an ensemble of edges. Figure 4(c) shows a profile that occurs only in Laplacian and Kirsch operators. The computation of indicators is as follows.

Slope – we measure the slope as the angle of the borders of an edge with respect to the

vertical direction. Widening – we measure the maximum width of an edge in pixels. Spatial location – we identify the spatial coordinate of the center of an edge. Contrast – we measure the contrast as the difference between the maximum value and the minimum value of an edge.

In order to complement our evaluation of edge enhancement we developed a computer code for the Canny and Cumani operators (Koschan and Abidi, 2005; Evans and Liu, 2006). The computer code was designed following the method explained in the article by Koschan and Abidi (2005). Two RGB false color composites were produced using the first three bands of ASTER and IKONOS images. Upon these images, the Canny and Cumani operators were applied. Such operators consist of a two-step procedure. The first step is the enhancement of the edges; the second step is the detection of the edges by means of a threshold operation. We present results only for the enhancement of the edges. Both operators, Canny and Cumani, carry a number of parameters that require a determination by heuristic procedures. There are no analytical methods to estimate such parameters in an optimal design. Instead, our methods are parameter-free.

Results and discussion

Results

The necessary algorithms to apply the methods described in previous section were developed using Delphi language running under Windows 7 in a PC. Several edge products are presented in our work. They are organized in two groups: (a) edges from widely used edge operators, (b) edges derived from the methods developed in our work. These groups are analyzed. In order to facilitate the comparison of these results,

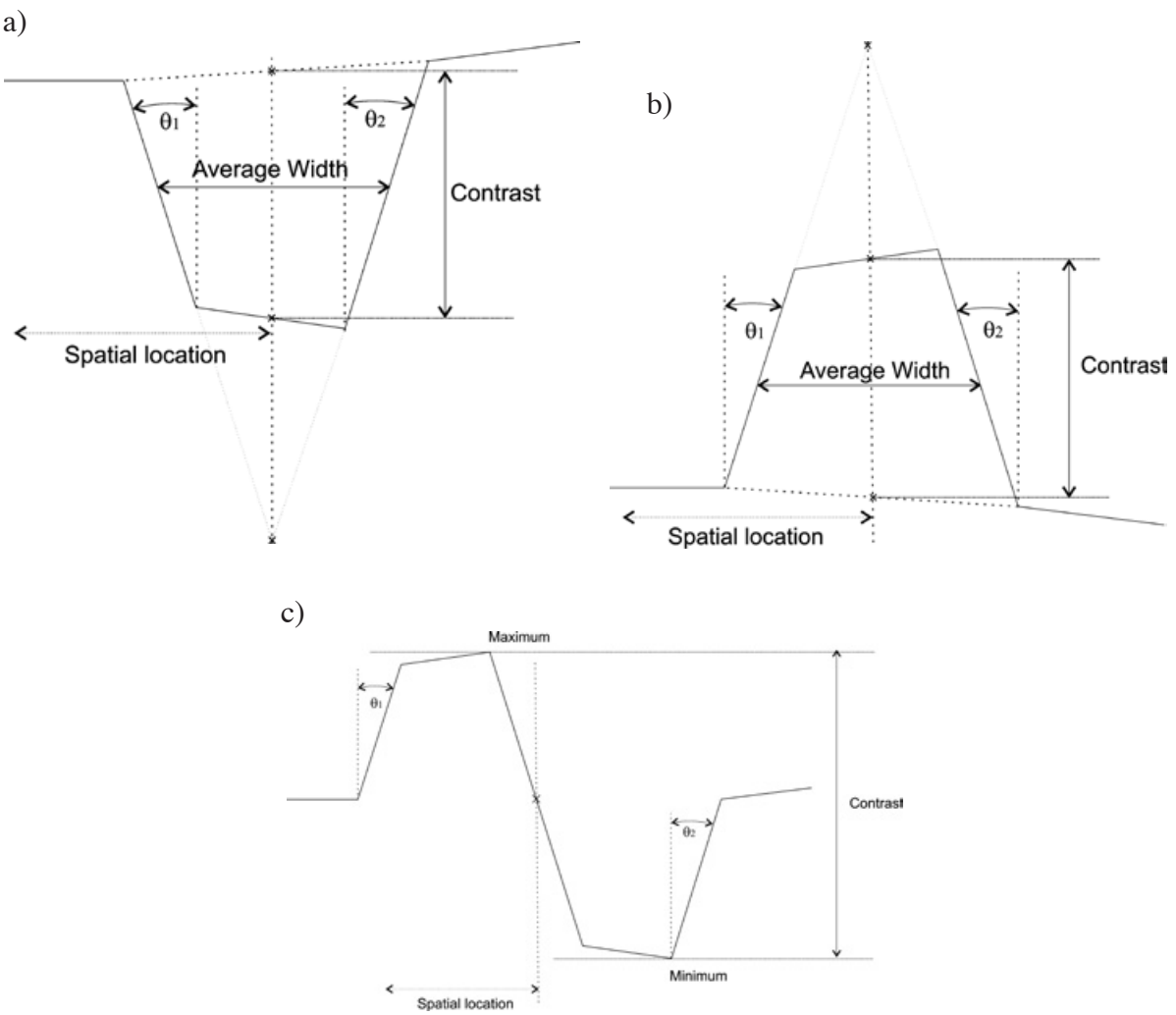

Figure 4. Schematic diagram of an edge and parameters of evaluation.

four mosaics of selected regions of the images were prepared. These mosaics include the multispectral edges derived from our method and results from the above mentioned edge operators. Boxes on figures 1 and 2 show the areas from which these mosaics were extracted. The mosaic prepared from boxes on the left of figures 1 and 2 are dubbed mosaic A, and those on the right are dubbed mosaic B.

A set of profiles are produced to evaluate the performance of edge enhancement of the methods compared in this research. Profiles are compared. A profile from the first principal component of the original image is compared against the profiles of all edge enhancement methods considered in our work.

The mosaics are used to perform the qualitative evaluation as discussed in previous section. The profiles are used to develop the quantitative evaluation as discussed in previous section. The above-mentioned groups show the following results.

1) Edges from vector differences in a moving window (multispectral gradient).

As explained in Section 3.1, a multispectral edge image is obtained. This multispectral image carries the same number of bands as the input image. The average of the bands of such multispectral edge image was used for quantitative evaluation. Figures 5 and 6 shows the enhancement of edges of the ASTER image resulting from such procedure. Figures 7 and 8 depict the enhancement of edges of the IKONOS image. For visual purposes, a linear saturation enhancement was applied to figures 5 - 8. The quantitative evaluation was performed upon original results.

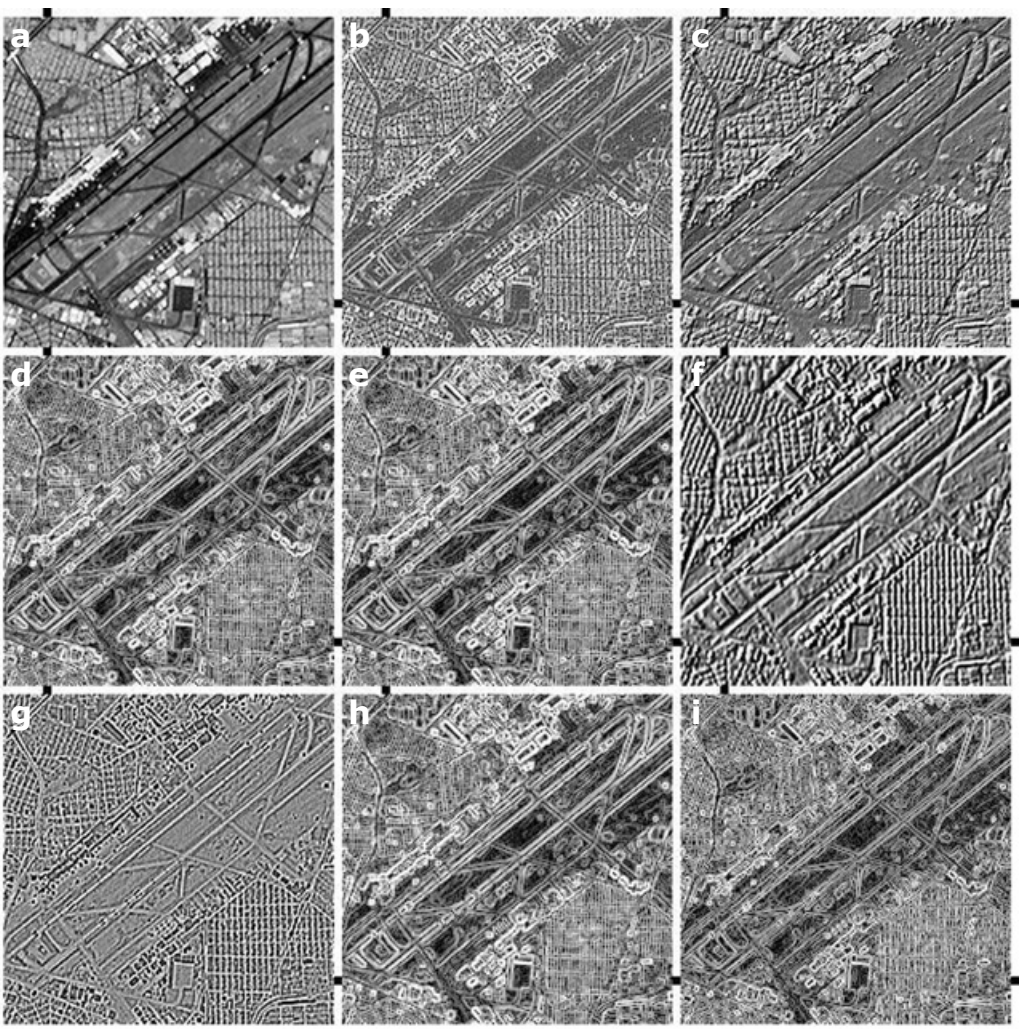

Figure 5. Mosaic ASTER A. (a) PC_1, (b) average of multispectral gradient, (c) multispectral Laplacian, (d) Sobel on PC_1, (e) Frei-Chen on PC_1, (f) Kirsch on PC_1, (g) scalar Laplacian on PC_1, (h) Prewitt on PC_1, (i) Roberts on PC_1.

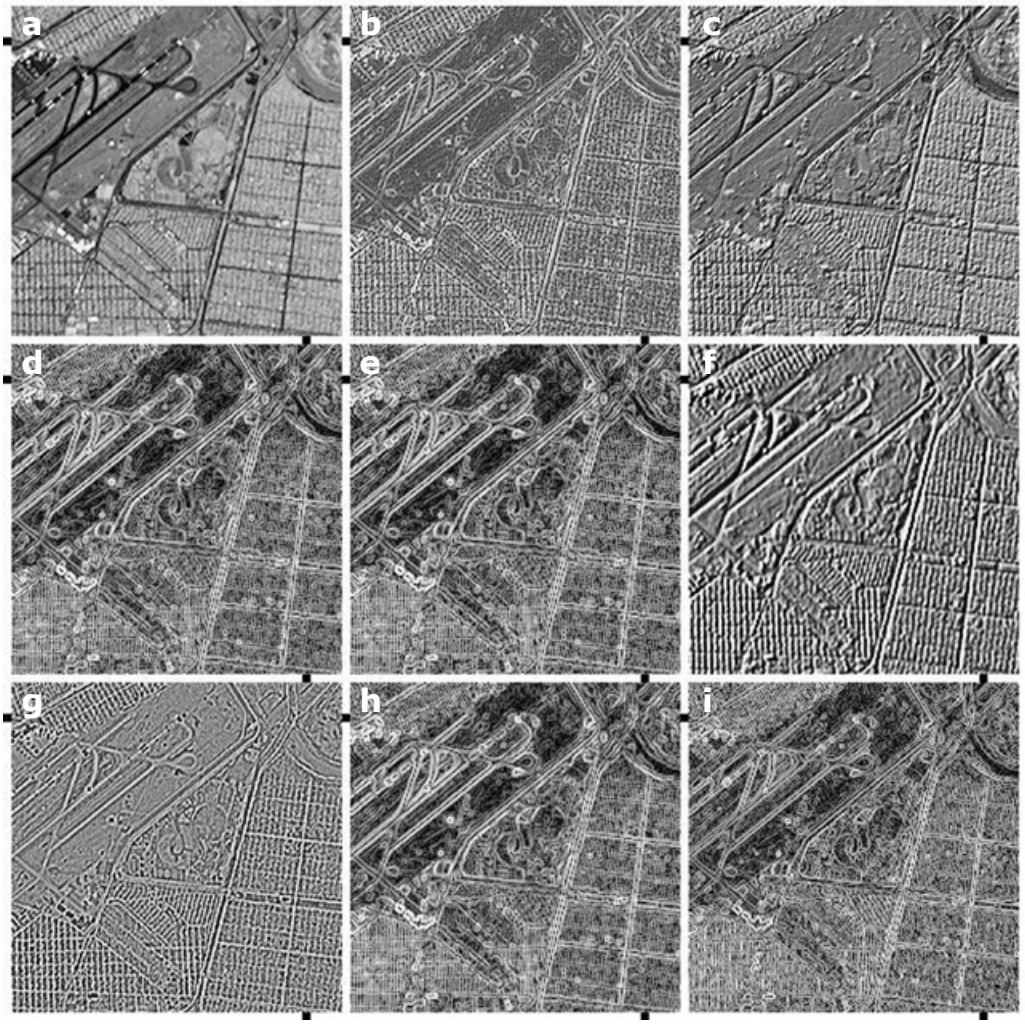

Figure 6. Mosaic ASTER B (a) PC_1, (b) average of multispectral gradient, (c) multispectral Laplacian, (d) Sobel on PC_1, (e) Frei-Chen on PC_1, (f) Kirsch on PC_1, (g) scalar Laplacian on PC_1, (h) Prewitt on PC_1, (i) Roberts on PC_1.

2) Edges from the multispectral Laplacian (Section 3.2).

The multispectral Laplacian derived from equation (10) was applied to both images, ASTER (figures 5 and 6) and IKONOS (figures 7 and 8).

3) Edges from the first principal component of images.

The following edge operators were applied to the first principal component of ASTER and IKONOS images: Sobel, Frei-Chen, Kirsch, scalar Laplacian, Prewitt and Roberts. Results are shown in figures 5 and 6 for ASTER image, and figures 7 and 8 for IKONOS image.

4) Edges from color operators

Two mosaics were prepared to show the results of Canny and Cumani operators (Figure 9). We applied a histogram saturation transformation to the images of the mosaics for visual appreciation purposes. An inspection of results shows an enhancement similar to the Sobel operator (Figure 6). There are two limitations to the Canny and Cumani operators. The first one is that they carry a number of parameters that need to be defined by experimental procedure. The second one is that they work for RGB color images only; no generalization exists for an arbitrary number of bands of a multispectral image.

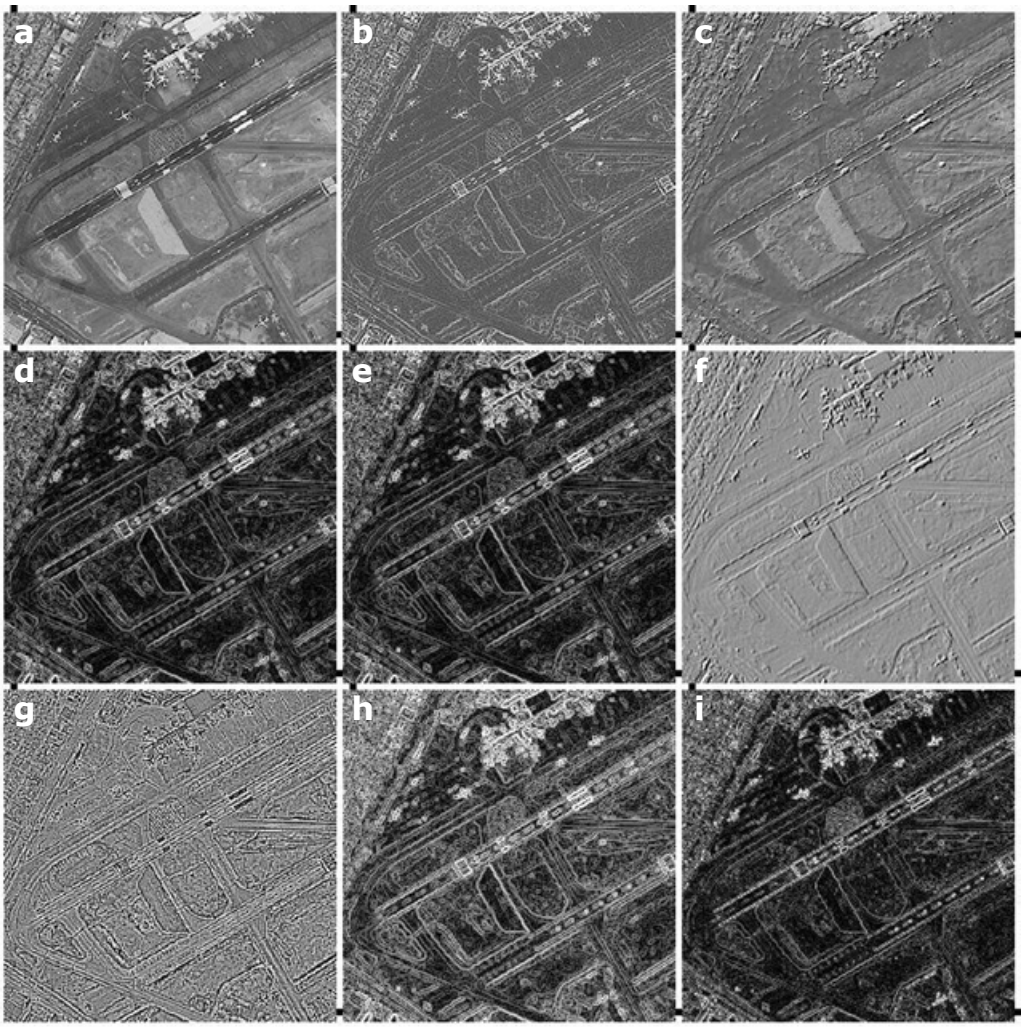

Figure 7. Mosaic IKONOS A. (a) PC_1, (b) average of multispectral gradient, (c) multispectral Laplacian, (d) Sobel on PC_1, (e) Frei-Chen on PC_1, (f) Kirsch on PC_1, (g) scalar Laplacian on PC_1, (h) Prewitt on PC_1, (i) Roberts on PC_1.

The profiles for all edge enhancement methods are shown in figures 11 and 12 for ASTER mosaics and figures 13 and 14 for IKONOS mosaics.

In order to complement the procedure of profile extraction (Figures 11 - 14), a mosaic of strip-images was prepared (Figure 10). The strip consist of a sub-image of 21 pixels long by 11 pixels wide. The dots indicate the line of pixels related to the profile. The mosaic is formed by 6 strips, one for each image of figure 6. We present one mosaic of strips.

5) The indicators (Figure 4) described in quantitative evaluation were measured for twenty profiles: ten for ASTER image and ten for IKONOS image. The measurement was carried out for the whole ensemble of edge operators considered in our research. Such measurement includes the first principal component of ASTER and IKONOS images. The value of the indicators was compared with the value of the original profile extracted from the first principal component. This comparison was calculated in relative error percentage and condenses in a single graph. The relative error percentage is the difference of an indicator from an edge enhanced image (Ie) minus the indicator from the first principal component (Icp) normalized by (Icp). Figure 15 shows the graph that summarizes the quantitative evaluation of the profiles. For ASTER image, figure 15(a) depicts the relative error percentage with respect to the original profile in first principal component.

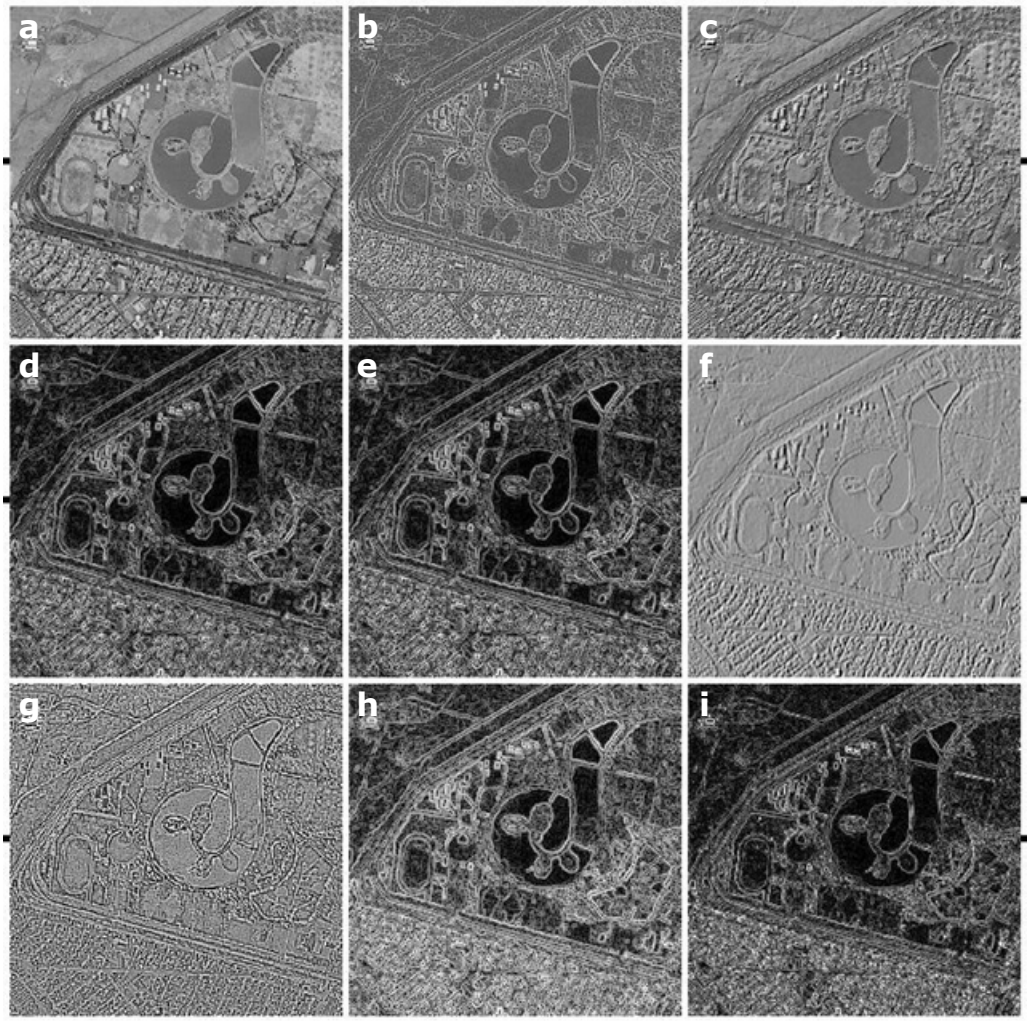

Figure 8. Mosaic IKONOS B. (a) PC_1, (b) average of multispectral gradient, (c) multispectral Laplacian, (d) Sobel on PC_1, (e) Frei-Chen on PC_1, (f) Kirsch on PC_1, (g) scalar Laplacian on PC_1, (h) Prewitt on PC_1, (i) Roberts on PC_1.

Figure 15(b) show results for IKONOS image. Angles q_1 and q_2 are not included in figure 15 for multispectral Laplacian and for Kirsch operators since, as explained above, the profile of figure 4(c) does not occur in the original image. Such operators introduce an inversion of contrast described in figure 4(c). None the less, the profile-type of figure 4(c) was compared among multispectral Laplacian and Kirsh operators. The contrast for all operators is presented in figure 16 for both sensors.

Discussion

Our discussion is divided in qualitative and quantitative evaluation as described in Section 3.4. The next two sections provide detailed description of such evaluation.

Qualitative discussion

A visual inspection of results, using the qualitative criteria described in Section 3.3, produces higher rating for our methods in comparison with any other edge-enhancement method considered in our research. For such inspection, we employed figures 5 to 8. In particular, and on the grounds of such rating, we may list the following evaluation

(a) Edges from Sobel, Frei-Chen, Prewitt and Roberts operators are widened for both images. The images from these operators appear unsharpened. The contrast is high and has a noisy appearance. Thin lines, points and linear objects are blurred or obliterated.

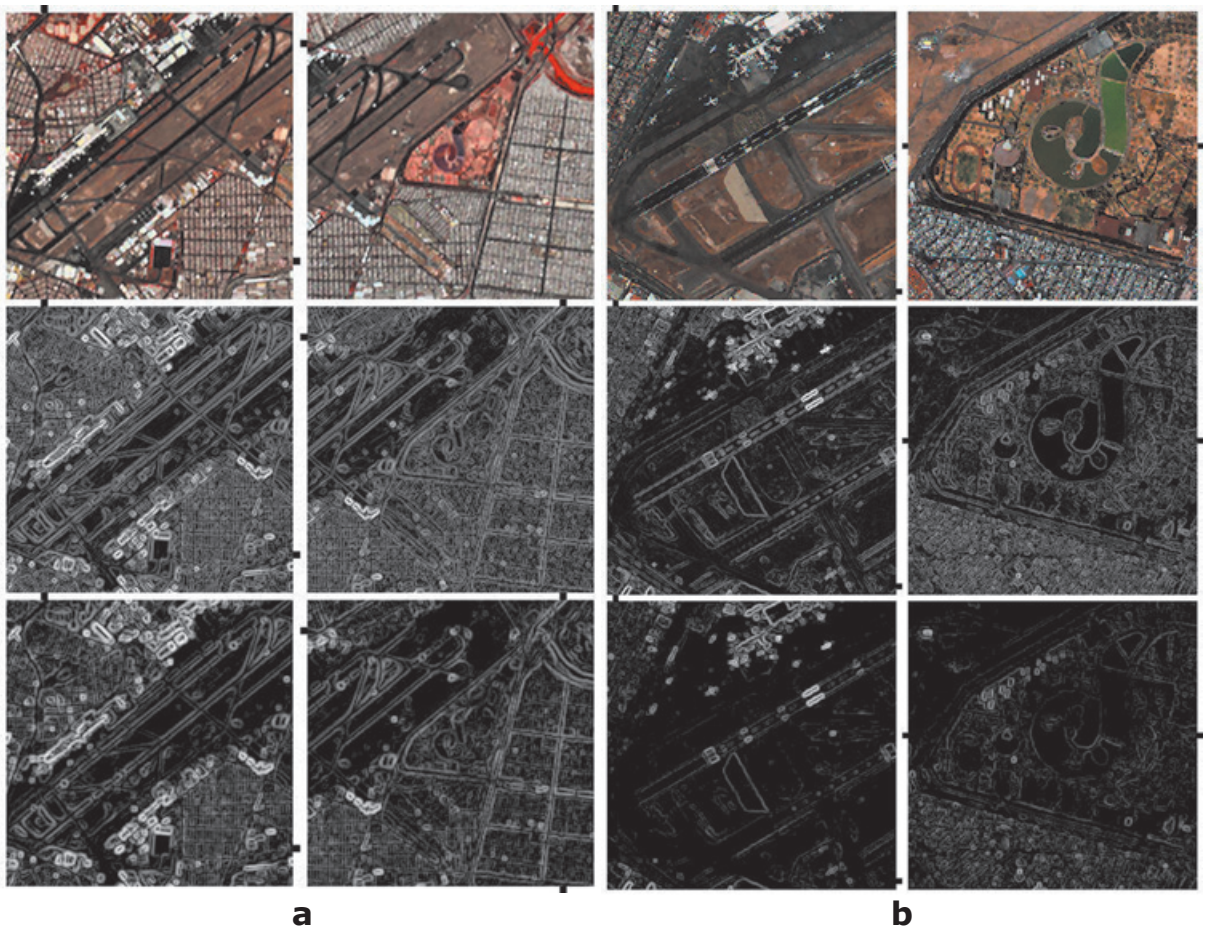

Figure 9. (a) - First row, RGB color composite of the first three bands of ASTER image. Second row, edge enhancement from Canny operator with σ = 0.5, window size = 3 x 3. Third row, edge enhacement from Cumani operator with σ = 0.5, threshold = 20.0. (b) - First row, RGB color composite of the first three bands of IKONOS image. Second row, edge enhancement from Canny operator with σ = 0.5, window size = 3 x 3. Third row, edge enhacement from Cumani operator with σ = 0.5, threshold = 20.0.

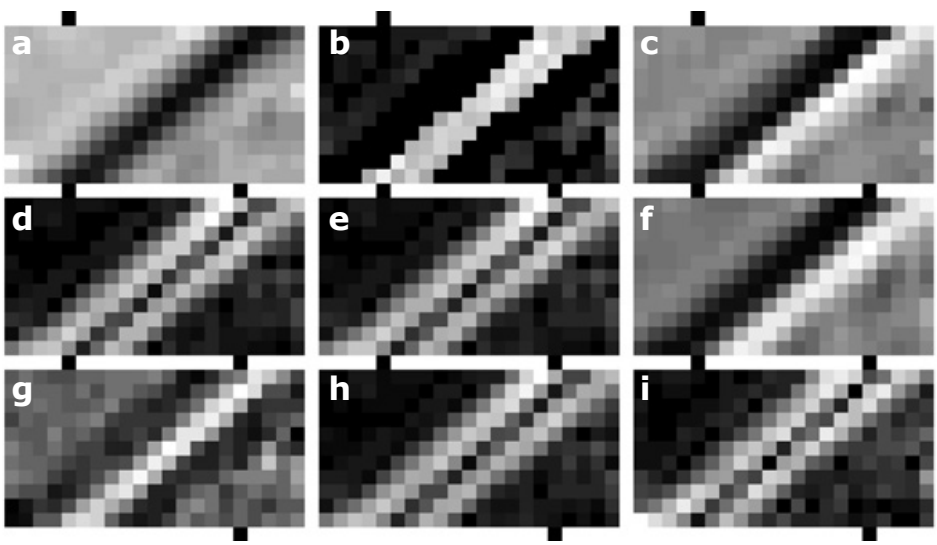

Figure 10. Mosaic of strips from line 91, column 118 and angle 135° from ASTER image (see Figure 11). (a) PC_1, (b) average of multispectral gradient, (c) multispectral Laplacian, (d) Sobel on PC_1, (e) Frei-Chen on PC_1, (f) Kirsch on PC_1, (g) scalar Laplacian on PC_1, (h) Prewitt on PC_1, (i) Roberts on PC_1.

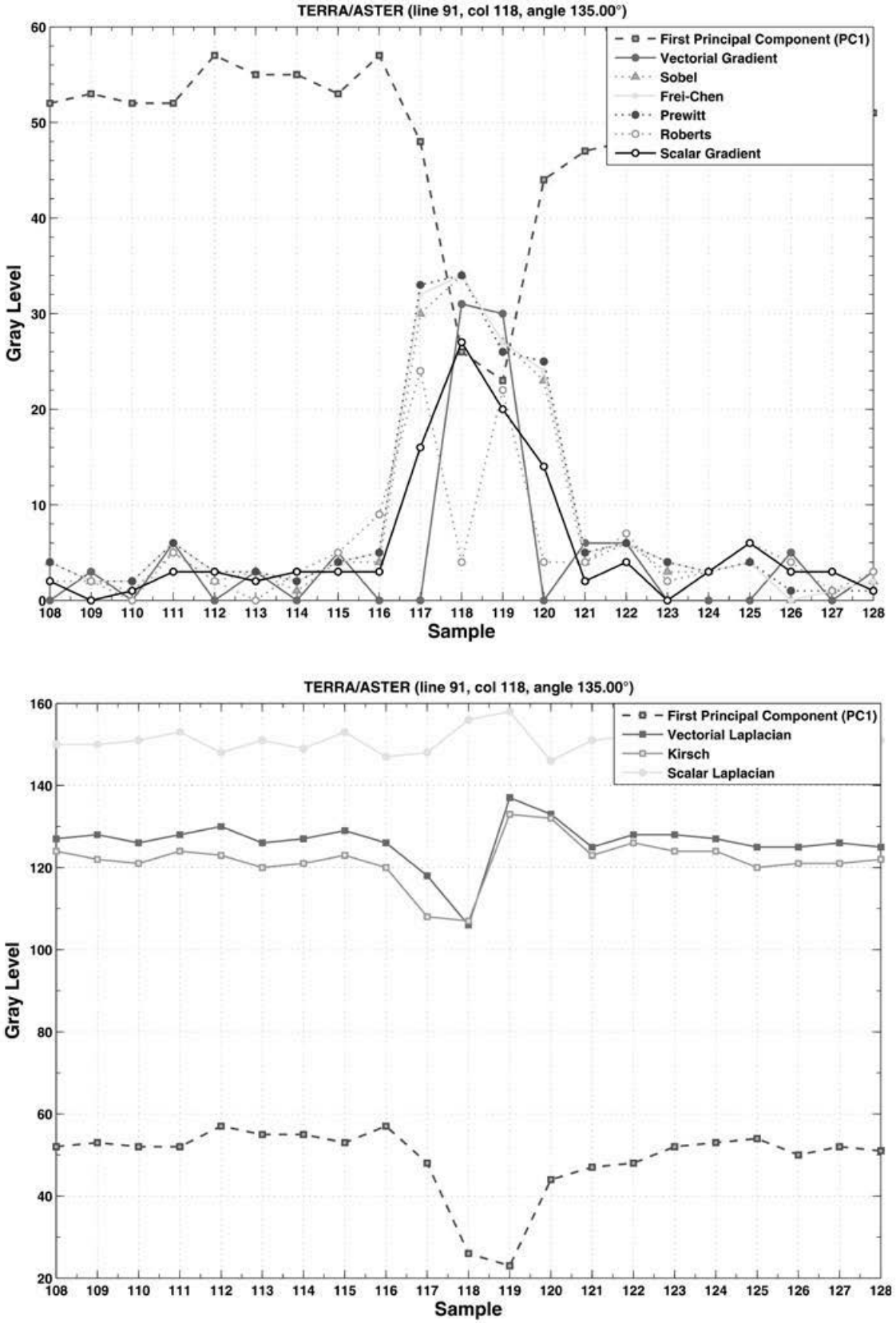

Figure 11. Profiles ASTER. Comparison of profiles of an edge located on line 91, column 118 and angle 135° of mosaic A. Dots on mosaic A of figure 5 indicate the direction of this line.

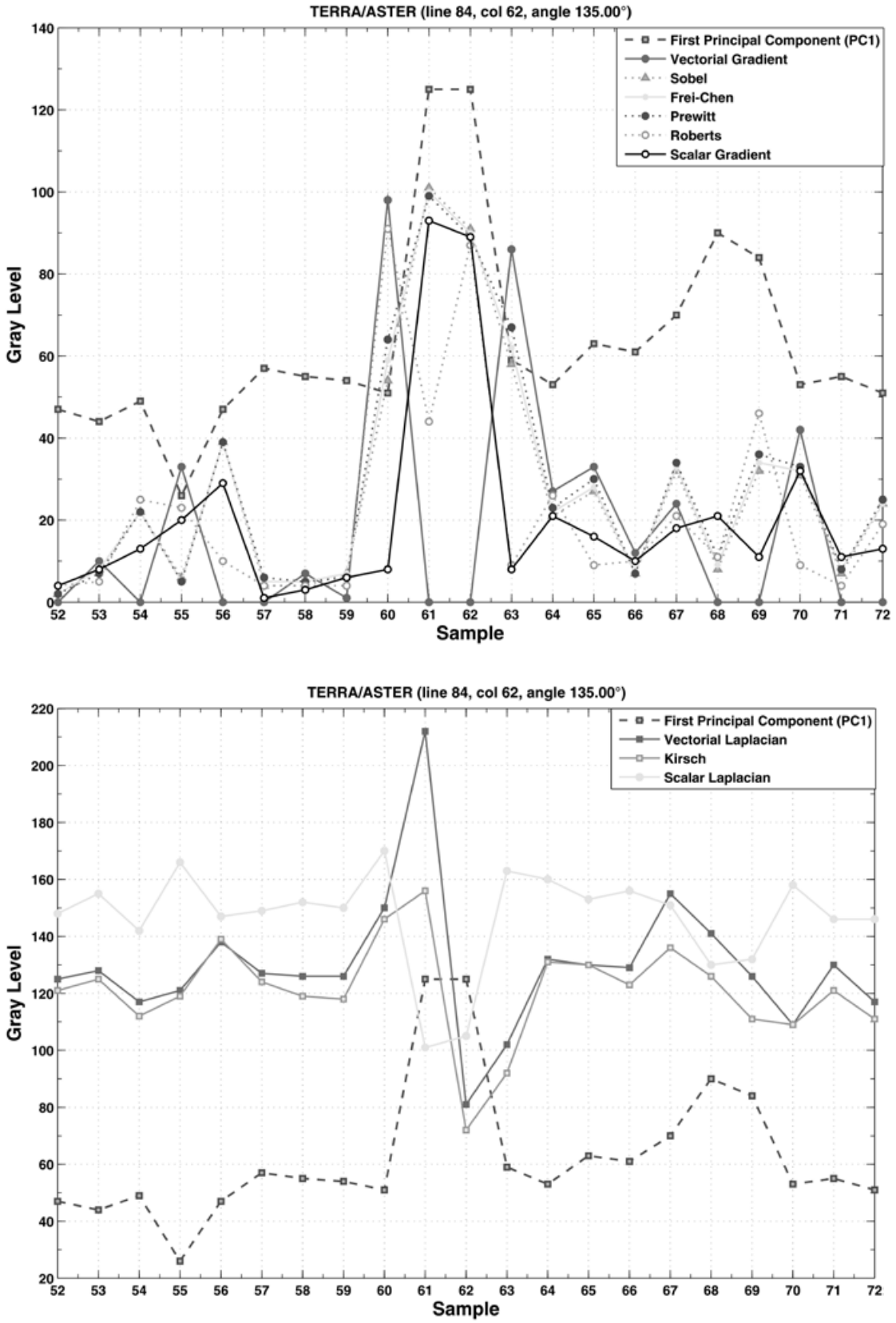

Figure 12. Profiles ASTER. Comparison of profiles of an edge located on line 84, column 62 and angle135° of mosaic B. Dots on mosaic B of figure 6 indicate the direction of this line.

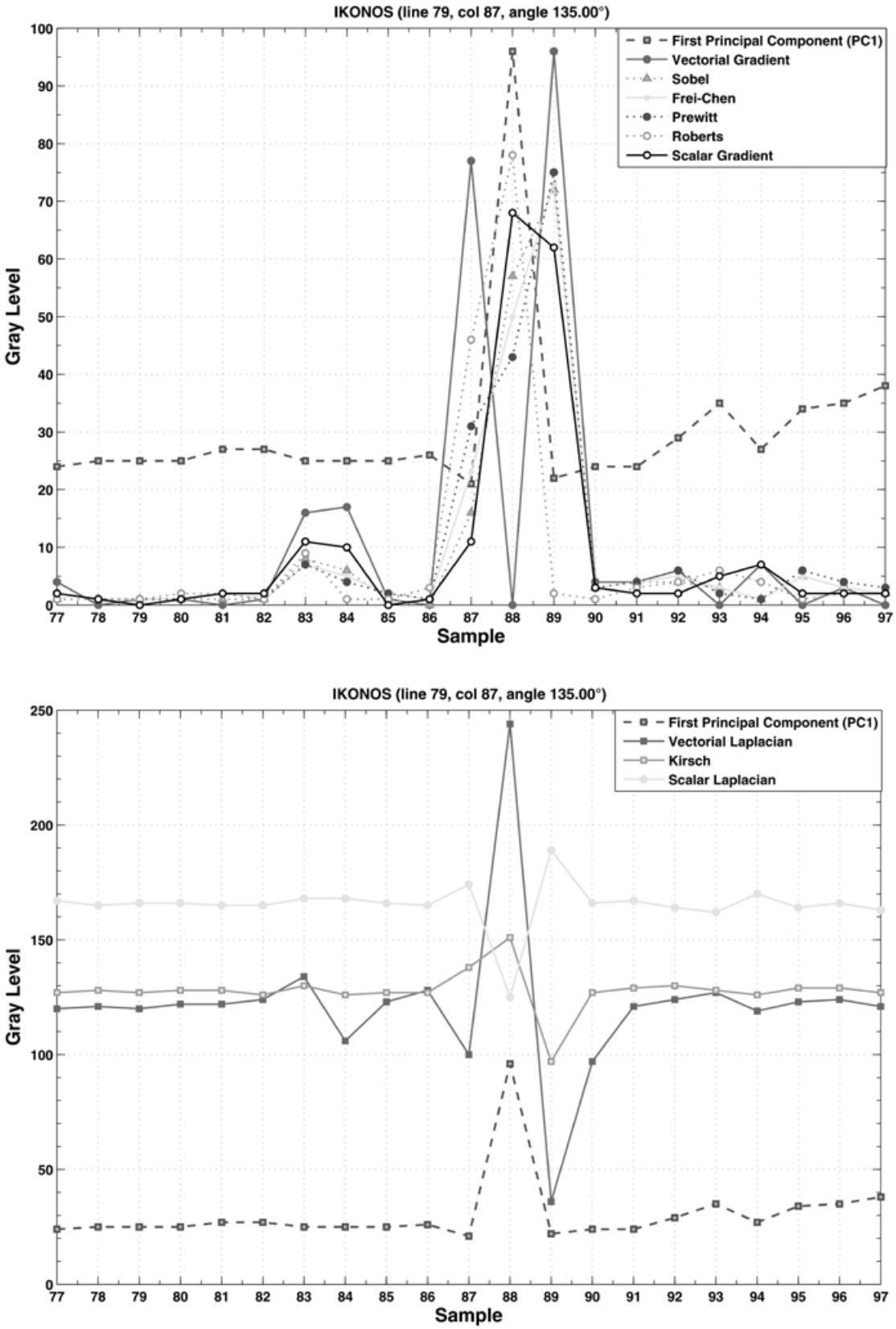

Figure 13. Profiles IKONOS. Comparison of profiles of an edge located on line 79, column 87 and angle 135° of mosaic A. Dots on mosaic A of figure 7 indicate the direction of this line.

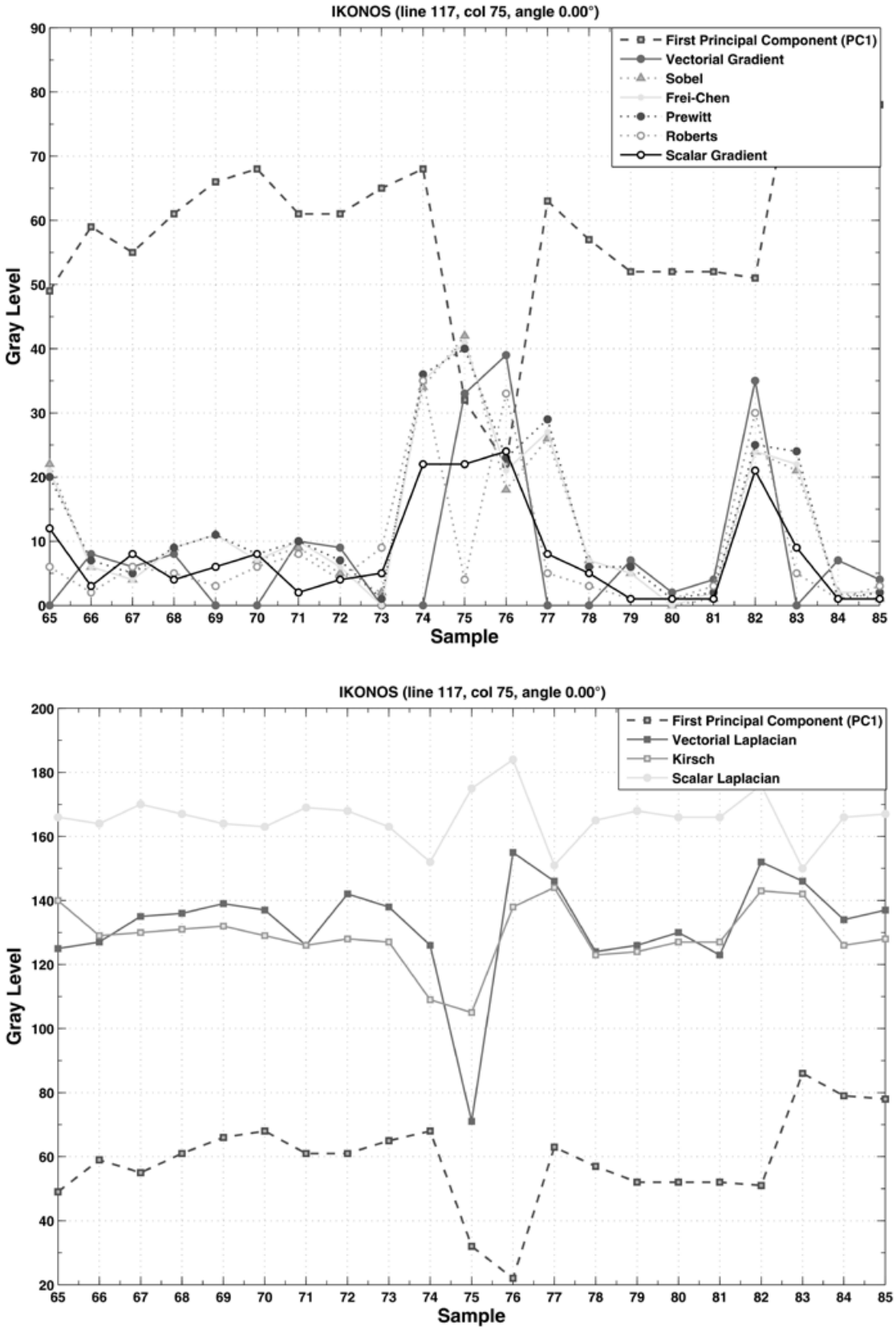

Figure 14. Profiles IKONOS. Comparison of profiles of an edge located on line 117, column 75 and angle 0° of mosaic A. Dots on mosaic B of figure 8 indicate the direction of this line.

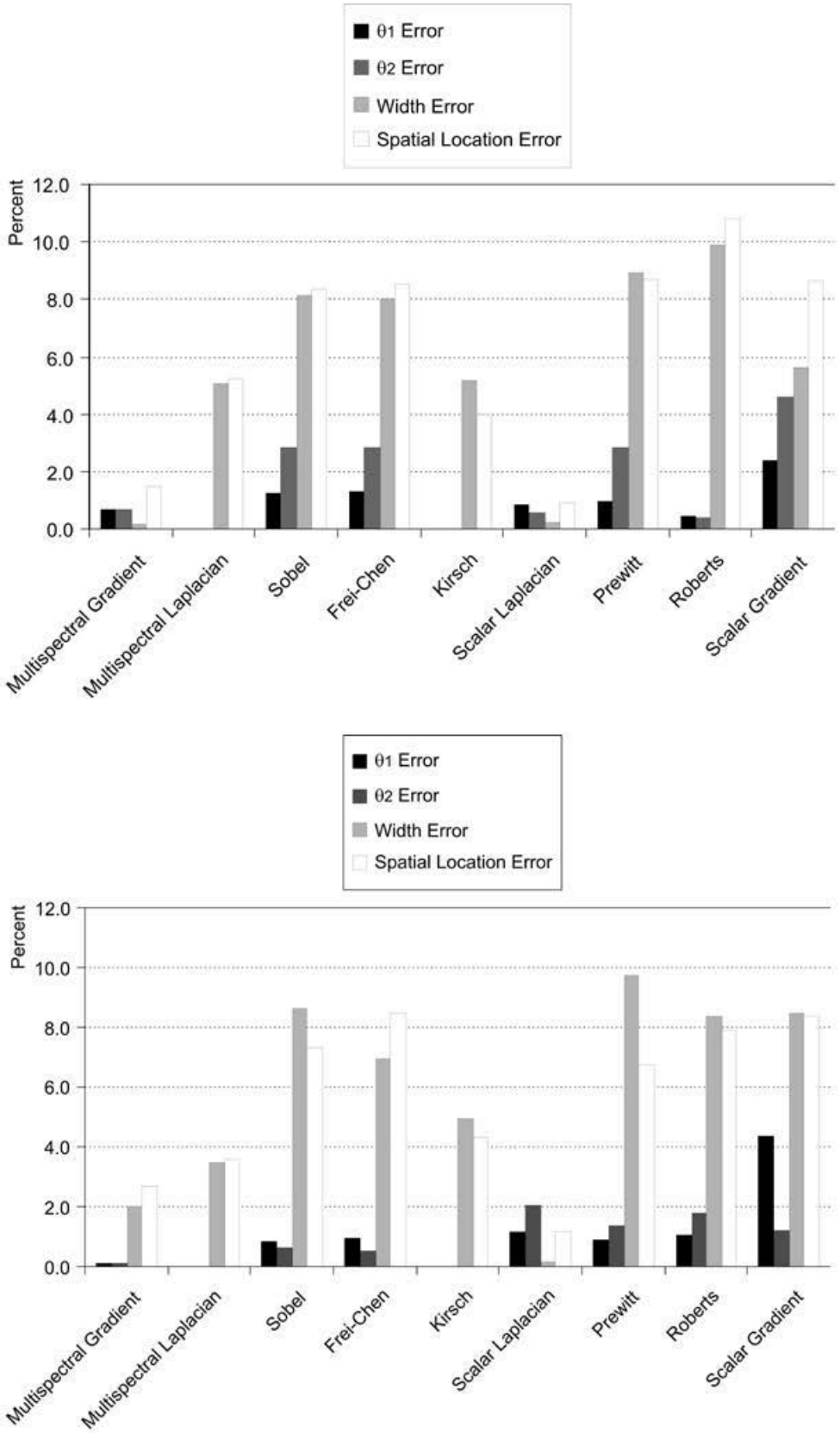

Figure 15. Relative error of ASTER profiles (a) and IKONOS profiles (b).

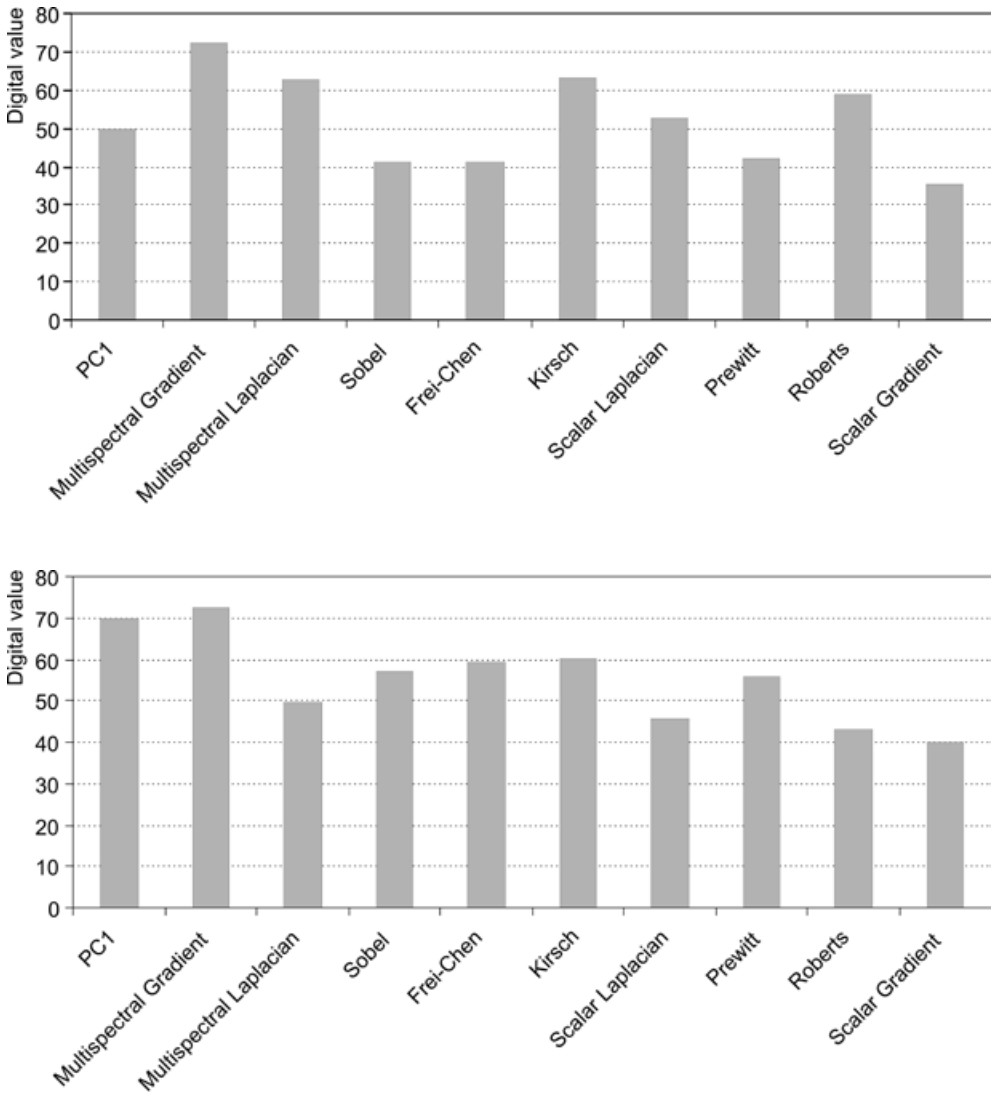

Figure 16. Contrast for ASTER profiles (a) and IKONOS profiles (b).

(b) Edges from the Kirsch operator show a relief-like appearance of urban buildings structure. The relief-like appearance is derived from the second derivative involved in the definition of this operator. Results look somewhat unsharpened and contrast is relatively small. There is no noisy appearance. Thin edges, points and linear objects are blurred.

(c) Edges from the scalar Laplacian operator are less widened than other operators. Results are sharp, thin edges, points and linear objects are preserved. However the contrast is low. No-noisy appearance is observed.

(d) The average of the bands of the image resulting from the multispectral gradient show sharp edges with good contrast. The contrast is higher than the scalar gradient, details such as thin lines and points are preserved. No noisy appearance is observed.

(e) The edge image resulting from the multispectral Laplacian show a relief-like appearance with better definition and similar than the Kirsch operator. The relief appearance of the multispectral Laplacian is sharpening with better preservation of fine details than the scalar Laplacian. The contrast is high and edges are sharp. No noise is observed.

(f) The sharpness of edges, the contrast, the noisiness appearance, and general quality of multispectral gradient and multispectral Laplacian are better than the edge operators compared in our work (Figure 15).

Quantitative discussion

As shown in figures 5 - 8, the dots on the border of the mosaics indicate the lines were pixel values profiles are extracted. These lines were selected to include sharp edges such as the lines of the landing fields of the airport and abrupt change of pixel values due to constructions or particular features with high contrast. The profiles extracted from the first principal component are compared to the profiles extracted form edge enhancement images. Many profiles were inspected at random. A selection of profiles was performed when they contained at least one of the edge-models of figure 4. We measured the above-described indicators (Figure 4) for twenty selected edge profiles: those with the best definition. From such measurements, we derived a list of conclusions.

Profiles of selected lines of the ASTER and IKONOS image-mosaics show the following:

(1) Sobel, Frei-Chen and Roberts operators wide and smooth the profiles of the original edges of the images.

(2) Kirsch and Prewitt operators wide and smooth the profiles but in a less degree than Sobel, Frei-Chen and Roberts operators.

(3) The relief-like appearance of the Kirsch images is due to the contrast inversion of some edges of the original profile.

(4) The scalar Laplacian operator does not wide nor smoothes the edges but reduces the contrast of the edges.

(5) The multispectral gradient and the multispectral Laplacian do not wide nor smooth the edges, and in addition to this, increase the contrast of the edges.

(6) The multispectral gradient and the multispectral Laplacian show good contrast of the enhanced edges.

(7) The spatial location error is highest for Roberts operator. The least error is for the scalar Laplacian.

(8) The steepness of the enhanced edges is less than the original edges for those operators that smooth and wide the edges.

(9) Overall, the multispectral gradient and the multispectral Laplacian show good conditions of contrast, steepness, spatial location and definition of edges with respect to the other operators.

Possible applications for multispectral edge enhancement are: identification of linear feature for geologic environments, identification of ancient highways in archeological studies, delineation of coastlines, studies of urban structures, delineation of water bodies and studies of coastal current patterns.

Conclusions

Two methods to extract edges from multispectral images are designed and discussed in this research. Such methods require the modeling of the original multispectral image as a vector field. Upon this vector field, we applied two vector operators to extract the edge content originally distributed through the bands of the images. These methods are parameter-free. A qualitative and quantitative evaluation show that our methods perform better than widely used edge enhancement procedures. The basic reason for this is that our methods extract the edge-content distributed through the original bands of a multispectral image. Our methods are not computing demanding, we use a fast Fourier transform to calculate the multispectral Laplacian. The calculation of the multispectral gradient is fast since it involves vector differences in a moving window. On a PC under Windows 7, the computing time for a 2000 ´ 2000 pixels multispectral image with 6 bands does not exceed three minutes. Our methods work for multispectral images with any number of bands, the limit is set by the available memory. A test on hyperspectral images is not yet performed.

References

Bigand A., Bouwmans T., Dubus J.P., 2001, Extraction of line segments from fuzzy images, *Pattern Recognition Letters*, 22**,** 13, 1405 – 1418.

Bowyer K., Kranenburg C., Doughert S., 2001, Edge detector evaluation using empirical ROC curves, *Computer Vision and Image Understanding*, 84**,** 1, 77 – 103.

Bracewell R.N., 2003, *Fourier Analysis and Imaging*, Kluwer Academic, New York.

Chen X., Chen H., 2010, A novel color edge detection algorithm in RGB color space,

IEEE 10th International Conference on Signal Processing, Beijin, China, pp. 793 - 796.

Chu J., Miao J., Zhang G., Wang L., 2013, Edge and corner detection by color invariants, *Optics and Laser Technology*, 45, 756 - 762.

Ebling J., Scheuermann J., 2005, Clifford Fourier transform on vector fields, *IEEE Transactions on Visualization and Computer Graphics*, 11, 469 – 479.

Escalante-Ramírez B., Lira J., 1996, Performance-oriented analysis and evaluation of modern adaptive speckle reduction techniques in SAR images, *Proceedings*, *SPIE's Visual Information Processing V*, Orlando, Florida, 2753, pp. 18-27.

Evans A.N., Liu X.U., 2006, A morphological gradient approach to color edge detection, *IEEE Transactions on Image Processing*, 15, 1454 - 1463.

Fan J.P., Aref W.G., Hacid H.S., EL Maguimid A.K., 2001, An improved automatic isotropic color edge detection techniques, *Pattern Recognition Letters*, 22, 13, 1419 – 1429.

Gao C.B., Zhou J.L., Hu J.R., Lang F.N., 2011, Edge detection of colour image based on quaternion fractional differential, *IET Image Processing*, 5, 261 - 272.

Koschan A., Abidi M., 2005, Detection and classification of edges in color images, *IEEE Signal Processing*, 22, 1, 64 – 73.

Li G.D., Min L.Q., Zang H.Y., 2008, Color edge detections based on Cellular Neural Network, *International Journal of Bifurcation and Chaos*, 18, 4, 1231 – 1242.

Lira J., Rodríguez A., 2006, A Divergence Operator to Quantify Texture From Multispectral Satellite Images, *International Journal of Remote Sensing*, 27, 2683 – 2702.

Lira J., 2010, *Tratamiento Digital de Imágenes Multiespectrales*, www.lulu.com

Nezhadarya E., Kreidieh R., 2011, A new scheme for robust gradient vector estimation on color image, *IEEE Transactions on Image Processing*, 20, 2211 - 2220.

Pratt W.K., 2001, *Digital Image Processing*, Wiley Interscience, New York.

Sundaram R., 2003, Analysis and implementation of an efficient edge detection algorithm, *Optical Engineering*, 42, 642 – 650.

Xu J., Ye L., Luo W., 2010, Color edge detection using multiscale quaternion convolution, *International Journal of Imaging Systems and Technology*, 20, 354 - 358.

Yoshida H., 2003, Multiscale edge-guided wavelet snake model for delineation of pulmonary nodules in chest radiographs, *Journal of Electronic Imaging*, 12, 1, 69 – 80.

Geofísica Internacional (2014) 53-3: 309-319

Original paper

Role of Lithology and Subsurface structures detected by potential field data in controlling the radioactive mineral accumulation at Natash area, Eastern Desert, Egypt

Shadia Elkhodary* and Taha Rabeh

Received: September 03, 2013; accepted: October 15, 2013; published on line: July 01, 2014

Resumen

La zona de Wadi Natash se encuentra en la parte sur del desierto del este de Egipto. Tiene una gran importancia, ya que cuenta con gran acumulación de minerales radiactivos, como uranio, torio y potasio. En esta zona se llevó a cabo un estudio de potencial integrado, con el objetivo de localizar a profundidades factibles cuerpos con susceptibilidad magnética suficiente para representar intrusiones magmáticas relacionadas con la radiactividad del lugar y delinear las estructuras del subsuelo que afectan la zona. Tanto los datos magnéticos y de Bouguer como los datos radiométricos se interpretaron rápidamente por la posición de la fuente y las profundidades. Lo anterior fue factible al utilizar la deconvolución de Euler y de Werner, además de técnicas de modelado en 3D. Los resultados deducidos del análisis de tendencias muestran que la tendencia de la falla principal que afecta a la zona tiene una dirección de NNW-SSE (Mar Rojo-Golfo hacia Suez) y atraviesa por el menos predominante NNE-SSW (El Golfo de Aqaba-dirección Mar Muerto) y por WnW-ese (sistema de falla Najd). Los organismos causantes fueron fotografiados a profundidades que van de 0,3 kilómetros hasta 1,5 km. Las profundidades a lo largo de las discontinuidades se deben a la presencia de la falla NNW-SSE y actúan como canales de paso para las soluciones hidrotermales.

Puede afirmarse que las acumulaciones de minerales radiactivos fueron causadas por las soluciones hidrotermales ricas en minerales radiactivos como resultado de la intrusión volcánica Natash a las rocas graníticas. Los clásticos Qouseir y la piedra de la arena Nudian se vieron afectados por estas soluciones y muestran una respuesta positiva de los minerales radiactivos.

Key words: magnético, litología, minerales radiactivos, modelo magnético en 3D.

Abstract

Wadi Natash area is located in the southern part of the Eastern desert of Egypt. It has a great importance for containing accumulations from the radioactive minerals of Uranium, Thorium and Potassium. An integrated potential study was carried out on the study area with the aim of locating depths to causative bodies with sufficient magnetic susceptibility that may represent magmatic intrusions with relation to the radioactivity location and delineate the subsurface structures affecting the area. Both magnetic and Bouguer data as well as radiometric data were interpreted rapidly for source positions and depths using Euler deconvolution, Werner deconvolution and 3D modeling techniques. The results deduced from the trend analyses show that the major fault trend affecting the area have NNW-SSE (Red Sea–Gulf of Suez trend) direction intersected by the less predominant NNE-SSW(The Gulf of Aqaba–Dead Sea trend) and WNW-ESE (Najd Fault System) fault trends. The causative bodies were imaged at depths ranging from 0.3 km to about 1.5 km. The depths along the interpreted profiles display discontinuities in potential field markers due to presence of the NNW-SSE fault trends act as pass channels for the hydrothermal solutions.

It can be stated that the radioactive mineral accumulations were caused by the hydrothermal solutions rich with radioactive minerals as a result of intruding Natash volcanic to the granitic rocks. The Qouseir clastics and the Nudian sand stone were affected by these solutions and show a positive response for the radioactive minerals.

Key words: magnetic, lithology, radioactive minerals, 3D magnetic model.

S. Elkhodary
Geology Department
Faculty of Science
Tanta University
Tanta, Egypt
*Corresponding author: S_elkhodary@hotmail.com

T. Rabeh
National Research Institute
of Astronomy and Geophysics
Cairo, Egypt

Introduction

The area under study is located in south Eastern Desert .It is delineated by longitudes 33° 00 to 34° 30′ E, and latitudes 24° 00′ and 25° 00′N (Figure1). Wadi Natash volcanics cropped out in different spots at the eastern part of the investigated area as alkaline basalts and some small trachytic intrusions which erupted during the Upper Cretaceous associated with regional uplift preceding the northern Red Sea rifting (Figure 1).

This study deals with an integrated interpretation of the observed aeromagnetic and gravity data of Wadi Natash area based on application of gradient (Euler, Werner deconvolution, trend analysis and three dimensional modeling) methods to study the effect of subsurface structures and lithology in controlling the radioactive accumulations.

Geologic Setting

The considered area is topographically graded between gentle to rough topography which traversed by many wadis trending NE-SW, NW-SE, WNW and E-W controlled by the structural directions and the rock types of the area.

The study area is covered with a variety of basement and sedimentary rocks ranging in age from Precambrian to Quaternary (Figure 1). Precambrian rocks consist of acidic metavolcanics (MVa), metasediments (MS) and calc-alkaline granites (gα and gβ) cover the southern eastern part of the area. The northern eastern part of the area is covered by Upper Cretaceous volcanics (wadi natash volcanics) and trachyte plugs (Hashad, *et al*., 1982). Meanwhile, the Upper Cretaceous Nubian sandstones cover the central and western parts of the area represented by (Abu-Aggag (Ku) and Um Barmil (Kub) Formations). Late cretaceous shall and limestone represented by Dakhla (kud) and Kiseiba (Tpl) occupying the northwestern corner of the area, (Conoco Report, 1989).

One of the extensive lava fields in the East Sahara Swell is that of Wadi Natash in the southern Egypt. Natash volcanics crop out in the study area at the southeastern corner, northeastern, northwestern, and southwestern corners of the study area. The volcanic rocks and their volcaniclastic sediments are nearly parallel to the boundary between the (upper and lower) Nubian sandstones. The lava flows form a dissected plateau with a stratified appearance which trends NNW-SSE. This plateau is formed of thick piles of volcanic flows; each of them extends laterally for more than 6km. They also include a number of cones and sills of olivine basalt. The cones are cone-shaped features, rising up to 26-86 m above wadi level, while sills are always encountered in the Nubian Formation in the form of flat lying bodies interbeded with the sandstones and measure up to 7m in thickness (Hashad, *et al.*, 1982). Ibrahim (2010) records for the first time the occurrence of laterites-bearing REEs in Natash area which form as horizons at the boundary between the Cretaceous sandstones and Natash flows.

The volcanic sequence is represented by three distinct flow unites, separated by two sequences of volcaniclastic sediments. Each of

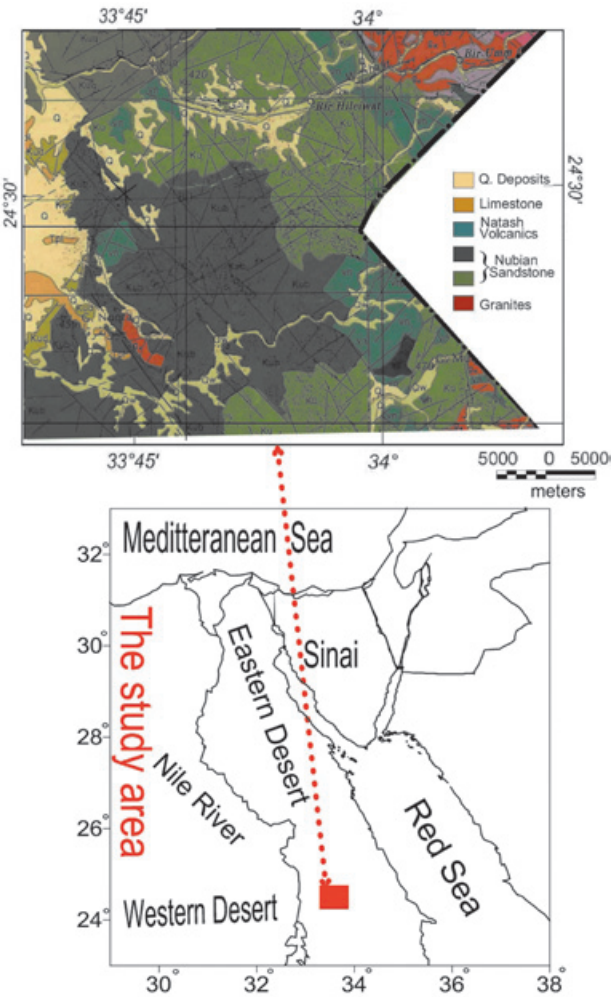

Figure 1. Location map and surface geologic map of the study area after CONOCO (1987).

the tree flow unites shows a gradual change in composition upwards from alkali olivine basalts through trachybasalts, trachyandesite, to trachytes. The volcaniclastic sediments comprise agglomerates and tuffs which contain leaf imprints of Cenomanian age (Crawford *et al*.,1984), which are in good agreements with a 90Ma K-Ar age for the lavas determined by Ressetar *et al.*, (1981). The age of these volcanics suggests that they are not directly associated with the actual mid-Tertiary Red Sea rifting but their alkaline nature implies that they were involved with a pre-rifting doming process (Crawford, *et. al*., 1982).

Structurally, Noweir, *et al.* (2003) concluded that the rocks of Wadi Natash have general linear trend outcrops conformable with the general structure trend. The linear trend suggests that these volcanic bodies were brought up along the intersection of the main NNW to NW fault trend with the E-W fault direction during the Turonain age.

Potential field data acquisition

An aeromagnetic survey conducted by Aero Service, (1984) was used to interpret the regional subsurface structures prevailing in the study area along with gravity data obtained from the 1-arc-minute gravity anomaly (mGal) grid by Sandwell and Smith (1997). The aeromagnetic survey was flown at 1km altitude with north-east flight lines every 1 km and tie-lines every 10 km in perpendicular directions to the flight lines. The aircraft was equipped with a tail-stinger of non-magnetic plastics of 1.5 meters long at the rear of the fuselage. The magnetic data were digitized by computer digitizing programs and both Bouguer and the total magnetic anomaly map were obtained (Figures 2 and 3).

Potential field data processing

The aeromagnetic data was digitized into a computer using a suitable Surfer Program v. 8.00 (Surfer, 2002). The first step in data

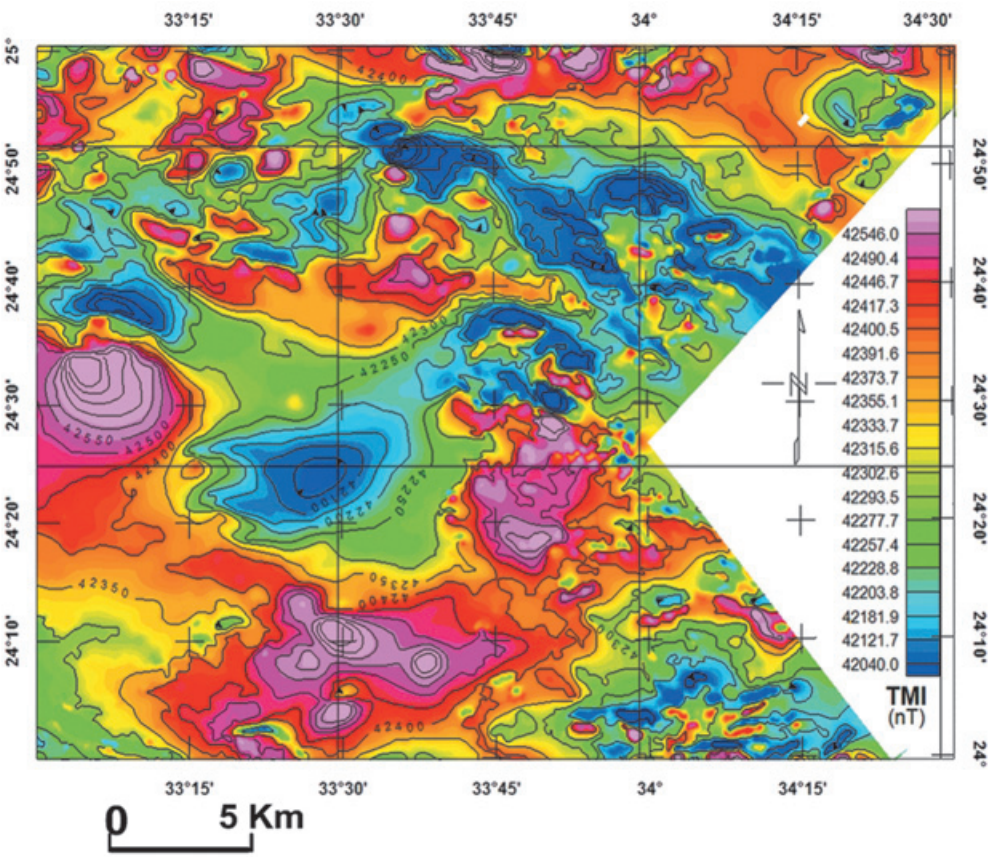

Figure 2. Total Intensity aeromagnetic map of study area (after Aero Service, 1984).

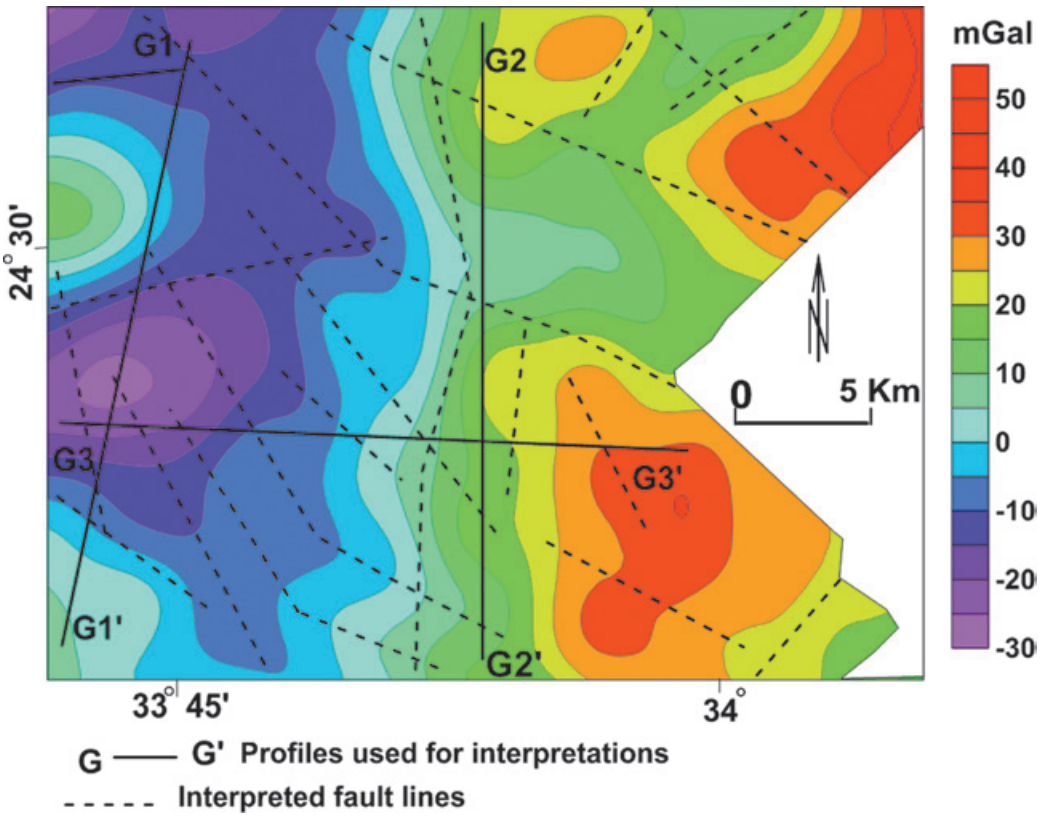

Figure 3. Bouguer anomaly map of the study area (after Sandwell and Smith, 1997) showing profiles and deduced fault trends.

processing was reduction to the magnetic north pole (RTP). This procedure has the advantage of compensating for the shift between sources and magnetic anomalies due to the non-verticality of both the normal field and the magnetization. Only induced magnetization was considered. Inclination and declination of the normal field were fixed at 32.8 N and 1.9 E. RTP was conducted in the Fourier domain (Blakely, 1995). The results are presented in (Figure 4) for the aeromagnetic survey. Both the Bouguer anomaly and the RTP aeromagnetic maps (Figures 3 and 4) indicate that most anomalies are aligned to NW, NE, and E-W which may be related to the Red Sea, and Gulf of Aqaba tectonics. The negative anomalies in the central part may be due to deep depths to the basement rocks or the lithology of negative magnetic effects.

The RTP aeromagnetic anomaly map (Figure 4) shows low and high frequency magnetic anomalies distributed along the study area. The elongated positive magnetic anomalies with a maximum value of 42850 nT were observed over the locations of southwest, west and north the study area. They are characterized by high frequency and high amplitude. Such magnetic anomalies are associated with acidic metavolcanics, metasediments and calc alkaline granites, Natash volcanic which are mainly characterized by high magnetic susceptibilities. These magnetic anomalies are bounded by steep magnetic gradients, which indicated the presence of two fault systems, trending in the NW-SE direction (Red sea) and NE-SW (Aqaba trend). The RTP map is marked by negative anomaly. A strong NE-SW trending anomaly truncated by the E-W trending is observed in the north-eastern and central parts of study area.

The variations in gravity anomalies were normally caused by variations in the density of subsurface rocks (Reynolds, 1997), and they usually indicated faults or lithological contacts. The Bouguer anomaly map of the study area (Figure 3) was generally in good coverage and it showed gravity values between +50 and -30 mGal. It is characterized by a group of positive and negative anomalies of different intensities and almost NE–SW, NW-SE and E-W orientation. The strongest positive gravity anomalies (50 mGal intensity) lie at the NW and SW corners of

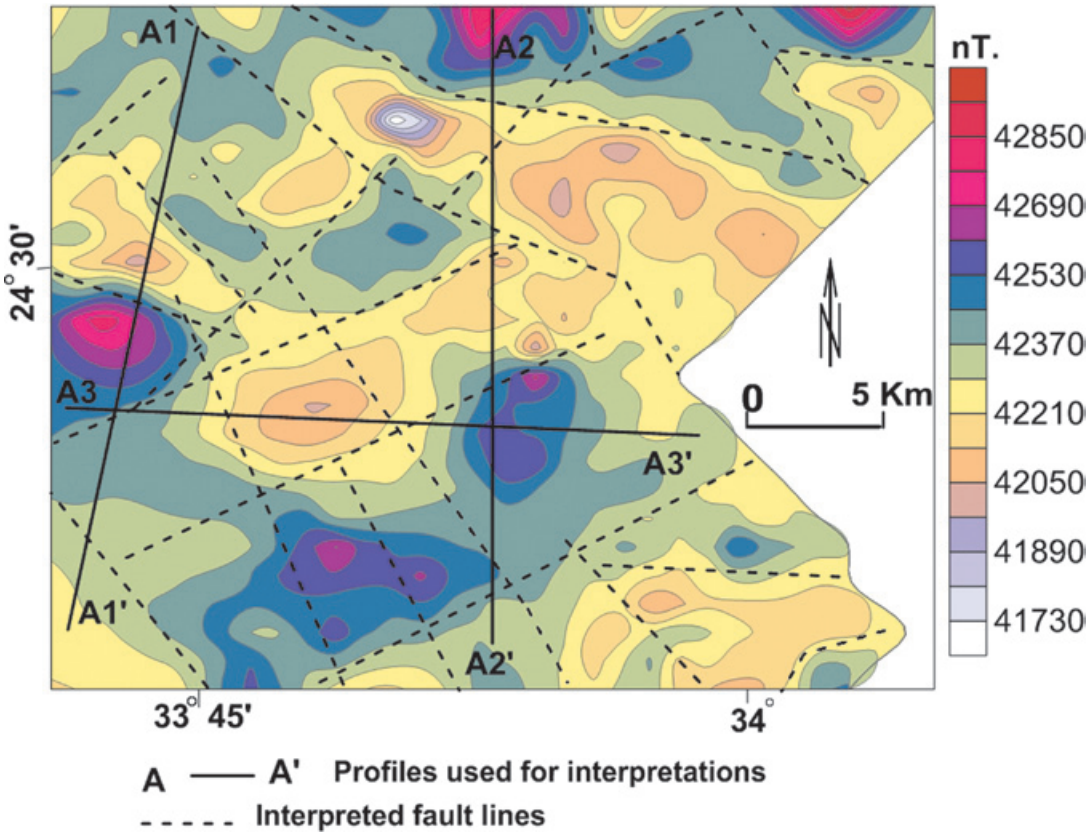

Figure 4. RTP anomaly map of the study area showing profiles and deduced fault trends.

the study area which associated with the Natash volcanic and the granitic rocks and is separated from the negative gravity anomaly by a very steep gradient. This steep gradient is of NNW trend and could be interpreted to be a normal fault down-throwing to the east. On the other hand the eastern side of the concerned area there is a large high negative anomaly (-30mGal intensity) trending NNE-SSW, associated with the Qena clastics and the limestone. This lithological variation on both sides of the fault as well as the magnitude of fault throw being upthrown to the west is behind the strong difference in the intensity of both positive and negative gravity on both sides of the fault.

a) Trend analysis

Other treatments of Potential Field data include trend analysis to delineate the subsurface fault trends based on the theory of **Grant & West (1965)** and on the **Linsser technique (1967)**, the first horizontal gradient method was applied to all RTP magnetic and the gravity maps. The peaks of the gradient curve were plotted along profiles covering these maps, and then connected together to show the deduced structure lines.

Close investigations of these maps (Figures 3 and 4) indicate that there are three main structural elements which aligned in direction that bounded both magnetic and gravity anomalies. These elements can be grouped in the following zones:

1) The NNW-SSE (Red Sea–Gulf of Suez trend) structural direction as the main structural elements occupying the central and the southern parts of the study area.

2) The NNE-SSW (The Gulf of Aqaba–Dead Sea trend) structural direction with less abundance in both maps. This trend located at the northern and southern parts of the area.

3) The WNW-ESE (Najd Fault System) structural direction which lying in the northern and southern corners of the study area which is the least prevailing fault system.

b) Werner deconvolution method:

Werner (1953) developed a method for identifying the geometry of magnetization contrasts based on successive determinations of small dikes with infinite strike length and depth extent, perpendicular to the measurement profiles, and which could be considered the source of the magnetic anomaly described by a set of four or more contiguous measurements. The basic expression for the magnetic anomaly of a single dike is:

$$T(x) = \frac{A(x - x_0) + B_z}{(x - x_0)^2 + z^2} \qquad (1)$$

where x_0 is the location of the magnetic step, z is the depth to the top, A and B are field functions to be determined, and x is the location at which we want to compute the magnetic anomaly. When several determinations cluster close to a specific location, we infer that the model describes the magnetic interface well. This approach was used by **Ku and Sharp (1983)**, in a method that has high computational efficiency.

We applied the Werner deconvolution method along set of profiles A-A' of the aeromagnetic map and G-G' of the gravity map Using clustering method. The outcomes from application clustering method allow us to show the interfaces of the subsurface structures for the aeromagnetic and gravity profiles. The deduced results (see Figure 5a and 5b) illustrated the exact depth of the magnetic and gravity sources where Werner solutions are clustering to each other. Analysis of these profiles showed that the depth to the basement ranges between 1.5 to 0.3km, which is nearly close to the depth of the volcanics deduced by Elawadi and Ismail (2006).The shallowest depths are found at the northern and southern parts of the study area where Natash volcanics and granitic rocks outcrop while the deepest parts occupy the central and western parts of the area where the Nubian sandstone and Qouseir clasts are found.

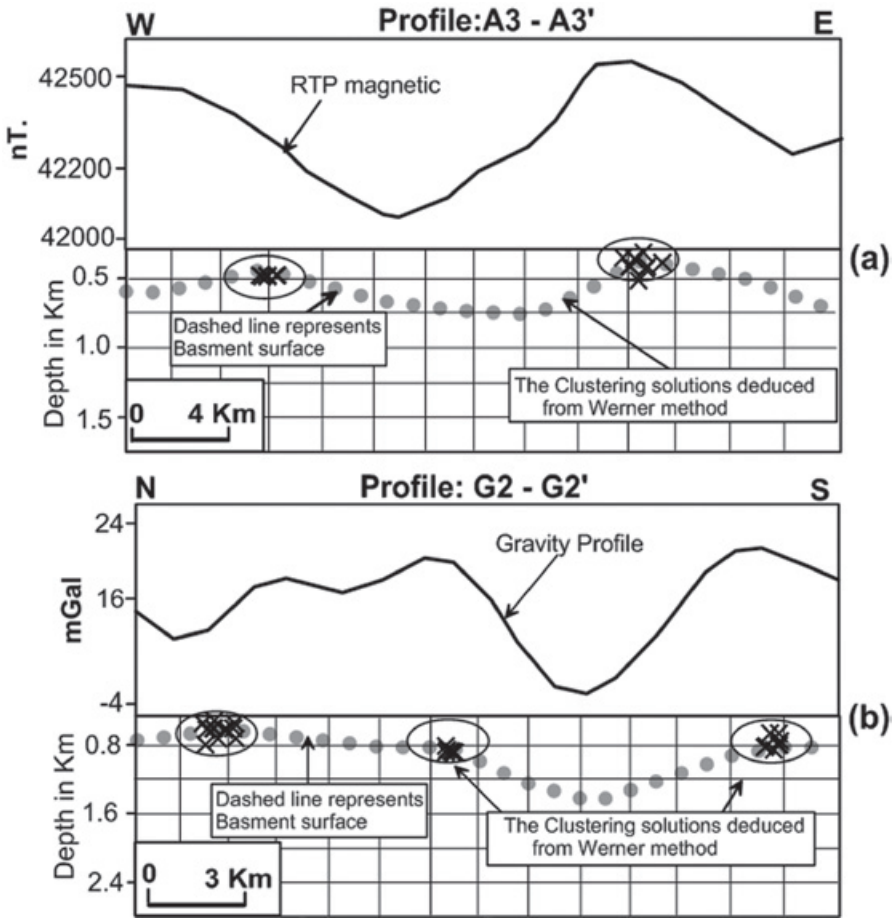

Figure 5. Werner deconvolution showing the depth to the basement rocks and the subsurface structures along Profiles; a) A3–A3' (location shown in Figure 4). b) G2-G2' (location shown in Figure 3).

c) Euler deconvolution method

The Euler deconvolution method delineates geological boundaries of magnetization or density and gives-estimates of depth to the basement. Also, this method can be used to determine the subsurface structures (Grauch, *et al*., 2001). Neil (1990) and Neil *et al*.(1991) applied this technique to magnetic data at Leeds. Few gravity applications have been reported. In this study the application of this technique to both gravity and magnetic data were attempted. The method was originally devised by Thompson (1982) for profile data and later developed for 3D gridded data by Reid *et al*. (1990).

The Euler deconvolution method was applied to the total field intensity along a set of profiles used for aeromagnetic and gravity interpretations (Figures 3 and 4). The windows size used in the process was 11 with applying the suitable dimensions of coordinates. The window slides and the solutions were calculated. The output of this method was representing by the horizontal and Euler solutions. Reid (2003) explained the significance of the deduced structural indices and listed them in Table (1).

Table 1. Structural indices of Euler, after Reid (2003).

Source Type	SI
Sphere or compact body at a distance	3
cylindrical pipe	2
Thin sheet edge (sill, dike, etc.)	1
Fault (small step)	0

The horizontal gradient was used to confirm the deduced subsurface structures. The peaks along these profiles illustrate the location of these structures. It can be noticed, that Euler solutions are clustering along these structures (Figures 6 and 7). Also It can be noticed that the most suitable structural indices (SI) representing the magnetic structures are restricted between 2 and 4 SI indicating an intruded magnetic bodies.

The results from the both magnetic and gravity profiles A2-A2' and G3-G3' (Figures 6 and 7) show that the Natash volcanic extends to a relatively shallow depth (300-100) meanwhile the faults which may be the cause of this volcanic trending NE-SW with depth reaching

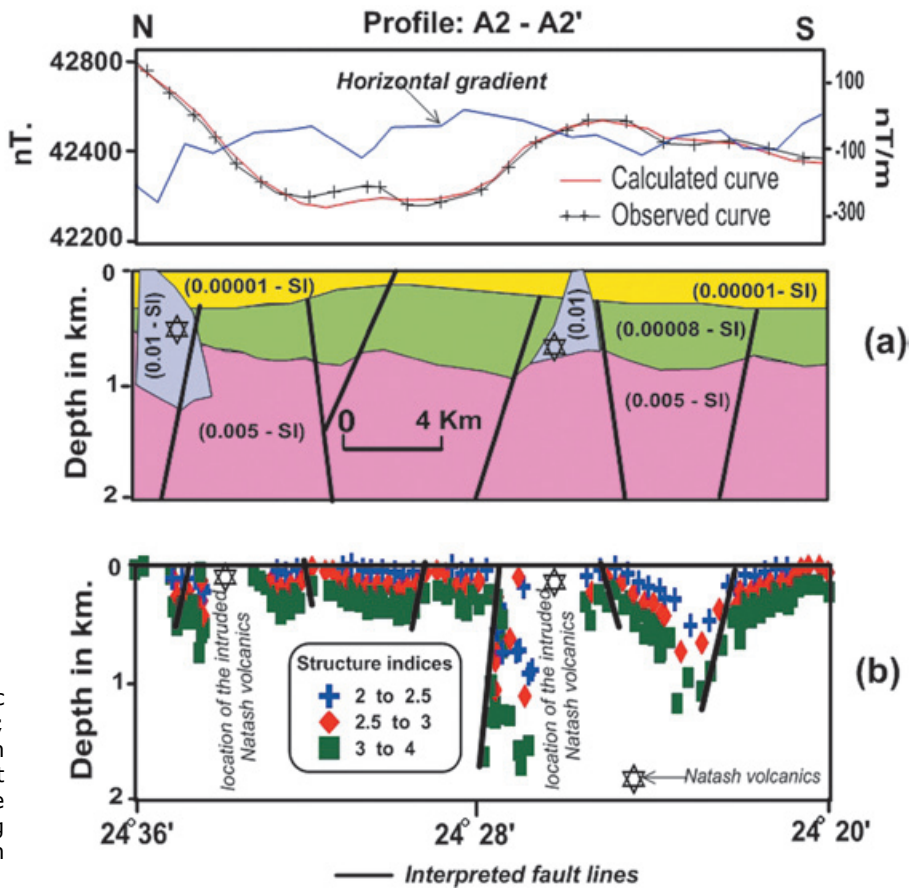

Figure 6. a) 3-D magnetic model for the Profile A2–A2'; b) 2-D Euler deconvolution and horizontal gradient confirming presence of the two fault systems along Profile A2–A2' (location shown in Figure 4).

more than 2km. It is noteworthy that this geophysical subsurface interpretation coincides with the geophysical results by El Gammal *et al* (2013).

d): 3D magnetic modeling

The magnetic field A at any external point r due to a volume v of rock which is magnetized with a dipole moment per unit volume M **(Grant and West, 1965)** is:

$$A(r)=\nabla \int_V M.\nabla\,[1/(|r-r_0|]d^3 r_0 \quad (2)$$

Where: $\int_v$ is a volume integration over the body, r is the distance restricted to the xz plane and r_0 is the distance from point A to the centre of the magnetic body.

If the magnetic body is not uniformly magnetized then the extent of the body is between y and –y axis and the observation points will be made along the x-axis across the middle of the body. Therefore, the three components of the magnetic intensity shall henceforth be referred to as the magnetic anomaly given by equation (2) for the magnetic body is:

$A_x = 2M_xP_x + 2M_zQ$, $A_y = -2M_yR$ and $A_z = 2M_xQ - 2M_zP_z$.

Where:

$P_x = a^2U/ax^2$, $P_z = -a^2U/az^2$, $R = -a^2U/ay^2$ and $Q = -a^2U/axaz^2$

and U is the Newtonian potential expressed by:

$$U = 1/2 \int_V M.\nabla\,[1/(|r-r_0|]d^3 r_0 \quad (3)$$

Based on **Grant and West,** (1965) and **Talwani** (1960) theories, the 3D modeling technique was applied to the magnetic data using **Encom ModelVision Pro (2004)** software. The technique was applied to the set of aeromagnetic and gravity profiles with different direction covering almost the area (Figures 3 and 4). Inspection of the magnetic profile (Figure 6) revealed that it composed of four bodies representing different lithological and tectonic units. The profile trending N-S showing the highest susceptibility unite (0.01 SI) representing Natash volcanic in the northern and southeastern parts of the profile, reflecting the prevailing fault trends NNW and NNE.

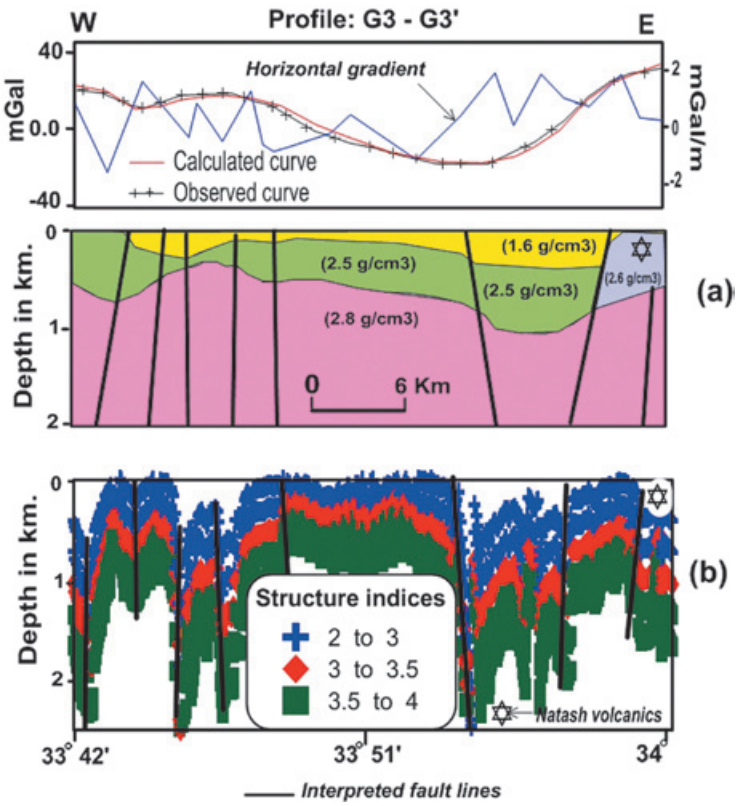

Figure 7. a) 3-D gravity model for the Profile G3-G3′; b)2-D Euler deconvolution and horizontal gradient confirming presence of the two fault systems along Profile G3–G3′(location shown in Figure 3).

Meanwhile, model for gravity (fig.7) consists of four bodies representing different lithological and tectonic units. This model shows the high density block (2.6g/cm^3) representing Natash volcanic located at the eastern part of the modeled area. The two fault systems trending NNW and NNE are clearly found with reaching a depth of more than 2km.

The interpreted structural features coincide with the Euler deconvolurion of the same trend.

e) Interpreted Structural map with prospected radioactive areas:

Using the radioactive minerals map (Figure 8) established by Elawadi *et al*. (2004) we were able to detect two zones with high concentration of radioactive minerals accumulations. They stated that the radioactive anomalies have been interpreted in younger granites and in adjacent the Nubian sandstones under Wadi Natash exhibits of strong radiometric responses and can be a good target for further mineral explorations. The radiometric data indicate that the granitoid rocks are larger than that present in the geologic map and indicate presence of emanations of radioactive minerals from granites to the surrounding metamorphic rocks due to contact metamorphism. These data indicate that dykes cause a zone of radiometric potential in the surrounding sedimentary rocks (El Gammal, *et al*., 2013).

The regional tectonic framework of the studied area (Figure 9) was established using the integration of all results of interpretation of the aeromagnetic and gravity analyses, in addition to the horizontal gradient method in which the peaks of the curves were plotted and connected together to show the possible structural fault lines affecting the study area. Also the 3D modeling to detect the subsurface structures and the depth to the basement rocks (figs 6&7). Visual inspection of the Potential Field data indicated that the most dominant trend in the area is of NNW–SSE related to the Red Sea- Gulf of Suez tectonic trend dissected by the second dominant one trending NNE–SSW related to the Gulf of Aqaba–Dead Sea trend and the WNW-ESE related to the Najd Fault System trend with less contribution in the area under consideration.

The NNW-SSE fault trends are connected with the Red Sea rifting. They occupy the detected zones of high radioactive minerals accumulations (Figure 9). According to Elawadi *et al.* (2004), the Qouseir clastics zone is characterized by radioactive Uranium minerals. Thus we can conclude that the radioactive zones are connected with the Red Sea tectonics and the intruded granitic rocks. The NNW-SSE major faults are controlling the hydrothermal solutions associated with the intrusion of granitic rocks and may be the cause of the formation of radioactive minerals.

Conclusion

The Bouguer, Magnetic and RTP anomalies maps are used to delineate the subsurface structural features prevailed in the study area. They were interpreted using trend analysis, 2D Euler deconvolution, Werner deconvolution and 3D modeling techniques. The results show that

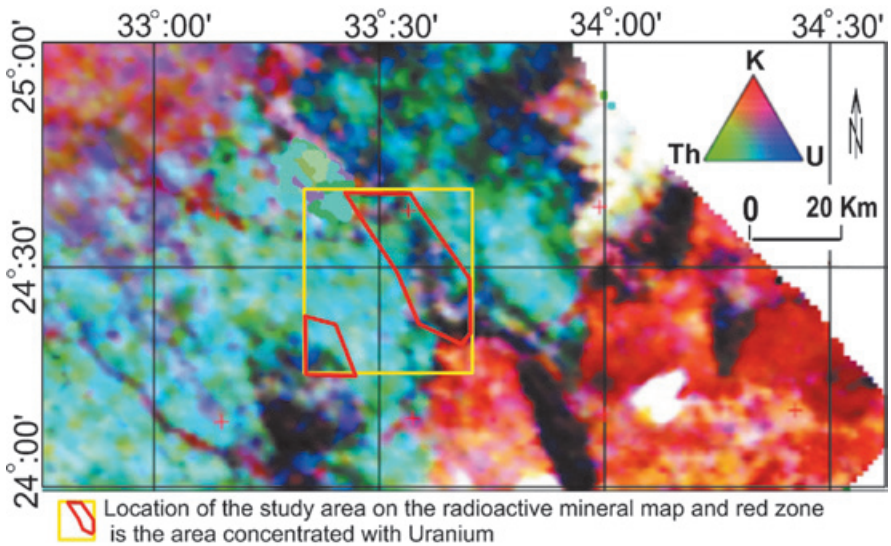

Figure 8. Radioelement composite image (after Elawadi *et al*. 2004) showing zones with radioactive minerals accumulations.

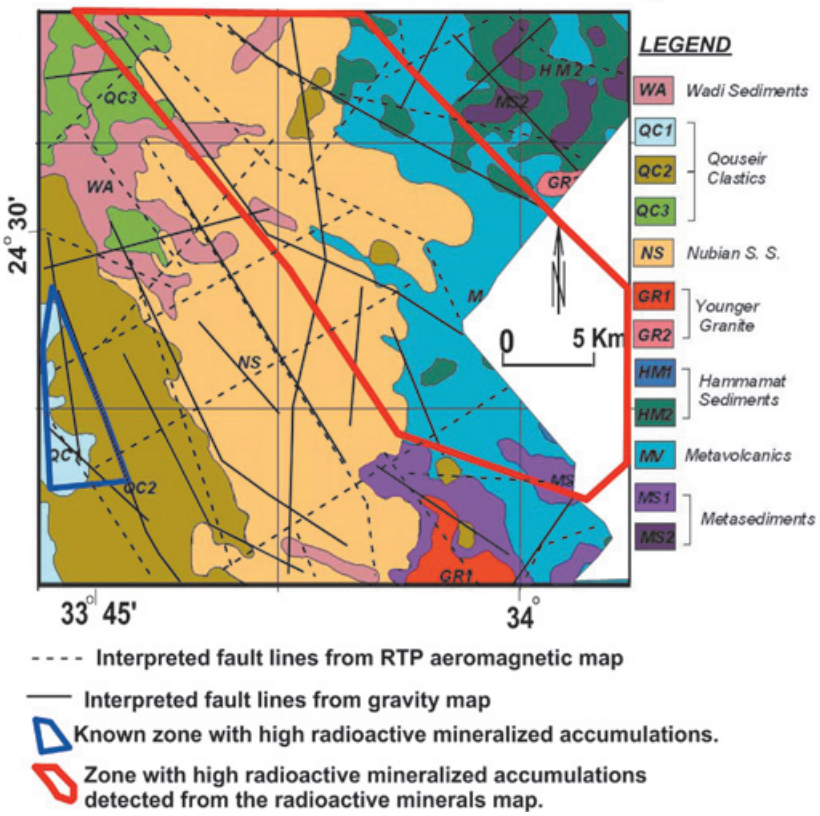

Figure 9. The interpreted basement tectonic map with promising location of radioactive elements.

the area is structurally controlled by major faults trending in the NNW-SSE direction related to the Red Sea tectonics. They are intersected by the less predominant fault structures which have NNE-SSW and WNW-ESE directions.

The study area was affected by mass granitic rock intrusions. The depths to the intruded rocks reach from 300m to 1500m. The Natash volcanic is intruded to granitic rocks and overlying Qousuir clastics and Nubian sandstone.The integrated results from gravity, magnetic and radiometry indicate the relationship between the NNW-SSE fault trends and intruded granitic rocks as well as the radioactive mineral accumulations exists. From the results deduced from all the interpretations and analyses techniques applied to both magnetic and gravity data, it can be concluded that the Qousuir clastics and the Nubian sandstone rocks were affected by the intrusion of the Natash volcanic which is post rifting the Red Sea and it would form radioactive mineral accumulation as a result of hydrothermal solution. The NNW-SSE fault trends act as path channels for these solutions rich with radioactive minerals.

References

Aero-Service, 1984, Final operational report of airborne magnetic/radiation survey in the Eastern Desert, Egypt. For the Egyptian General Petroleum Corporation (EGPC) and the Egyptian Geological Survey and Mining Authority (EGSMA). Aero-Service Division, Houston, Texas, USA, Six Volumes.

Conoco and Egyptian General Petroleum Corporation, 1987. Geological map of Egypt, Scale 1:500,000, Cairo.

Conoco Inc., 1989, Stratigraphic lexicon and explanatory notes to the geological map of Egypt 1:500,000. Conoco Inc., Cairo, Egypt, P. 262.

Crawford W.A., Coulter D.H., Hubbard J.H.B., 1982, Wadi Natash olivine alkali basalt volcanic series a harbinger of Red Sea rifting, *Geol. Soc. Am.*, 14, 469.

Crawford W.A., Coulter D.H., Hubbard J.H.B., 1984, The aerial distribution, stratigraphy and major element chemistry of Wadi Natash volcanic series, Eastern Desert, *Egypt.J. Afr. Earth Sci*., 2, pp. 119-128.

El Gammal, El Sayed A., Salem S.M., Greiling Reinhard O., 2013 , Geology, Morphotectonics And Geophysical Interpretation Of Wadi Garara Graben, East Aswan Egypt, Using Landsat Images. *Australian Journal of Basic and Applied Sciences*, 7, 1, pp. 263-277.

Elawadi Eslam A., Ismail Atef A.,2006, Aeromagnetic imaging of Wadi Natash volcanics, South Eastern Desert, Egypt. submitted to the 8th SEGJ conference, Kyoto, Japan.

Elawadi E., Ammar A., Elsirafy A., 2004, Mapping surface geology using airborne gamma-ray spectrometric survey data- A case study, Proceedings of the 7th SEGJ International Symposium, Japan, November 24-26, 2004.

Encom ModelVision Pro, 2004, software for PC developed and supported by Encom Technology Pty Ltd. Version 6.00 September 2004: Head Office Level 2, 118 Alfred St, Milsons Point, New South Wales, Australia 2061.

Grant F.S., West G.F., 1965, Interpretation theory in applied geophysics, MacGraw- Hill, pp. 584-588.

Grauch V.J.S., Hudson M.R., Minor S.A., 2001, Aeromagnetic expression offaults that offset basin fill, Albuquerque Basin, New Mexico: *Geophysics*, 66, 707-720.

Hashad A.H., Hassan M.A., Aboul Gadayel A.A. 1982, Geologicol and petrological study of wad. Natash late Cretaceous volcanic, Egypt. *J. Geol*., 26, pp. 19 – 37.

Ibrahim M.E., 2010, Laterites Bearing-REEs, Wadi Natash, Southeastern Desert, Egypt. *Journal of Rare Earth*, 28, 3, pp. 471-476.

Ku C.C., Sharp J.A., 1983, Werner deconvolution for automated magnetic interpretation and its refinement using Marquardt's inverse modeling, *Geophysics*., 48, pp. 754 - 774.

Linsser H., 1967, Investigation of tectonics by gravity detailing. *Geophysical Prospecting*, 15.

Neil C., 1990, A computer program to interpret automatically potential field data using Euler's equation of homogeneity: Unpublished M.Sc. thesis, University of Leeds, 72p.

Neil C., Whaler K.A., Reid A.B., 1991, Extensions to Euler's method for three-dimensional potential field interpretation: (Abstract) Presented at EAEG, Florence.

Noweir A.M., Lebda E.M., Noweir M.A., Nassim A.S., Elkholiefy E.M., 2003, Tectonic evolution geochemistry and petrogenesis of the alkaline volcanic rocks of Wadi Natash, Egypt. *Jour. Geol*., 47, pp. 541-568.

Reid A.B., Allsop J.M., Granser H., Millett A.J., Somerton I.W., 1990, Magnetic interpretation in three dimensions using Euler deconvolution, *Geophysics*, 55, 1, pp. 80-91.

Reid A.B., 2003, Euler magnetic structural index of a thin-bed fault. *Geophysics*, 68, 1255-1256.

Ressetar R.D., Nairn A.E.M., Monrad J.R., 1981, Two phases of Cretaceous- Tertiary magmatism in the Eastern Desert of Egypt: paleomagnetic, chemical an K-Ar evidence. *Tectonophysics*, 73, pp. 169-193.

Reynolds John M., 1997, An Introduction to Applied and Environmental Geophysics. John Wileyand Sons, Ltd. New York.

Richard J. Blakely, 1995, Potential Theory in Gravity and Magnetic Applications, Cambridge University Press, New York, P. 441.

Sandwell D.T., Smith W.H.F., 1997, Marine gravity anomaly from Geosat and ERS-1satellite altimetry. J. Geophys. Res. 102, 10039–10050 available at http://topex.ucsd.edu/cgi-bin/get_data.cgi.

SURFER, 2002, Surfer® Version 8.00, Feb 11, 2002 (Golden Software Inc., Golden, CO, U.S.A.).

Talwani M., 1960, Rapid computation of gravitational and Ewing, M. attraction of three-dimensional bodies of arbitrary shape. *Geophys*., 25, pp. 203-225.

Thompson D.T., 1982, EULDPH – A new technique for making computer-assisted depth estimates from magnetic data. *Geophysics*, 47, 31 – 37.

Werner S., 1953, Interpretation of magnetic anomalies at sheet-like bodies. Sveriges Geologiska Underso¨kning 43.C _ 2009 University of Lisbon, Geophysical Prospecting, 57, 447–459.

Geofísica Internacional (2014) 53-3: 321-332

Original paper

The intersective Hough transform for geophysical applications

F. Alejandro Nava

Received: September 09, 2013; accepted: October 15, 2013; published on line: July 01, 2014

Resumen

La transformada de Hough es una herramienta ampliamente utilizada para identificación de alineamientos, pero el método de votación utilizado usualmente en esta transformada presenta serios problemas cuando las alineaciones no son exactas. Proponemos un método de votación basado directamente en intersecciones en el espacio de Hough, que es más eficiente y soluciona los problemas mencionados; el método propuesto también da un método directo para cuantificar cada alineamiento. El método intersectivo puede obviar el uso de espacios de Hough divididos en celdas acumuladoras, y trabajar directamente sobre cúmulos de intersecciones, de manera que todo el proceso de identificación de alineamientos puede ser automatizado. Un ejemplo sintético que representa una aplicación geofísica de la transformada de Hough, identificación de alineamientos inexactos en presencia de ruido, es usado para ilustrar el método propuesto y para discutir otras aplicaciones. Un metodo opcional de ponderación de los datos puede ser usado para tomar en cuenta posibles incertidumbres en éstos. Tanto para alineamientos exactos como inexactos, el método intersectivo da mejores resultados que el método tradicional

Palabras clave: transformada de Hough, identificación de alineamientos, alineamientos geofísicos.

Abstract

The Hough transform is a widely used tool for alignment identification, but the voting scheme usually used in this transform presents serious problems when alignments are not exact. We propose a voting scheme based directly on intersections in Hough space, which is more efficient and solves the above mentioned problems; the proposed scheme also provides a straightforward way of quantifying each alignment. The intersective approach can even dispense with gridded Hough spaces and accumulator cells, through direct clustering of intersections, so that the whole alignment identification process can be done automatically. A synthetic example representing a geophysical application of the Hough transform, identification of inexact alignments in the presence of noise, is used to illustrate the proposed method and to discuss further applications. An optional data-weighting scheme takes into account possible uncertainties in the data. For both exact and inexact alignments, the intersective method yields better results than the traditional one.

Keywords: Hough transform; alignment identification, geophysical alignments.

F. A. Nava
Seismology Dept., CICESE,
Carr.Tijuana-Ensenada 3918,
Ensenada, B.C., 22860, México
Tel: 52-646-1750500 x26519
Fax: 52-646-1750559
Corresponding author: *fnava@cicese.mx*

Introduction

The Hough Transform is a widely used tool in many applications ranging from detection and analysis of alignments in point distributions to image analysis and computer vision (e.g. Illingworth and Kitler, 1988; Hart,2009; Shapiro and Stockman, 2001; Wikipedia, 2012). Originally meant to detect alignments of points or objects along straight lines (Hough, 1959), it has been extended to detect other kinds of alignments (Duda and Hart, 1972; Ballard, 1981); we will restrict our treatment to detection of straight lines.

The usual, or traditional, Hough Transform (HT) (Hough, 1959) determines the presence of alignments of points in the physical, or observational, space, based on "votes" cast by each point onto accumulator cells in the Hough space (this process will be reviewed below). However, this voting scheme presents serious problems when the alignments are not perfect, and results in confusing Hough space diagrams when a large number of alignments is being considered.

For many geophysical applications, such as identifying alignments in earthquake epicentral (or hypocentral section) distributions, the main problem with the HT is that events are not perfectly aligned. Misalignments can occur because of location errors, but the main source of misalignment is that geophysical alignments do not occur along perfect zero-width straight lines. Hence, their curves in Hough space do not intersect at one point, and their intersections are spread over some region.

O'Gorman and Clowes (1976) proposed a method which uses the local gradient direction of image intensity to approximate the angles of lines, but this approach is appropriate for lines consisting of neighboring pixels and is not appropriate for sparsely populated alignments, like most in geophysical applications.

Fernandes and Oliveira (2008) improve the voting scheme by looking for clusters of approximately collinear points (or pixels) in observational space and casting votes using a Gaussian elliptical kernel oriented according to the direction of the line that best fits each cluster. This method is complicated because it carries out the search for lines largely in observational space. Other methods for improving the Hough transform are found in Kiryati *et al*. (1991), Li *et al*. (1986), and Furukawa and Shinagawa (2003).

We propose a new straightforward voting scheme which can be used to obtain much cleaner and easy to use accumulations in Hough space, or to dispense altogether with accumulator cells.

The traditional Hough transform

Here, we will briefly review some basic concepts of the HT, mainly to introduce our notation and to define terms that will be repeatedly used, as well as to point out characteristics of the usual HT that will be improved by our proposed approach.

The HT, as proposed by P.Hough (1959), is based on the representation of straight lines occurring in physical 2D (x, y) space by points in a 2D parameter space, the *Hough space.* The parameterization most commonly used is that proposed by Duda and Hart (1972), which represents each straight line in the physical space by a point in the (θ, r) Hough space, where r is the shortest distance from the origin to the line (measured along the r line, which is a straight line perpendicular to the original one and passing through the (x, y) origin), and θ is the angle between the r line and the X axis (Figure 1). The usual ranges of these parameters are $0 \le \theta \le \pi$ and $-\infty < r < \infty$, where r is considered negative if the line passes below the origin.

The (θ, r) parameters are related to the a and m parameters of the usual $y=a+mx$ representation by

$$\theta = \arctan\left(\frac{-1}{m}\right) \qquad (1)$$

and

$$r = a \sin(\mathrm{q}) \qquad (2)$$

The line $y = a + mx$ goes through the point (0, a) and makes an angle α with the X axis; perpendicular to this line and passing through the origin is a line with length r which makes an angle θ with the X axis.

A point (x_i, y_i) in the X, Y plane can be considered as the locus through which pass an infinite number of straight lines, each characterized by an angle θ and a distance r, according to

$$r = x_i \cos(\mathrm{q}) + y_i \sin(\mathrm{q}) \qquad (3)$$

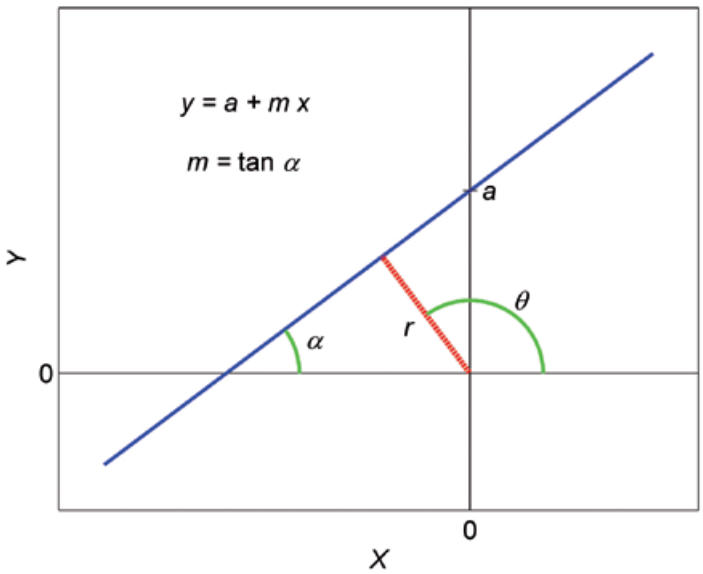

Figura 1. Definition of the θ and r parameters that characterize a straight line. The line $y=a+mx$ goes through the point $(0,a)$ and makes an angle α with the X axis; perpendicular to this line and passing through the origin is a line with length r which makes an angle θ with the X axis.

and this family of lines corresponds to points along the curve defined by equation (3) in the Hough (θ, r) space.

For two points, (x_i, y_i) and (x_j, y_j), there is only one line common to both, and hence only one common point where the two corresponding curves in the Hough (θ, r) space intersect. For any number of points, in the physical space, their (θ, r) curves intersect at as many points as there are pairs of (x, y) points, but all points along a straight line will intersect at the same (θ, r) point. Thus, significant straight alignments, i.e. those with many aligned elements, are identified as points in the space where many curves intersect.

The traditional HT then identifies the alignments using the following scheme. The (θ, r) plane is discretized into "accumulator" cells each of $\Delta\theta$ x Δr size, and each (x_i, y_i) point "votes" through its corresponding curve (3) increasing by one the content of each cell traversed by the curve. Finally, cells with large values (where large numbers of curves coincide) are chosen, either numerically or visually from a color-coded representation, as representing straight lines corresponding to alignments in physical space. The number of votes in a cell, which we will denote by q, is a measure of the number of points in the line defined by the cell parameters.

This traditional scheme works well when alignments are perfect, but when alignments are not perfect, as in most cases dealing with geophysical data, the accumulator cell map is distorted, so that it may be impossible to get a sufficiently accurate identification. We will now present an illustration of the problem and discuss its general causes.

To illustrate this point, let us consider a set of 60 points (which could represent epicenters or other geophysical features) distributed over the plane shown in Figure 2 as:

- Line 1: 9 events along $y = 0.300 + 0.900x$ (at random x values), corresponding to point $\theta_{L1} = 131.987°$, $r_{L1} = 0.223$ km in Hough space,
- Line 2: 9 events along $y = 0.700 - 0.400x$ (at random x values), corresponding to point $\theta_{L2} = 68.199°$, $r_{L2} = 0.650$ km,
- 42 events distributed randomly with uniform probability over the plane.

The random events, more than twice the aligned ones, representing noise were included in order to have a distribution in which alignments would not be obvious, and could test the capabilities of each method. Noise is always present in geophysical observations, and the example distribution can very well represent a typical case of epicentral distribution.

The HT of this set, using cells $\Delta\theta = 1.5°$ by $\Delta r = 0.015$ km, is shown in Figure 3. The brighter cells correctly identify the two lines, although none of them attained the expected $q=9$ incidences, due to the actual location of the cells and to numerical approximations

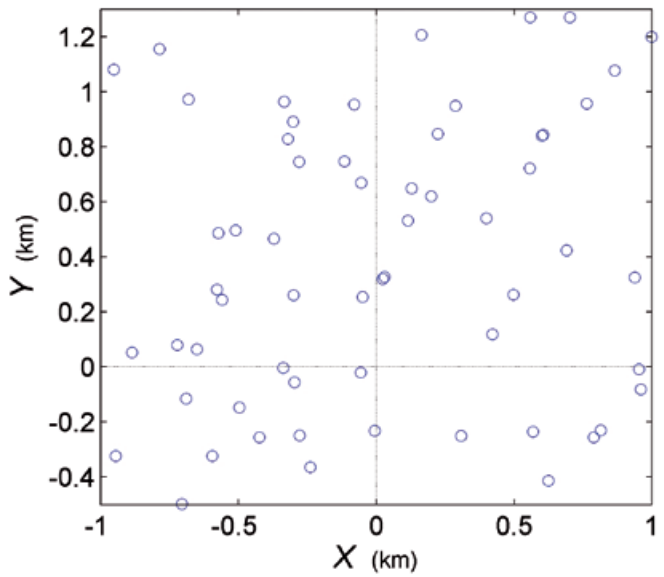

Figure 2. First sample set of points in observational space; the set includes two subsets of perfectly aligned points.

(seven decimal places in x and y); the maximum corresponding to Line 2 is spread over several neighboring cells. The identified lines are Line 1: $\theta_{L1} = 132.000°$, $r_{L1} = 0.208$ km, $y = 0.208+0.900x$, and Line 2: $\theta_{L2} = 69.000°$, $r_{L2} = 0.643$ km, $y = 0.689-0.384x$. Thus, we see that the HT works reasonably well for a set of points including some "perfect" alignments, although the precision is always limited by the size of the cells.

Now let us slightly distort the alignment by adding Gaussian variations from exact alignment, having zero mean and standard deviation 0.02 km, to the points in both lines (Figure 4). The sizes of the symbols are proportional to optional weights discussed later. It should be noted that small departures from alignment can cause, for points that are close together, large changes in the angle of the line through them that result in intersections that locate far from the other intersections of the line; however, for distant points the angle does not change very much and intersections locate close to the location of the original line.

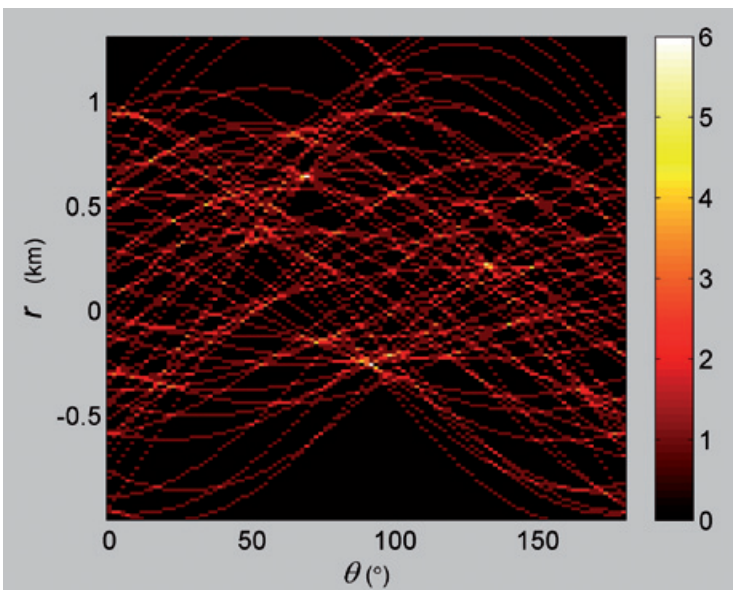

Figure 3. Accumulator cells in Hough space corresponding to the HT of the first sample set of points

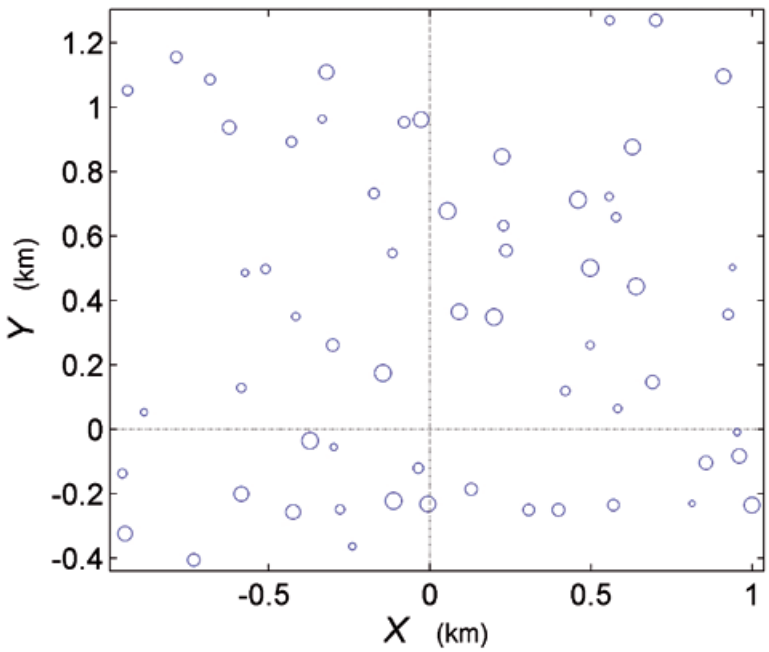

Figure 4. Second sample set of points in observational space; the set includes two subsets of imperfectly aligned points.

The HT, shown in Figure 5, is now quite complicated, there are more cells with relatively high q, but the maximal numbers have decreased. The overall difference between high and low values is less than it should be. There are now many candidates for alignments, and the transform is incapable of distinguishing which are the high values which correspond to true, but noisy, alignments.The problem, of course, is that curves corresponding to points along a given line, but not exactly on it, do not intersect at a single point, and some of these curves may cross in different cells, which complicates the inherent ambiguity in using cells. When intersection points are located near the border(s) of a cell, they will be distributed among several cells, so the HT results depend on the actual location of the cells. If larger cells are used, to ensure that all intersections fall within the same cell, this results in less precise results, since parameter values can only be determined within $\pm\Delta\theta/2$ and $\pm\Delta r/2$.

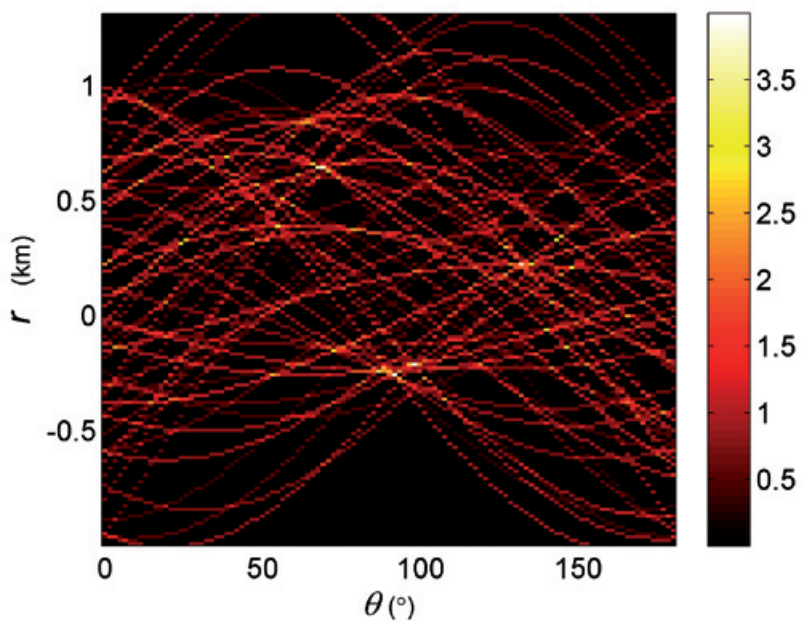

Figure 5. Accumulator cells in Hough space corresponding to the HT of the second sample set of points. Note that maximum values have decreased from those in figure 6, and there are now many cells with relatively high values.

If smaller cells are used, the probability of having one alignment spread over several cells increases, and, most important, large values in neighboring cells cannot be used to determine the correct parameter values, because of the main flaw in the voting method of the HT: the HT cannot distinguish between lines that cross within a given cell and lines that just pass through it.

For the HT voting method, if q lines intersect within a given cell, a minimum of $2q$ incidences will occur within the 8 surrounding cells (for typical curvatures); in fact since (3) can be written as $r = \alpha \sin(\theta + \beta)$, where $\alpha = \sqrt{x_i^2 + y_i^2}$ and $\beta = \arctan(x_i / y_i)$, the absolute value of its slope cannot be larger that α, so that for points distributed all over the physical space most of these $2q+$ incidences will occur within neighboring cells having the same r value. The resulting high values, which correspond to non-intersecting lines, cannot be distinguished, a priori, from those from intersecting lines. If one tries to determine where the intersections should be by averaging over neighboring cells, the average will include both intersections and simple traversals, and is essentially meaningless.

Thus, it is clear that for non-exact alignments, like those associated with geophysical observations, a new voting method is needed.

The Intersective Hough Transform

Intersective voting

Since we are interested in the intersections of the (θ, r) curves, not on the curves themselves, we propose voting directly with the curve intersections. This we will call the Intersective Hough Transform (IHT)

From equation (3), the cosenoids for points (x_i, y_i) and (x_j, y_j) intersect at θ_{ij} such that

$$x_i \cos(\theta_{ij}) + y_i \sin(\theta_{ij}) = x_j \cos(\theta_{ij}) + y_j \sin(\theta_{ij})$$

so that

$$\theta_{ij} = \arctan\left(\frac{x_i - x_j}{y_j - y_i}\right) \tag{4}$$

and the corresponding is given by

$$r_{ij} = x_i \cos(\theta_{ij}) + \sin(\theta_{ij}) = x_j \cos(\theta_{ij}) + y_j \sin(\theta_{ij}) \tag{5}$$

We will vote by increasing the value only for cells within which fall the intersection coordinates (θ_{ij}, r_{ij}).

Figure 6 shows the accumulator cells from intersective voting for the same point set of Figure 2, using, for illustration purposes, the same cell sizes as for the HT (as will be explained below, the IHT works better with cells much smaller than those for the HT). Note that there are only two cells with large values, and a comparison with Figure 3 shows how much clearer straight-line identification is with the IHT. Also, the quantification of the alignments is much more reliable and straightforward, since there is no noise from lines that do not correspond to intersections.

Voting with intersections also results in much better definition of cells corresponding to lines, because an alignment of p points, which results in $q \le p$ HT votes ($q = p$ only if the alignment is perfect and all curves cross within the same cell), will result in $q \le p\,(p\text{-}1)\,/\,2$ IHT votes, a number which grows very fast compared to p for $p > 3$; compare the q (color) scales in Figures 3 and 6.

It is for noisy data that the IHT proves even more advantageous, because it allows better definition by using smaller cells. After a run with large cells to identify the approximate location intersection clusters for each alignment, much smaller cells can be used; then intersections will be spread among many cells as shown in Figures 7 and 8, but this is now no problem, since these cells can be combined to correctly identify the alignment.

Let q_{mn} be the number of intersections falling in the cell located in column m and row n, and let L be the set of indices of a group of (neighboring) cells containing all or most of the intersections from a given line (the group may easily be chosen interactively, as in Figure 8, or automatically). The total value assigned to the alignment is

$$q_L = \sum_{(m,n)\in L} q_{mn} \tag{6}$$

and the alignment parameters can be estimated as

$$\theta_L = \frac{1}{q_L} \sum_{(m,n)\in L} \theta_m^c q_{mn}, \quad r_L = \frac{1}{q_L} \sum_{(m,n)\in L} r_n^c q_{mn} \tag{7}$$

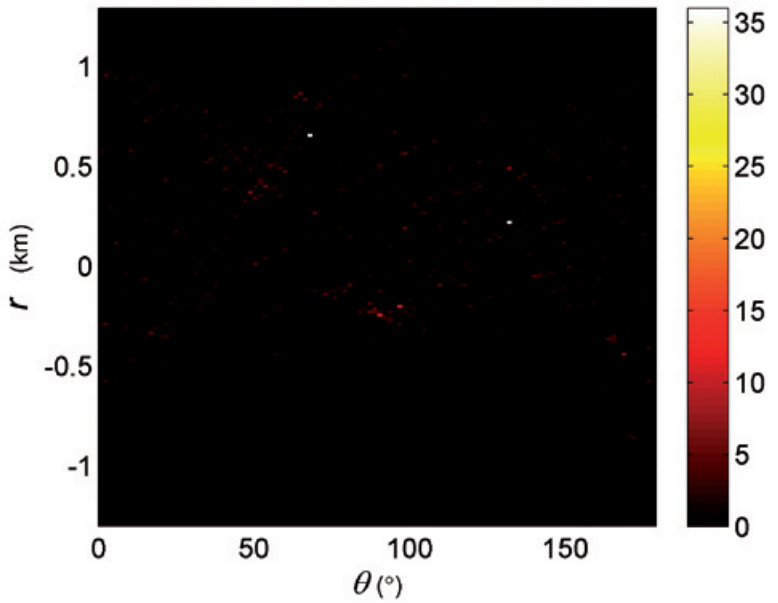

Figure 6. Accumulator cells in Hough space corresponding to the IHT of the first sample set of points. Note that only two points are clearly significant, and that their values are much higher than those of Figure 6.

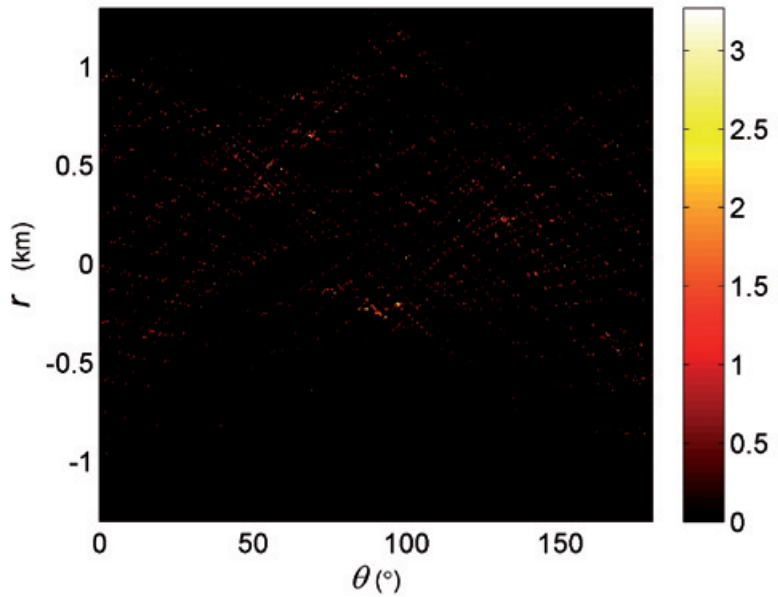

Figure 7. Accumulator cells in Hough space corresponding to the IHT of the second (misaligned) sample set of points, for small cells with $\Delta\theta$ = 4º and Δr = 0.01km.

where θ_m^c and r_m^c are the and r values corresponding to the middle of the cells in column m and row n, respectively. Thus, cell sizes for the IHT can be smaller than for the HT, and their location is not as critical.

Figure 8 shows a close-up of the cells having contributions from the example alignments, and the rectangles, chosen interactively, contain the cells which are used to estimate the alignment parameters. The left picture corresponds to intersections for line 1, which yield the very good estimates $\theta_{L1} = 131.840^o$, $r_{L1} = 0.222$km, with $q_{L1} = 34$, that correspond to line $y = 0.299 + 0.895x$. From the selected cells in the picture on the right, parameters for the second line are estimated as $\theta_{L2} = 68.212^o$ and $r_{L2} = 0.648$km, with $q_{L2} = 42$, which correspond to line $y = 0.698 - 0.400x$. The (cyan) diamond in each picture indicates de estimated (θ, r) value for each line, while the (blue) circle shows the true value.

The estimated alignments are plotted in Figure 9 together with the true ones; it is clear that estimated is almost indistinguishable from true.

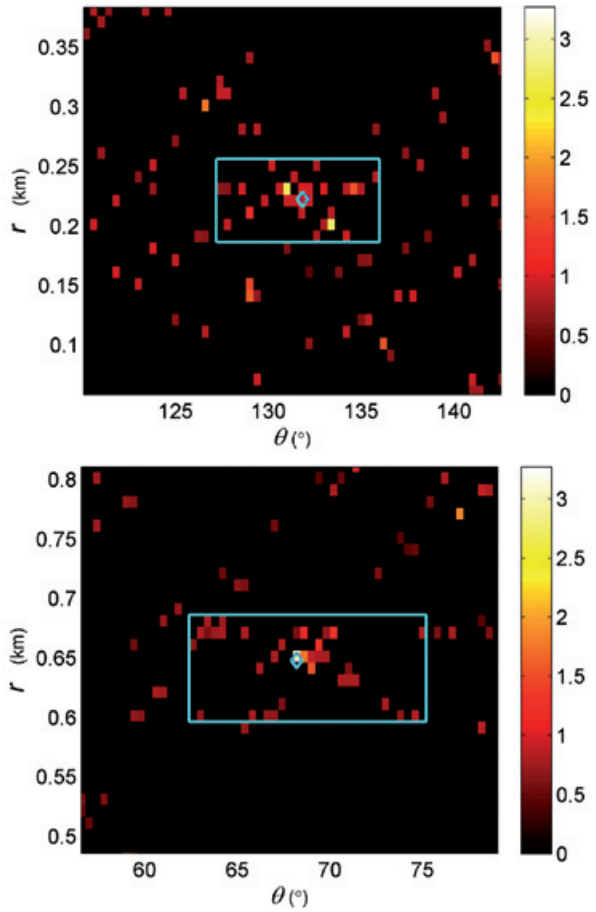

Figure 8. Close-up of the accumulator cells used for determining the values of the parameters of lines 1 (top) and 2 (bottom). The rectangles contained the cells used, the determinations are shown as diamonds, and the true values are indicated by circles

The cluster intersective hough transform

Accumulator cells can be dispensed with, by directly identifying clusters of (θ_{ij}, r_{ij}) intersection points and using their centers of mass (or expected values) to estimate the parameters of straight lines in the space. We will call this the Cluster Intersective Hough Transform (CIHT).

A cluster is a set of points all of which are within some $\Delta\theta$ and Δr of another member of the set. These proximity criteria are chosen so as to optimize results for each particular r range and misalignment level; for the example shown here $\Delta\theta = 1.4°$ and $\Delta r = 0.0175$km.

The cluster approach has the further advantage that the Hough space coordinates used for estimating the parameters of a given cluster are the actual values for each intersection belonging to the cluster, not the average values for some cell. We work with a list of instersection locations, instead of with a matrix of accumulator cells. Thus, once the set L of index pairs belonging to a given cluster has been determined, the parameters of the corresponding alignment can be estimated directly as:

$$q_L = \sum_{(i,j)\in L} 1 \tag{8}$$

the total number associated with the cluster, and

$$\theta_L = \frac{1}{q_L}\sum_{(i,j)\in L}\theta_{ij}, \quad r_L = \frac{1}{q_L}\sum_{(i,j)\in L} r_{ij} \tag{9}$$

where θ_{ij} and r_{ij} are the intersection values from equations (4) and (5).

An additional advantage of this approach is that practical uncertainty estimates of the determined parameters can be calculated from the standard deviations of the intersection parameters. In what follows, the error margins indicated correspond to one standard deviation.

Figure 10 shows close-ups of the (automatic) cluster determinations for our example noisy alignments. The diamonds indicate the locations of the estimated parameters,

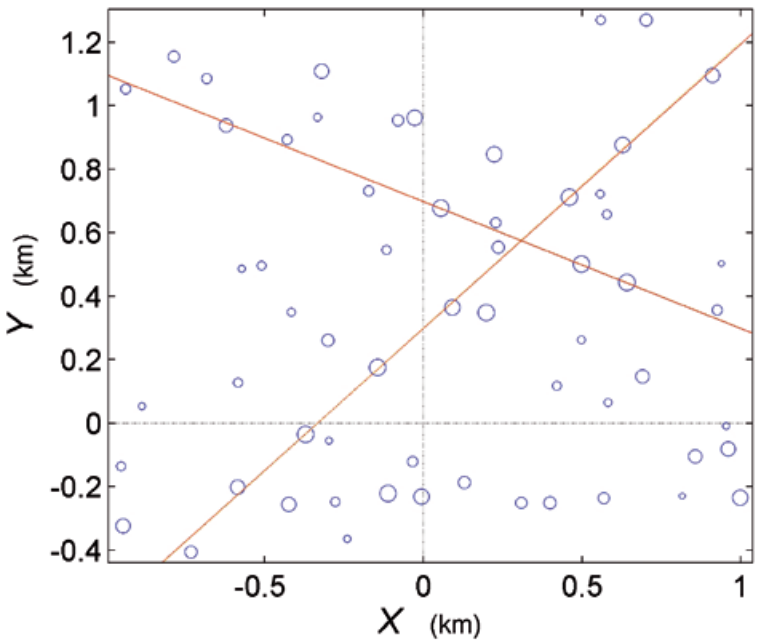

Figure 9. Data points and alignments; straight (red) lines are those identified using the IHT, dashed lines are the true lines

where the short horizontal and vertical lines indicated the neighboring criteria (the same for both alignments) and crosses represent the intersections.

For Line 1, the estimated parameters are: $\theta_{L1} = 131.830 \pm 2.566°$, and r_{L1} 0.221 ± 0.014 km, with $q_{L1} = 33$, which correspond to the line $y = 0.297 \pm 0.0009 + (0.895 \pm 0.065)x$. For Line 2, the estimated parameters are: $\theta_{L2} = 68.649 \pm 0.995°$ and $r_{L2} = 0.655 \pm 0.009$ km, with $h_v = 18.382$, $q_{L1} = 21$, which correspond to the line $y = 0.704 \pm 0.015\text{-}(0.391 \pm 0.020)x$.

The resulting alignments are shown in Figure 11, together with (and for all practical purposes indistinguishable from) the true alignments.

A fortuitous alignment of the randomly positioned events is shown as a dashed line in figure 11.

Weighted Voting

The concept of weighted voting is an optional feature of the IHT and the CIHT, and can also be applied to the HT. It should be emphasized that weighted voting is not essential for intersective voting.

Usually the quality or reliability or representativity is not homogeneous for a given set of data, and this is always the case for geophysical data. For epicentral or hypocentral locations the goodness or reliability depends on many factors, such as the signal to noise ratio, the seismographic coverage, the character, impulsive or emergent, of seismic phase arrivals, etc.; because of this, locations of large earthquakes are usually more reliable than those of small earthquakes. Most location programs give estimates of inversion residuals and location quality or uncertainty. Also, large earthquakes that break large areas of a fault may be considered to be more representative of the fault.

Thus, weights can be assigned to data in order to ensure that results depend heavily on good data, while poor quality data can be made less important, or even irrelevant. So, let us suppose that each datum in physical space is assigned a weight, for the i'th point. Weights can take any values, but using weights in the [0, 1] range allows a straightforward interpretation of results. If no weighting is desired, then weights can be given all the same value (unity by preference).

For the data along the lines in the example set, weights have been assigned depending on the size of the mislocation errors, while non-aligned events have been assigned random weights. Data points physical space are plotted, from Figure 4 on, with symbol sizes proportional to their weights.

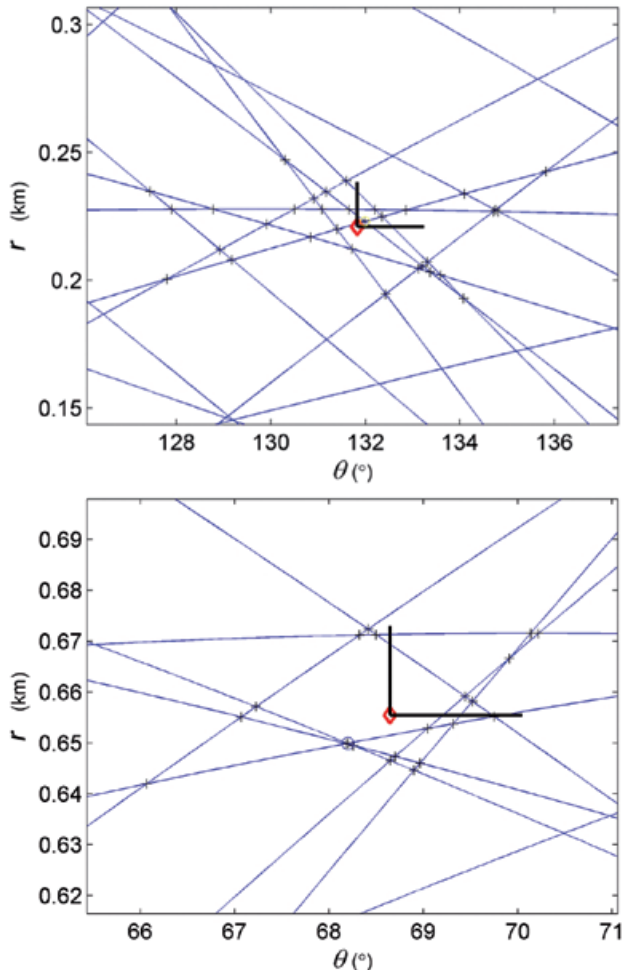

Figure 10. Close-up of the clusters used for determining the values of the parameters of alignments 1 (top) and 2 (bottom) in the example of imperfectly aligned data. The crosses represent the used intersections (sections of the cosenoid curves are shown for illustration purposes only; they are not used in the analysis), the parameter determinations are indicated by diamonds, and the circles show the locations of the true values.

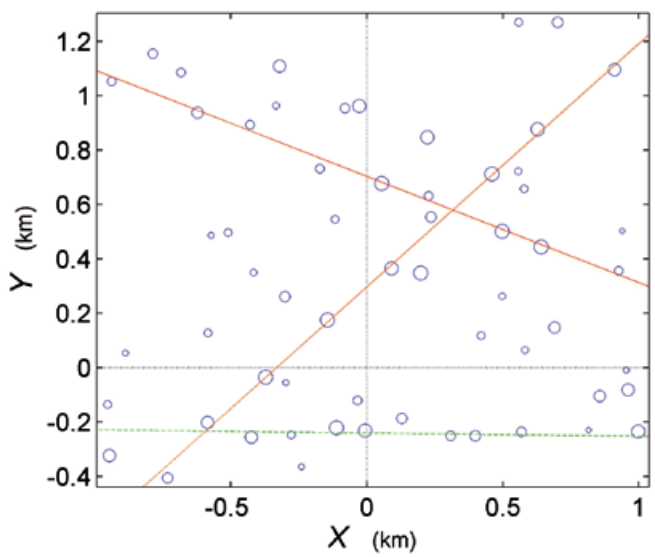

Figure 11. Data points and alignments; straight (red) lines are those identified using the CIHT, dashed lines are the true lines. The dashed (green) line is an example of fortuitous alignment.

For the HT, instead of increasing by one the value in each accumulator cell the i'th curve crosses, the value is increased by the weight .

For both the IHT and the CIHT, the vote of each intersection, (θ_{ij}, r_{ij}) can be weighted as

$$w_{ij} = \sqrt{w_i w_j} \tag{10}$$

so that intersections involving data with zero weight will have zero weight themselves, while intersections involving data having equal weights will have the same weight as each of the data.

For the IHT, Let w^c_{mn} be the sum of the weights of the intersections falling in the cell located in column m and row n, and let L be the set of indices of a group of (neighboring) cells containing all or most of the intersections from a given line. The total value assigned to the alignment is

$$w_L = \sum_{(m,n)\in L} w^c_{mn} \tag{11}$$

and the alignment parameters can be estimated as

$$\theta_L = \frac{1}{w_L}\sum_{(m,n)\in L} \theta^c_m w^c_{mn}, \quad r_L = \frac{1}{w_L}\sum_{(m,n)\in L} r^c_n w^c_{mn} \tag{12}$$

where θ^c_m and r^c_m are the θ and r values corresponding to the middle of the cells in column m and row n, respectively.

For the CIHT, if L is the set of indices of intersections belonging to a given cluster in Hough space, the alignment parameters can be estimated directly as:

$$w_L = \sum_{(i,j)\in L} w_{ij} \tag{13}$$

the total weight associated with the cluster, and

$$\theta_L = \frac{1}{w_L}\sum_{(i,j)\in L} \theta_{ij} w_{ij}, \quad r_L = \frac{1}{w_L}\sum_{(i,j)\in L} r_{ij} w_{ij} \tag{14}$$

where θ_{ij} and r_{ij} are the intersection values from equations (4) and (5).

For weights all equal to unity, equations (11) to (14) are equivalent to equations (6) to (9).

When using weights, both q_L and w_L can be used to have two slightly different characterizations or gradings of the estimated parameters, and the w_L / q_L ratio evaluates the relative quality of the data actually used for parameter identification.

Actually, the IHT and CIHT determinations shown above were done using weights, and the corresponding estimates are: $w_{L1} = 29.31$ and $w_{L2} = 31.44$ for the IHT, and $w_{L1} = 29.31$ and $w_{L2} = 16.21$ for the CIHT.

Conclusions

The Intersective Hough Transform (IHT), based on voting directly with the intersections of the cosenoids corresponding to each pair of points in observation space, yields a much clearer transform, where each non-zero value is significant. The IHT allows (much) smaller accumulation cells that can be grouped together to yield better estimates than those from the traditional Hough transform (HT). The Cluster Interceptive Hough Transform (CIHT) works without accumulator cells and allows estimating the uncertainty in the determination of each line; the CIHT can be completely automated.

Trials using synthetic data sets show that, for exact alignments, both IHT and CIHT give almost exact determinations, generally better than those from the traditional HT, even in the presence of noise consisting of large numbers of randomly located points. For inexact alignments the number of coinciding or clustering intercepts decreases according to the how much the locations depart from exact alignment; in some of these cases, and when random points are many, fortuitous alignments of random points may have total values larger than those of the desired alignments, but usually these are still recognizable. In all cases IHT and CIHT alignment identification performance is superior to that of the traditional HT.

Acknowledgments:

The author wishes to express his thanks to the reviewers and the editor.

References

Ballard D., 1981, Generalizing the Hough transform to detect arbitrary shapes. *Pattern Recognition*, 13 111-122.

Duda R., Hart P., 1972, Use of the Hough transformation to detect lines and curves in pictures. Communications of the Association for *Computing Machinery*, 15 11-15.

Fernandes L., Oliveira M., 2008, Real-time line detection through an improved Hough transform voting scheme. *Pattern Recognition,* 41 299-314.

Furukawa Y., Shinagawa Y., 2003, Accurate and robust line segment extraction by analyzing distribution around peaks in Hough space. *Computer Vision and Image Understanding,* 92 1-25.

Hart P., 2009, How the Hough transform was invented. *IEEE Signal Processing Magazine* 26 18-22.

Hough P., 1959, Machine Analysis of Bubble Chamber Pictures. *Proc. Int. Conf. High Energy Accelerators and Instrumentation*, 1959.

Illingworth J., Kitler J., 1988, A survey on the Hough transform. *Computer Vision, Graphics, and Image Processing,* 44 87-116.

Kiryati N., Eldar Y., Bruckstein A., 1991, A probabilistic Hough transform. *Pattern Recognition,* 24 303-316.

Li H., Lavin M., LeMaster R., 1986, Fast Hough transform: A hierarchical approach. *Computer Vision, Graphics, and Image Processing,* 36 139-161.

O'Gorman F., Clowes M., 1976, Finding picture edges through collinearity of feature points. *IEEE Transactions Computers*, 25 449-45.

Shapiro L., Stockman G., 2001, Computer Vision. Prentice-Hall, Inc.

Wikipedia, http://en.wikipedia.org/wiki/Hough_transform. Accessed 20 November 2012.

Geofísica Internacional (2014) 53-3: 333-341

Original paper

Density modeling of the Escollos Alijos Seamount from inversion of its geoid undulation anomaly

Juan García-Abdeslem

Received: September 20, 2013; accepted: March 20, 2014; published on line: July 01, 2014

Resumen

El Monte Marino Alijos se localiza en el Océano Pacífico nororiental a unos 300 km de la Península de Baja California. La edad y el análisis geoquímico de las rocas volcánicas que coronan este gran monte marino indican magmatismo reciente, que ha resultado de un proceso de diferenciación magmática a partir de magma basáltico medianamente alcalino.
El Monte Marino Alijos está situado hacia el borde oriental de un mínimo de ondulación geoidal, de gran longitud de onda, que alcanza -47 m con respecto al elipsoide del WGS84, y que se extiende sobre el Océano Pacífico nororiental. Restando de la ondulación geoidal su componente de gran longitud de onda y la ondulación debida a la topografía del monte marino, persiste una anomalía de ondulación negativa que indica un déficit de masa a profundidad. La inversión lineal de ésta anomalía de ondulación sugiere una región caracterizada por un contraste en densidad negativo, localizado por debajo del monte marino a profundidad entre 9 y 13 km.
La edad y composición química del monte marino y el déficit de masa inferido, sugieren que existe magma atrapado entre la corteza oceánica y el manto superior, que explica la actividad magmática en tiempos recientes.

Palabras clave: Monte Marino Alijos, ondulación geoidal, modelación inversa, magmatic underplating.

Abstract

Escollos Alijos is a large seamount located in the NE Pacific Ocean about 300 km off the Baja California Peninsula. Geochronology and geochemical analysis of volcanic rocks capping the seamount indicate recent magmatism that resulted from extensive differentiation of a mildly alkalic basalt parent magma.
Escollos Alijos is located towards the eastern edge of a long-wavelength geoid undulation minimum, of up to -47 m with respect of the WGS84 ellipsoid, which extends over the northeastern Pacific Ocean. Subtracting from the geoid undulation its long-wavelength component and the undulation due to the seamount topography itself, a negative undulation anomaly persists that indicates a mass deficit at depth. Linear inversion of the undulation anomaly yields a region characterized by a negative density contrast, localized under the seamount at a depth between 9 and 13 km.
The age and chemical composition of Escollos Alijos, and the inferred mass deficit suggest magma trapped between the oceanic crust and the uppermost mantle, which explains the magmatic activity in recent times.

Key words: Escollos Alijos Seamount, inverse modeling, geoid undulation, magmatic underplating.

J. García-Abdeslem
CICESE
División de Ciencias de la Tierra
Departamento de Geofísica Aplicada
Carretera Tijuana Ensenada No. 3918
Fraccionamiento Zona Playitas
Ensenada, 22860
Baja California, México
Corresponding author: jgarcia@cicese.mx

Introduction

The Escollos Alijos seamount is located at 24º 50'N latitude and 115º 34'W longitude, about 300 km off the western continental margin of the Baja California peninsula (Figure 1). The bathymetry shows that the seamount is a compound of two flat-topped edifices, about 60 km by 40 km long at its base, and it sits on the seafloor at a depth of ~ 4000 m. On the sea surface Escollos Alijos consists of three craggy pinnacles, which rise to a maximum of 30 m above sea level over an area of about 1000 m^2.

Davis *et al*. (1995) describe these rocks as europium-deficient trachyte that evolved by differentiation from a mildly alkalic parent basalt, and has laser fusion $^{40}Ar/^{39}Ar$ age of 270 ± 16ka. These authors point out that the chemical composition of the volcanic rocks from Escollos Alijos is similar to that of Guadalupe Island (Figure1). Batiza (1977) describes Guadalupe Island as an alkalic basalt seamount formed on a NS oriented spreading center with K-Ar age of 7.0 ± 2.0 Ma. Later, Batiza *et al*. (1979) reported $^{40}Ar/^{39}Ar$ ages of 5.4 ± 0.8 Ma and 3.7 ± 0.4 Ma, as well as some volcanic rocks that were too young to be dated.

Marine magnetic anomalies (Lonsdale, 1991, Figure 9) suggest that Escollos Alijos sits on a 16-17 Ma old sea floor (Chron 5C), at about 200 km from the Pacific–Farallon Ridge (Figure 1) that stopped spreading in mid-Miocene time, about 12 Ma ago, while Guadalupe and Magdalena plates stopped subducting. Escollos Alijos is elongated in the EW direction, parallel to a fracture zone (Figure 1) inferred by Lonsdale (1991) from marine magnetic anomalies. From the trachyte composition of rocks capping Escollos Alijos, and from magmatic activity in recent times, we may expect low-density magma in a localized magmatic chamber at depth, where differentiation takes place.

Except for work reported by Davis *et al*. (1995) and sparse marine gravity and magnetic data along ship tracks, Escollos Alijos Seamount and its surroundings remain unexplored. However, a homogeneous coverage of geoid undulations and free-air gravity anomalies from satellite altimetry with a spatial resolution of 1 arc minute, are available.

The geoid undulation from the Earth Gravitational Model 2008 (EGM2008) (Pavlis *et al*., 2012) over the northeastern Pacific Ocean

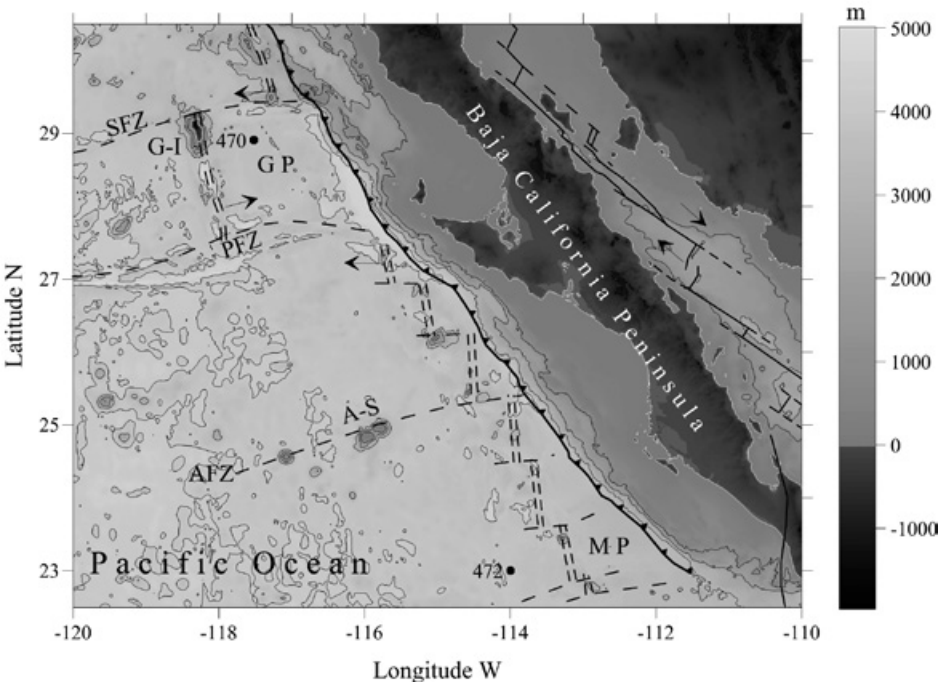

Figure 1. Study area showing bathymetry and topography at a contour interval of 1000 m. Tectonic features of the Pacific Plate off Baja California adapted from Lonsdale (1991). The dashed lines represent fracture zones: Shirley (SFZ), Popcorn (PFZ) and Alijos (AFZ). Solid triangles indicate the fossil Cedros subduction zone. Remnants of Farallon plate: Guadalupe (GP) and Magdalena (MP) micro plates. Circles show DSDP holes 470 and 472. G-I is Guadalupe Island and A-S is Alijos seamount.

(Figure 2) is characterized by a long-wavelength elliptically shaped -47 m minimum referred to the World Geodetic System (WGS84) ellipsoid. The geoid undulation highlights several fracture zones, roughly oriented in an E-W direction, plus many seamounts.

Geoid undulations are due to density anomalies, as the geoid is warped up above mass excesses and down above mass deficiencies. Long-wavelength geoid features, as shown in Figure 2, have been attributed to density variations from mantle convection (McKenzie, 1983). Several long linear features shown in Figure 2, such as the Mendocino and the Tehuantepec fracture zones, among others, disrupt this geoid minimum. Since seamounts may be associated with short-wavelength geoid undulations, where the geoid is warped up, in this work I use geoid undulation data from the EGM2008 to infer, from linear inverse modeling, the subsurface density structure of Escollos Alijos.

The residual geoid undulation

In order to extract the geoid signal due to Escollos Alijos, one must estimate and remove the long-wavelength elliptical geoid undulation, attributed to density variations deep in the mantle. A review of geophysical applications of satellite altimetry (Cazenave and Roger, 2001) describes a widely used approach to estimate long-wavelength geoid undulations from geopotential solutions developed in spherical harmonics, up to a low degree of expansion (Sandwell and Renkin, 1988; Hager and Richards, 1989; Hager and Clayton, 1989). Another approach consists of applying a 2-D low-pass filter to gridded geoid data (Cazenave *et al*., 1992, 1996).

To extract the geoid undulation due to Escollos Alijos, an estimate of the long-wavelength component of the geoid was found by fitting, in the least squares sense, a bilinear polynomial surface to the geoid undulation from the EGM2008, in the vicinity of Escollos Alijos. The bilinear surface (Figure 3) nearly follows the long-wavelength geoid undulation trend, and was assumed that this surface locally represents the long-wavelength geoid undulation. This surface was subtracted from the EGM2008 geoid undulation to obtain a residual geoid undulation (Nr). The geoid undulation, the bilinear polynomial surface, and the residual geoid undulation in the vicinity of Alijos Seamount are shown in Figure 4.

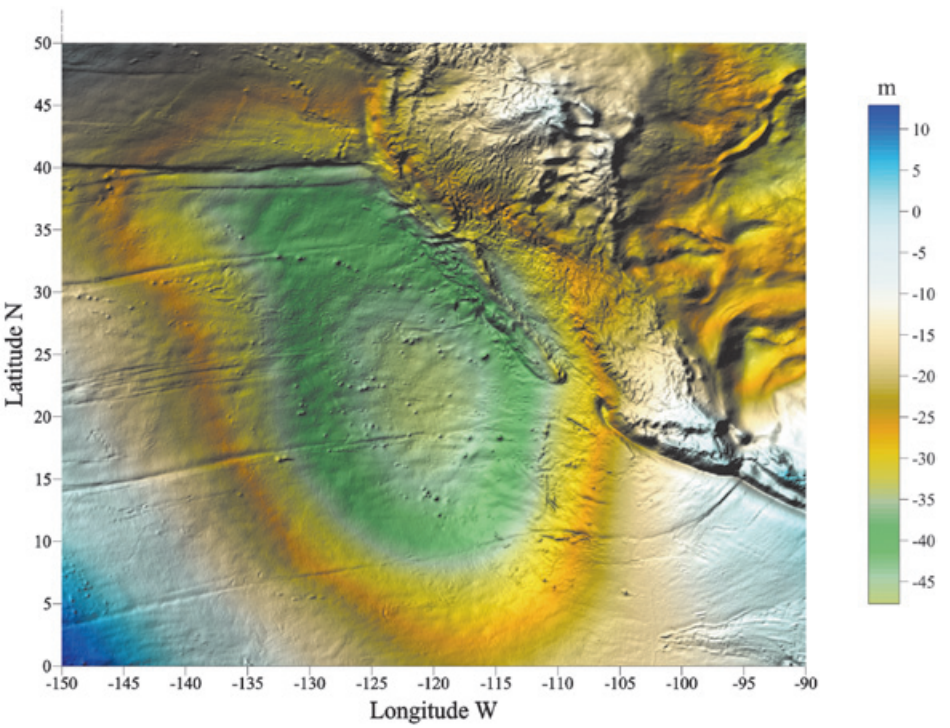

Figure 2. Geoid undulation from the Earth Gravity Model 2008 (EGM2008) over the northeastern Pacific Ocean, exposing seamounts, oceanic islands, and fracture zones. The undulation associated to these physiographic features is within a long-wavelength undulation-minimum, with elliptical signature, that reaches about -47 m with respect of the WGS84 ellipsoid.

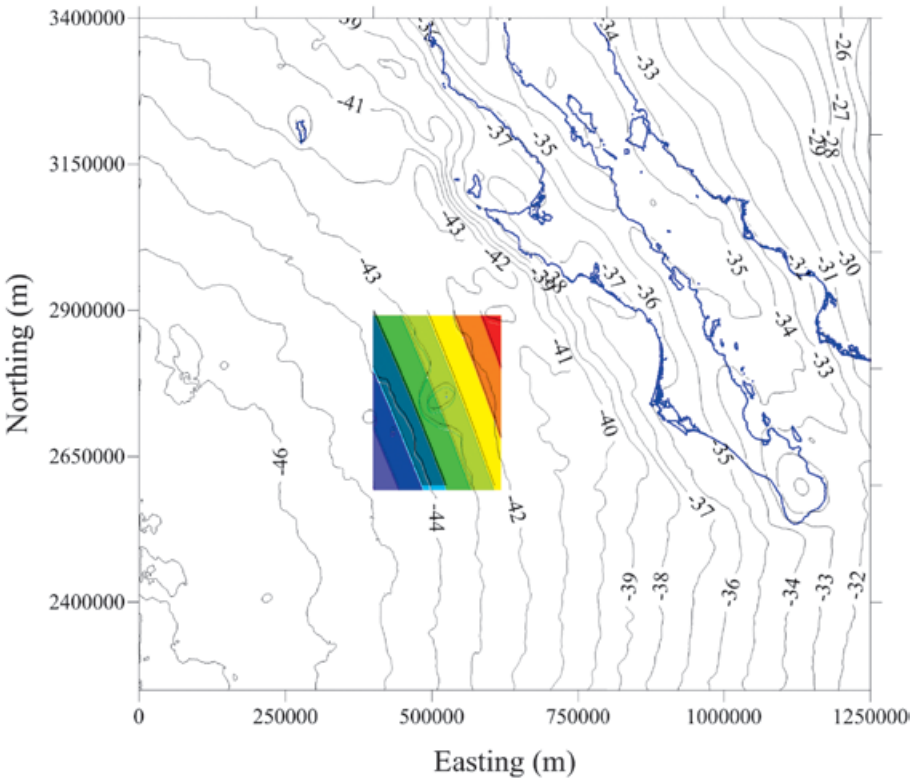

Figure 3. The geoid undulation in a TM projection, with central meridian at -116° W longitude and false East at 500000 m. Contour lines in m with respect to the WGS84 ellipsoid. The colored zone, in the vicinity of Alijos seamount, is a bilinear surface that locally represents the long-wavelength geoid undulation.

The residual undulation (Figure 4c) is an elliptical feature with amplitudes varying from -0.273 to 1.877 m. In the following section a solution to Bruns equation is derived to calculate the undulation due to a prism of constant density. This solution will later be used to discern if the residual undulation may be explained by the seamount topography alone.

Undulation due to a prism of constant density

The undulation N at the point $P(x_0, y_0, z_0)$ caused by a prism of density ρ bounded by the planes $x = x_1, x_2$; $y = y_1, y_2$; $z = z_1, z_2$, is found from solving Bruns equation

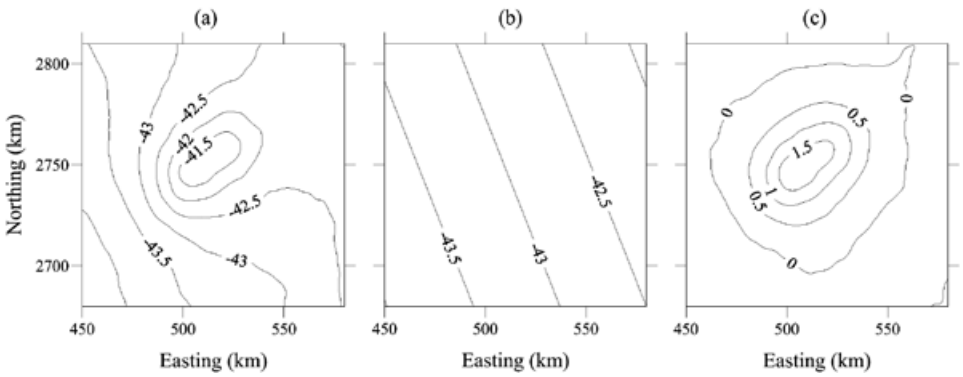

Figure 4. Data processing sequence to obtain the undulation anomaly in the vicinity of Alijos seamount: (a) Geoid undulation, (b) bilinear surface that represents the long-wavelength geoid undulation, (c) residual geoid undulation. All contour lines are shown in m with respect of the WGS84 ellipsoid.

$$N_P = \frac{G\rho}{g}\int_{x_1}^{x_2} dx \int_{y_1}^{y_2} dy \int_{z_1}^{z_2} dz \frac{1}{R} \ , \qquad (1)$$

where $g = 9.81$ [ms^{-2}] is the normal gravity, $G \approx 6.674$ x 10-11 [$m^3kg^{-1}s^{-2}$] is Newton's gravitational constant, $R = (X^2+Y^2+Z^2)^{1/2}$; $X = x - x_0$, $Y = y - y_0$, and $Z = z - z_0$. As $dX = dx$, $dY = dy$, $dZ = dz$, equation (1) may be written

$$N_P = \frac{G\rho}{g}\int_{X_1}^{X_2} dX \int_{Y_1}^{Y_2} dY \int_{Z_1}^{Z_2} dZ \left[\frac{1}{R}\right] . \qquad (2)$$

The integral in (2) with respect to the Z variable was obtained from Gradshtein and Ryzhic (1980) with the following result:

$$N_p = \frac{G\rho}{g}\int_{X_1}^{X_2} dX \int_{Y_1}^{Y_2} dY \left[\mathrm{Ln}(Z+R)\right]_{Z_1}^{Z_2} . \qquad (3)$$

By partial integration, the integration of equation (3) with respect to Z yields

$$N_p = \frac{G\rho}{g}\int_{X_1}^{X_2} dX \left[Y \ln(Z+R) + Z \ln(Y+R) - X \arctan\frac{YZ}{XR}\right]_{Y_1}^{Y_2}{}_{Z_1}^{Z_2} . \qquad (4)$$

Similarly, integrating equation (4) with respect to X finally yields the desired solution

$$N_p = \frac{G\rho}{g}\left\{\left[XZ\,\mathrm{Ln}(Y+R) + YZ\,\mathrm{Ln}(X+R) + XY\,\mathrm{Ln}(Z+R)\right] - \left[\frac{X^2}{2}\arctan\left(\frac{YZ}{XR}\right) + \frac{Y^2}{2}\arctan\left(\frac{XZ}{YR}\right) + \frac{Z^2}{2}\arctan\left(\frac{XY}{ZR}\right)\right]\right\}_{X_1}^{X_2}{}_{Y_1}^{Y_2}{}_{Z_1}^{Z_2} . \qquad (5)$$

As an example, the undulation caused by a prism of constant density computed using equation (5) is shown in Figure 5.

Undulation due to Escollos Alijos and the surrounding sea floor

The undulation due to Escollos Alijos and the surrounding sea floor was computed using an array of rectangular prisms, each of 1 km by 1 km in its horizontal dimensions, in a model that includes the seamount, the sedimentary Layer 1, and the basaltic Layer 2.

In this calculation, the top of Layer 1 (Figure 6a) was defined by the bathymetry from the General Bathymetric Chart of the Oceans, and its thickness from a global estimate of sedimentary thickness by NOAA (<www.ngdc.noaa.gov/mgg/sedthick/>). The top of Layer 2 is conformable to layer 1 and its bottom extends down to 4200 m below sea level, just exceeding the maximum thickness of the sedimentary layer (138 m).

Densities were assumed from density-logs at sites 470 and 472 (Figure 1) from Leg 63 of the Deep Sea Drilling Project (Yates *et al*., 1970), where the stratigraphic column consists of a sequence of Neogene sediments overlying basaltic pillow lavas of MORB composition. At site 472 the density (1500 kg/m^3) and seismic P-wave velocity (1420 m/s) are nearly uniform throughout the sedimentary section down to 162 m depth, and the basaltic layer has a density of 2770 kg/m^3 and seismic P-wave velocity of 5490 m/s. At site 470 the density (1470 kg/m^3) and seismic P-wave velocity (1500 m/s) are also uniform throughout the sedimentary section down to 112 m depth, and the average density and P-wave velocity of the basaltic layer are 2790 kg/m^3 and 5510 m/s.

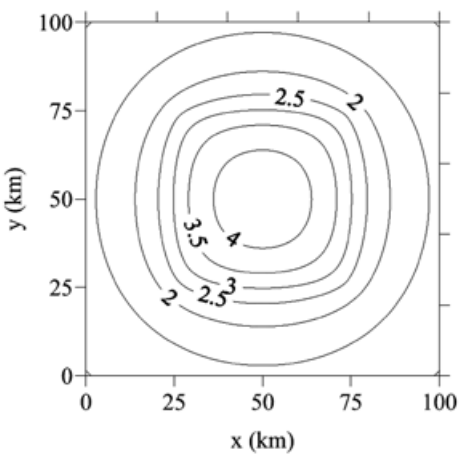

Figure 5. Undulation at the surface $z_0=0$, due to a rectangular prism with a density contrast of 1000 kg/m^3 with contours every 0.5 m. The location of the prism is indicated by the square, and it extends down from 1 to 5 km depth.

The undulation due to the sediments and the basaltic layer 2 was calculated using a density contrast with respect to the seawater density (1030 kg/m^3). The density contrast of sediments was set to 470 kg/m^3, and the density contrast of the basaltic layer 2 was set to 1750 kg/m^3. Escollos Alijos was modeled, assuming the average density of trachyte (2600 kg/m^3), with a density contrast of 1570 kg/m^3.

The undulation computed from forward modeling (Figure 6b) varies between 1.264 m and 5.201 m, and its subtraction from the residual undulation (Nr) yields the undulation anomaly (Na) shown in Figure 6c, with values that vary between -1.243 m and -3.405 m. The negative undulation anomaly indicates a mass deficit below 4200 m depth below sea level.

Studies using the teleseismic receiver function inversion technique at oceanic islands (Rarotonga, Kiribati, Tahiti, and Hawaii) with recent or active surface volcanism have found that between the lower crust and uppermost mantle, an anomalously slow seismic velocity is present, which has been interpreted as due to magmatic underplating (Leahy and Park, 2005; Leahy *et al*. 2010). The negative undulation anomaly at Escollos Alijos may also indicate magmatic underplating, as explored in the following section.

Inverse modeling the undulation anomaly

Inverse modeling of an undulation anomaly may yield an infinite number of density models. As a preferred density model (or a set of models) is desired as an outcome from the inversion, this objective is achieved by applying some regularization or physically reasonably constraints in the inverse problem (Jackson, 1979, Tarantola 2005) to find a particular solution to a non-unique inverse problem.

The geometry for the inversion is a cuboid that consists of a rectangular array of prismatic bodies. These prisms are arranged in layers; each layer has constant thickness and is constituted by a regular array of prisms. Each prism has fixed horizontal dimensions, and within every prism the density contrast is constant.

The model parameters, i.e. the density contrasts of the prisms in the cuboid, are represented by a vector $\mathbf{m}$ of dimension P that corresponds to the number of prisms in the cuboid. Vectors $\mathbf{d}$ and $\mathbf{d}_o$, of dimension Q that denotes the number of data, respectively represent the solution to the forward problem and the undulation anomaly. With this notation the solution to the forward problem may be expressed as

$$\mathbf{d} = \mathbf{A}\mathbf{m} \ , \qquad (6)$$

where each column of matrix $\mathbf{A}$ of dimension (Q, P) represents the solution of the forward problem for a prism of unit density. Assuming a priori Gaussian probability density functions for the data and model, with covariance matrices $\mathbf{C}_d$ and $\mathbf{C}_m$, respectively, a solution to equation (6) may be found minimizing the following linear functional

$$2\phi(\mathbf{m}) = \left\|\mathbf{A}\mathbf{m} - \mathbf{d}_o\right\|^2_{\mathbf{C}_d} + \left\|\mathbf{m} - \mathbf{m}_p\right\|^2_{\mathbf{C}_m} + \alpha\left\|\mathbf{D}\mathbf{m}\right\|^2 . \qquad (7)$$

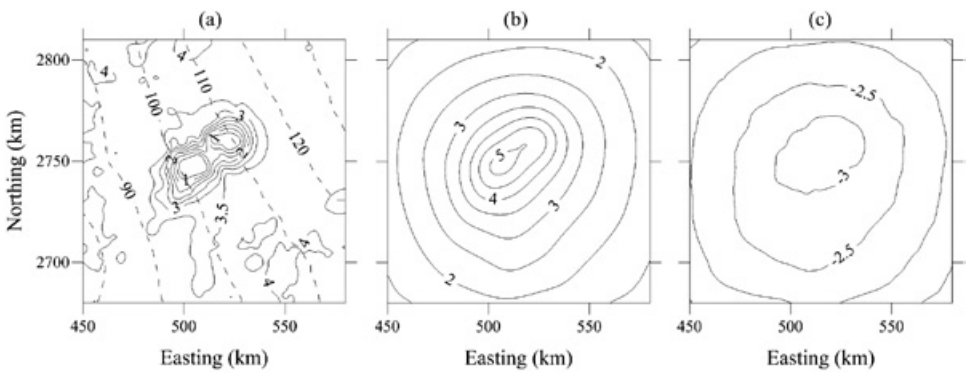

Figure 6. Graphic description of the data processing sequence: from the geoid undulation to the undulation anomaly in the vicinity of Alijos seamount. All contour lines are labeled in m, but the bathymetry that is labeled in km. (a) Bathymetry (ellipsoidal height) and thickness of the sedimentary layer with contours every 10 m. (b) Undulation caused by the sedimentary Layer 1, the basaltic Layer 2, and the seamount core down to the base-level depth at 4200 m. (c) Undulation anomaly.

The right hand side of equation (7) consist of a misfit term weighted by $\mathbf{C}_d = \varepsilon^2\mathbf{I}$, where ε^2 is the estimated data error variance, a model norm term weighted by $\mathbf{C}_m = \sigma_j^2\mathbf{I}$, where σ_j assigns a level of confidence in selected elements of the prior model $\mathbf{m}_p$, and a norm term that helps to impose smoothness in the solution, where α is a positive scalar that assigns importance to this constrain, and matrix $\mathbf{D}$, of dimension (P, P) is a first- derivative operator that acts upon the model along the x, y, and z directions. Explicitly, the functional to be minimized is

$$2\phi(\mathbf{m}) = (\mathbf{Am}-\mathbf{d}_o)^T\mathbf{Cd}^{-1}(\mathbf{Am}-\mathbf{d}_o)+(\mathbf{m}-\mathbf{m}_p)^T\mathbf{C}_m^{-1}(\mathbf{m}-\mathbf{m}_p) +(\mathbf{Dm})^T(\mathbf{Dm}). \quad (8)$$

Setting $\partial\phi(\mathbf{m})/\partial\mathbf{m}$ to zero, the solution of this inverse linear problem may be expressed as

$$\mathbf{m} = \mathbf{m}_p +(\mathbf{A}^T\mathbf{C}_d^{-1}\mathbf{A}+\alpha\mathbf{D}+\mathbf{C}_m^{-1})^{-1}\mathbf{A}^T\mathbf{C}_d^{-1}(\mathbf{d}_o-\mathbf{Am}_p). \quad (8)$$

Results of the inverse modeling

The preferred model was found using a cuboid consisting of 11 layers of constant thickness, the layer 1 from 4.2 to 5 km has a thickness of 800 m, and from layer 2 to layer 11 the thickness was set to 1 km, thus the cuboid model extends down to 15 km below sea level. Each layer consist of a regular grid of 35 by 35 rectangular prisms, and each prism has horizontal dimensions of 4 km by 4 km. The value of α was set to 1000, and the prior model for each layer and their assumed variance are listed in Table 1. The overdetermined linear inverse problem was solved with 17161 undulation anomaly data (Q), distributed in a regular grid with nodes spaced appart 1 km, assuming ε^2=0.0001 as the data error variance.

The observed and computed undulation anomalies and their misfit are shown in Figure 7. It is worth noting the smoothness of the computed undulation as compared with the undulation anomaly. The maximum misfit (Figure 7c) is located in the vicinity of Alijos seamount, where it varies between -10 and -20 cm. In the region surrounding the seamount the misfit is less than ± 5 cm. Figure 8 shows a 3D representation of the density contrast model, which varies between -293 to 15 kg/m^3 and the minimum value is found in layer 7, between 10 to 11 km depth, at the base of the oceanic crust, just under the seamount.

Table 1. 11 layers of constant thickness, listed in m, for the cuboid model. For each layer, constituted by a regular array of 35 by 35 prisms, a prior ($\mathbf{m}_p$) density contrast (kg/m^3) and variance (σ_j^2) was assumed.

Layer	Z-top	Z-bottom	$\mathbf{m}_p$	σ_j^2
1	4200	5000	0	0.0000001
2	5000	6000	-5	0.00001
3	6000	7000	-10	0.0001
4	7000	8000	-15	0.001
5	8000	9000	-20	0.01
6	9000	10000	-30	.1
7	10000	11000	-50	0.01
8	11000	12000	-100	0.001
9	12000	13000	-50	0.0001
10	13000	14000	-30	0.00001
11	14000	15000	0	0.000001

Conclusions

A negative undulation anomaly was found after subtracting from the EGM2008 geoid undulation an estimate of its long-wavelength undulation component and the undulation due to the seamount down to a base level at 4200 m depth. The linear inverse modeling of the

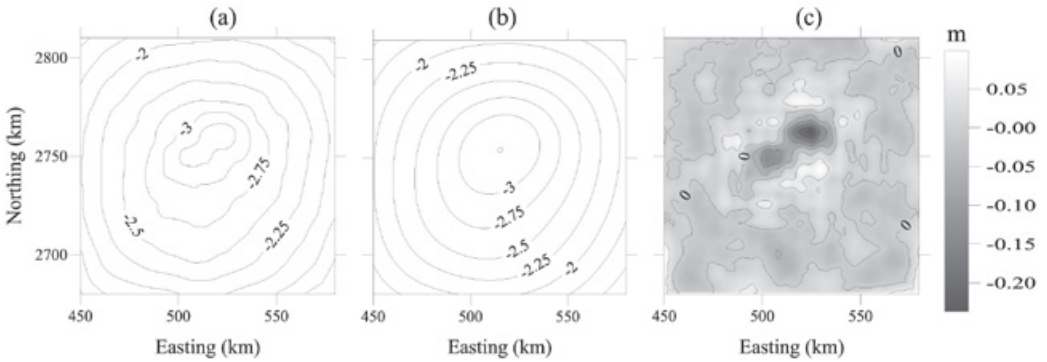

Figure 7. The undulation anomaly (a) and the calculated undulation (b) that resulted from inverse modeling are shown with contours every 0.25 m. The misfit, which has a ~ 3.5 % *rms* error, is shown (c) with contours every 5 cm.

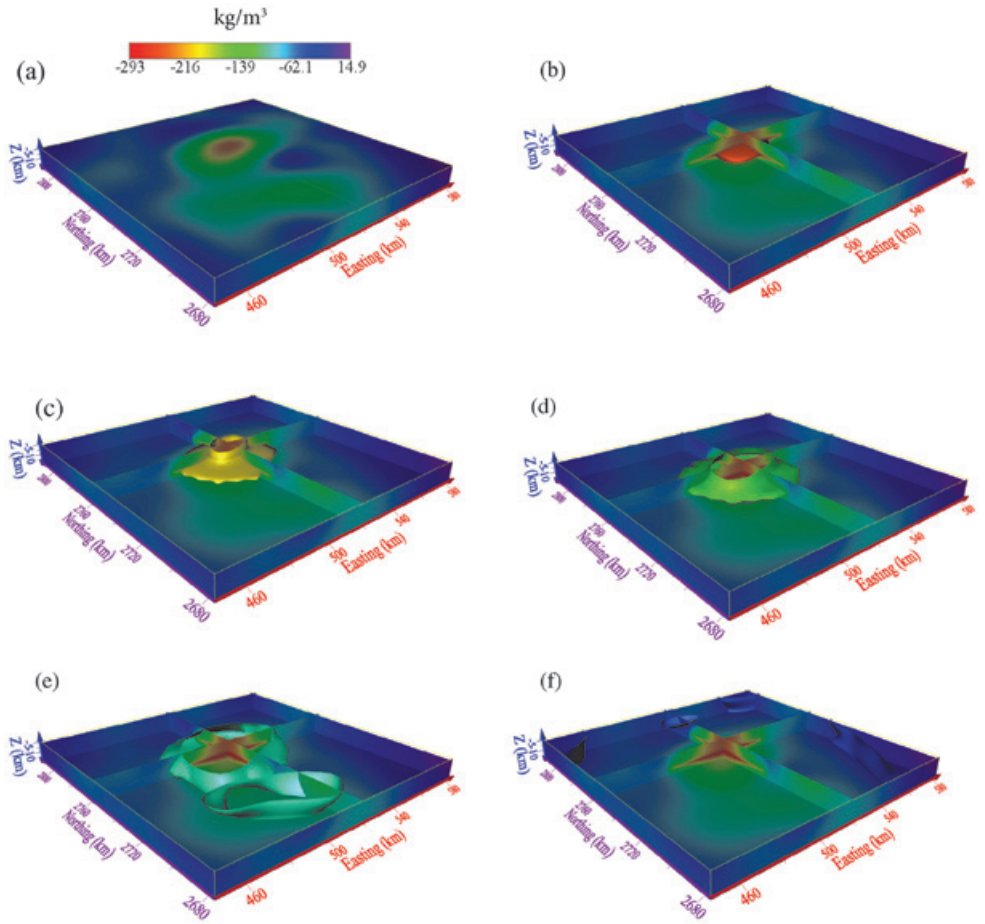

Figure 8. 3D perspective views from the SW corner of the density contrast model from a cuboid constituted by 35x35x11 prisms. The density contrast values are assumed at nodes located at the centroid of the prisms. The top surface density contrast is shown in (a). From (b) to (f) are shown *iso*-surfaces of the following density contrasts: -250, -200, -150, -100, and -50 (kg/m^3); two sections that cross the model at the minimum density contrast show the interior of the model.

undulation anomaly yields a localized region with negative density contrast, situated at the base of the oceanic crust, which is interpreted as the possible source of the magma that sustains volcanic activity at Escollos Alijos in recent times. The mass deficit that produces the negative undulation anomaly, in addition to the young magmatic activity at Escollos Alijos and its chemical composition, supports the possibility of magmatic underplating at Escollos Alijos.

Acknowledgements

I gratefully acknowledge the review and comments by Alejandro Nava, Cinna Lomnitz, one anonymous reviewer, and the technical support by Victor Frías, Sergio Arregui and Julián Delgado. I acknowledge the work of the EGM2008 development team and the public release of geoid undulation data. This research was financed with fiscal funds provided to CICESE by Mexico's Federal Government.

References

Batiza R., 1977, Petrology and geochemistry of Guadalupe Island: An alkalic seamount on a fossil ridge crest: *Geology*, 5, 760-764.

Batiza R., Bernatowicz T.J., Hohenberg C.M., Podosek F.A., 1979, Relations of noble gas abundances to petrogenesis and magmatic evolution of some oceanic basalts and related differentiated volcanic rocks. *Contributions to Mineralogy and Petrology*, 69, 301-313.

Cazenave A., Houry S., Lago B., Dominh K., 1992, Geosat-derived geoid anomalies at medium-wavelength. *Journal of Geophysical Research*, 97, 7081-7096.

Cazenave A., Shaeffer P., Bergé M., Brossier C., Dominh K., Genero M.C., 1996, High resolution mean sea surface computed with altimeter data of ERS-1 (geodetic mission) and T/P. *Geophysical Journal International*, 125, 696-704.

Cazenave A., Roger J.Y., 2001, Applications to Marine Geophysics, *in* Satellite Altimetry in Earth Sciences, a handbook of techniques and applications (*Eds*. Fu and Cazenave). Academic Press, pp. 407-440.

Davis A.S., Gunn S.H., Bohrson W.A., Gray L.B., Hein J.R., 1995, Chemically diverse, sporadic volcanism at seamounts offshore southern and Baja California. *Geological Society of America Bulletin*, 107, 5, 554-570.

Gradshteyn I.S., Ryzhic, 1980, Table of Integrals Series and Products. Academic Press, Inc.

Hager B.H., Richards M., 1989, Long-wave-length variations in Earth's geoid, physical models and dynamical implications. *Phil. Trans. R. Soc. London*, 7328, 309-328.

Hager B.H., Clayton R.W., 1989, Constraints on the structure of mantle convection using seismic observations, flows models and the geoid: *in* Mantle Convection (W. R. Peltier, ed), Gordon and Breach, New York, pp. 657-765.

Jackson D.D., 1979, The use of a priori data to resolve non uniqueness in linear inversion. *Geophysical Journal of the Royal Astronomical Society*, 57, 1, 137-157.

Leahy G.M., Park J., 2005, Hunting for oceanic island Moho. *Geophysical Journal International*, 160, 1020-1026.

Leahy G.M., Collins J.A., Wolfe C.J., Lake G., Solomon S.C., 2010, Underplating of the Hawaiian Swell: evidence from teleseismic receiver functions. *Geophysical Journal International*, 183, 313-329.

Lonsdale P., 1991, Structural patterns of the Pacific seafloor offshore of peninsular California: *in* The Gulf and Peninsular Province of the Californias. (Eds. J. P. Dauphin and B. Simoneit): American Association of Petroleum Geologist, Memoir 47, pp. 87-125.

Pavlis N.K., Holmes S.A., Kenyon S.C., Factor J.K., 2012, The development and evaluation of the Earth Gravitational Model 2008 (EGM2008). *Journal of Geophysical Research*, 117, B04406, doi:10.1029/2011JB008916.

McKenzie D.P., 1983, The Earth's mantle: Scientific American, 249**,** 3, 50-67.

Sandwell D.T., Renkin M.L., 1988, Compensation of swells and plateaus in the North Pacific: no direct evidence from mantle convection. *Journal of Geophysical Research*, 87, 3949-3958.

Tarantola A., 2005, Inverse Theory and Methods for Model Parameter Estimation. Society for Industrial and Applied Mathematics.

Yeats R.S., and the scientific party, 1973, Initial Reports of the Deep Sea Drilling Project, Leg 63, Washington (U.S. Govt. Printing Office).

Geofísica Internacional (2014) 53-3: 343-363

Review

Meteorite paleomagnetism - From magnetic domains to planetary fields and core dynamos

Jaime Urrutia-Fucugauchi*, Ligia Pérez-Cruz and Daniel Flores-Gutiérrez

Received: April 02, 2014; accepted: April 29, 2014; published on line: July 01, 2014

Resumen

Los meteoritos condríticos representan los registros más tempranos de la evolución del Sistema Solar, proveyendo información sobre las condiciones, procesos y cronología de la formación de los primeros materiales sólidos, planetesimales y cuerpos diferenciados. La evidencia sobre los campos magnéticos en las etapas tempranas de evolución del sistema solar se ha obtenido a partir de estudios en meteoritos condríticos. Estos meteoritos se caracterizan por la abundancia de cóndrulos, que constituyen pequeñas esferas de silicatos de tamaño milimétrico, formadas a partir del polvo en la nebulosa y que fueron calentadas y enfriadas rápidamente. Los condrulos retienen un registro de magnetización remanente, que data del tiempo de calentamiento y enfriamiento durante la formación de cóndrulos y su acreción en planetesimales. Los estudios sobre las diferentes clases de meteoritos, incluyendo a los meteoritos condríticos ordinarios y los meteoritos condriticos carbonáceos han documentado resultados contrastantes con una rango amplio de magnitudes de los campos magnéticos en el disco protoplanetario. Ello ha dificultado definir la naturaleza de los campos magnéticos en las etapas iniciales de evolución. Los desarrollos recientes en instrumentación y técnicas de análisis de magnetismo de rocas y paleointensidades permiten una mayor precisión. Los análisis de micromagnetismo, geoquímica, petrografía y microscopía electrónica proveen de una alta resolución, previamente no disponible, para caracterizar las propiedades magnéticas e interacciones a escalas de dominio magnético. En este trabajo revisamos los estudios en cóndrulos del meteorito condrítico Allende, que revelan relaciones entre los parámetros magnéticos de histéresis y propiedades físicas. Los parámetros y cocientes de coercitividad, magnetización remanente y magnetización de saturación muestran correlaciones con la densidad y tamaño de los cóndrulos, los cuales están relacionados a la estructura interna, mineralogía, composición y morfología. Los cóndrulos compuestos, fragmentados y con anillos de recubrimiento se caracterizan por propiedades de histéresis magnética distintas, asociadas a la composición y arreglos mineralógicos y microestructuras. Los registros de magnetización remanente y las estimaciones de paleointensidades derivadas en estudios del Allende y otras condrítas carbonáceas apoyan adquisición de la magnetización bajo la influencia de campos magnéticos internos dentro de planetesimales. Los resultados apoyan una rápida diferenciación, siguiendo la formación de las inclusiones de calcio y aluminio y condrulos para formar los planetesimales. Los planetesimales se caracterizarían por una estructura diferenciada con núcleos metálicos con capacidad de dinamo autosustentable por periodos de varios millones de años. El meteorito condrítico Allende se formó y derivó de un planetesimal parcialmente diferenciado, con un núcleo de hierro capaz de sostener un campo magnético interno.

Palabras clave: Paleomagnetismo, meteoritos, campos magnéticos, dínamos, Sistema Solar.

J. Urrutia-Fucugauchi*
L. Pérez-Cruz
Programa Universitario de Perforaciones en Océanos y Continentes
Instituto de Geofísica
Universidad Nacional Autónoma de México
Coyoacán 04510
México D.F., México

D. Flores-Gutiérrez
Instituto de Astronomía
Universidad Nacional Autónoma de México
Coyoacán 04510
México D.F., México

Abstract

Meteorites represent the earliest records of the evolution of the solar system, providing information on the conditions, processes and chronology for formation of first solids, planetesimals and differentiated bodies. Evidence on the nature of magnetic fields in the early solar system has been derived from chondritic meteorites. Chondrules, which are millimeter sized silicate spherules formed by rapid melting and cooling, have been shown to retain remanent magnetization records dating from the time of chondrule formation and accretion of planetesimals. Studies on different meteorite classes, including ordinary and carbonaceous chondrites, have however provided contrasting results with wide ranges for protoplanetary disk magnetic fields. Developments on instrumentation and techniques for rock magnetic and paleointensity analyses are allowing increased precision. Micromagnetic and an array of geochemical, petrographic and electronic microscopy analyses provide unprecedented resolution, characterizing rock magnetic properties at magnetic domain scales. We review studies on chondrules from the Allende meteorite that reveal relationships among hysteresis parameters and physical properties. Coercivity, remanent and saturation remanence parameters correlate with chondrule size and density; in turn related to internal chondrule structure, mineralogy and morphology. Compound, fragmented and rimmed chondrules show distinct hysteresis properties, related to mineral composition and microstructures. The remanent magnetization record and paleointensity estimates derived from the Allende and other chondrites support remanent acquisition under influence of internal magnetic fields within parent planetesimals. Results support that rapid differentiation following formation of calcium-aluminum inclusions and chondrules gave rise to differentiated planetesimals with iron cores, capable of generating and sustaining dynamo action for million year periods. The Allende chondrite may have derived from a partly differentiated planetesimal which sustained an internal magnetic field.

Key words: Paleomagnetism, meteorites, magnetic fields, dynamos, Solar System.

Introduction

Studies of meteorites provide the earliest records concerning the conditions and evolution of the planetary system (Wood, 1988; Cameron, 1988; Lauretta and McSween, 2006). Meteorites constitute the oldest rocks preserved from the initial stages of planetary accretion. Information on the age of the solar system, conditions and chronology for formation of first solids, planetesimals and early differentiated bodies is based on studies of chondrites and other primitive meteorites (Wood, 1988; Hewins *et al*., 1996; Scott, 2007; Connelly *et al*., 2012). Chondrites are composed by millimeter sized silicate spherules named chondrules and calcium-aluminum rich inclusions (CAIs) embedded in a fine grained silicate matrix. In recent years research on the origin and evolution of the solar system has expanded, with developments from planetary missions, astronomical observations, discovery of exoplanets and theoretical and numerical simulation models. The multi-and interdisciplinary approaches and new data are providing fresh insights on the origin of planetary systems. Major questions on fundamental aspects still remain open, including conditions and chronology in the early phases.

Many studies on meteorites focused on the petrography and geochemistry, which permitted to distinguish and characterize distinct classes of meteorites. Meteorites are divided into primitive and differentiated classes, which include ordinary and carbonaceous chondrites and achondrites and iron meteorites, respectively (Weisberg *et al*., 2006). Chondrules represent molted droplets of aggregated fine silicate dust, recording transient heating events in the solar nebula (Hewins, 1997; Zanda, 2004; Scott, 2007). They show different textures and mineral assemblages, with some containing fragments of other chondrules and rare CAIs. Preservation of chondrules indicates that chondrites were not melted through their subsequent history after formation. In contrast, differentiated meteorites, which include iron and iron-silicate meteorites, were subject to various degrees of melting and metamorphism, and interpreted as derived from planetesimals later fragmented by collisions.

Understanding the early stages of planetary system evolution has remained a complex difficult task. Considerable effort is spent in characterizing the distinct classes of meteorites, which are investigated with a wide range of analytical techniques. Studies have documented new minerals and unraveled evidence on the formation and alteration histories of meteorites and parent planetesimals with increasing detail (Taylor *et al*., 1987; Nyquist *et al*., 2009; Weiss and Elkins-Tanton, 2013). The conditions and nature of processes involved in the formation of the proto-Sun, chondrules, CAIs, and early accreted planetesimals remain poorly constrained.

We review micromagnetic and microstructural studies on chondrites with particular emphasis on the Allende chondrite (Figure 1), focusing on the early magnetic fields in the solar system and how they relate to the evolution of meteorite parent planetesimals. Developments of analytical techniques and better understanding of rock magnetic properties and magnetization mechanisms are allowing improved resolution in characterizing the magnetic records of meteorites.

The nature and role of magnetic fields in the protoplanetary nebula, with formation of the proto-stars and accretionary disk had long been examined (Kulsrud, 1999; Ossendrijver, 2003; Vallée, 2011). Interest in magnetic fields and their role in the evolution of protoplanetary nebulas have been sparked by recent studies with detection of magnetic fields in accretion disks (Donati *et al*., 2005). Studies on meteorite records of the solar protoplanetary nebula have focused on characterizing magnetic properties and mineralogy and in paleointensity determinations. The magnetic field magnitude is estimated from remanent magnetization records in chondrites and individual chondrules (e.g., Butler, 1972; Nagata, 1979). Early estimates gave a wide range of field magnitudes with relatively large uncertainties, which prompted search of alternative paleointensity determination methods. In the past years, the field of meteoritics has significantly evolved and expanded. In this review we address recent developments in using micromagnetic analyses and studies on early differentiated bodies with potential for sustained internal magnetic field generation. Results from individual chondrules provide more consistent data with improved analytical resolution (Acton *et al*., 2007; Flores-Gutierrez *et al*., 2010a,b; Emmerton *et al*., 2011). Formation of differentiated bodies with iron cores and capacity for generating internal magnetic fields have added to the interest in documenting the characteristics and presence of magnetic fields in the protoplanetary nebula (Carporzen *et al*., 2010; Fu *et al*., 2012; Tarduno *et al*., 2012; Sterenborg and Crowley, 2013).

Chondritic meteorites

Chondrites are part of the primitive meteorites, characterized by the abundance of chondrules. Several classes have been distinguished in petrographic and geochemical studies. Chondrites are classified into ordinary (H, L and LL), carbonaceous (CB, CH, CI, CK, CM,

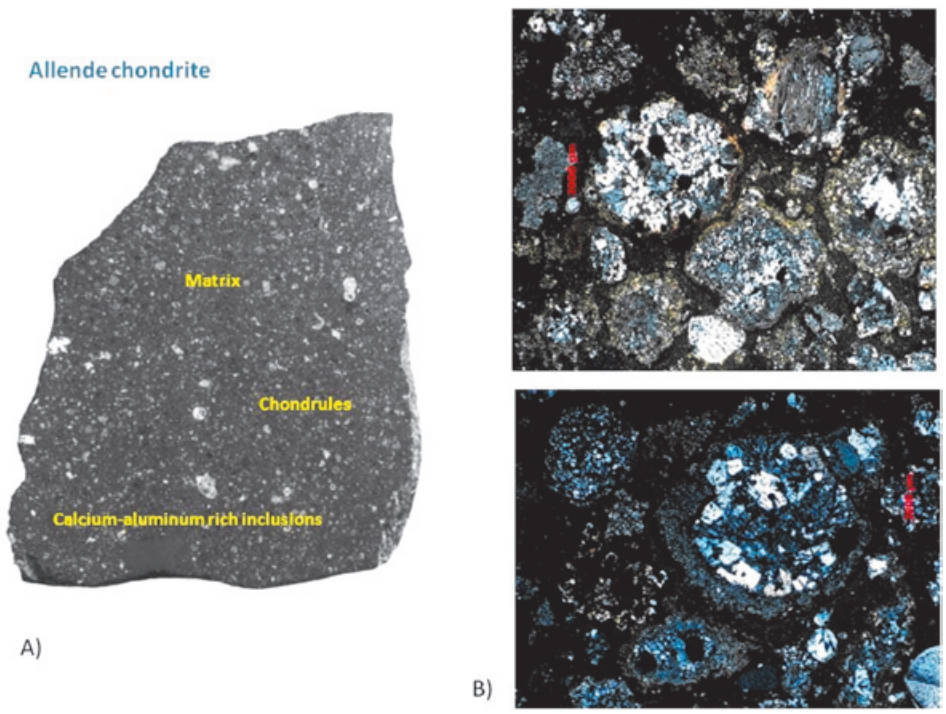

Figure 1. (A) Image of a slab fragment of the Allende CV3 chondritic meteorite showing the chondrules, refractory calcium-aluminum rich inclusions and fine grained silicate matrix. (B) Thin-section microphotographs of Allende chondrules, showing the diversity of textures, morphologies and mineral compositions.

CO, CR and CV), enstatites (EH and EL) and R and K chondrites. Ordinary chondrites represent the most abundant, making up to 80-85 % of falls. The three major groups H, L and LL are characterized by the distinct petrologic types 3 to 6, interpreted as derived from three separate parent planetesimals (Weisberg *et al*., 2006). Carbonaceous chondrites are relatively rare, representing a small percentage of falls. In general, the different groups have been interpreted as derived from distinct parent planetesimals (Weisberg *et al*., 2006). Genetic relationships are being investigated for different chondrite, iron and other meteorites, relating differentiated and undifferentiated types (Greenwood *et al*., 2010).

Other meteorites include the achondrites and the primitive achondrites (Weisberg *et al*., 2006; Rochette *et al*., 2009; Macke *et al*., 2011). The achondrites represent the group of differentiated meteorites, characterized by variable degrees of melting and metamorphism, divided into angrites, aubrites, howardites-diogenites-eucrites (HED meteorites), mesosiderites, pallasites and iron meteorites. These groups include several subgroups (e.g., iron meteorites and pallasites), with several ungrouped meteorites with distinct mineralogical and chemical assemblages. Primitive achondrites include acapulcoites, lodrinites, ureilites and winonaites. Silicate inclusions in IAB and IIICD iron meteorites are part of this group, probably derived from partial melting of chondrites in a parent planetesimal. H chondrites and iron IIE meteorites are probably coming from a partly differentiated parent planetesimal. Differentiated meteorites include those derived from known planetary sources such as the lunar and martian meteorites.

Meteorite classification schemes have evolved over time, reflecting development of new analytical techniques. Classification schemes are based on petrologic, mineralogic, geochemical and isotopic analyses. Van Shamus and Wood (1967) proposed a widely used classification system for chondrites based on compositional groups and six petrologic types. Petrologic types 1 and 2 correspond to unmetamorphosed chondrites affected by varying degrees of aqueous alteration and types 3–6 represent to distinct levels of thermal metamorphism (McSween, 1987, 1979). For several groups of carbonaceous chondrites, there have no petrologic type 4 (e.g., CI, CH, CM, CO, CR and CV). The classification has been modified over the years (Weisberg *et al*., 2006), including inclusion of type 7 chondrites (Hus *et al*., 2006). Differences in magnetic properties have been used to characterize and distinguish the different meteorite classes, where the wide ranges in magnetic susceptibility and other physical properties are used to characterize ordinary chondrites, enstatites and achondrites (Rochette *et al*., 2003, 2009; Macke *et al*., 2010, 2011).

Another aspect to consider in characterizing meteorites is the effects of hydrothermal and aqueous metamorphic alterations (Rubin, 2000). Studies have shown that most chondrites were affected by various degrees of metal/silicate and refractory/volatile fractionation. The fractionation has been associated with chondrule formation processes; although some studies have suggested fractionation mechanisms triggered by nebular condensation. Chondrule formation modified the composition of the nebula. CI chondrites, characterized by olivine and pyroxene minerals and rare to absent chondrules, preserve the chemical and isotopic composition of the solar nebula. CI chondrites, including the CV Allende carbonaceous chondrite, were affected by aqueous metamorphism, highlighting further study of alteration and metamorphic processes.

Chondrules are relatively abundant in the different chondrite classes, constituting volumetrically from 15 vol % up to 80 vol % (Zanda, 2004; Scott, 2007). The abundance of chondrules supports that chondrule formation was a major widespread process in the solar nebula. The rapid melting and cooling of the silicate droplets operated over an extended period, overlapping with CAI formation (Itoh and Yurimoto, 2003; Bizarro *et al*., 2004). Chondrule sizes are dominantly sub-millimeter and show characteristic ranges in the different chondrite classes. Chondrules show distinct internal structures, textures and mineralogical assemblages (e.g., Figure 1B). Rimmed, fragmented and composite chondrules indicate a dynamic complex formation history, involving several heating events and extended formation period in the nebula. Several contrasting mechanisms have been proposed to account for the transient heating and chondrule formation and for their later incorporation within fine-grained silicate matrix, and eventually into planetesimals (Hewins *et al*., 1996; Rubin, 2000; Connelly *et al*., 2012).

Magnetic studies of meteorites

Study of rock magnetic properties and remanent magnetization records are the field of paleomagnetism and rock magnetism (Dunlop and Ozdemir, 1997). Early recognition that magnetic minerals with domain states corresponding to single (SD) and pseudo-single

(PSD) domains are able to preserve records on time scales of the order of the solar system age provided a tool for studies of ancient fields (Weiss *et al*., 2010). Studies on chondritic meteorites suggested that magnetizations could have been acquired at their time of formation, opening the possibility of investigating the presence and nature of magnetic fields in the solar nebula. Measurements of magnetic properties on meteorites documented the presence of remanent magnetizations, with different coercivity and unblocking temperature characteristics (Butler, 1972; Lanoix *et al*., 1978; Nagata, 1979; Sugiura *et al*., 1979; Fuller and Cisowski, 1987).

Different paleointensity methods for estimating the magnitude of the magnetizing field have been applied. Occurrence of alterations induced by heating in the laboratory has limited application of thermal methods, in particular the double-heating Thellier method, in which the natural remanent magnetization (NRM) is assumed to be dominantly a thermoremanent magnetization (TRM). The Thellier double-heating method is widely applied in terrestrial igneous rocks, where it provides accurate estimates of the ancient paleofield magnitudes. Microcoercivity, thermomagnetic and microscopy techniques have been developed to investigate on the magnetic properties, mineralogy, domain state and magnetic interactions are available for igneous rocks (Davis and Evans, 1976; Day *et al*., 1977; Urrutia-Fucugauchi *et al*., 1984; Dunlop and Ozdemir, 1997), which are expanded by an array of high-resolution imaging techniques (Uehara and Nakamura, 2006; Uehara *et al*., 2011; Feinberg *et al*., 2006; Harrison *et al*., 2002). Analytical tests to detect heating-induced alterations and effects of anisotropy, cooling time and magnetic interactions have been developed (e.g., Dunlop and Yu, 2010; Lawrence *et al*., 2008; Yu, 2006; Urrutia-Fucugauchi, 1979; Coe, 1967). The alteration problems in meteorites have limited use of Thellier method (Butler, 1972; Nagata, 1979) and alternative non-heating methods using laboratory imparted remanences, like the isothermal remanent magnetization (IRM), have been developed using NRM/IRM ratio determinations (Gattacceca and Rochette, 2004; Yu, 2006; Muxworthy *et al*., 2011).

Paleointensity estimates reported in the early studies showed relatively high scatter. Studies focused on chondritic meteorites, where presence of CAIs and chondrules supports that they have not been affected by melting since they were first accreted, but have also been carried out on other meteorite classes. Banerjee and Hargraves (1972) reported estimates of 110 mT from Thellier experiments. Lenoix *et al*. (1978) reported values from 100 to 700 mT, and Wasilewski (1981) reported estimates of 1.2 to 15 mT. Complexities of paleomagnetic records and technique limitations hampered the studies resolution. Recent studies on individual chondrules using the non-heating REM, REMc and Preisach methods have provided new paleointensity estimates. Acton *et al*. (2006) summarized paleointensity estimates using the REM methods on bulk samples and chondrules from different meteorites with ranged between 3 and 147 mT (Figure 2A). Results using the REMc method yielded consistently lower values, between <1 and 11 mT. Emmerton *et al*. (2011) reported paleointensity determinations ranging between 13 and 60 mT and 3 to 56 mT, for Allende and Mokoia chondrules, respectively. The ranges are wide, and authors suggest that Mokoia is possible affected by remagnetization, while Allende might carry a primary remanence, partly affected by post accretionary remagnetization.

Magnetic property studies focused on characterizing the magnetic mineralogy with the iron-nickel minerals and iron-titanium oxides (Lanoix *et al*., 1978; Nagata, 1979). Studies on C1 and C2 carbonaceous chondrites documented grouped remanent magnetization directions, with AF coercivity spectra suggesting thermal or thermochemical remanences consistent with acquisition during accretion (Banerjee and Hargraves, 1972). CV3 chondrites, like the Allende meteorite, which were affected by secondary aqueous alteration also yielded stable magnetizations, interpreted as primary accretion or post-accretion magnetizations (Butler, 1972). Optical and scanning electron microprobe analyses indicated that taenite and possibly awaruite were the major iron minerals. Thermomagnetic analyses by Butler (1972) indicated 95 wt% taenite with 67% Ni and 5 wt% taenite with 36% Ni. The results were consistent with data for a range of chondrites (E, H, L, LL and C chondrites) and achondrites, with dominant iron-nickel minerals (Nagata, 1979).

The origin and acquisition age of remanent magnetization have been investigated using different experimental approaches, including stepwise demagnetization and application of conglomerate tests on chondrites (Sugiura *et al.*, 1979). The initial studies were made on whole-rock samples, as needed for measuring in spinner magnetometers, with cylindrical specimens cut from meteorite fragments, comprising mixtures of chondrules, CAIs and matrix. Results indicate that the remanence is probably ancient, and not significantly modified by terrestrial processes. Studies identified and isolated remanent magnetizations acquired during meteorite entry

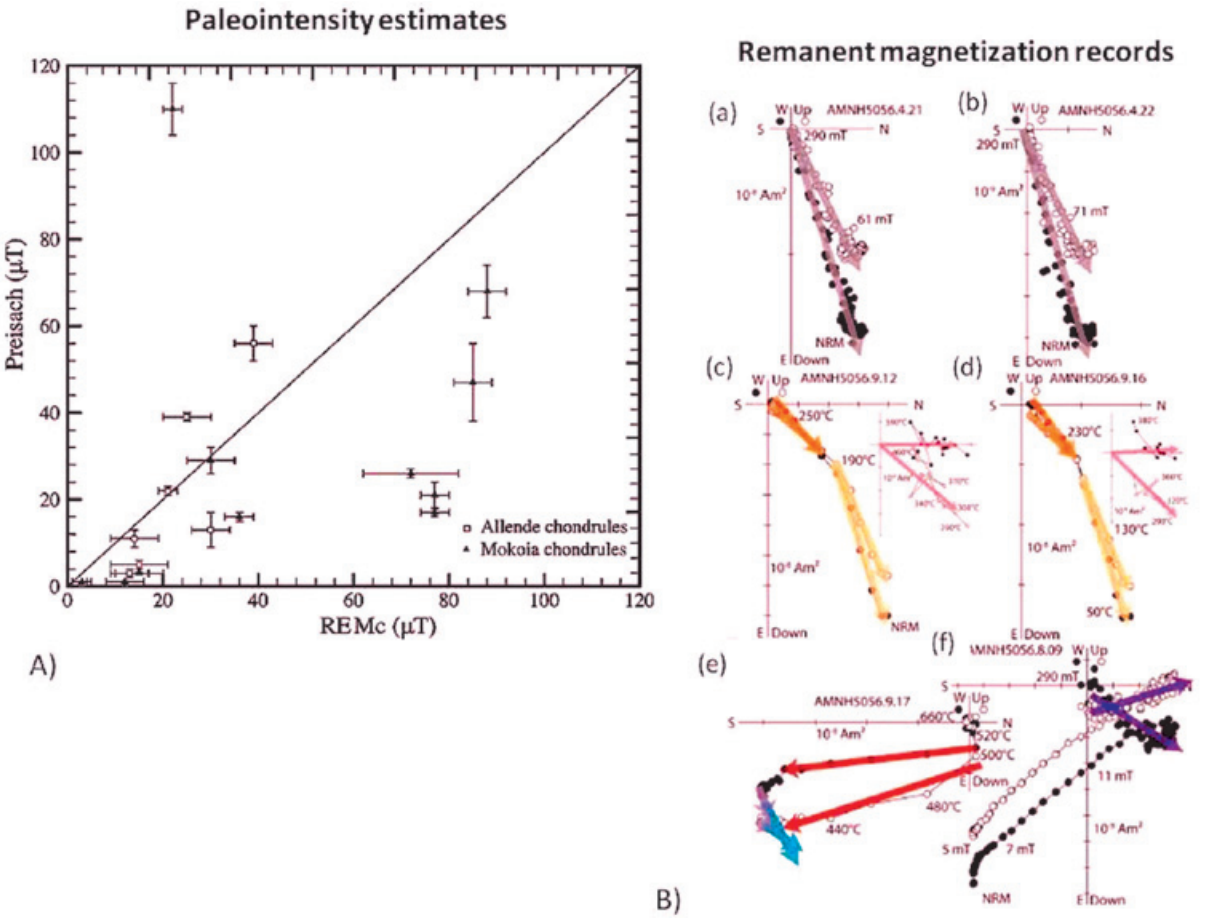

Figure 2. (A) Summary of paleointensity estimates on chondrules from the Allende and Mokoia meteorites. The graph shows the comparison of estimates obtained using the Preisach and REMc methods (after Emmerton et al., 2011). Mean and associated error bars are indicated; for Preisach method it is the weighted mean for individual demagnetization steps and for REMc method it is the arithmetic mean for selected AF demagnetization steps. (B) Vector plots for AF and thermal demagnetization of Allende samples, showing the characteristic univectorial and multi-component magnetizations, marked by the vector demagnetization trajectories in different colors. Plots (c) and (d) after thermal demagnetization reveal the dominant lower unblocking temperature component and the intermediate middle unblocking temperature component unblocked between 190° C and 290° C. In the insets, plots depict the high temperature components (taken from Carporzen *et al*., 2011).

into earth´s atmosphere, characterizing the fusion thin crusts. Stepwise demagnetization shows remanence is characterized by low, intermediate and high coercivity and unblocking temperature components (Figure 2B; Carporzen *et al*., 2011).

The contrasting paleomagnetic records, analytical problems and complex magnetic mineralogy have stimulated studying the magnetic properties of meteorites at increasingly finer resolution using micromagnetic techniques (Flores-Gutierrez and Urrutia-Fucugauchi, 2002; Acton *et al*., 2007; Emmerton *et al*., 2011). Studies focused on chondritic meteorites, where presence of CAIs and chondrules supports that they have not been affected by melting since they were first accreted, but have also been carried out on other meteorite classes.

Magnetic hysteresis measurements have been carried out in bulk samples and in individual chondrules. Data show occurrence of ferrimagnetic minerals with high saturation values and intermediate and low coercivities, indicating magnetite and low-Ti titanomagnetites. Hysteresis parameter ratio plots show chondrules are characterized by dominantly PSD and multidomain (MD) states (e.g., Weiss *et al*., 2010; Acton *et al*., 2007; Emmerton *et al*., 2011; Flores-Gutierrez and Urrutia-Fucugauchi, 2002). Emmerton *et al*. (2011)

presented magnetic data for 28 and 17 chondrules from the Mokoia and Allende chondrites, respectively. The dominant magnetic phase in the chondrites was interpreted as an FeNi phase (taenite, kamacite or awarite), contributing about 48 % in Mokoia and about 42 % in Allende. The Mokoia chondrules showed higher magnetic mineral concentrations, wide range of magnetic properties and dominant SD domain states. Allende chondrules showed low coercivity distributions and limited magnetic interactions. Alternating field (AF) and thermal demagnetization of chondrules and bulk samples reveal univectorial to multicomponent magnetizations. Some chondrules carry complex magnetizations, which are not resolved using AF or thermal demagnetization. Acton *et al*. (2006) report magnetic hysteresis ratio plots for chondrules and matrix for the Allende, Karoonda and Bjurbole chondrites showing wide variation ranges, with Mr/Ms ratios between 0.03 and 0.39 and Hcr/Hc ratios between 0.1 and 9. Mokoia chondrules plot in the PSD field showing a restricted trend, while Allende chondrules show more variability plotting in the PSD and MD fields, similar to other CV3 and C chondrites. Mokoia chondrules show variation trends suggesting mixtures of SD and MD particles, contrasting with the scattered pattern shown in the Allende chondrules and matrix (Figure 3).

Coercivity distribution in chondritic meteorites suggest they may be affected by overprinting, during metamorphism or collisions, alteration in planetesimal bodies, and also exposed to ambient conditions on Earth after atmospheric entry including high magnetic fields, lighting strikes, etc (Weiss *et al*., 2010). This has suggested that reliable paleointensity estimates are more likely to be obtained from the high coercivity spectra in chondrules. Sugiura *et al*. (1979) and Sugiura and Strangway (1983) reported data supporting that chondrules retain a remanent magnetization acquired prior to their incorporation into the chondritic meteorite using a form of conglomerate test (Weiss *et al*., 2010). The relationships uncovered for the magnetization ratio and coercivity in the Allende chondrite may permit to better understand the coercivity distribution (Flores-Gutierrez and Urrutia-Fucugauchi, 2002). The connections to internal chondrule structure and morphologies, with compound chondrules, alteration rims, fracturing can be used for sample selection for paleointensity experiments.

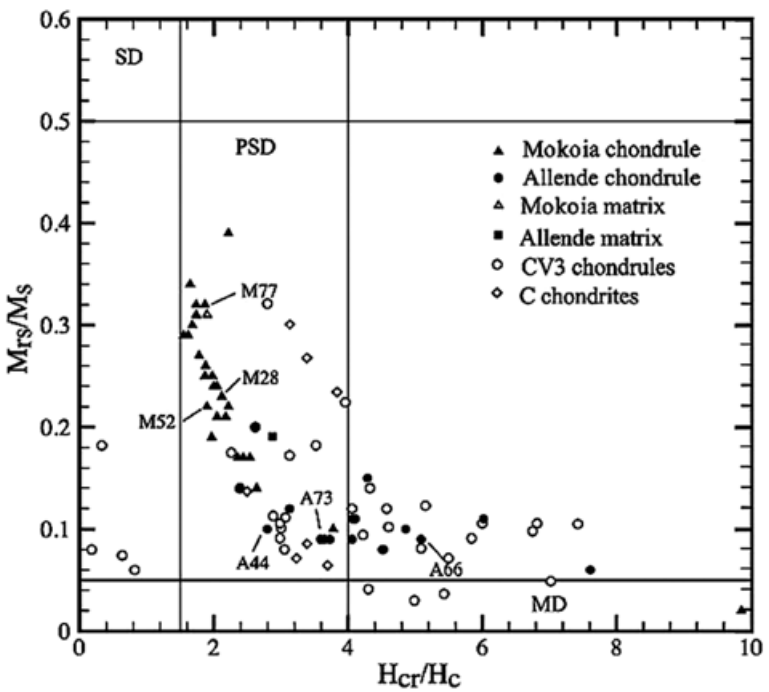

Fig. 3. Example of magnetic hysteresis data for chondrules and matrix samples from Allende and Mokoia meteorites, plotted in a hysteresis parameter ratio plot (from Emmerton *et al*., 2011). Domain state fields are indicated (Day *et al*., 1977); observe data points plot in pseudo-single domain (PSD) and multidomain (MD) fields. Mokoia chondrules show a mixture trend of single domain (SD) and MD behavior; in contrast to the scattered pattern for Allende chondrules (see text for discussion).

Allende Chondrite

The Allende meteorite is an oxidized CV3 carbonaceous chondrite (Figure 1). These chondrites are relatively rare as compared to other types such as the ordinary chondrites. Its fall in the area of Allende town, Chihuahua, northern Mexico on February 1969 was well documented, with a relatively large amount of fragments up to 2 tons recovered (Clarke *et al*., 1970). At the time, samples were distributed to numerous laboratories, making Allende one of the most intensively investigated meteorites. Several major findings have been first reported in Allende samples, including evidence for short lived Mg-Al isotope system supporting a supernova explosion at the early stage of nebula condensation (Lee *et al*., 1976).

Allende is characterized by high magnesium and iron contents, with olivine (MgO 47-49 %, FeO 7-9%, SiO_2 42-44%), awaruite (FeO 28-32%, NiO 68%), and enstatite (MgO 35-36%, FeO 0.8%, Al_2O_3 1.2%, SiO_2 60%). Other minerals present are kamacite, taenite, troilite, mackinawite, antigorite, majorite and pentlandite, with magnetite, chromite, Ni-Fe alloys, sulfides and sulfates and anorthite as accessory minerals. Chondrules show different textures and mineral compositions (e.g., Figure 1B), characterized by anhedral, euhedral and recrystallized olivine chondrules, barred olivine chondrules, pyroxene olivine chondrules and pyroxene chondrules. Major magnetic minerals are magnetite, taenite and iron sulfides.

Two different chondrules types are observed: FeO-poor reduced type I chondrules with iron metal blebs and olivines and FeO-rich oxidized type II chondrules with no metal blebs and olivines (McSween, 1979, 1987). The Allende chondrite is characterized by FeO-poor chondrules and low-volatile rich. Divisions of CV chondrite sub-groups depend on relative contents of metal and magnetite, which is reflected on the modal ratios of metal to magnetite.

Magnetite formation in oxidized and reduced chondrites have been intensively studied, with different mechanisms proposed, including crystallization from oxidized melts, oxidation of metallic nodules in the solar nebula, and secondary oxidation of metallic chondrule nodules in planetesimals (Krot *et al*., 1995). In the Allende, magnetite appears mainly in porphyritic olivine chondrules as spherical nodules, in association with Ni rich alloys and sulfides. Flores-Gutierrez *et al*. (2010a) study shows that Fe is associated with Si and Mg (fosterite to fayalite), with higher concentrations in chondrule rims. Fe forms FeNi alloys and trolite. Si is a major element in chondrule composition; in low concentrations it tends to be uniformly distributed and in higher concentrations it is distributed in wide regions and in the rims. In one of the chondrules analyzed, Si shows higher relative contents in the interstitial zones. Nickel distribution in Ni-rich minerals and alloys seems an important indicator of alteration, with metamorphism allowing Ni to migrate, recording metamorphic temperatures in pentlandite-bearing chondrites. The mineralogy suggests secondary events following chondrule formation in the solar nebula. Kring (1991) considered the high-temperature chondrule rims as indicators of fluctuating conditions, with accretion of dust rims occurring under turbulence in particle rich regions up to several hundred of kilometers in scale (Cuzzi and Alexander, 2006).

Analysis of hysteresis ratio plots and compilation of hysteresis data show a relatively higher scatter for the Allende and other chondrites, in contrast to data for chondrites characterized by less variability and trends of SD and MD domain particles (Figure 3). Flores-Gutierrez and Urrutia-Fucugauchi (2002) and Flores-Gutierrez *et al*. (2010a) investigated the domain state pattern for Allende chondrules and found that Allende is characterized by a variation range in hysteresis parameter ratio plots related to chondrule size (Figure 4).

Hysteresis magnetization ratios (Mr/Ms) vary from 0 to 0.22, showing a linear relation as a function of coercivity (Hc), which varies from 3 to 24 mT. The variation trend correlates with internal microstructure and composition, with compound chondrules showing higher hysteresis ratio and parameter values. Chondrules with hysteresis parameters falling outside the major trend show internal structures, composition and textures of compound, fragmented or altered chondrules. The relationships between chondrule size and hysteresis parameters were not expected from previous studies, suggesting possible deeper associations with chondrule composition. Flores-Gutierrez *et al*. (2010a) analyzed the internal chondrule structures and compositions using scanning electron microscope on individual chondrules. Separation of chondrules and CAIs from the fine-grained silicate matrix is time consuming, and studies use generally a few chondrule samples. Results from 100 individual chondrules permit to evaluate the relations of chondrule size, density and hysteresis parameters and parameter ratios (Figure 4). Chondrule densities vary from about 2 to 3.5 kg/m^3, showing a rough trend to decrease with increasing chondrule size.

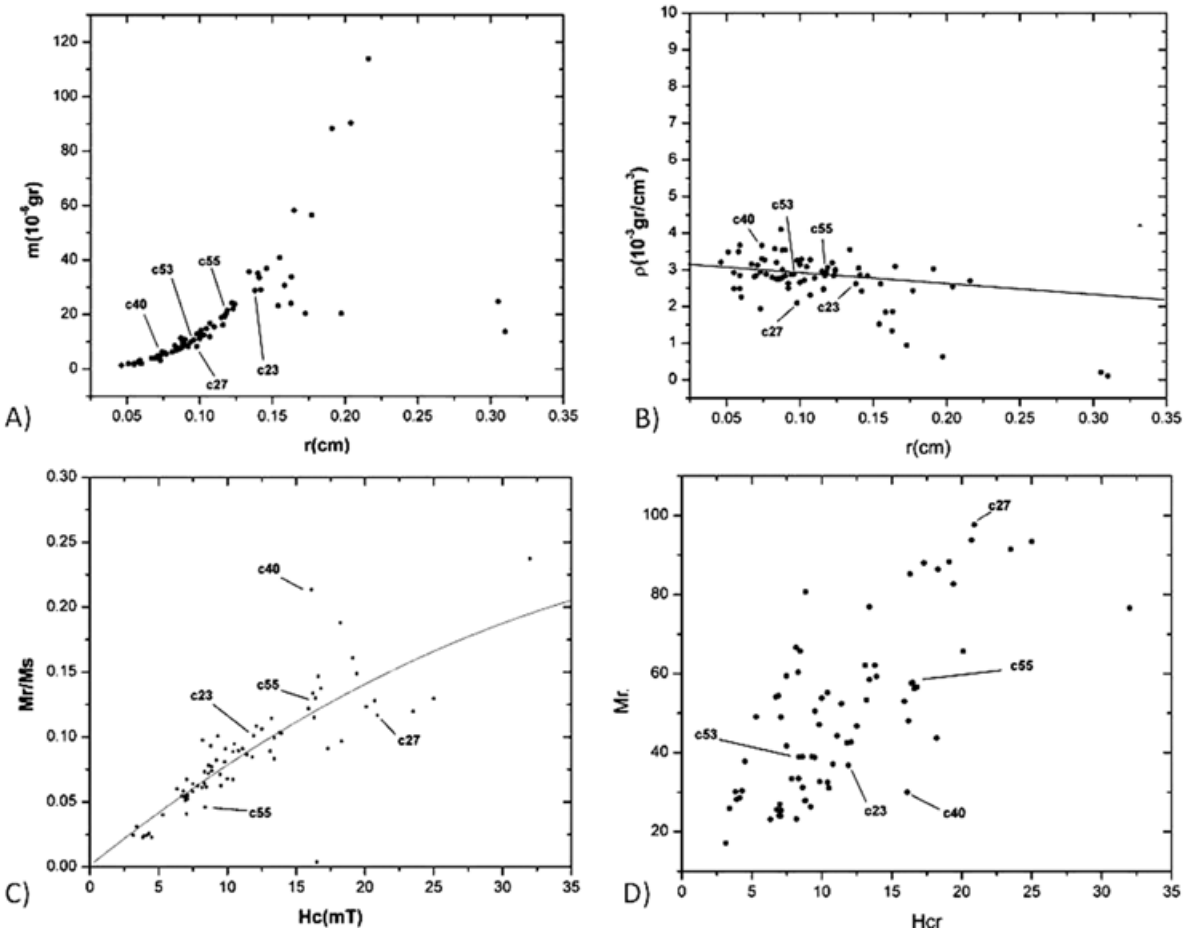

Figure 4. (A) Plot of mass as a function of chondrule radii (B) density as a function of chondrule radii (C) magnetization ratio as a function of coercivity (D) Remanent magnetization as a function of remanence coercivity (after Flores-Gutierrez *et al*., 2010a,b). Selected chondrules marked are also shown in the microprobe analyses in Figure 5 B (see text for discussion).

Plot as a function of chondrule radii show a wide scatter, with a decreasing trend. Some chondrules show lower densities, particularly the larger ones with radius larger than 0.07 mm and up to 0.16 mm. Magnetic hysteresis parameters were associated with chondrule structure, mineralogical composition and morphology. Analyses of chondrules within the scatter plot relations and outsiders documented that chondrules showed characteristic behaviors related to their internal structure and properties.

Magnetic hysteresis parameter ratios show simple linear relationships between the magnetization ratio and coercivity (Figure 4). Magnetization ratios are low, lower than 0.225, with the linear relationship present up to 0.17. Coercivity is low, lower than 24 mT. The linear relationship covers the range from about 2 mT to 17 mT. These low values suggest that chondrules are susceptible to alteration and remagnetization, which has implications for retrieval of paleointensity estimates for the early planetary magnetic fields. Reliable paleointensity estimates might be better obtained from high coercivity spectra.

Analysis of chondrules within the linear relation field and outliers show that magnetic properties correlate with chondrule internal structure and mineral composition (Figure 5). Chondrules falling outside the relation are compound, with partial aggregation rims and/or fractured (chondrules c40, c27 and c23), in contrast to those chondrules with low coercivity Hc and magnetization Mr/Ms ratios, which appear homogeneous (chondrules c53 and c55). Silica maps characterize chondrule structures, which can be correlated with chondrule size, external morphology and shapes.

Results show that closely-spaced chondrules in given fragments of Allende are characterized by highly variable Fe, Ni and S composition.

Differences in magnetic properties relate to characteristic sizes, textures and mineralogy. Spatial distributions suggest chondrules record distinct shock and alteration processes during formation stages. Scanning electron microscope (SEM) analyses constrain the composite nature, with fragmented chondrules, different accretionary rims, mineralogic and elemental compositions and coalesced compound chondrules.

The relationship uncovered for the magnetization ratio and coercivity (Figure 5A) permit to better constrain the coercivity distribution and relations to internal structure, with compound chondrules, alteration rims, fracturing appear useful criteria for sample selection in paleointensity experiments. The combined hysteresis data and microscope observations permit to characterize populations of chondrules, with distinct magnetic mineralogy, morphology and internal structure.

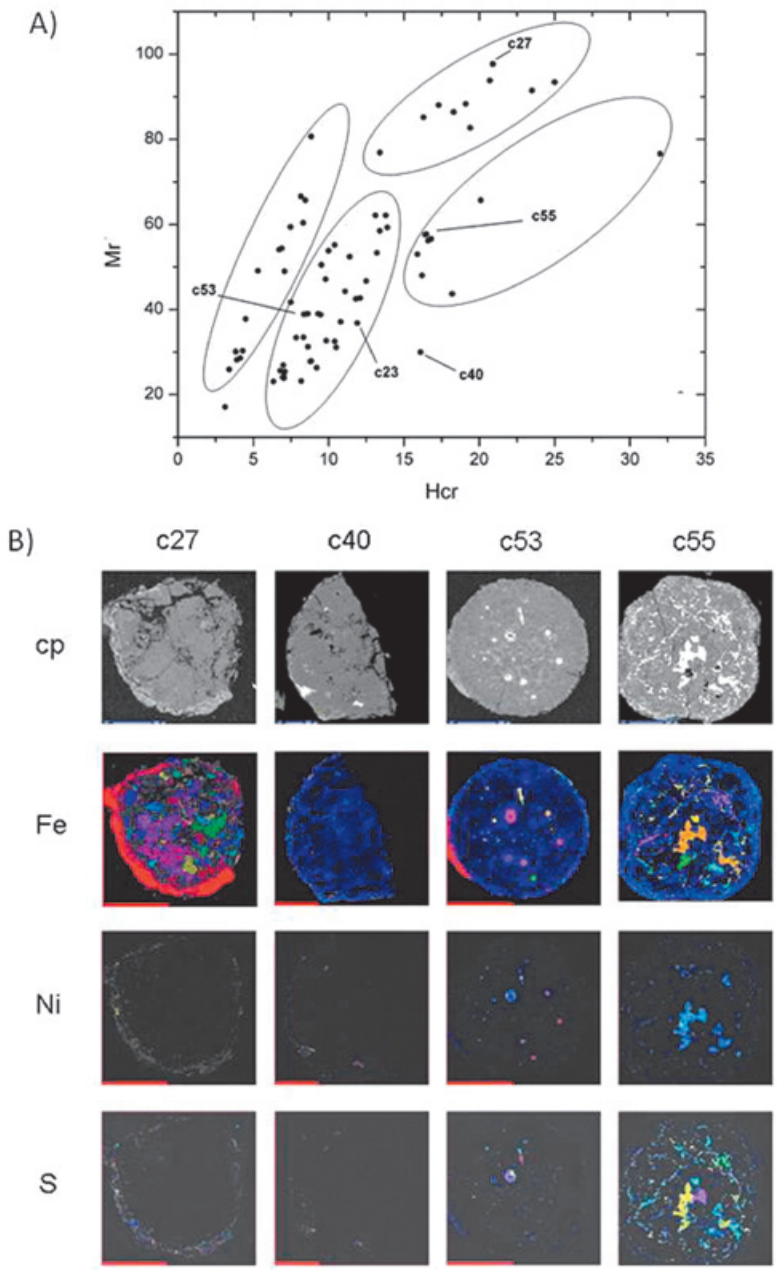

Figure 5. (A) Remanent magnetization-coercivity diagram, showing interpreted chondrule distributions. Compare with diagram in Figure 4 D. (B) scanning electron microscope and elemental analyses (Flores-Gutiérrez *et al*., 2010b).

Observations provide further evidence on multiple heating events and long time scales involved in chondrule formation (Scott, 2007). The wide range of internal structures and mineralogical compositions in a single fragment of the Allende indicate that Allende chondrite formed from a heterogeneous assemblage of chondrules, which underwent complex pre-accretionary histories (Figure 6). This is further examined below in relation to the chronological constrains on the early stages of evolution of the protoplanetary disk.

Chronology of solar system early evolution

The age of ~4,568 millions of years derived from radiometric studies of meteorites is obtained from dating CAIs and chondrules from chondrites and other primitive meteorites (Connelly *et al.*, 2012). Chondrules and refractory inclusions in carbonaceous chondrites give the oldest radiometric dates, providing a chronology of events in the accreting protoplanetary disk. Radiometric dating on primitive angrites, eucrites, and chondrules, refractory inclusions and olivine aggregates from chondrites provides a chronology for solar system early stages (Amelin *et al*., 2002; Bouvier and Wadhwa, 2010; Connelly *et al*., 2012).

Chondrules and CAIs formed from dust agglomerates by short-lived heating events that affected the gas nebula. Transient temperatures may have reached up to 1400° to 1800° C with rapid heating/cooling. Mechanisms proposed for melting of fine-grained solid matter include a wide range of processes. Chondrules appear to have been formed at a later time than refractory inclusions, as suggested from isotopic analyses and petrographic and microstructural observations (Figure 7). Isotopic analyses of the Al and Mg systematics completed in Allende chondrite provided constraints for the event chronology of CAIs and chondrules and solar nebula conditions (Lee *et al*., 1976; Scott, 2007). Analyses of ^{26}Al isotopic differences in CAIs and chondrules have been discussed in terms of orderly or overlapping sequence of events (Itoh and Yurimoto, 2003; Bizarro *et al*., 2004; Krot *et al*., 2005). Refractory inclusions appear having started to form 1 to 4 million years earlier (Scott, 2007). Additional detailed studies of CAIs and chondrules are required to constrain the chronology of early events, processes and their spatial relationships (Itoh and Yurimoto, 2003; Bizarro *et al*., 2004; Krot *et al*., 2005). Experimental evidence on an early origin of CAIs includes the findings of relict CAIs inside chondrules. Studies have also reported findings of a chondrule inside a CAI,

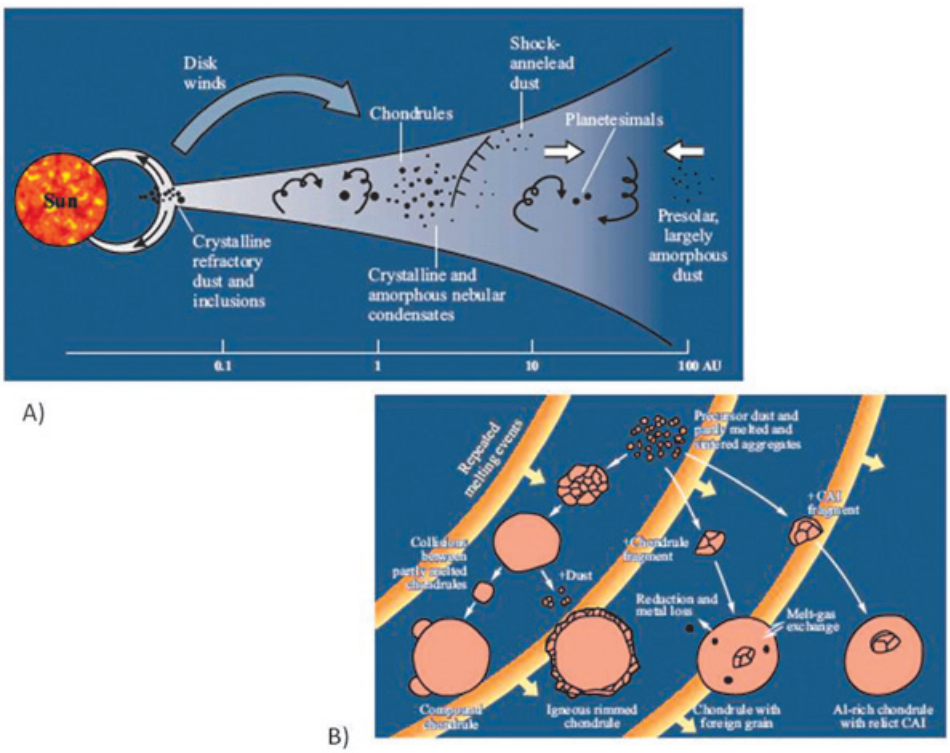

Figure 6. (A) Model for the accretion disk, showing the chondrule and refractory calcium-aluminum inclusions formation sectors. (B) protoplanetary disk zone of crystalline and amorphous condensates, showing the distinct chondrule morphologies (modified after Scott, 2007).

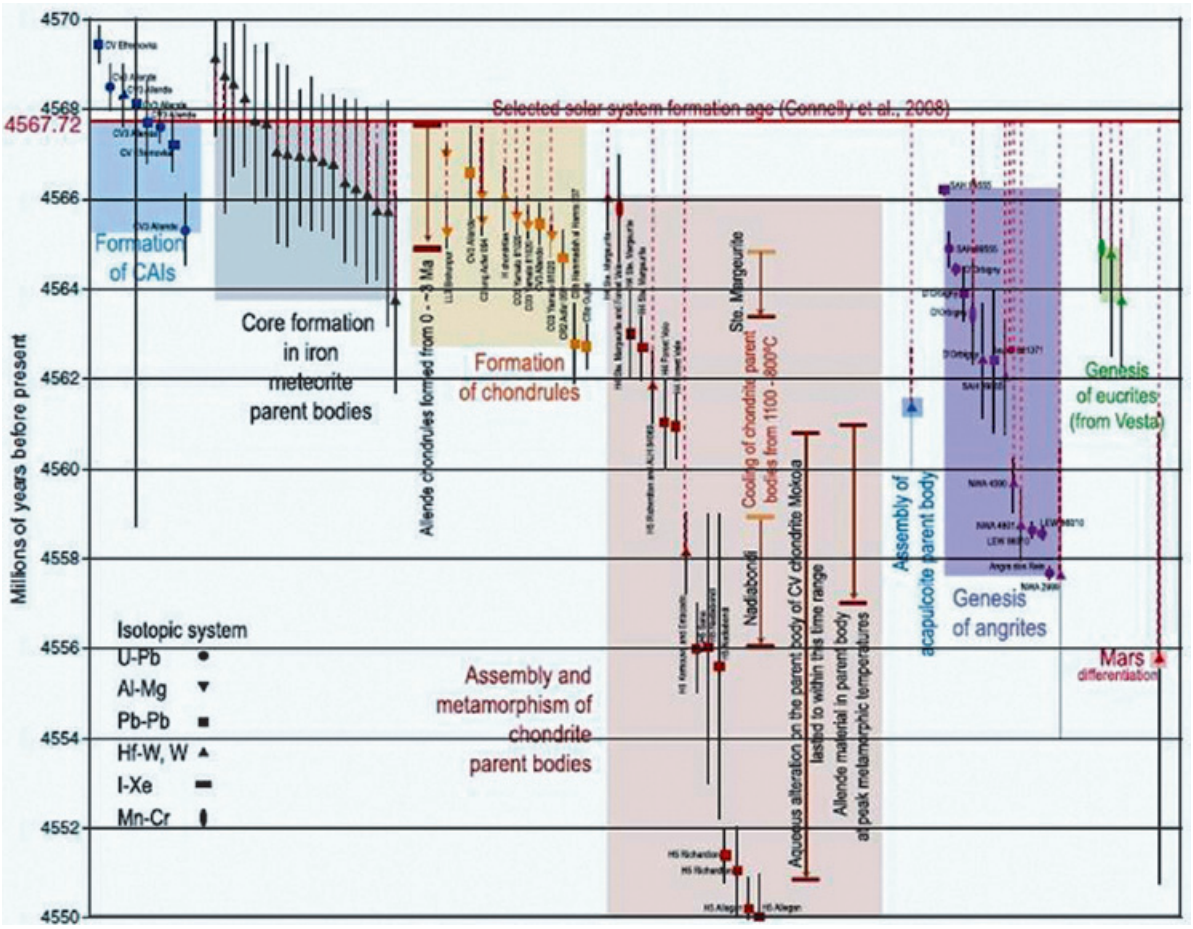

Figure 7. Age plot for the first millions of years, for formation of refractory inclusions, chondrules and iron, chondrite, angrite and eucrite parent planetesimals (after Elkins-Tanton *et al*., 2011).

which support contemporaneous formation of CAIs and chondrules, and an extended period of chondrule formation (Itoh and Yurimoto, 2003; Krot *et al*., 2005).

A chronology of events that incorporates the rapid accretion of differentiated palanetesimals within the first millon years, constrained by ages from different isotopic systems, is illustrated in Figure7 (Kleine *et al*., 2002; Weiss and Elkins-Tanton, 2013). In this model, accretion of chondrite parent planetesimals occurred shortly after chondrule formation with an extended period marked by hydrous alteration and thermal metamorphism. Carbonaceous chondrites developed in the crust of partly differentiated planetesimals, large enough to have metallic cores and internal magnetic fields (Figure 8; Elkins-Tanton *et al*., 2011; Carporzen *et al*., 2011; Sahijpal and Gupta, 2011). Dynamo action was sustained for several millions of years, consistent with thermal evolution and rapid differentiation processes. The early stage was marked by collisions, which fragmented the planetesimals, leading to the partial or complete disruption, producing the differentiated and undifferentiated meteorite types (Figure 8B). Depending on the crustal level, distinct chondrite types originate, marked by varying hydrous alteration and metamorphic degrees (Figure 8A). CK chondrites come from deep crustal levels, whereas Allende CV3 chondrite comes from an intermediate crustal level.

Use of short lived radioisotopes like the Al-Mg system provides temporal resolution for asteroid accretion, differentiation and secondary alterations (Nyquist *et al*., 2009). Isotope geochemical studies on the Allende carbonaceous chondrite and other chondrites documented presence of the radioactive isotope aluminium-26, which indicates that a supernova exploded in the vicinity of the solar nebula, initiating compression of the gas and dust molecular cloud.

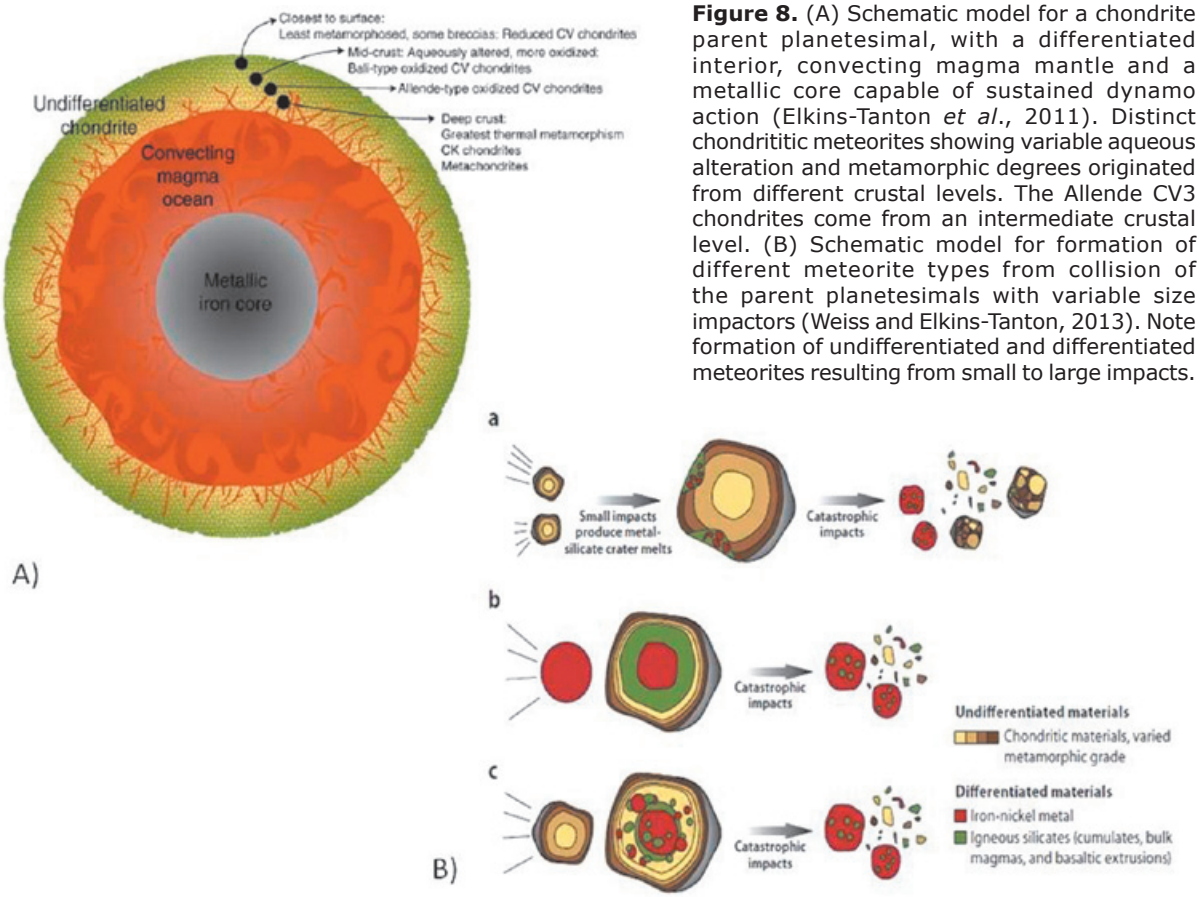

Figure 8. (A) Schematic model for a chondrite parent planetesimal, with a differentiated interior, convecting magma mantle and a metallic core capable of sustained dynamo action (Elkins-Tanton *et al*., 2011). Distinct chondritic meteorites showing variable aqueous alteration and metamorphic degrees originated from different crustal levels. The Allende CV3 chondrites come from an intermediate crustal level. (B) Schematic model for formation of different meteorite types from collision of the parent planetesimals with variable size impactors (Weiss and Elkins-Tanton, 2013). Note formation of undifferentiated and differentiated meteorites resulting from small to large impacts.

CAI fragments inside chondrules are consistent with the older ages for CAIs, also indicating that chondrule formation occurred in a nebula sector with CAIs present. There are different models for formation of chondrules and refractory inclusions, some involving distinct separate sectors in the nebula (Figure 6A). Radiometric dates constrain the period for CAI and chondrule formation. Chondrule size varies among different chondrite classes, which has been interpreted in terms of distinct regions for chondrite formation and/or chondrule sorting mechanisms. Chondrules showing fragmentation, coalesced composite chondrules, chondrule fragments inside chondrules and chondrules with rims (Figure 6B) support relatively large spans for the formation with multiple fast heating events.

The observations on individual chondrules from a fragment of the Allende meteorite show that highly diverse types coexist with fragmented, rimmed and composite chondrules characterized by distinct mineralogy (Figure 5B). Findings support a dynamic evolution of chondrule formation, fragmentation and partial metasomatism before and during chondrule aggregation (Scott, 2007). The recent reports of chondrule fragments inside CAIs add support for overlapping chondrule and refractory inclusion formation, within given sectors of the nebula (Itoh and Yurimoto, 2003; Bizarro *et al*., 2004).

Discussion

In recent years, improvements on instrumentation and analytical techniques provide increased resolution in studying and characterizing the various classes of meteorites. Use of microanalytical methods permits to investigate meteorite constituent minerals at increasing detail. In the case of chondrites studies focus on the CAIs, chondrules, metal grains and matrix, to investigate the early evolution stages of the solar system. Radiometric dating on CAIs and chondrites give the oldest dates, constraining the chronology of accretion. Chemical and isotopic analyses on CI and carbonaceous chondrites show they preserve the composition of the solar nebula.

Chondrites are characterized by a trend from 'reduced' with Fe in metallic form to 'oxidized' with Fe in silicates and oxides. Magnetic minerals in CV3 chondrites are FeNi, iron-titanium

oxides and magnetite in olivines, with magnetite formed by aqueous alteration. The results from the hysteresis analyses of individual chondrules show magnetite as dominant phase with PSD and MD domain states, which along with taenite and iron sulfides make the magnetic signal of Allende.

Chondrules examined in a fragment of the Allende chondrite display relations between mass and size (Figure 4A). The relation is partly dependent on density (Figure 4B), with density decreasing with size. Examination of the apparent scatter in the size-density plot shows a dependency on internal structure and mineralogical assemblage. The composite and fragmented nature of some chondrules is related to outliers in the plots. The study also uncovered simple relationships among the magnetic hysteresis properties, which need further consideration using detailed petrographic and geochemical analyses on a larger group of chondrules. The magnetization ratio shows a dependency on the coercivity (Figure 4C). The plot of remanent magnetization as a function of remenent coercivity shows a trend of increasing intensity with increasing coercivity (Figure 4D). There is however significant scatter, in contrast to the pattern shown using the magnetization ratio. The examination of the internal structure and mineralogical assemblage uncovers correlations between the magnetic properties, variation patterns and chondrule characteristics (Figure 5A, B).

The wide range of variation in chondrule structures, composition and hysteresis properties has implications for the paleomagnetic and paleointensity studies (Flores-Gutierrez *et al*., 2010a, b), indicating that the differences in magnetization vector components and paleointensity record relate to chondrule structure and mineralogy. Magnetic hysteresis parameters and domain structure are related to chondrule morphology, size and density, which in turn reflect internal structure and mineralogic differences (Figure 5A, B). A next step is to obtain paleointensity estimates and expand the analyses and correlations between magnetic hysteresis properties and chndrule structure and mineralogical composition.

The studies, reviewed in the previous section on paleomagnetic records in chondrites, show that they are secondary with remanent magnetizations acquired in the planetesimals under ambient fields generated by active internal dynamo action (Carporzen *et al*., 2011; Elkins-Tanton *et al*., 2011). The paleomagnetic evidence for differentiated planetesimals with iron cores and sustained internal magnetic fields rests on the magnetization record and remanence acquisition mechanism. Carporzen *et al*. (2011) summarized the records for unidirectional magnetizations in the Allende, residing in middle unblocking temperature components, interpreted as up to ~290 C partial TRM (pTRM) or thermochemical (CTRM) magnetizations (e.g., Figure 2B). This secondary component is carried in magnetite, pyrrothite and awaruite, which formed as a result of hydrous alteration (which is further discussed below). The ambient magnetic field under which the magnetization was blocked is constrained from paleointensity estimates from both Thellier and laboratory imparted AF demagnetization methods, which Carporzen *et al*. (2011) set at minimum fields of 20 mT and up to about 60 mT. The high magnetic field magnitude is compatible with internal fields. The other requirement in this interpretation of the Allende paleomagnetic record is the timing and duration for remanence acquisition, which are constrained from the isotope chronometers. In the study, chondrules are considered to have formed over an interval of 1.2 to 3 Ma, starting at about 200 ka after formation of refractory inclusions. Carporzen *et al*. (2011) discussed the temporal constrains in further detail, concluding that an extended period of elevated temperatures and hydrous alteration was involved in the acquisition of the paleomagnetic record.

The scenario for magnetization acquisition in the crust of a differentiated parent planetesimal appears consistent with magnetite formation as an alteration product. CV chondrites have been divided into magnetite-rich and magnetite-poor subgroups, marked by the modal ratio of magnetite to metal (McSween, 1977; McMahon and Haggerty, 1980). Different mechanisms for magnetite formation have been proposed, with some occurring in the solar nebula and some in planetesimals (Krot *et al*., 1995). Choi *et al*. (1997) analyzed the oxygen isotope compositions of magnetites and olivines in the Allende, where they are closely related. Magnetite is present as spherical nodules in porphyritic-olivine chondrules, associated with Ni-rich metal and sulfides. The oxygen isotopes differ, implying that magnetite and olivine are in isotopic disequilibrium, with more negative magnetite δ-O than those expected for the solar nebula. Choi *et al*. (1997) interpreted that magnetite formed by aqueous oxidation of metal, which had already undergone oxygen isotope exchange with fine-grained silicate material in the parent planetesimal.

Modeling of the size and internal structure of differentiated bodies with iron cores and undifferentiated crusts has been used to further constrain the early thermal state evolution

(e.g., Elkins-Tanton *et al*., 2011; Sahijpal and Gupta, 2011; Storenberg and Crowley, 2013). Models show that dynamo action might have been sustained for several million years. Further modeling incorporating stringent boundary conditions on thermal state and heat transport are needed to constrain the evolution of the planetesimal dynamos. The crustal structure and thickness and temperature-pressure profiles, fluids and layering in parent planetesimals remain to be incorporated in the modeling, including the magnetization acquisition mechanisms at different crustal levels.

Paleomagnetic data for meteorites inferred to originate at various levels marked by distinct hydrous alteration and metamorphic grades (Figure 8A) might allow testing and refining the differentiated planetesimal model. Paleomagnetic data for terrestrial lower crust, metamorphic lithologies and crustal and mantle xenoliths might provide some potentially useful analogies. Modeling of expected paleomagnetic records and rock magnetic property variations with depth within the crust might allow testing the remanent acquisition mechanisms. The effects of the large impacts involved in fragmenting the planetesimals (Figure 8B), including shock remagnetization, need also to be investigated in the paleomagnetic records of the different meteorites.

Forward modeling and inversion of crustal magnetic anomalies on the Moon and Mars have been used to estimate paleomagnetic poles and derive constraints on the internal dynamo generated magnetic fields (e.g., Cisowski *et al*., 1983; Scott and Fuller, 2004; Lillis *et al*., 2013). Occurrence of polarity reversals of the core dynamos has also been analyzed from modeling of crustal magnetic field anomalies (Arkani-Hamed, 2001). This cannot be accomplished for the fragmented chondrite parent planetesimals, but might be possible to be eventually investigated for the large differentiated asteroids Ceres and Pallas.

Paleomagnetic analyses of different meteorite types, including carbonaceous chondrites, eucrites and pallasites, suggest that their acquired remanent magnetizations under the influence of internal magnetic fields (Weiss *et al*., 2008; Carporzen *et al*., 2011; Tarduno *et al*., 2012; Weiss and Elkins-Tanton, 2013). This implies differentiated planetesimals with convecting cores capable of sustaining dynamo action for extended periods. To sustain dynamo action an energy source is required, plus a thermal state and evolution that allows the crust and upper mantle to cool enough for magnetization acquisition. Most of these differentiated bodies were later destroyed by collisions or other disturbances such as tide forces. Part of the differentiated bodies have been preserved forming the planets, satellites, dwarf planets and specially the large asteroids Ceres and Pallas in the asteroid belt (Elkins-Tanton *et al*., 2011).

The studies on eucrite meteorites support that their acquired remanent magnetizations in a magnetic field, consistent with an internal field with surface magnitude of around 2 microtesla (Fu *et al*.,2012). The asteroid Vesta in the asteroid belt is the smallest differentiated body known. The paleomagnetic record suggests that Vesta might had had a convecting metallic core in the early stages.

Stony-iron meteorites have been assumed to form in the interior of differentiated planetesimals, near the core-mantle boundary. Therefore, they come from differentiated bodies with developed cores that could sustain dynamo action. Paleomagnetic analysis of stony-iron meteorites such as the main group pallasites could provide information on planetesimals´ magnetic fields Paleomagnetic analyses of pallasites characterized soft coercivity highly anisotropic magnetizations, likely associated with the Fe-Ni metal (Nagata, 1979). Pallasites, characterized by metal-silicate assemblages composed of olivines and Fe-Ni are particularly interesting, since olivine and metal phases tend to separate, so a mechanism seems required to keep them without segregation.

The different types of iron meteorites and achondrites indicate different parent planetesimals, which supports widespread formation of differentiated bodies in the early stages. Burbine *et al*. (2002) estimated that more than 100 parent planetesimals are required to account for the diversity in achondrites and iron meteorites, including the early estimates by Wasson (1990) on the probable large numbers of iron meteorite parent planetesimals. Ungrouped iron meteorites have been related to some 50 parent planetesimals (Goldstein *et al*., 2009), as suggested by the differences in sulfur compositions. Goldstein *et al*. (2009) propose that iron meteorites were derived from relatively large parent bodies, with sizes up to 1000 km or more, which formed before chondrite accretion outside the asteroid belt zone.

The widespread early formation of differentiated planetesimals and apparent lack of such bodies in the asteroid belt has been discussed in several studies. Surface weathering and impact debris cover may have masked the spectroscopic observations (e.g., Nakamura

et al., 2011). Other effects may include the preservation of primitive undifferentiated crusts (Weiss end Elkins-Tanton, 2013). The layered internal structures in planetesimals offers an explanation of the genetic relations uncovered for distinct meteorite classes, where they originate upon collision fragmentation from different levels from the iron cores, mantles and crusts. The paleomagnetic record for the Allende chondrite supports an origin from an intermediate crustal level in a partly differentiated parent planetesimal. Carporzen *et al*. (2011) showed that the magnetization in the Allende was likely acquired over an extended period under the influence of an internal magnetic field. The characteristic magnetization is univectorial acquired in a magnetic field of about 20 mT, likely corresponding to a partial TRM or a thermochemical C-TRM. The magnetic carriers, magnetite, pyrrothite and awaruite, are consistent with this interpretation, corresponding to secondary minerals formed from hydrous alteration and thermal metamorphism.

Fu and Elkins-Tanton (2013) examined the thermal evolution of planetesimals in which short lived radiogenic isotopes provided sufficient heat for differentiation with formation of layered structures. In those bodies, heat dissipation involved magmatic processes resulting in magmas ascending through the crust. Modeling by Fu and Elkins-Tanton (2013) supports that magmas were volatile-depleted, and likely emplaced through enstatite crusts but likely not through CV and CM crusts, as indicated by the paleomagnetic constraints.

Conclusions

In recent years, planetary missions, Earth-based astrophysical observations, use of a range of analytical techniques of microscopy, isotope geochemistry and magnetic properties, discovery of exoplanets, and development of evolutionary models for planetary nebula have opened new research multidisciplinary fields, with the potential of integrative approaches.

Meteorites represent the earliest rocks preserved from the initial stages of formation of the solar system, providing the record on the conditions, processes and chronology for formation of first solids, planetesimals and differentiated bodies. Refractory calcium-aluminum inclusions and chondrules give the oldest radiometric dates. New dating studies provide higher resolution on the chronology of events, constraining the formation of CAIs and chondrules and accretion of differentiated planetesimals.

Evidence on the nature of magnetic fields in the early solar system has been derived from chondritic meteorites. Chondrites and in particular chondrules, which are millimeter sized silicate spherules formed by rapid melting and cooling, have remanent magnetization records which in some cases date from the time of chondrule formation and accretion of planetesimals. Studies on different meteorite classes, including ordinary and carbonaceous chondrites, have provided contrasting results, with a range of estimates for proto-planetary magnetic fields.

Developments on instrumentation and techniques for rock magnetic and paleointensity analyses are allowing increasing precision. Micromagnetic measurements and a range of geochemical and electronic microscopy analyses are providing unprecedented resolution, characterizing rock magnetic properties at magnetic domain scales. Magnetic hysteresis analyses on individual chondrules from the Allende CV3 chondrite reveal relationships among hysteresis parameters and physical properties (Figure 4). Coercivity, remanent and saturation remanence parameters correlate with chondrule size and density; related to internal chondrule structure, mineralogy and morphology (Flores-Gutierrez *et al*., 2010a,b). Compound, fragmented and rimmed chondrules have distinct hysteresis properties, related to mineral composition (Figure 5).

The remanent magnetization record and paleointensity estimates derived from the Allende and other chondrites support remanent acquisition under influence of internal magnetic fields within parent planetesimals. Rapid differentiation in the first 10 Ma following formation of refractory inclusions and chondrules gave rise to planetesimals with metallic cores (Fig. 7), capable of generating and sustaining dynamo action for million year periods (Weiss and Elkins-Tanton, 2013). Observations on turbulent circumstellar disks also indicate rapid planetesimal formation (Johansen *et al*., 2007), providing a broad perspective for evolution of planetary systems. Paleomagnetic and thermal modeling constrain the evolution of early planetesimals, which might presently be represented by large sized asteroids such as Vesta (Fu *et al*., 2012). The Allende chondrite and other undifferentiated meteorites may have formed by fragmentation from collisions, representing different crustal levels in their parent planetesimals (Figure 8; Carporzen *et al*., 2011; Elkins-Tanton and Weiss, 2011). Constraining the crustal levels, temperature/pressure profiles, role of fluids and conditions for aqueous alteration and metamorphism are

part of the major open questions remaining. Models of heat sources and transfer mechanisms and thermal state evolution are being used to better define accretion processes and possible boundary conditions (Elkins-Tanton *et al*., 2011; Sahijpal and Gupta, 2011). The crustal thickness and layering may have been different, depending on the internal structure, accretion history and size/timing of last major accretion event.

Recent studies of molecular clouds, discovery of exoplanets and detection of magnetic fields in protoplanetary accretion disks are opening new avenues. Integrative interdisciplinary approaches involving astronomical, astrophysical and planetary sciences provide a broad perspective, allowing a better understanding for formation of planetary systems.

Acknowledgments

This study forms part of UNAM PaleoMeteor research program. We thank Carlos Linares, Raquel Díaz, Paloma Díaz and Avedis Urrutia for collaboration in the studies and discussions. Partial economic support from PAPIIT IN-111112 grant is acknowledged. The Allende chondrite samples that are being studied are part of the meteorite collection of the Institute of Astronomy, UNAM.

References

Acton G., *et al*., 2007. Micromagnetic coercivity distributions and interaction in chondrules with implications for paleointensities of the early solar system. *Journal Geophysical Research*, 112, 10.1029/2006JB004655.

Amelin Y., Krot A.N., Hutcheon I.D., Ulyanov A.A., 2002, Lead isotopic ages of chondrules and calcium-aluminum rich inclusions. *Science*, 297, p. 1678-1683.

Arkani-Hamed J., 2001, Paleomagnetic pole positions and pole reversals of Mars. *Geophysical Research Letters*, 28, p. 3409-3412.

Banerjee S.K., Hargraves R.B., 1972, Natural remanent magnetizations of carbonaceous chondrites and the magnetic field in the early solar system. *Earth Planetary Science Letters*, 17, p. 110-119.

Bizarro M., Baker J.A., Haack H., 2004, Mg isotope evidence for contemporaneous formation of chondrules and refractory inclusions, *Nature*, 431, p. 275-278.

Bouvier A., Wadhwa M., 2010. The age of the solar system redefined by the oldest Pb-Pb age of a meteorite inclusion. *Nature Geoscience*, 3, p. 637-641.

Burbine T.H., McCoy T.J., Meibom A., Gladman B., Keil K., 2002, Meteoritic parent bodies: their number and identification. In: Bottke, WF, Cellino A, Paolicchi P, Binzel RP (Eds), Asteroids III, Tucson, Univ. Ariz. Press, p. 653-667.

Butler R.F., 1972, Natural remanent magnetization and thermomagnetic properties of the Allende meteorite. *Earth Planetary Science Letters*, 17, p. 120-128.

Cameron A.G.W., 1988, Origin of the solar system: *Annual Reviews of Astronomy Astrophysics*, 26, p. 441-472.

Carporzen L., Weiss B.P., Elkins-Tanton L.T., Shuster D.L., Ebel D., Gattacceca J., 2011, Magnetic evidence for a partially differentiated carbonaceous chondrite parent body, Proc. National. Academy Sciences, 108, 16, 6386–6389, doi:10.1073/pnas.1017165108.

Choi B.G., McKeegan K.D., Leshin L.A., Wasson J.T., 1997, Origin of magnetite in oxidized CV chondrites: in situ measurement of oxygen isotope compositions of Allende magnetite and olivine. *Earth Planetary Science Letters*, 146, p. 337-349.

Cisowski S.M., Collinson D.W., Runcorn S.K., Stephenson A., 1983, A review of lunar paleointensity data and implications for the origin of lunar magnetism. *Journal Geophysical Research*, 88, p. A691-A704.

Clarke R.S., Jarosewich E., Mason B., Nelen J., Gomez M., Hyde J.R., 1970, The Allende, Mexico, meteorite shower. Smithsonian Contributions Earth Sciences, 5, p. 1-53.

Coe R.S., 1967, Paleo-intensities of the Earth's magnetic field determined from Tertiary and Quaternary rocks, *Journal Geophysical Research*, 72, p. 3247–3262.

Connelly J.N., Bizarro M., Krot A.N., Nordlunz A., Wieland D., Ivanova M.A., 2012, The absolute chronology and thermal processing of solids in the solar protoplanetary disk. *Science*, 338, p. 651-655.

Cuzzi J.N., Alexander C.M.O.D., 2006, Chondrule formation in particle-rich nebular regions at least several hundred of kilometers across. *Nature*, 441, p. 483-485.

Davis P.M., Evans M.E., 1976, Interacting single-domain properties of magnetite intergrowths. *Journal Geophysical Research*, 81, p. 989-994.

Day R., Fuller M., Schmidt V.A., 1977, Hysteresis properties of titanomagnetites: Grain size and compositional dependence, *Physics Earth Planetary Interiors*, 13, 4, p. 260–267, doi:10.1016/0031-9201(77)90108-X.

Donati J.F., Paletou F., Bouvier J., Ferreira J., 2005, Direct detection of a magnetic field in the innermost regions of an accretion disk, *Nature*, 438, 466–469, doi:10.1038/nature04253.

Dunlop D.J., Ozdemir Ö., 1997, Rock Magnetism: Fundamentals and Frontiers. Cambridge Univ. Press, Cambridge, 573 pp.

Dunlop D.J., Yu Y., 2003, Testing an inverse Thellier method of paleointensity determination. *Journal Geophysical research*, 108 doi:1029/2003JB002469

Elkins-Tanton L.T., Weiss B.P., Zuber M.T., 2011, Chondrites as samples of differentiated planetesimals. *Earth Planetary Science Letters*, 305, p. 1-10.

Emmerton S., Muxworthy A.R., Hezel D.C., Bland P.A., 2011, Magnetic characteristics of CV chondrules with paleointensity implications. *Journal Geophysical Research*, 116, E12007.

Feinberg J.M., Harrison R.J., Kasama T., Dunin-Borkowski R.E., Scott G.R., Renne P.R., 2006, Effects of internal mineral structures on magnetic remanence of silicate-hosted titanomagnetite inclusions: an electron holography study, *Journal Geophysical Research*, 111, B12S15, doi:10.1029/2006JB004498.

Flores-Gutierrez D., Urrutia Fucugauchi J., 2002, Hysteresis properties of chondritic meteorites-New results for chondrules from the Allende meteorite. *Geofísica Internacional*, 41, p. 179-188.

Flores-Gutiérrez D., Urrutia-Fucugauchi J., Pérez-Cruz L., Linares-López C., 2010a, Micromagnetic and microstructural analyses in chondrules of the Allende meteorite. *Revista Mexicana de Ciencias Geologicas*, 27, p. 162-174.

Flores-Gutiérrez D., Urrutia-Fucugauchi J., Pérez-Cruz L., Diaz, R. and Linares-López, C., 2010b, Scanning electron microscopy characterization of iron, nickel and sulfur in chondrules from the Allende meteorite - Further evidence for between-chondrules major compositional differences. *Revista Mexicana de Ciencias Geologicas*, 27,p. 338-346.

Fu R.R., Elkins-Tanton L., 2013, The fate of magmas in planetesimals and the retention of primitive chondritic crusts. *Earth Planetary Science Letters*, 390, p. 128-132.

Fu R.R., Weiss B.P., Shuster D.L., Gattacceca J., Grove T.L., Suavet C., Lima E.A., Li L., Kuan A.T., 2012, An ancient core dynamo in asteroid Vesta. *Science*, 338, p. 238-241.

Fuller M.D., Cisowski S.M., 1987, Lunar paleomagnetism. In: Jacobs, J.A. (Ed), Geomagnetism 2, Academic Press, Orlando, p. 307-455.

Gattacceca J., Rochette P., 2004, Toward a robust normalized magnetic paleointensity method applied to meteorites. *Earth and Planetary Science Letters*, 227, p. 377- 393.

Goldstein J.I., Scott E.R.D., Chabot N.L., 2009, Iron meteorites: Crystallization, thermal history, parent bodies, and origin. *Chemie der Erde*, 69, p. 293-325.

Greenwood R.C., Franchi I.A., Kearsley A.T., Alard O., 2010, The relationship between CK and CV chondrites. *Geochimica Cosmochimica Acta*, 74, p.1684–705.

Harrison R.J., Dunin-Borkowski R.E., Putnis A., 2002, Direct imaging of nanoscale interactions in minerals. *Proceedings National Academy Sciences*, 99, p. 16556-16561.

Hewins R.H., 1997, Chondrules. Annual Reviews *Earth Planetary Sciences*, 25, 619–659.

Hewins R.H., Jones R.H., Scott E.D.R. (Eds), 1996, Chondrules and the Protoplanetary Disk. Cambridge University Press, Cambridge, U.K.

Huss G.R., Rubin A.E., Grossman J.N., 2006, Thermal metamorphism in chondrites. In: Lauretta D.S. and McSween, H.Y. (Eds),

Meteorites and the Early Solar System II. University Arizona Press, Tucson, pp. 567–586.

Itoh S., Yurimoto H., 2003, Contemporaneous formation of chondrules and refractory inclusions in the early Solar System. *Nature*, 423, p. 728-731.

Johansen A., Oishi J.S., MacLow M.M., Klahr H., Henning T., Youdin A., 2007, Rapid planetesimal formation in turbulent circumstellar disks. *Nature*, 448, p. 1022-1025.

Kleine T., Munker C., Mezger K., Palme H., 2002, Rapid accretion and early core formation on asteroids and the terrestrial planets from Hf-W chronometry. *Nature*, 418, p. 952-955.

Kring D., 1991, High temperature rims around chondrules in primitive chondrites: evidence for fluctuating conditions in the solar nebula. *Earth Planetary Science Letters*, 105, p. 65-80.

Krot A.N., Scott E.R.D., Zolensky M.E., 1995, Mineralogical and chemical modification of components in CV3 chondrites: Nebular or asteroidal processing? *Meteoritics*, 30, p. 748-775.

Krot A.N., Yurimoto H., Hutcheon I.D., MacPherson G.J., 2005, Chronology of the early Solar System from chondrule-bearing calcium-aluminium rich inclusions. *Nature*, 434, p. 998-1001.

Kulsrud R.M., 1999, A critical review of galactic dynamos. *Annual Reviews Astronomy Astrophysics*, 37, 37-64.

Lanoix M., Strangway D.W., Pearce G.W., 1978, The primordial magnetic field preserved in chondrules of the Allende meteorite. *Geophysical Research Letters*, 5, p. 73-76.

Lauretta D.S., McSween H.Y. (Eds), 2006, Meteorites and the Early Solar System II. Tucson: University of Arizona Press, 943 pp

Lawrence K., Johnson C., Tauxe L., Gee J., 2008, Lunar paleointensity measurements: implications for lunar magnetic evolution. *Physics Earth Planetary Interiors*, 168, p.71-87.

Lauretta D.S., McSween H.Y., 2006, Meteorites and the Early Solar System II. Univ. Arizona Press

Lee T., Papanastassiou D.A., Wasserburg G.J., 1976, Demonstration of Mg excess in Allende and evidence for Al. *Geophysical Research Letters*, 3, p. 109-112.

Lillis R.J., Robbins S., Manga M., Halekas J.S., Frey H.V., 2013, Time history of the Martian dynamo from crater magnetic field analysis. *Journal Geophysical Research*, 118, p. 1-24 doi:10.1002/jgre.20105.

Macke R.J., Consolmagno G.J., Britt D.T., Hutson M.L. 2010, Enstatite chondrite density, magnetic susceptibility and porosity. *Meteoritics & Planetary Science*, 45, p. 1513–1526.

Macke R.J., Britt D.T., Consolmagno G.J., 2011, Density, porosity and magnetic susceptibility of achondritic meteorites. *Meteoritics & Planetary Science*, 46, p. 311–326.

McMahon B.M., Haggerty S.E., 1980, Experimental bearing on the magnetite-alloy-sulfide association in the Allende meteorite: constraints on the conditions of chondrule formation. Proceed. Lunar Planetary Science Conerence 11th, p. l003-1025.

McSween H.Y., 1979, Are carbonaceous chondrites primitive or processed? A review. *Reviews Geophysics Space Physics*, 17, p. 1059-1078.

McSween H.Y., 1987, Aqueous alteration in carbonaceous chondrites: Mass balance constraints on matrix mineralogy. Geochimica Cosmochimica Acta, 51, p. 2469-2477.

Muxworthy A.R., Heslop D., Paterson G.A., Michalk D., 2011, A Preisach methodology to determining absolute paleointensities: 2. Field testing, *Journal Geophysical Research*, 116, B04103, doi:10.1029/2010JB007844.

Nagata T., 1979, Meteorite magnetism and the early solar system magnetic field. *Physics Earth Planetary Interiors*, 20, p. 324-341.

Nakamura T. *et al*., 2011, Itokawa dust particles: A direct link between S-type asteroids and ordinary chondrites. *Science*, 333,1113-1116 DOI: 10.1126/science.1207758

Nyquist L.E., Kleine T., Shih C.Y., Reese Y.D., 2009, The distribution of short-lived radioisotopes in the early solar system and chronology of asteroid accretion, differentiation and secondary mineralization. *Geochimica and Cosmochimica Acta*, 73, p. 5115-5136.

Ossendrijver M., 2003, The solar dynamo. *Astron. Astrophys. Reviews*, 11, p. 287-367.

Rochette P., Sagnotti L., Bourot-Denise M., Consolmagno G., Folco L., Gattacceca J., Osete M.L., Pesonen L., 2003, Magnetic classification of stony meteorites; 1, Ordinary chondrites, *Meteoritics Planetary Sciences*, 38, p. 251– 268.

Rochette P., Gattacceca J., Bourot-Denise M., Consolmagno G., Folco L., Kohout T., Pesonen L., Sagnotti L., 2009, Magnetic classification of stony meteorites: 3. Achondrites, Meteorit. Planet. *Science*, 44, p. 405–427, doi:10.1111/j.1945-5100.2009.tb00741.x.

Rubin A.E., 2000, Petrologic, geochemical and experimental constraints on models of chondrule formation, *Earth-Science Reviews*, 50, p. 3–27.

Sahijpal S., Gupta, G., 2011, Did the carbonaceous chondrites evolve in the crustal regions of partially differentiated asteroids?, *Journal Geophysical Research*, 116, E06004

Scott E.R.D., 2007, Chondrites and the protoplanetary disk. *Annual Reviews Earth Planetary Sciences*, 35, p. 577-620.

Scott E.R.D., Fuller M.D., 2004, A possible source for the Martian crustal magnetic field. *Earth Planetary Science Letters*, 220, p. 83-90

Sterenborg M.G., Crowley J.W., 2013, Thermal evolution of early solar system planetesimals and the possibility of sustained dynamos. *Physics Earth Planetary Interiors*, 214, p. 53-73.

Sugiura N., Strangway D.W., 1983, A paleomagnetic conglomerate test using the Abee E4 meteorite. *Earth Planetary Science Letters*, 62, p. 169-179.

Sugiura N., Lanoix M., Strangway D.W., 1979, Magnetic fields of the solar nebula as recorded in chondrules from the Allende meteorite. *Physics of the Earth and Planetary Interiors*, 20, p. 342-349.

Tarduno J.A. *et al*., 2012, Evidence for a dynamo in the main group pallasite parent body. *Science*, 338, p. 939-942.

Taylor G.J., Maggione P., Scott E., Rubin A., Keil K., 1987, Original structures, and fragmentation and reassembly histories of asteroids: evidence from meteorites. *Icarus*, 69, p. 1-13.

Uehara M., Nakamura N., 2006 Experimental constrains on magnetite stability of chondrules and the paleomagnetic significance of dusty olivines. *Earth Planetary Science Letters*, 250, p. 292-305.

Uehara M., Gattacceca J., Leroux H., Jacob D., van der Beek C.J., 2011, Magnetic microstructures of metal grains in equilibrated ordinary chondrites and implications for paleomagnetism of meteorites, *Earth Planet. Sci. Lett*., doi:10.1016/j.epsl.2011.04.008.

Urrutia-Fucugauchi J., 1979, Further reliability tests for determination of palaeointensities of the Earth's magnetic field. Geophysical *Journal Royal Astronomical Society*, 61, p. 243-251

Urrutia-Fucugauchi J., Radhakrishnamurthy C., Negendank J.F.W., 1984, Magnetic properties of a columnar basalt from central Mexico. *Geophysical Research Letters*, 11, p. 832-835.

Vallée J.P., 2011, Magnetic fields in the nearby Universe, as observed in solar and planetary realms, stars, and interstellar star forming nurseries. *New Astron. Rev*., 55, p. 23-90.

Van Schmus W.R., Wood J.A., 1967, A chemical-petrologic classification for the chondritic meteorites, *Geochimica Cosmochimica Acta*, 31, p. 747–765, doi:10.1016/S0016-7037(67)80030-9.

Wasilewski P., 1981, New magnetic results from Allende C3(V). *Physics of the Earth and Planetary Interiors*, 26, p. 134-148.

Wasson J.T., 1990, Ungrouped iron meteorites in Antarctica: origin of anomalously high abundance. *Science*, 249, p. 900–902.

Weisberg M.K., McCoy T.J., Krot A.N., 2006, Systematics and Evaluation of Meteorite Classification Meteorites and the Early Solar System II, D. S. Lauretta and H. Y. McSween Jr. (eds.), University of Arizona Press, Tucson, p.19-52

Weiss B.P., Berdhal J.S., Elkins-Tanton L., Stanley S., Lima E.A., Carporzen L., 2008, Magnetism on the angrite parent body and the early differentiation of planetesimals. *Science*, 322, p. 713-716.

Weiss B., Gattacceca J., Stanley S., Rochette P., Christensen U., 2010, Paleomagnetic records of meteorites and early planetesimal differentiation, *Space Science Reviews*, 152, p. 341–390.

Weiss B.P., Elkins-Tanton L.T., 2013, Differentiated planetesimals and the parent bodies of chondrites. *Annual Reviews Earth Planetary Sciences*, 41, p. 529-560.

Wood J.A., 1988, Chondritic meteorites and the solar nebula. *Annual Reviews Earth Planetary Sciences*, 16, p. 53-72.

Yu Y., 2006, How accurately can NRM/SIRM determine the ancient planetary magnetic field intensity? *Earth Planetary Science Letters*, 250, p. 27-37.

Zanda B., 2004, Chondrules. *Earth Planetary Science Letters*, 224, p. 1-17.